Contactless Voltage Measurements and Their Applications for Silicon and Tandem Cells

Soma Zandi

A thesis in fulfilment of the requirements for the degree of

Doctor of Philosophy

School of Photovoltaic and Renewable Energy Engineering

Faculty of Engineering

The University of New South Wales

October 2025

Abstract

The acceleration of climate change and global warming motivates the urgent need for our transition to low-carbon and renewable energy sources. Among these, photovoltaic (PV) devices have emerged as the lowest cost and most rapidly growing technologies, with silicon (Si) solar cells currently dominating the PV market. However, as Si solar cells approach their theoretical efficiency limits, tandem devices, particularly perovskite/silicon (PVK/Si) configurations, are emerging as a highly promising next-generation technology. Despite their impressive efficiency potential, PVK/Si tandem cells face considerable challenges, including non-uniform degradation and accelerated performance losses. Addressing these issues requires advanced characterisation techniques to accurately identify the underlying sources of performance loss. Photoluminescence (PL) and electroluminescence (EL) imaging are powerful tools for evaluating the optoelectronic properties of semiconductor devices. Both techniques can provide spatially resolved data of the implied voltage ($\mathrm{i}V$), a critical parameter for assessing single-junction devices, and individual analysis of subcells in tandem and multijunction devices. Extracting quantitative $\mathrm{i}V$ information from luminescence signals requires a calibration process and, in practice, conventional calibration methods are hindered by optical variations between samples. This necessitates repeated calibration for distinct device structures, making the process time-consuming and impractical for rapid diagnostics in industrial or early-stage research fabrication settings.

To overcome this limitation, this thesis introduces a novel and robust calibration approach that simplifies the process through the selection of an appropriate optical filter. By restricting the detection range to the high-energy tail of luminescence emission, the influence of sample-specific optical variations on the luminescence signal is reduced to negligible levels. This allows rapid quantification of $\mathrm{i}V$ images without requiring detailed knowledge or optical characterisation of each sample. The accuracy of the method is validated on both Si solar cells and PVK/Si tandem devices with distinctly different optoelectronic properties. A detailed uncertainty analysis is also presented to assess the robustness and broader applicability of the proposed method.

Building on the capabilities of contactless and universal luminescence imaging, this thesis also presents a PL-based technique to determine intrinsic carrier concentration (n_i), a key semiconductor parameter. By integrating the novel iV calibration process with a previously established dynamic calibration method for excess carrier concentration extraction, n_i can be obtained in a fully contactless manner. This approach eliminates the complexities associated with conventional experimental techniques that depend on detailed knowledge of material properties or specific device structures. This is particularly useful for determining n_i within emerging semiconductors, such as PVK devices, where material parameters are subject to significant uncertainty.

The developed calibration methods in this thesis enable rapid voltage-loss diagnosis, defect localisation, and materials benchmarking, all of which are essential for addressing the performance limits of PVK/Si tandem cells and future high-efficiency multijunction devices. The techniques are generalisable and applicable to a broad range of PV and emerging semiconductor materials. This work has provided a practical and scalable framework for advancing semiconductor modelling and analysis, supporting global R&D efforts toward high-throughput manufacturing of next-generation PV devices.

Acknowledgement

I would like to express my gratitude to my supervisor, Ziv Hameiri, for his guidance and commitment throughout my PhD. He motivated me to think more critically and refine my ideas. His detailed feedback on papers, presentations, and thesis drafts, along with countless dry runs before conferences, helped me grow in both understanding and clarity. His mentorship provided skills and insights that strengthened the quality of my research. My sincere thanks also go to my joint supervisor, Thorsten Trupke, whose knowledge and valuable feedback helped me see problems from new angles. His patience in explaining complex concepts, from the basics upward, gave me a deeper understanding that enriched my learning and strengthened this thesis.

I owe special thanks to Juergen Weber for his exceptional support in the lab and his thoughtful advice. His technical expertise and patient, step-by-step explanations for building experimental setups were invaluable to my work. I am grateful to my secondary supervisors, Yan Zhu and Shuai Nie, for their mentorship and support throughout my PhD. I also extend my thanks to Arman Mahboubi Soufiani, whose supervision during my first year helped me settle into the group and understand the fundamental concepts.

Being part of the ACDC research group was a privilege. I was fortunate to work with colleagues who were always willing to share their expertise and encouragement. I would like to thank all members: Abhnil Prasad, Ahilan Kanagasundaram, Ali Shakiba, Anh Huy Tuan (Anh) Le, Aryan Aryan, Aref Samedi, Arthur Julien, Brendan Wright, Felix Gayot, Gaia Maria Nolasco Javier, Grace Liu, Hugo Bucquet, Ivar Raheim, John Rodriguez, Juergen Weber, Simon Zhang, Tanushree JB Nath, Lucas Ehret, Oliver Fischer, Rodrigo del Prado Santamaria, Zi Lin, Priya Dwivedi, Robert (μRob) Lee Chin, Chang (Ryan) Sun, Saman Jafari, Yoann Buratti, Sijin Wang, Rama Sharma, Yun Li, Zhiwen Zheng, and Zubair Abdullah-Vetter. A special thanks to Zubair Abdullah-Vetter, Saman Jafari, and Yoann Buratti for their early support in helping me adjust. I'm especially grateful to Gaia and Tanushree for their friendship, support in research and daily life, and for always cheering me up. I sincerely thank John Rodriguez for his thoughtful advice, positive energy, motivation, and the generous time he gave me throughout my PhD. I'm also grateful to μRob for his incredible support, particularly during my first international conference. My appreciation

extends to Lab 360 members, particularly Oliver Kunz and Gerold Kloos, for their support. Thank you all for making this journey enjoyable.

I would like to acknowledge my review panel members, Gavin Conibeer, Stephen Bremner, and Mahesh Suryawanshi, for their constructive feedback during the annual reviews. My thanks also go to the LDOT team at SPREE, especially Bernhard Vogl, Kian Chin, and Alan Yee, for their assistance with lab access, including after hours. I am also grateful to N. J. Ekins-Daukes and Julie Lui for their help in keeping my PhD on track and to the SPREE administrative team for their assistance. Finally, I would like to thank all members of SPREE whose kindness made my time here enjoyable.

This work was supported by many external collaborators. I sincerely appreciate Daniel MacDonald and his group at the Australian National University (ANU), in particular Anh Dinh Bui, Khoa Nguyen, Lachlan Black, Maureen Brauers, and Kean Chern Fong, for welcoming me during my visit and providing generous help with experiments in Chapter 5. I also thank Wei Wang and Dang-Thuan Nguyen at ANU for providing single-junction perovskite cells used in Chapter 5. At the University of New South Wales (UNSW), I sincerely thank Hamid Mehrvarz and Anh Le for providing silicon solar cells used in Chapters 3 and 6, as well as Ziyue Feng and Xu Liu for supplying the single-junction perovskite devices used in Chapters 4 and 5. I would also like to acknowledge Jianghui Zheng and Guoliang Wang at the University of Sydney (USYD) for providing both single-junction perovskite and perovskite/silicon tandem devices used in Chapters 4 and 5. Finally, my thanks go to Thomas G. Allen, Erkan Aydin, and Esma Ugur at King Abdullah University of Science and Technology (KAUST) for supplying additional perovskite/silicon tandem devices used in Chapters 4 and 5.

I gratefully acknowledge the financial support provided by the Australian Government through the Australian Renewable Energy Agency (ARENA) and the Australian Centre for Advanced Photovoltaics (ACAP) throughout my PhD.

Beyond research, I truly appreciate my friends and all those who helped me reach this milestone. To Arastoo Temouri, Zahra Donyavi, Sharareh Akbarian, Zeinab Ebrahimi, Keivan Rahimi, Sara Sharifi, Elaheh Ghodusi, Parisa Hosseinabadi, Xinyao (Grace) Guo, Chaudhry Furqan, Ryan Hall, Yuhao Cheng, Mohsen Jamshidi Seresht, Asiyeh Kheradmand, Sareh Shahrabifarahani, Yousof Haghshenas, Hugh Gottlieb, Ayush Pratik, Natalie Vivas, Svetlana Postnova, Asma Zandi, and Sebastian Raison, thank you for always cheering me up and encouraging me along the way. I am especially grateful to my friend Svetlana Postnova and Sebastian Raison, whose care, advice, and positivity helped me manage the most

stressful months of my PhD. To my cousin and close friend Asma, thank you for always motivating me and lifting my spirits, even from afar.

My deepest thanks go to my family. To my parents, for their unconditional love and belief in me, which gave me the strength to continue even during the most challenging moments of immigration. To my siblings, Behzad, Rezgar, and Seiran, for always supporting me as the youngest in the family, and for stepping in to care for our parents when I could not, something I sincerely appreciate. Behzad and Rezgar, thank you for the strength, care, and sense of security you have always provided. And to my sister Seiran: from the very beginning, you have helped shape the person standing here today, writing the acknowledgments of this PhD thesis. Your support, your courage to explore new things, and your encouragement to look beyond obstacles and see possibilities have always guided me. You have brightened my path and helped me grow into a stronger and better version of myself. Thank you for being so patient, for reminding me not to doubt myself, and for inspiring me to follow my dreams even when things were not going well. Your understanding and willingness to help have gone far beyond what anyone could expect from a sister.

Table of contents

Abbreviations and Symbols

Abbreviations

AlGaInP	Aluminium gallium indium phosphide
AMP	Preamplifiers
BGN	Bandgap narrowing
BPF	Bandpass filter
C_{60}	Fullerene
CCD	Charge-coupled device (camera sensor)
CMOS	Complementary metal–oxide–semiconductor (camera sensor)
c-Si	Crystalline silicon
DAC	Data acquisition card
DDT	1-dodecanethiol
DRM	Depletion region modulation
EL	Electroluminescence
EQE	External quantum efficiency
ETL	Electron transport layer
HJT	Heterojunction
HTL	Hole transport layer
IBC	Interdigitated back contact
InGaAs	Indium gallium arsenide (detector material)
ITO	Indium tin oxide
I–V (J–V)	Current–voltage (current density–voltage)
IZO	Indium zinc oxide
KCl	Potassium chloride
LC	Luminescence coupling
LCOE	Levelised cost of electricity
LED	Light-emitting diode

LiF	Lithium fluoride
LPF	Longpass filter
MPP	Maximum power point
NA	Numerical aperture
non-QSS	Non-quasi-steady-state
PC	Photoconductance
PD	Photodiode
PERC	Passivated emitter and rear contact
Ph-2PACz	(2-(3,6-diphenyl-9H-carbazol-9-yl)ethyl) phosphonic acid
PL	Photoluminescence
Pseudo-dark J–iV	Pseudo-dark current density–implied voltage
PVK	Perovskite
QSS	Quasi-steady-state
RF	Radio-frequency
ROI	Region of interest
Si	Silicon
SMU	Source-measure unit
SnO_2	Tin oxide
SNR	Signal-to-noise ratio
SPF	Shortpass filter
Spiro-OMeTAD	2,2′,7,7′-tetrakis(N,N-di-p-methoxyphenylamine)-9,9′-spirobifluorene
SQ	Shockley-Queisser
STC	Standard test condition
2PACz	[2-(9H-carbazol-9-yl)ethyl] phosphonic acid

Symbols

q	Elementary charge [1.602×10^{-19} C]
k_B	Boltzmann constant [8.617×10^{-5} $\mathrm{eV \cdot K^{-1}}$]
h	Planck’s constant [4.1357×10^{-15} $\mathrm{eV \cdot s}$]
c	Speed of light in vacuum [2.998×10^{10} $\mathrm{cm \cdot s^{-1}}$]
V_T	Thermal voltage [V]
E_g	Bandgap [eV]
n_i	Intrinsic carrier concentration [$\mathrm{cm^{-3}}$]
$n_\mathrm{i,eff}$	Effective intrinsic carrier concentration [$\mathrm{cm^{-3}}$]
B_rad	Radiative recombination coefficient [$\mathrm{cm^{3} \cdot s^{-1}}$]
C	Wavelength-independent calibration constant
α	Absorption coefficient [$\mathrm{cm^{-1}}$]
n_r	Refractive index
k	Extinction coefficient
n, p	Electron, hole concentration [$\mathrm{cm^{-3}}$]
N_dop	Doping density [$\mathrm{cm^{-3}}$]
$\Delta n, \Delta p$	Excess electron, hole concentrations [$\mathrm{cm^{-3}}$]
μ_n, μ_p	Electron, hole mobilities [$\mathrm{cm^{2} \cdot V^{-1} \cdot s^{-1}}$]
τ	Carrier lifetime [s]
G	Generation rate [$\mathrm{cm^{-3} \cdot s^{-1}}$]
$\Delta\sigma$	Change in photoconductance [$\mathrm{S \cdot cm^{-1}}$]
d	Thickness [μm]
E_i	Intrinsic Fermi level [eV]
$E_\mathrm{fn}, E_\mathrm{fp}$	Electron, hole quasi-Fermi level [eV]
$\Delta\mu$	Quasi-Fermi level splitting [eV]
λ	Wavelength [nm]
E	Photon energy [eV]
λ_1	Cut-on wavelength (lower edge of the detection band) [nm]
λ_2	Cut-off wavelength (upper edge of the detection band) [nm]
R	Front reflectance

R_{tot}	Total reflectance
T_{trans}	Transmittance
A_{tot}	Total absorptivity
A_{BB} (=A)	Band-to-band absorptivity
A	Absorptivity
A_{BB}	Band-to-band absorptivity
A_{FC}	Free-carrier absorptivity
EQE	External quantum efficiency
η_c	Carrier collection efficiency
ϕ_{inc}	Photon flux of the incident light [$\mathrm{cm}^{-2}\cdot\mathrm{s}^{-1}$]
ϕ_{BB}	Blackbody spectral photon flux per unit wavelength [$\mathrm{cm}^{-2}\cdot\mathrm{s}^{-1}\cdot\mathrm{nm}^{-1}$] or energy [$\mathrm{cm}^{-2}\cdot\mathrm{s}^{-1}\cdot\mathrm{eV}^{-1}$]
$\Delta\phi_{\mathrm{BB}}$	Spectrally integrated of the blackbody photon flux [$\mathrm{cm}^{-2}\cdot\mathrm{s}^{-1}$]
ϕ^{absolute}	Absolute luminescence spectral photon flux per unit wavelength [$\mathrm{cm}^{-2}\cdot\mathrm{s}^{-1}\cdot\mathrm{nm}^{-1}$] or energy [$\mathrm{cm}^{-2}\cdot\mathrm{s}^{-1}\cdot\mathrm{eV}^{-1}$]
ϕ^{detect}	Detected luminescence spectrum [a.u.]
$\Delta\phi^{\mathrm{detect}}$	Spectrally integrated detected luminescence [a.u.]
X_{calib}	Corresponding parameters to the calibration device
X_{cell}	Corresponding parameters to the measured device
X_{light}	Corresponding parameters to the calibration lamp
$\mathrm{QE}_{\mathrm{camera}}$	Quantum efficiency of the camera
f	Overall spectral response of the detection system
f_1	Scaling constant for the fraction of luminescence collected by the detector
f_2	Wavelength-dependent optical response of the system
$\mathrm{i}V$	Implied voltage [V]
V_{oc}	Open-circuit voltage [V]
V_{term}	Terminal voltage [V]
$\mathrm{i}V_{\mathrm{true}}$	True implied voltage in modelling [V]
J_{sc}	Short-circuit current density [$\mathrm{A}\cdot\mathrm{cm}^{-2}$]
J	Current density [$\mathrm{A}\cdot\mathrm{cm}^{-2}$]
J_{ph}	Photocurrent density [$\mathrm{A}\cdot\mathrm{cm}^{-2}$]
J_0	Diode saturation current density [$\mathrm{A}\cdot\mathrm{cm}^{-2}$]

n_{d}	Ideality factor
R_{s}	Series resistance [$\Omega\cdot\mathrm{cm}^2$]
R_{sh}	Shunt resistance [$\Omega\cdot\mathrm{cm}^2$]
P_{max}	Maximum output power per unit area [$\mathrm{W}\cdot\mathrm{cm}^{-2}$]
FF	Fill factor
η	Power conversion efficiency [%]
T	Temperature [°C][*]
T_{set}	Setpoint temperature [°C]
p	Optical path-length enhancement factor
A_{i}	Calibration constant linking luminescence intensity to excess carrier density
S_{c}	Signal recorded by the camera after dark subtraction [counts]
N_{c}	Total noise reported by the camera [counts]
g	Camera gain [electrons/count]
S_{e}	Measured signal in photoelectrons [electrons]
N_{e}	Total noise in photoelectrons [electrons]
N_{dark}	Dark-noise contribution [electrons]
N_{read}	Read-noise contribution [electrons]
N_{shot}	Shot-noise contribution [electrons]
$^{\dagger}I_{\mathrm{dark}}$	Dark current [A]
t_{exp}	Exposure time [s]
t	Time [s]
t_G	Illumination duration [s]
$\delta\mathrm{i}V$	Total uncertainty in iV [V]
$\delta R_{\mathrm{F/B}}$	Uncertainty in iV from front/back reflectance [V]
δE_{g}	Uncertainty in iV from bandgap mismatch [V]
δT_{temp}	Uncertainty in iV from temperature variation [V]
$\delta n_{\mathrm{i},\Delta n}$	Uncertainties in n_{i} due to Δn [%]
$\delta n_{\mathrm{i,i}V}$	Uncertainties in n_{i} due to iV [%]
δn_{i}	Total uncertainty in n_{i} [%]

---

[*] All temperatures are reported in °C. The use of K in specific cases, such as theoretical equations, is explicitly noted.

Publication List

Journal publications

1. **S. Zandi**, S. Nie, Y. Zhu, T. G. Allen, E. Aydin, E. Ugur, J. Zheng, G. Wang, X. Liu, X. Hao, A. Ho-Baillie, S. De Wolf, T. Trupke, Z. Hameiri, "Luminescence-based implied voltage imaging of tandem solar cells using bandpass filters," *Small Methods*, vol. 9, p. 2401003, 2025. (S. Zandi and S. Nie contributed equally to this work)
2. F. Gayot, Y. Zhu, J. W. Weber, Z. Zheng, **S. Zandi**, Z. Feng, M. Zhang, T. Hou, J. Liu, Y. Huang, X. Hao, Z. Hameiri, "Outdoor implied open-circuit voltage imaging of perovskite solar cells using sunlight excitation," *Joule,* vol. 9, p. 101946, 2025.
3. **S. Zandi**, Z. Hameiri, A. M. Soufiani, J. W. Weber, T. Trupke, "Simplified method for the conversion of luminescence signals from silicon wafers and solar cells into implied voltages," *Solar Energy Materials and Solar Cells*, vol. 269, p. 112716, 2024.

Conference publications

1. **S. Zandi**, S. Nie, Y. Zhu, T. G. Allen, E. Aydin, E. Ugur, J. Zheng, G. Wang, X. Liu, A. Ho-Baillie, X. Hao, S. De Wolf, T. Trupke, Z. Hameiri, "Implied voltage of subcells in tandem devices from luminescence images – The beauty of using a narrow bandpass filter," 41st European Photovoltaic Solar Energy Conference, 2024. **(Nominated for the Best Student Paper Award)**
2. **S. Zandi**, Y. Zhu, A. H. T. Le, J. W. Weber, R. L. Chin, T. Trupke, Z. Hameiri, "Contactless approach for estimating intrinsic carrier concentration using luminescence measurements," Asia Pacific Solar Research Conference, 2024.
3. F. Gayot, Y. Zhu, J. W. Weber, R. L. Chin, **S. Zandi**, Z. Hameiri, "Contactless external quantum efficiency measurements of non-silicon solar cells," Asia Pacific Solar Research Conference, 2024.
4. F. Gayot, R. L. Chin, Y. Zhu, **S. Zandi,** J. W. Weber, Z. Hameiri, "Contactless external quantum efficiency evaluation of perovskite solar cells," 52nd IEEE Photovoltaic Specialist Conference, 2024.

5. **S. Zandi**, A. M. Soufiani, J. W. Weber, Z. Hameiri, T. Trupke, “Novel method for the extraction of implied voltages of silicon wafers and solar cells from luminescence-based measurements,” 40th European Photovoltaic Solar Energy Conference, 2023. **(Won the Best Student Paper Award)**
6. **S. Zandi**, S. Nie, R. L. Chin, Y. Zhu, J. W. Weber, J. Zheng, A. Ho-Baillie, T. Trupke, Z. Hameiri, “Implied voltage images of each subcell in perovskite/Si tandem solar cells using luminescence measurements”, Asia Pacific Solar Research Conference, 2023. **(Nominated for the Best Student Paper Award)**
7. S. Nie, **S. Zandi**, R. L. Chin, Y. Zhu, J. W. Weber, G. Wang, J. Zheng, A. Ho-Baillie, Z. Hameiri, “Luminescence-based implied voltage imaging of tandem solar cells via bandpass filter method,” 34th International Photovoltaic Science and Engineering Conference, 2023.

Chapter 1 – Introduction

We are in a state of climate emergency, where global warming poses a clear and escalating threat to both ecological systems and human societies. According to the National Aeronautics and Space Administration (NASA) [1], the global average surface temperature has increased steadily since the late 19th century, with a pronounced acceleration in recent decades. In 2024, the temperature reached a historic peak, with Earth's surface averaging 1.47 °C above the pre-industrial (1850–1900) baseline, highlighting the urgency of climate action [1]. This continued rise in temperature is expected to intensify extreme weather events, accelerate sea-level rise, and disrupt both ecological and human well-being. According to the Intergovernmental Panel on Climate Change (IPCC), carbon dioxide (CO_2) emissions are the most significant contributor to global warming, accounting for approximately 66% of the total warming effect from all greenhouse gases [2]. Therefore, reducing CO_2 emissions is a critical strategy for slowing the rate of global warming. To achieve this, transitioning to renewable energy sources is essential, as it directly reduces the use of fossil fuels, the primary source of CO_2 emissions.

Photovoltaic (PV) technologies, by converting solar energy into electricity, are widely recognised as one of the most abundant, scalable, and cost-effective solutions for decarbonising the global energy system. In just one hour, the sun supplies more energy than the world's annual electricity demand, highlighting its potential to meet long-term global needs [3]. The modular design of PV systems allows installation in diverse environments, from individual rooftops to large-scale utility farms, supporting both decentralised and centralised energy solutions [4, 5].

Furthermore, over the past decade, PV technology has become increasingly affordable. The levelised cost of electricity (LCOE) for utility-scale solar PV has dropped by nearly 83%, from an average of USD 358/MWh in 2009 to USD 58/MWh in 2025 [6], and is projected to further decline to around USD 20/MWh by 2050 [7]. The global PV market is undergoing robust expansion, with projections indicating a substantial surge to approximately USD 2.8 trillion by 2034, growing at a compound annual growth rate of 21.5% from 2025 to 2034 [8]. In 2024, PV installations reached a record of 597 GW, marking a substantial 33% increase over 2023, with solar energy contributing a remarkable 81% of all new renewable capacity added worldwide [9]. Hence, it is predicted that PV will become the leading force in renewable energy growth by the end of this decade [5].

1.1 Thesis motivation and objective

Single-junction crystalline silicon (c-Si) solar cells have dominated the global PV market, with a market share of over 98% of the total solar cell installations [5]. Its continued dominance in the PV industry stems from the abundance of the Si material [10, 11], a suitable bandgap (E_g) for light harvesting [11-13], material stability [11, 14], and compatibility with a broad range of applications, from residential rooftops to utility-scale power plants [10, 11, 15-18]. Decades of dedicated development have steadily advanced c-Si efficiency, bringing the technology to a mature and industrially optimised state [11, 17, 18].

Extensive research and industrial development have led to remarkable efficiencies exceeding 27% [19], approaching their theoretical limit of ~29.4%, known as the Shockley-Queisser (SQ) limit [20]. The SQ limit is the maximum theoretical efficiency that a single-junction solar cell can achieve under standard test conditions, accounting for fundamental losses such as radiative recombination and thermalisation [21]. To surpass this efficiency limit and unlock further performance gains, tandem solar cells have emerged as a promising structure [22]. Tandem devices stack two absorber layers with complementary bandgaps, allowing for a more efficient use of the solar spectrum and reduced energy losses [22, 23]. The top cell, designed with a higher E_g, absorbs the higher-energy (short-wavelength) photons, while the bottom captures the lower-energy (long-wavelength) photons that pass through the top cell [22, 23].

Among the various tandem configurations, perovskite/silicon (PVK/Si) tandems have gained significant attention in recent years due to their potential to achieve high efficiency at low cost [24, 25]. Figure 1.1 (a) illustrates the spectral absorption ranges of the PVK and Si subcells in a tandem device, while (b) shows the corresponding device structure. PVK materials are ideal top-cell candidates owing to their tunable bandgaps ($E_g \approx 1.67$–1.75 eV) [26], which aligns well with Si's bandgap ($E_g \approx 1.12$ eV) [27], their high absorption coefficients [28], and low fabrication costs [29]. In a monolithic (two-terminal) configuration, the long-term stability and industrial maturity of c-Si are complemented by the superior optoelectronic properties of PVK [22, 30], making PVK/Si tandems a promising candidate for next-generation PVs [22, 24, 25, 30].

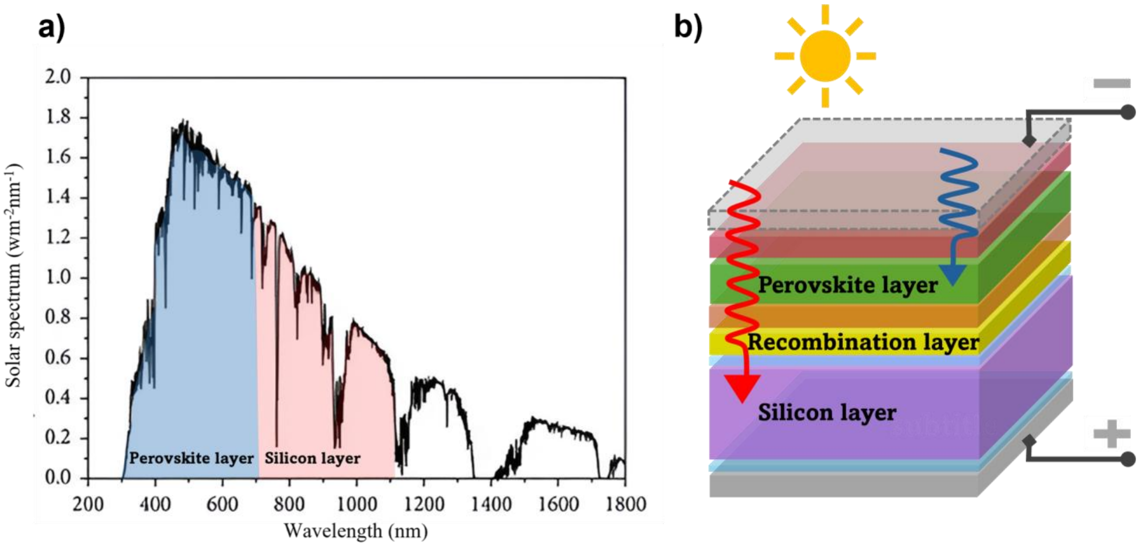

Figure 1. 1 – (a) Solar spectrum with absorption ranges of PVK (blue shaded) and Si (red shaded) layers, (b) schematic of a monolithic PVK/Si tandem solar cell.

Despite their remarkable efficiency potential, with a record of 34.9% on lab-scale devices (~1 cm^2) [31], the commercialisation of PVK/Si tandem devices is currently hindered by two main challenges: long-term operational stability and the scalability of fabrication processes [32-34]. Environmental factors such as heat, moisture, and continuous illumination can induce degradation and severely compromise the long-term stability of PVK materials [32-34]. Fabrication methods optimised for high-efficiency lab-scale devices pose significant challenges when scaled to industrial production, often compromising PVK film uniformity and reproducibility [32-34].

To overcome these limitations and achieve further performance improvements, it is critical to gain a deeper understanding of device physics, including identifying the origins of losses and mapping spatial non-uniformities. In this context, reliable characterisation techniques play a pivotal role. Spatially resolved methods such as photoluminescence (PL) [35] and electroluminescence (EL) [36] imaging are widely implemented in both research laboratories and industrial production lines to evaluate optoelectronic performance and ensure device quality control [37-44]. Their rapid, non-destructive, and spatially resolved nature makes them highly effective for quality assessment of precursors (in PL), solar cells, and modules [37-44]. Therefore, they are well-suited for applications such as in-line inspection in high-volume manufacturing lines. When applied to tandem structures, these techniques are particularly valuable, as they can provide spatially resolved information on each subcell, enabling targeted analysis of performance losses and informed optimisation strategies.

One key parameter that can be extracted from PL or EL measurements is the implied voltage (iV), a valuable metric for evaluating the performance of PV devices [45]. Implied voltage represents the theoretical maximum open-circuit voltage (V_{oc}) that a solar cell could achieve [46]. While V_{oc} measured at the terminals provides only a global value, iV, when extracted from luminescence imaging, offers spatially resolved insight into local voltage variations across the device [37, 47-52]. Importantly, iV can be determined early in the fabrication process, before metallisation [53]. Spatial iV mapping reveals critical material properties, enabling the identification of non-uniform defect regions, dominant recombination pathways and variations in series resistance (R_{s})-related losses [41-44, 54-56]. Furthermore, the strong connection between iV and recombination dynamics facilitates the contactless estimation of the intrinsic carrier concentration (n_{i}) (see Chapter 2 and Chapter 6 for more details) [57, 58].

In monolithic tandem devices, iV can be measured for each subcell individually, allowing identification of voltage losses within each subcell and guiding targeted performance optimisation [59, 60]. Additionally, iV imaging across varying excitation conditions enables the extraction of local pseudo-dark current density–implied voltage (pseudo-dark J–iV) [61-64].

Although PL and EL imaging have been widely used for spatial iV visualisation, extracting absolute iV values from luminescence images requires a calibration process. However, often the calibration process is complex as the luminescence intensity is inherently linked to both electrical and optical properties of the device, which vary across different samples, along with the optical response of the detection system. For most of the conventional calibration methods, prior knowledge of device optical properties is required [38, 49, 59], or the calibration process must be repeated for each sample [38, 45, 59], particularly when their surface morphology, structure, or material composition differ. This challenge is even more pronounced for tandem solar cells, where determining the optical response of each subcell is a topic of complexity and uncertainty. Moreover, the optical response of the detection system, including filters, lenses, and camera sensitivity, further influences the signal and introduces additional uncertainty. These dependencies make the calibration process time-consuming and limit its practicality for rapid diagnostics, especially when working across diverse device types or during early-stage development.

To address these challenges, **this thesis aims to introduce a robust and simple calibration method for extracting spatially resolved iV from luminescence imaging**. The proposed approach eliminates the need for sample-specific calibration and additional information about the optical properties of either the sample or the measurement system. The suitability of the method is demonstrated across Si wafers, cells and PVK/Si tandem devices, all featuring distinct compositions and optical properties. In the tandem case, the method further enables the extraction of spatially resolved pseudo-dark J–iV characteristics for each subcell, essential for identifying subcell-specific performance losses and electrical mismatches.

The developed technique for iV extraction also establishes the basis **for a second key objective: determining n_i of semiconductor materials in a fully contactless manner**. This is achieved by integrating the calibration method developed in this thesis for iV determination with a previously developed method for extracting excess carrier density (Δn) from PL images. Unlike conventional methods, this approach does not rely on structural assumptions or detailed material parameters, making it particularly well-suited for emerging materials such as PVKs, where key electronic and optical properties are often unknown.

1.2 Thesis outlines

Chapter 2 presents the theoretical background for iV and n_i determination. It reviews the main existing calibration methods for spatially resolved iV imaging in Si and PVK/Si tandem devices. The strengths and limitations of these approaches are discussed to highlight key challenges in existing frameworks. A comprehensive review of n_i extraction methods is provided separately in Chapter 6.

Chapter 3 introduces the proposed calibration method for spatially resolved iV imaging in Si wafers and solar cells using a single calibration cell. It presents a systematic framework that minimises the calibration's sensitivity to sample-specific optical properties. The influence of key parameters such as surface texture, reflectance, and absorber thickness is analysed through optical modelling. The method is experimentally validated with both PL and EL imaging, using a calibration cell whose optical properties differ from those of the measured samples.

Chapter 4 extends the presented calibration method to enable subcell-resolved iV imaging in monolithic PVK/Si tandem solar cells. Besides the calibration method presented in Chapter 3, another method that employs a calibration lamp is discussed. The latter is based on a simplified form of Planck's law, in which the optical properties of both the sample and the detection system are approximated as wavelength-independent constants. Both methods are evaluated through optical simulations and experimental validation. The suitability of the proposed method for spatially resolved extraction of pseudo-dark J–iV characteristics for each subcell is demonstrated.

Chapter 5 presents a comprehensive uncertainty analysis of the proposed iV extraction method for PVK/Si tandem solar cells. Key uncertainty sources are identified, categorised, and quantitatively assessed through simulations and experimental validation.

Chapter 6 demonstrates the application of the proposed iV extraction method for determining n_i in Si. The chapter first reviews existing n_i extraction methods for Si. It then presents the new approach, integrates the introduced iV-calibration method, with a previously established method for obtaining Δn. A comprehensive uncertainty analysis is presented to assess the accuracy of the technique. Experimental validation is carried out by comparing the extracted n_i values with well-established references from the literature.

Chapter 7 summarises the core contributions of this thesis by highlighting the key findings presented in each chapter. It also outlines future research directions to further improve and broaden the applicability of the presented method across diverse PV materials and device structures.

Chapter 2 – Theoretical Background and Literature Review

This chapter provides a comprehensive theoretical background and discusses the main approaches proposed for the quantitative determination of iV in Si, PVK, and PVK/Si tandem solar cells. Section 2.1 explains the fundamental definition and theoretical concepts of iV. Section 2.2 discusses various characterisation techniques for iV determination. Section 2.3 then summarises prior work on calibration methods for quantitative iV mapping from luminescence, highlighting the main approaches. Section 2.4 describes the supplementary experimental characterisation techniques often needed for iV determination. Finally, Section 2.5 presents the practical applications of extracted iV, particularly in deriving pseudo-dark J–iV curves and extracting n_i.

It should be noted that the primary focus of this chapter is iV. Therefore, a detailed discussion of n_i, including the relevant literature, will be presented in Chapter 6.

2.1 Definition of implied voltage in semiconductor

Under thermal equilibrium, when no illumination or electrical bias is applied, a semiconductor is characterised by a single Fermi level that defines the statistical distribution of free electrons and holes throughout the material [Figure 2.1(a)]. However, once the semiconductor is excited by light or electrical injection, the system deviates from equilibrium as the carrier populations are altered [65-67]. In this non-equilibrium condition, two distinct quasi-Fermi levels emerge: the electron quasi-Fermi level (E_{fn}) for electrons in the conduction band and the hole quasi-Fermi level (E_{fp}) for holes in the valence band [Figure 2.1(b)] [65-67].

Under such conditions (non-equilibrium), the electron (n) and hole (p) concentrations can be expressed as [65-67]:

$$n = n_{\mathrm{i}} \cdot \exp\left[\frac{E_{\mathrm{fn}} - E_{\mathrm{i}}}{k_{\mathrm{B}}T}\right] \tag{2.1}$$

$$p = n_{\mathrm{i}} \cdot \exp\left[\frac{E_{\mathrm{i}} - E_{\mathrm{fp}}}{k_{\mathrm{B}}T}\right] \tag{2.2}$$

where E_i is the intrinsic Fermi level, k_B is the Boltzmann constant, and T is the temperature. By multiplying Equations 2.1 and 2.2:

$$E_\mathrm{fn} - E_\mathrm{fp} = k_\mathrm{B}T \cdot \ln\left[\frac{n \cdot p}{{n_\mathrm{i}}^2}\right] \tag{2.3}$$

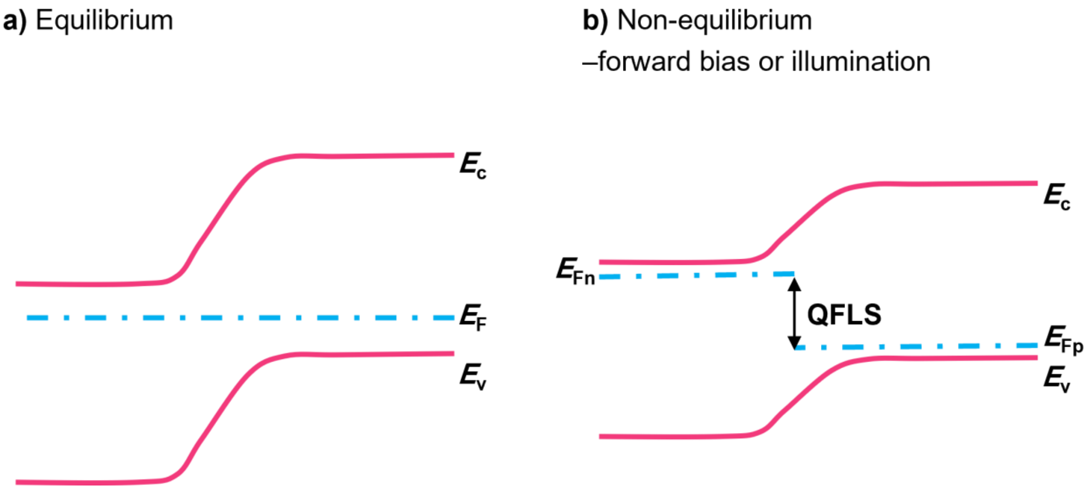

Figure 2. 1 – Schematic of energy band diagrams of a p–n junction (a) under thermodynamic equilibrium at open-circuit and (b) forward electrical bias or illumination at open-circuit.

The energy difference between the electron and hole quasi-Fermi levels ($E_\mathrm{fn}-E_\mathrm{fp}$) under non-equilibrium conditions is known as the quasi-Fermi levels splitting ($\Delta\mu$). In PV, $\Delta\mu$ is a critical parameter as it represents the maximum electrochemical potential available within the absorber [65-68]. To make this energy value more practical for device analysis, it is commonly expressed as a voltage, known as implied voltage iV. This is achieved by dividing it by the elementary charge, q [65-68]:

$$\mathrm{i}V = \frac{\Delta\mu}{q} \tag{2.4}$$

The term “implied” emphasises that this voltage is deduced from material properties, rather than directly measured at the terminals. A terminal voltage measurement, in turn, may be affected by R_s and other losses associated with charge carrier extraction at the contacts and interfaces of solar cells [65-68].

The two main approaches for determining iV are photoconductance (PC) and luminescence, which are discussed in the following section.

2.2 Methods for implied voltage determination

2.2.1 Photoconductance and implied voltage

For a doped semiconductor, a material in which the carrier concentration is intentionally modified by introducing electrically active impurities, the majority carrier concentration under equilibrium conditions is determined by the doping density (N_{dop}). Under non-equilibrium conditions (illumination or electrical injection), excess electron and hole concentrations, Δn and Δp, respectively, are generated. The charge-neutrality principle states that the total positive and negative charges in a semiconductor must remain balanced [65, 67]. Thus, under uniform excitation, these excess electron and hole concentrations are equal, i.e., $\Delta n = \Delta p$. Accordingly, the total carrier concentrations can be expressed in terms of a single excess carrier concentration, Δn.

For an n-type material, where electrons are the majority carriers due to donor doping, the total electron and hole concentrations become $n = N_{\mathrm{dop}} + \Delta n$ and $p = \Delta n$, respectively. Conversely, in a p-type material, where holes are the majority carriers due to acceptor doping, $p = N_{\mathrm{dop}} + \Delta n$ and $n = \Delta n$. Substituting these expressions into Equation 2.3 and applying the charge-neutrality principle yields [65, 67]:

$$\mathrm{i}V = V_T.\ln\left[\frac{\Delta n(N_{\mathrm{dop}} + \Delta n)}{n_{\mathrm{i}}^2}\right] \tag{2.5}$$

where $V_T = \frac{k_{\mathrm{B}} \cdot T}{q}$ is thermal voltage.

To determine iV from the above relation, one must first determine Δn. The PC method achieves this by measuring the change in the sample's conductance under illumination. The change in photoconductance($\Delta\sigma$) is proportional to the excess electron and hole concentrations [65, 67]:

$$\Delta\sigma = q \cdot d(\mu_n \Delta n + \mu_p \Delta p) \tag{2.6}$$

Where d is the sample thickness, μ_n and μ_p are the electron and hole mobilities, respectively.

Based on the principle of charge neutrality ($\Delta p = \Delta n$), the above equation can be simplified to:

$$\Delta n = \frac{\Delta\sigma}{q \cdot d(\mu_n + \mu_p)} \tag{2.7}$$

For common materials, such as Si, the μ_n and μ_p are well-established, and their dependence on both N_{dop} and Δn has been known [65, 69-71]. This enables Δn, and the sum of the carrier mobilities, to be determined by iteratively solving Equation 2.7 from the measured $\Delta\sigma$ [58].

Once Δn is estimated, it can be substituted into Equation 2.5 to determine iV. This calculation also requires two additional parameters: N_{dop} and n_{i}. Typically, N_{dop} is provided by the wafer manufacturer or can be measured using standard techniques such as the four-point probe method or capacitance-voltage profiling [72-74]. While n_i is well-established for Si, its accurate determination in emerging materials remains a challenge. A detailed introduction to this fundamental parameter is provided in Section 2.5.2. Furthermore, Chapter 6 presents a comprehensive review of established methods for estimating n_i in Si.

2.2.1.1 Photoconductance setup

The standard instrument for PC measurements, such as the one developed by Sinton Instruments [75], is shown in Figure 2.2. The setup consists of a calibrated flash lamp that generates a controlled light pulse, which in turn creates excess electron–hole pairs in the sample. An inductive radio-frequency (RF) coil, placed beneath the sample, detects $\Delta\sigma$ by detecting variations in the coil's impedance. Simultaneously, a calibrated reference photodiode (PD) measures the real-time intensity profile of the light pulse. A data acquisition card (DAC) then records the time-varying signals from both the coil and the reference photodiode.

This setup, widely used in the PV industry, was initially developed to measure the effective carrier lifetime (τ) and was later applied to extract the iV. These parameters can be determined by operating the instrument in two primary modes: quasi-steady-state (QSS) and transient.

QSS Mode: This mode employs a long, slowly varying light pulse where the intensity changes at a rate much slower than the sample's effective carrier lifetime. In this case, the effective lifetime is determined using the continuity equation:

$$\tau = \frac{\Delta n}{G - \frac{d\Delta n}{dt}} \tag{2.8}$$

where G is the generation rate.

Transient Mode: In this mode, a very short light pulse is used to excite the sample. The analysis is performed after the light is off ($G = 0$), and the lifetime is found from the photoconductance decay slope. A key advantage of the transient mode is that the lifetime is independent of the generation rate, thereby reducing measurement uncertainty [76]. This approach is particularly suitable for samples with lifetimes much longer than the light source turn-off time, typically with $\tau > 100$ µs [74]. The lifetime is calculated as:

$$\tau = -\frac{\Delta n}{\frac{d\Delta n}{dt}} \tag{2.9}$$

It is important to note that, regardless of whether the QSS or transient mode is used, the final value for iV is identical [58]. In both apporaches, Δn is determined and then substituted into Equation 2.5. Therefore, the resulting iV is expected to be identical at any given value of Δn.

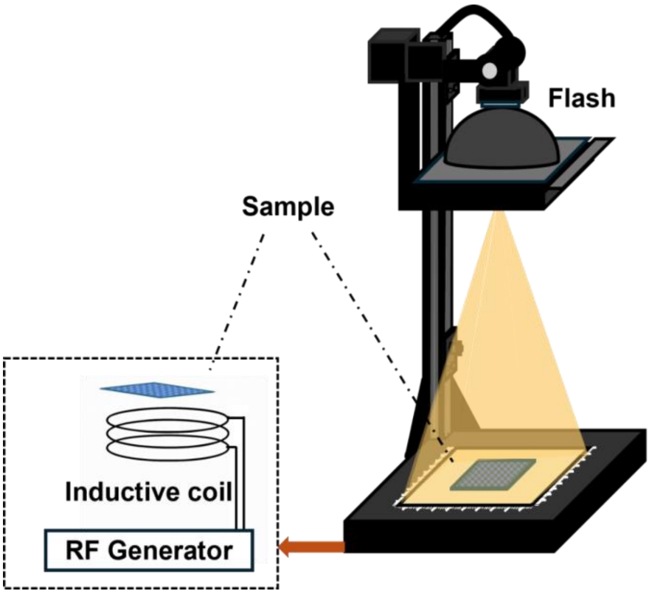

Figure 2. 2 – Diagram of a typical PC setup.

2.2.1.2 Photoconductance limitation

Although the PC approach offers significant benefits of non-contact measurement and is highly effective for wafer characterisation, it has inherent limitations [76]. Particularly for determining iV:

- **Uncertainty in material parameters**: The PC method is highly sensitive to inaccuracies in the wafer's assumed physical properties, primarily its thickness and doping concentration [76, 77]. Any uncertainties in the measured wafer thickness yield significant uncertainties in the iV calculation, as the error propagates directly into the determination of the excess carrier density [76, 77]. While inaccuracies in the assumed doping concentration also contribute to the final error, this effect is considered secondary and is most pronounced only at low injection levels, often having a negligible impact on the overall uncertainty.
- **Generation rate uncertainty (in QSSPC):** The QSSPC method's accuracy is critically dependent on the calculation of the optical generation rate [77, 78]. This is a dominant source of error and includes several factors: uncertainty in the reference cell calibration, spectral mismatch between the xenon flash lamp and the standard solar spectrum, and inaccurate knowledge of the sample's optical properties (reflectance and transmittance) affecting the "optical constant input" [77, 78].

- **Susceptibility to carrier trapping:** The PC method is susceptible to artifacts from carrier trapping, a phenomenon where minority carriers are temporarily localised at defect sites instead of immediately recombining [79, 80]. Since these trapped carriers contribute to the sample's overall conductivity, the PC measurement cannot distinguish them from free carriers [79, 80]. This leads to an overestimation of the true free excess carrier density [79, 80], which in turn yields artificially high, or "apparent," iV. The artifact is particularly pronounced at low injection levels, where the trapped carrier population can become a significant fraction of the Δn [79, 80].
- **Challenges with metallised samples:** While the technique is ideal for bare wafers, the presence of metal contacts on finished solar cells can interfere with the inductive RF coil [58, 65]. This interference can compromise measurement accuracy by altering the conductive paths being measured [58, 65].
- **Lack of spatial resolution**: The PC technique only provides a single value [76]. It cannot resolve local variations in material quality or identify the impact of localised defects, which can be critical for understanding device performance.
- **Depletion region modulation (DRM) artifacts:** In samples containing a p-n junction or a strong surface inversion layer, changes in the depletion region width under illumination can contribute to the measured photoconductance signal [81]. This effect, known as DRM, can also lead to an artificially high iV, particularly at low injection levels [81].

To address these limitations, alternative characterisation techniques such as luminescence-based imaging are utilised, providing spatially resolved iV measurements with reduced sensitivity to sample-specific properties.

2.2.2 Luminescence and implied voltage

The determination of the iV from a semiconductor's luminescence emission is fundamentally rooted in the physics of thermal radiation, as described by Planck's law for a blackbody [66, 82]. Understanding blackbody emission provides a clear framework for interpreting the relationship between luminescence emission and the iV.

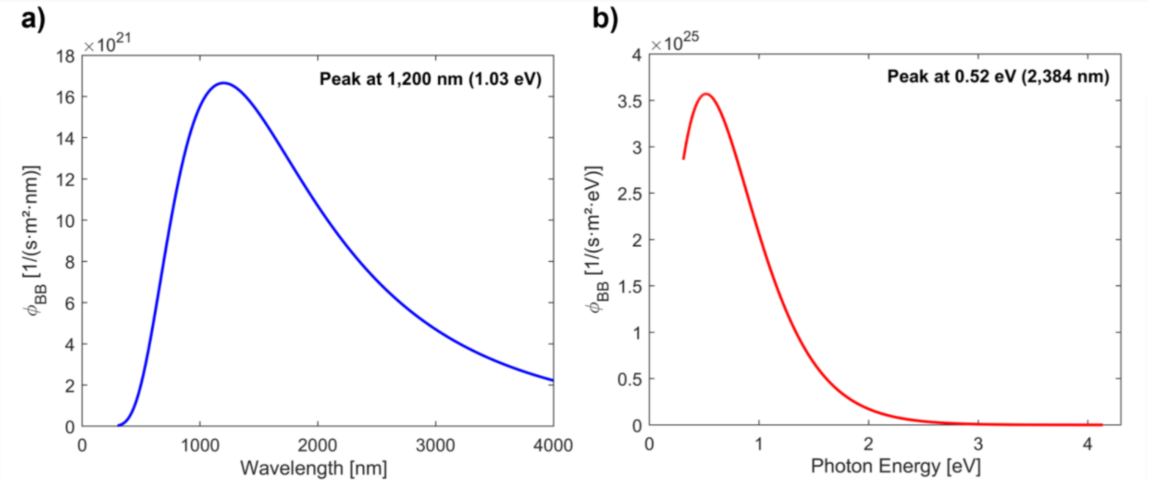

Figure 2. 3 – Spectral photon flux of ϕ_{BB} at T = 3,000 K. Plot (a) shows the photon flux per wavelength interval versus wavelength, while plot (b) shows the photon flux per unit energy interval versus photon energy. The peaks occur at (a) 1,200 nm (1.03 eV) and (b) 0.52 eV (2,384 nm), respectively.

A blackbody is a perfect absorber that absorbs all incident electromagnetic radiation and re-emits it as thermal radiation with a continuous spectrum that depends only on its temperature [66, 82]. The spectral photon flux of a blackbody (ϕ_{BB}) can be described as a function of either wavelength (λ) or photon energy (E).

The expression for the blackbody spectrum in terms of the photon flux per wavelength interval as a function of wavelength [$\phi_{\mathrm{BB}}(\lambda, T)$] is given by [46, 66, 83]:

$$\phi_{\mathrm{BB}}(\lambda, T) = \frac{2 \cdot \mathrm{c} \cdot \pi}{\lambda^4} \cdot \exp\left(-\frac{h \cdot c}{\lambda \cdot k_B \cdot T}\right) \mathrm{d}\lambda \tag{2.10}$$

where c is the speed of light and h is Planck's constant.

Alternatively, since photon energy and wavelength are related by $E = h.c/\lambda$, the blackbody spectrum in terms of photon flux per energy interval as a function of photon energy [$\phi_{\mathrm{BB}}(E, T)$] can be expressed as:

$$\phi_{\mathrm{BB}}(E, T) = \frac{2\pi \cdot E^2}{h^3 \cdot c^2} \cdot exp\left(\frac{-E}{k_B \cdot T}\right) dE \tag{2.11}$$

It is critically important to recognise that these two expressions for the blackbody spectrum are not mathematically interchangeable by simply substituting E with λ. The spectrum's shape is weighted by a λ^{-4} in the wavelength domain, while in the energy domain it is weighted by E^2. These weightings affect the spectral shape and shift the peak position of the blackbody emission. For instance, as shown in Figure 2.3 (a), at 3,000 K, the spectral peak of ϕ_{BB} lies at ~1,200 nm when plotted against wavelength, (b) whereas it shifts to ~0.52 eV (equivalent to 2,834 nm) in the energy domain.

This discrepancy arises from the non-linear relationship between energy and wavelength, which means that a constant energy interval is not equivalent to a constant wavelength interval. As the integrated photon flux over the entire spectrum must remain the same when switching between domains, a Jacobian transformation is required for correct conversion [46, 66, 83]:

$$dE = -\frac{h \cdot c}{\lambda^2} d\lambda \tag{2.12}$$

where dE is the differential energy interval and $d\lambda$ is the corresponding wavelength interval. Note that, as the photon flux is a non-negative quantity, the absolute value of this differential need to be used. Applying the incorrect form of the blackbody equation for a given analysis, whether in the energy or wavelength domain, will lead to significant errors in the interpretation of emission spectra and in the quantitative extraction of key parameters such as iV.

While a solar cell is not an ideal blackbody, its light emission is governed by the same underlying principles of thermal radiation, adapted for non-equilibrium conditions. At thermal equilibrium, a cell's emission is related to its absorption by the principle of detailed balance [66]. However, under illumination or electrical bias, the generation of excess carriers drives the system into non-equilibrium. This increased population of carriers enhances the rate of radiative recombination, resulting in light emission (luminescence) [66]. Therefore, the resulting luminescence is accurately described by the generalised Planck's law, which models the emission as a blackbody spectrum modified by two key factors:

- Absorptivity (A): The device only emits photons at energies it can absorb. The spectral absorptivity of the device scales the ideal blackbody spectrum. Conventionally, A is used when the device is excited by light (in PL), while for EL analysis, it is replaced by the external quantum efficiency (EQE) to account for imperfect carrier collection efficiency (η_c). Nevertheless, for modern high-efficiency solar cells, η_c is typically close to unity, and A and EQE are generally considered equivalent [37, 84, 85]. Accordingly, A and EQE are treated as interchangeable throughout this thesis. Further discussion of A and EQE is provided in Sections 2.4.2 and 2.4.3, respectively.
- Implied Voltage (iV): As established in Section 2.1, the presence of excess carriers leads to a quasi-fermi level splitting $\Delta\mu$. This splitting, measured as the iV, exponentially enhances the luminescence emission by increasing the rate of radiative recombination.

Incorporating these two modification factors with the ideal blackbody spectrum provides the final expression for the generalised Planck law to describe the luminescence emission of semiconductor devices [83]. Therefore, the absolute spectral photon flux, ϕ^{absolute}, per wavelength interval $(\text{photons} \cdot \text{s}^{-1} \cdot \text{nm}^{-1})$ is given by [83, 86]:

$$\phi^{\text{absolute}}(\lambda) = A(\lambda) \cdot \phi_{\text{BB}}(\lambda) \cdot \exp\left(\frac{\text{i}V}{V_T}\right) \tag{2.13}$$

This equation illustrates that the luminescence spectrum follows the characteristic spectral shape of a blackbody, modulated by the device's A and amplified exponentially by the iV. This exponential dependence makes luminescence a highly sensitive probe of the device's voltage.

The emitted luminescence signal must pass through several optical components—such as lenses, filters, and the camera sensor—before being collected by the detection system. Each component has its own transmittance or spectral response. The detected luminescence spectrum (ϕ^{detect}) can thus be expressed as:

$$\phi^{\text{detect}}(\lambda) = f(\lambda) \cdot A(\lambda) \cdot \phi_{\text{BB}}(\lambda) \cdot \exp\left(\frac{\text{i}V}{V_T}\right) \tag{2.14}$$

where f is the spectral response of the detected system. It is defined as [38]:

$$f(\lambda) = f_1 \cdot f_2(\lambda) \tag{2.15}$$

where f_1 is a scaling constant that accounts for the limited fraction of the emitted luminescence collected by the detector and f_2 is the wavelength-dependent optical response of the entire detection system (such as camera, lenses and filters).

In imaging systems, the detected luminescence intensity ($\Delta\phi^{\text{detect}}$) at each pixel is defined as the integrated detected spectral photon flux, i.e., the product of the emitted luminescence from the sample and the optical response of the imaging system, evaluated at the corresponding local position:

$$\Delta\phi^{\text{detect}} = \int_{\lambda_1}^{\lambda_2} \phi^{\text{detect}}(\lambda) d\lambda \tag{2.16}$$

where λ_1 and λ_2 indicate the wavelength limits over which the emitted luminescence signal is detected by the system.

Using Equations 2.14 and 2.16, iV can then be determined by:

$$\text{i}V = V_{\text{T}} \times \ln\left(\frac{\Delta\phi^{\text{detect}}}{\int_{\lambda_1}^{\lambda_2} f(\lambda) \cdot A(\lambda) \cdot \phi_{\text{BB}}(\lambda) d\lambda}\right) \tag{2.17}$$

Determining the absolute iV with this equation, however, presents a significant practical challenge. It requires precise knowledge of the optical properties of the system and the sample (f and A), which are often difficult to measure accurately.

While finding the absolute iV is challenging, the relationship allows for a powerful **relative analysis**. This approach is widely used for rapid quality control and comparative studies. By comparing two luminescence measurements ($\Delta\phi_1^{\text{detect}}$ and $\Delta\phi_2^{\text{detect}}$) under identical conditions, the difference in implied voltage (iV_1 and iV_2) can be determined directly:

$$\mathrm{i}V_2 - \mathrm{i}V_1 = V_{\mathrm{T}} \times \ln\left(\frac{\Delta\phi_2^{\text{detect}}}{\Delta\phi_1^{\text{detect}}}\right) \qquad (2.18)$$

This relative approach is highly effective for quality control and comparative studies, as the unknown optical factors (A and f) cancel out in the ratio. However, it cannot determine the absolute iV, which is essential for predicting device performance.

Therefore, to quantitatively extract the **absolute i*V*** from the detected luminescence, an appropriate **calibration approach** is required. Section 2.3 provides an overview of the widely adopted calibration approaches in the literature for determining spatially resolved iV. Prior to that, the standard PL/EL experimental setups are briefly outlined.

2.2.2.1 PL/EL imaging setup

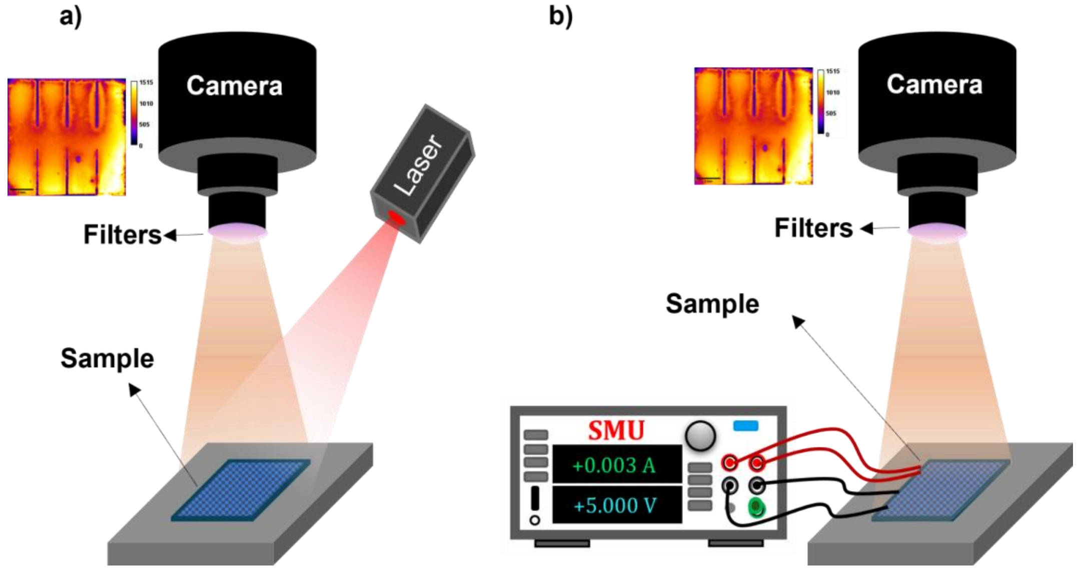

Figure 2. 4 – Schematic of PL (a) and EL (b) setup.

Figure 2.4 illustrates the typical configurations for luminescence imaging, with PL shown in panel (a) and EL in panel (b). The primary difference lies in the excitation method. In **PL imaging**, a laser or narrow-band light-emitting diode (LED) provides optical excitation. Because PL does not require electrical contacts, it is a versatile technique that can be applied to uncontacted wafers and partially processed devices. In **EL imaging**, a source-measure unit (SMU) injects carriers electrically by applying a forward voltage or current. For both techniques, if a device is contacted, the SMU can be used to simultaneously record the terminal voltage (V_{term}) and current (I). The luminescence is collected by an objective lens and directed through wavelength-selective filters that block the excitation light and, if required, narrow the detection band before it reaches the camera. For instance, in tandem devices to isolate the emission from each subcell, filters with a transmission range of 700–800 nm for the PVK subcell and above 950 nm for the Si subcell should be placed in front of the camera. The filtered signal is then recorded by a camera that typically employs either a Si or an indium gallium arsenide (InGaAs) detector. Si detectors exhibit high quantum efficiency across the visible wavelengths, while InGaAs detectors provide higher sensitivity in the near-infrared region.

The quality of luminescence images strongly depends on the signal-to-noise ratio (SNR), which quantifies the balance between the detected luminescence signal and noise contributions arising from the detector and measurement setup (including shot noise, read noise, and dark noise). SNR is therefore an important consideration when selecting spectral filters, as narrowing the detection window can reduce signal levels and lower SNR. A detailed SNR formulation and its application to the imaging system used in this thesis are provided in Section 3.4.

PL measurements on a contacted device offer the flexibility to probe different operating points. For instance, under open-circuit conditions, the net current is zero, and the measured terminal voltage (V_{term}) provides a direct measure of the iV. Under short-circuit conditions, the measured current is the short-circuit current (I_{sc}), which directly reflects the efficiency of carrier collection. In contrast, EL is performed under forward bias (applying voltage or current injection), meaning an injection current is always flowing through the device. For many solar cells, the terminal voltage measured, V_{term}, during EL is a good approximation of the iV, particularly at low current densities where resistive losses are negligible.

2.2.2.2 PL/EL spectroscopy setup

PL/EL spectroscopy techniques measure luminescence intensity as a function of wavelength instead of generating spatially resolved luminescence images. In these methods, samples are excited either optically using a laser or LED (PL), or electrically by current injection (EL), and the emitted luminescence is spectrally dispersed using a spectrometer. Figure 2.5 shows the typical schematic of PL (a) and EL (b) spectrometer setup. The dispersed light is then detected by a spectrometer equipped with appropriate photodetectors (Si or InGaAs), selected based on the spectral region of interest. Si detectors are used for the visible to near-infrared range (approximately 350–1,100 nm), whereas InGaAs detectors are employed for longer near-infrared wavelengths (approximately 900–1,700 nm, with extended capabilities up to 2,600 nm).

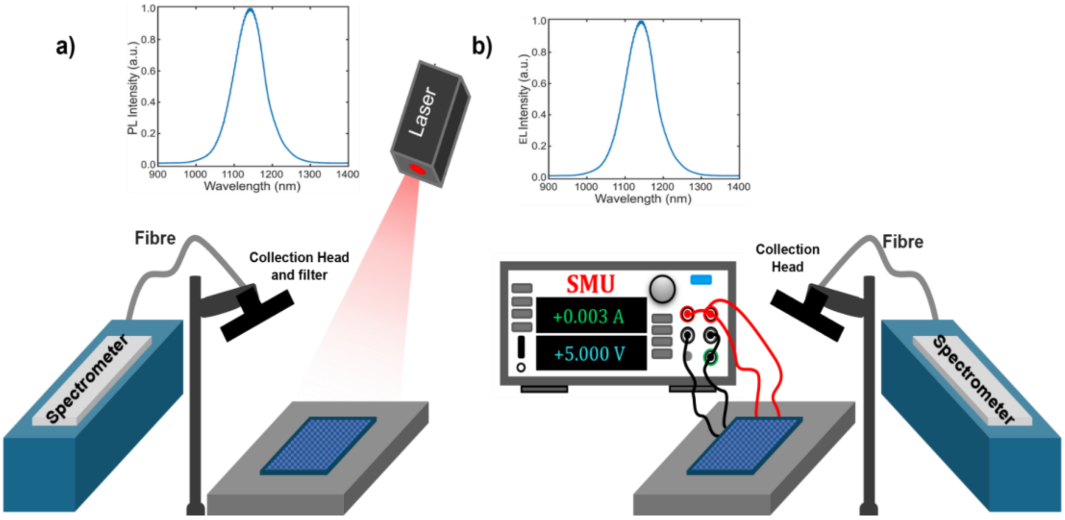

Figure 2. 5 – Schematic of (a) PL and (b) EL spectrometry setup.

2.3 Literature review on calibration methods for implied voltage

This section provides an overview of the key calibration approaches for extracting spatially resolved i*V* in PVK, Si, and each subcell of PVK/Si tandem devices.

2.3.1 Calibration based on fitting of spectra

Implied voltage (i*V*) can be extracted from fitting the high-energy tail of an absolute PL or EL spectrum with the generalised Planck's law [47, 49, 84, 87].

A key requirement for this is that the luminescence spectrum must be expressed in absolute units of photon flux. As mentioned earlier, because a detector's raw signal is in arbitrary units, a calibration procedure is necessary. To achieve this, the spectral response of the entire detection system, f, is determined by measuring a calibration lamp with a known, certified spectral photon flux (ϕ_{light}). The lamp is typically coupled to an integrating sphere to ensure uniform illumination. The system's optical response is then given by:

$$f(\lambda) = \frac{\phi_{\text{light}}^{\text{detect}}(\lambda)}{\phi_{\text{light}}(\lambda)} \tag{2.19}$$

where $\phi_{\text{light}}^{\text{detect}}$ is the measured signal of the calibration lamp. Once f is known, any measured luminescence signal (ϕ^{detect}) can be converted into its absolute photon flux as follow:

$$\phi^{\text{absolute}}(\lambda) = \frac{\phi^{\text{detect}}(\lambda)}{f(\lambda)} \tag{2.20}$$

While the spectrum is now calibrated in the wavelength domain, the fitting procedure to extract iV is conventionally performed in the energy domain. This is because the generalised Planck law simplifies to a linear relationship when plotted against photon energy (E). Therefore, the spectrum must be converted from a function of wavelength to a function of energy. Importantly, this requires using the correct form of the blackbody expression in the energy domain, as given in Equation 2.11.

With the luminescence spectrum correctly expressed per unit energy, $\phi^{\text{absolute}}(E)$, it can then be fit to the generalised Planck's law to extract the iV [83]. The theoretical relationship, rearranged for a linear fit, is given by [47, 49, 84, 87]:

$$\ln\left(\frac{\phi^{\text{absolute}}(E)}{\left(\frac{2\cdot\pi}{h^3\cdot c^2}\right)\cdot E^2\cdot A(E)}\right) = \frac{\text{i}V}{V_T} - \frac{E}{kT} \tag{2.21}$$

It is worth mentioning that full-spectrum fitting of ϕ^{absolute} requires precise knowledge of both temperature (T), and absorptivity (A) of the sample [49], which can be challenging to determine precisely [88].

To overcome this challenge, the fitting procedure is often restricted to the high-energy tail of the spectrum. In this region, well above the E_{g}, the absorptivity is approximately constant and can be assumed to be unity ($A \approx 1$). This simplification makes the fitting process significantly more practical and is a widely used approach for estimating iV [47, 84, 87].

This method is widely used for estimating spatially resolved iV, within single-junction solar cells and also individual subcells in PVK/Si tandem devices through micro-PL mapping or hyperspectral system [47, 84, 87]. Micro-PL mapping involves point-by-point excitation of the sample using a focused laser beam, with the emitted PL spectrum collected at each position [47]. This provides spatially resolved luminescence spectra across the sample. Nevertheless, the point-by-point scanning approach makes the measurement process significantly time-consuming, limiting the practicality of the technique for large-scale or high-throughput characterisation [47]. In contrast, hyperspectral imaging is a wide-field technique that images an entire area at once, simultaneously acquiring the full emission spectrum for each pixel [84, 87]. This method rapidly generates a complete dataset, or "datacube," of spatial (x, y) and spectral (λ) information, making it vastly faster than Micro-PL mapping for high-throughput analysis [84, 87].

Figure 2.6 provides an example of an extracted iV image via hyperspectral setups, reproduced from [84]. The left panel (a) shows the ϕ^{absolute} of a representative PCBM-based device via PL and EL, with the high-energy tail fitted using a simplified form of the generalised Planck law. Applying this fitting procedure at each pixel, a spatial map of $\Delta\mu$ is obtained from the PL image, as shown in the right panel (b). The $\Delta\mu$ map highlights significant inhomogeneities in the $\Delta\mu$ (= i$V{\cdot}q$) across the device surface.

However, the accuracy of this approach is highly sensitive to the selected fitting region, as small variations in the chosen wavelength range alter the fitted slope parameters, which can significantly affect the extracted iV values [48].

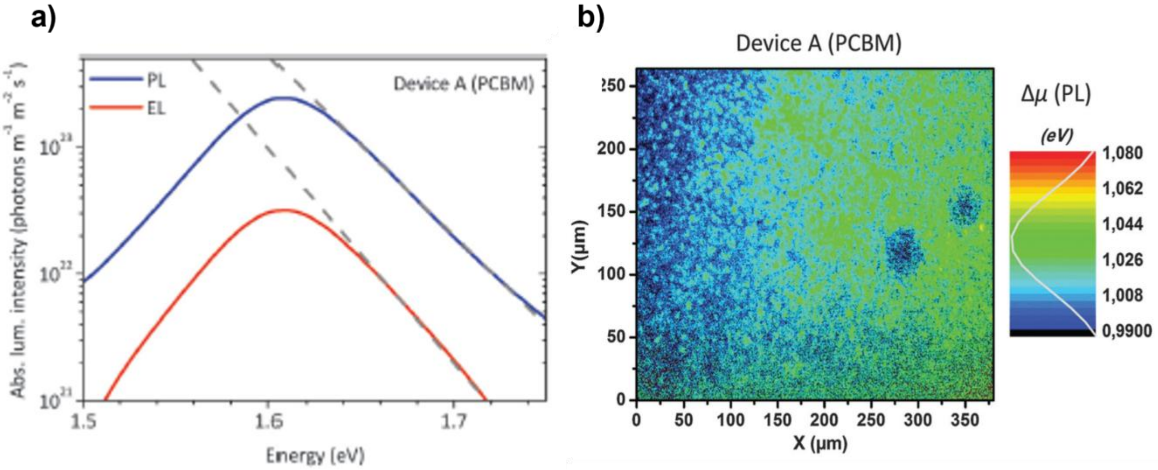

Figure 2. 6 – a) ϕ^{absolute} of Device A (PCBM) via PL and EL, with the high-energy tail fitted using a simplified form of the generalised Planck law. b) Corresponding spatial map of $\Delta\mu$ extracted from hyperspectral PL, revealing local electronic variations. Reproduced from El-Hajje et al. [84].

2.3.2 Bandpass filter approach

As an alternative to spectrally resolved fitting, Soufiani et al. developed a simplified method for extracting iV by restricting the detection range to the high-energy tail of the luminescence spectrum using a narrow bandpass filter (BPF) [50]. A key advantage of this approach is that it does not require spectrally resolved information from either the sample or the detection system.

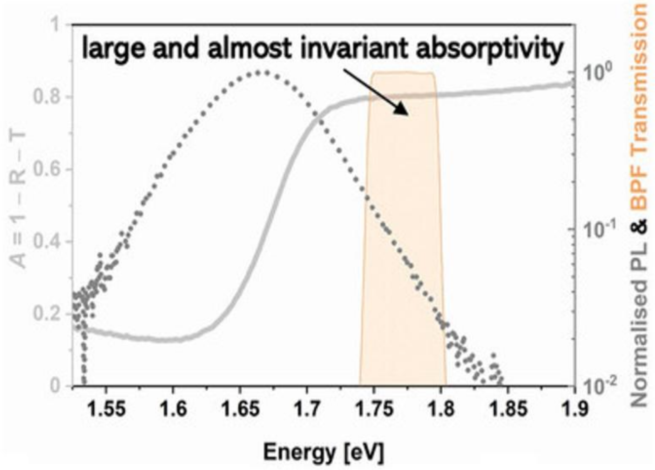

Figure 2. 7 – PL and measured absorptivity spectrum of a PVK film, showing the near-unity and almost constant absorptivity within the BPF transmission range, enabling simplified iV extraction. Reproduced from Soufiani et al. [50].

The method relies on two main simplifications. First, by using a narrow BPF positioned in the high-energy region of the spectrum, the sample's absorptivity can be approximated as a single constant value close to unity (see Figure 2.7, reproduced from [50]). Second, because the camera integrates the signal over a very narrow spectral range (e.g., 13 nm), the wavelength-dependent system response (f) can also be approximated by a single constant value [50].

With these assumptions, the system can be calibrated in a single step by imaging a uniform halogen lamp with a known integrated photon flux through the same BPF. The term f can then be determined as:

$$f \approx \frac{\Delta\phi_{\text{light}}^{\text{detect}}}{\Delta\phi_{\text{light}}} \tag{2.22}$$

where $\Delta\phi_{\text{light}}^{\text{detect}}$ is the spatially resolved signal detected from the lamp by the camera and $\Delta\phi_{\text{light}}$ is the known integrated absolute photon flux of the lamp over the BPF's transmission range.

Once the calibration constant, f, is known, and assuming a constant value for A, iV can be extracted using the simplified form of the generalised Planck law [83] (Equation 2.17):

$$\text{i}V = V_{\text{T}} \times \ln\left(\frac{\Delta\phi^{\text{detect}}}{f \cdot A \cdot \Delta\phi_{\text{BB}}}\right) \tag{2.23}$$

where $\Delta\phi_{\text{BB}}$ is the integrated blackbody photon flux over the BPF's transmission range. This simplification allows for the direct extraction of the iV map without requiring the full spectral properties of the sample or detection system.

This method was validated on neat PVK films and non-metallised device stacks with absorber thicknesses of 400–600 nm, using BPFs centred at 720 nm and 740 nm (each with a 13 nm bandwidth)

[50]. Figure 2.8, reproduced from [50], depicts the PL image and the corresponding iV map at open-circuit condition (referred to as iV_{oc}), of a non-metallised PVK inverted device stack with the composition $Cs_{0.05}(FA_{0.85}MA_{0.15})_{0.95}Pb(I_{0.85}Br_{0.15})_3$, using a BPF centred at 720 nm.

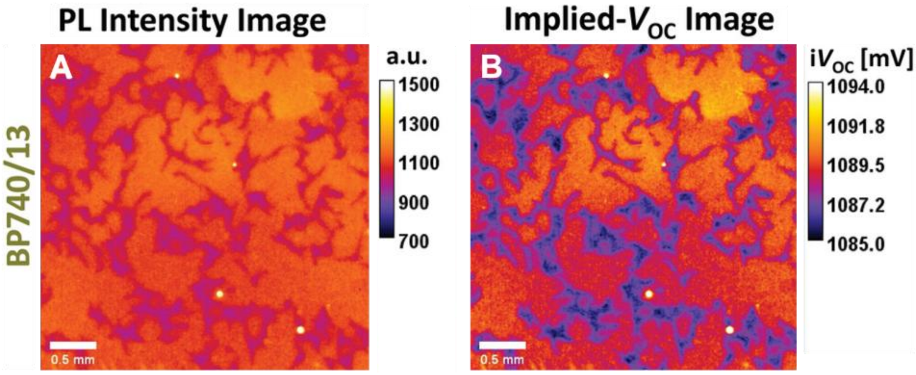

Figure 2. 8 – (a) PL intensity image, and (b) corresponding iV at open-circuit of a $Cs_{0.05}(FA_{0.85}MA_{0.15})_{0.95}Pb(I_{0.85}Br_{0.15})_3$ non-metallised inverted device stack measured using a BPF centred at 740 nm with a 13 nm bandwidth. Adapted from Soufiani et al. [50], where implied-V_{oc} and iV_{oc} denote the iV at open-circuit conditions.

While the method simplifies calibration, its broader accuracy requires further investigation. The method relies on approximating A as a single constant value. It has been shown that for optically thick films, A is high and nearly constant, but a clear procedure for selecting this value is not provided. For example, for thinner PVK layers, which are commonly used in tandem solar cells, this assumption of $A \approx 1$ becomes less reliable and may introduce uncertainties that requires further analysis. Furthermore, the method was validated using only two narrow BPFs (720 ± 13 nm and 740 ± 13 nm). However, the study does not provide a systematic guideline for selecting the optimal BPF for materials with different bandgaps. Therefore, establishing a robust procedure for determining the appropriate value of A and proper BPF selection is essential to ensure the method's accuracy for samples with different structures and bandgaps.

2.3.3 Scaling factor-based approach

A recently developed calibration approach enables spatially resolved extraction of iV in both single-junction devices and individual subcells in tandem solar cells [38, 59]. Like the previous methods, it leverages the well-established relationship between iV and luminescence (see Equation 2.17) [38, 59]. However, it differs significantly from the narrow BPF approach by design, as it requires accurate, spectrally resolved knowledge of both the sample's optical properties (A or alternatively its EQE), the spectral responsivity of the detection system (f).

To determine $f(\lambda)$, this method separately quantifies the two components f_1 and $f_2(\lambda)$ [Equation 2.15]. The scaling factor f_1 is quantified by imaging a calibration lamp coupled to an integrating sphere with a known and uniform photon flux (ϕ_{light}), and is given by:

$$f_1 = \frac{\Delta\phi_{\text{light}}^{\text{detect}}}{\int_{\lambda_1}^{\lambda_2} f_2(\lambda) \cdot \phi_{\text{light}}(\lambda)\, \mathrm{d}(\lambda)} \tag{2.24}$$

As mentioned earlier, the term $f_2(\lambda)$ accounts for the spectral properties of the optical path, including the quantum efficiency of the camera [$\mathrm{QE}_{\text{camera}}(\lambda)$] and the transmittance of lenses and filters. While $\mathrm{QE}_{\text{camera}}(\lambda)$ is typically obtained from the manufacturer's datasheet, the remaining components are experimentally characterised using a spectrophotometer (see Section 2.4.3). Once both f_1 and f_2 are established, the full spectrum response f is determined (using Equation 2.15). This, together with the measured A (or EQE) of the device, allows the iV images to be computed using Equation 2.17.

This method was demonstrated across a range of device architectures, including neat PVK films, Si wafers, and fully integrated tandem devices [38, 59]. The method's accuracy was verified to be within 1% across all structures [38, 59]. Figure 2.9 illustrates the extracted iV images for the (a) PVK and (b) Si subcells in a monolithic PVK/Si tandem structure (reproduced from Ref. [59]). To isolate the emission from individual subcells in the tandem device, this method employs different BPFs. For the PVK subcell, a wide BPF with a transmission range of 650–750 nm was used, while a filter in the 950–1000 nm range was used for the Si subcell [59]. The use of such a wide BPF for the PVK subcell allows for strong signal collection over a broad wavelength range; however, it also introduces a significant limitation. Unlike the narrow BPF approach (discussed in Section 2.3.2) where both A and f can reasonably be assumed constant, utilising such a wide BPF in this method necessitates an accurate, wavelength-dependent calibration. Neglecting the spectral variation of A and f across the broad BPF leads to systematic errors in the extracted iV, particularly for thin or highly structured absorbers.

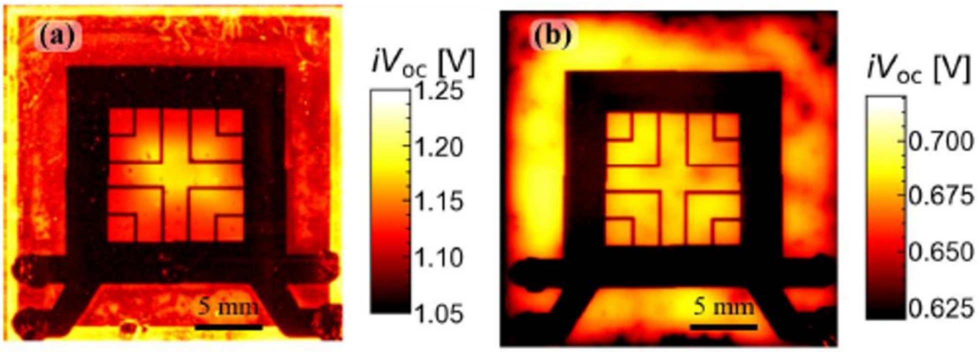

Figure 2. 9 – Extracted iV images of the (a) PVK and (b) Si subcells in a PVK/Si tandem device. Reproduced from Fischer et al. [59], where iV_{oc} is referred to as iV measured at open-circuit conditions.

Although this calibration approach is versatile, several practical challenges remain. First, accurate characterisation of $\mathrm{QE_{camera}}$ is often limited by uncertainties in manufacturer specifications, which can introduce wavelength-dependent errors in f_2, particularly near the detection limits (e.g., 950–1000 nm). Second, precise determination of the sample's optical properties, A or EQE, in completed tandem devices involves inherent challenges and complexities. Accurately quantifying A of fully metallised devices or individual subcells in tandem solar cells over such a **wide BPF** detection range imposes significant challenges [88]. Furthermore, although EQE measurements approximate A, they require a complete tandem cell and are not suitable during the early stages of fabrication. Beyond that, extracting the properties of individual subcells from EQE measurements of tandem devices is subject to a wide range of other complications [89].

2.3.4 Calibration cell-based approach

One widely used method to extract iV from the detected luminescence signal is to employ a calibration sample with a predetermined iV [45, 90, 91]. For a calibration sample with a known iV (iV_{calib}), the optical properties of the system and the sample can be combined into a single integration term, which is determined by rearranging Equation 2.17:

$$\int_{\lambda_1}^{\lambda_2} f(\lambda) \cdot A(\lambda, T) \cdot \phi_{\mathrm{BB}}(\lambda, T) d\lambda = \frac{\Delta\phi_{\mathrm{calib}}^{\mathrm{detect}}}{\exp(\frac{\mathrm{i}V_{\mathrm{calib}}}{V_{\mathrm{T}}})} \tag{2.25}$$

where $\Delta\phi_{\mathrm{calib}}^{\mathrm{detect}}$ is the corresponding detected luminescence signal from the calibration sample. Therefore, assuming this integration term remains the same for a measured sample (test sample), its iV can be calculated from a simple ratio of the luminescence signals:

$$\mathrm{i}V = \mathrm{i}V_{\mathrm{calib}} + V_T \cdot \ln\left[\frac{\Delta\phi_{\mathrm{cell}}^{\mathrm{detect}}}{\Delta\phi_{\mathrm{calib}}^{\mathrm{detect}}}\right] \tag{2.26}$$

where $\Delta\phi_{\mathrm{cell}}^{\mathrm{detect}}$ is the corresponding detected luminescence signal from the measured cell. This approach has been successfully applied to both pre-metallisation and fully processed devices [45, 90, 91].

For non-metallised samples, the calibration value, iV_{calib}, is typically obtained from an independent measurement. For instance, in c-Si wafers, QSSPC measurement (see Section 2.2.1) is commonly used to determine the iV of the wafers employed as a calibration sample [45]. Following this a PL image of this wafer (calibration sample) is captured under the identical illumination intensity. Since the PL signal and the iV are determined independently, this method is best suited to materials with stable optoelectronic properties and is typically not recommended for PVK films, which may degrade or evolve between measurements.

For metallised samples (fully fabricated solar cells), calibration process is performed by imaging a high-performance cell acting as a calibration cell with a known terminal voltage ($V_{\text{term,calib}}$) [45, 90, 91]. In EL-based calibration, $\Delta\phi_{\text{calib}}^{\text{detect}}$ is captured at low current injection levels while simultaneously recording $V_{\text{term,calib}}$. At such low injection levels, the voltage drops across the series resistance, $V_{\text{Rs}} = R_s \cdot I$, is negligible and $V_{\text{term,calib}}$ provides a good estimation of cell's implied voltage iV. In PL-based calibration, $\Delta\phi_{\text{calib}}^{\text{detect}}$ is recorded mostly under standard illumination (1 sun), and the corresponding $V_{\text{term,calib}}$ can be obtained either from a separate J–V measurement (see Section 2.4.2) or by simultaneously recording the voltage at open-circuit during the PL acquisition. For both EL/PL approaches, the iV_{calib} term in the equation above is substituted with the known $V_{\text{term,calib}}$, yielding:

$$\mathrm{i}V = V_{\text{term,calib}} + V_T \cdot \ln\left[\frac{\Delta\phi_{\text{cell}}^{\text{detect}}}{\Delta\phi_{\text{calib}}^{\text{detect}}}\right] \tag{2.27}$$

This method enables the accurate extraction of spatially resolved iV images without requiring direct determination of the optical response of the measured cell (A or EQE) and the detection system (f) [45, 91]. However, the primary limitation of this technique lies in its key assumption that the **optical properties of the calibration and measured cells must be identical.** Therefore, samples with different optical characteristics, such as different surface textures, require a new calibration sample with matching features for accurate iV estimation using this method [45, 91].

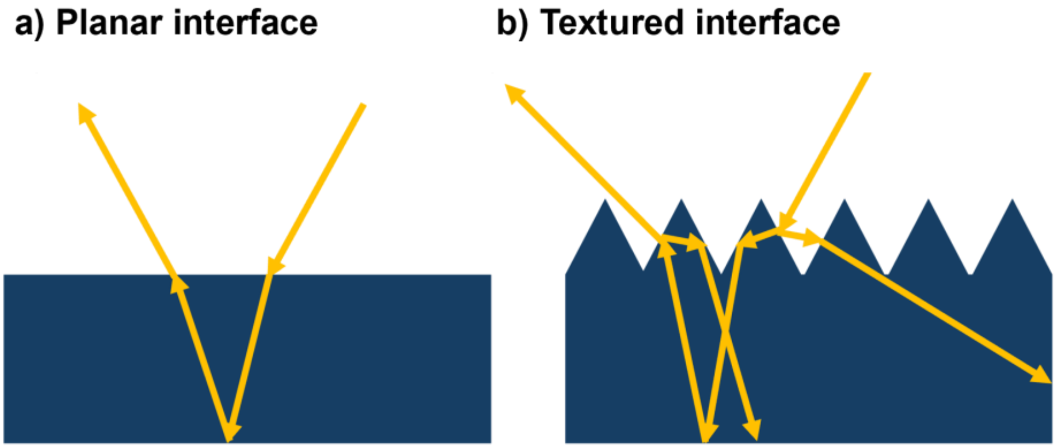

Figure 2. 10 – Light paths in solar cells with (a) planar vs. (b) textured interfaces.

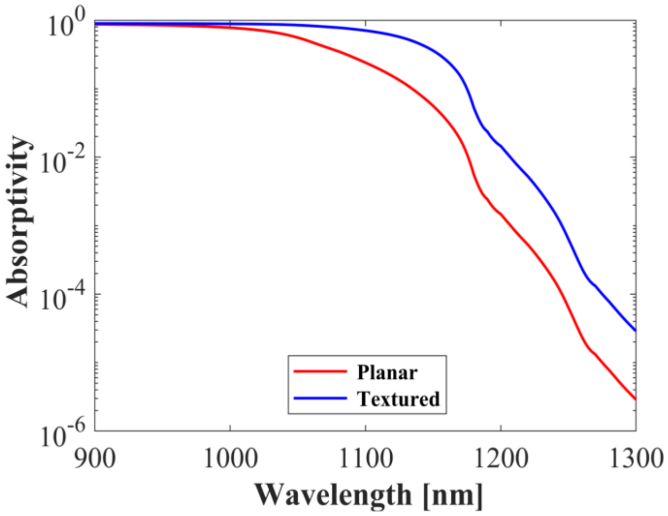

Figure 2. 11 – An example of the absorptivity spectra for planar (p = 5) and textured (p = 50) Si cells, calculated using the optical model in Section 3.1.

This critical dependence on optical properties is due to light trapping within the cell. The optical path length is the total distance a weakly absorbed photon travels within the active region of a solar cell before it either escapes or is lost to parasitic absorption [92, 93]. This distance depends on both the absorber thickness and the internal scattering of light within the structure. To quantify this effect, the optical path length enhancement factor (p) is introduced [92, 93]. The factor p measures the enhancement of a photon's path length relative to the absorber thickness due to light trapping.

As illustrated in Figure 2.10(a), the refraction angles at a planar surface typically allow photons to escape the cell after a few reflections, resulting in low p. In contrast, a textured surface [Figure 2.10(b)] refracts and reflects photons multiple times, effectively increasing their travel distance and resulting in significantly higher p [92]. As p increases, the probability of light absorption at longer wavelengths also rises, leading to a substantial improvement in absorptivity where the material's intrinsic absorption is weak. Figure 2.11 shows an example of calculated absorptivity spectra for typical planar and textured Si samples. These spectra were generated using the optical model detailed in Section 3.1**,** assuming p of 5 for the planar case and 50 for the textured case. At shorter wavelengths, where absorption is strong, both samples behave similarly. However, in the near-band-edge region, the extended optical path in the textured sample results in a substantial increase in absorptivity. Since luminescence emission is directly proportional to absorptivity (Equation 2.13), samples with varying p will emit different luminescence intensities, even if their iV values are identical [85, 93].

In Chapter 3, the impact of varying optical properties on iV estimation is investigated in further detail. This chapter also introduces a novel method based on a well-selected BPF that enables accurate iV extraction from samples with different optical properties using only a single calibration cell.

2.3.5 Comparative summary of calibration methods

Table 2. 1 - Comparison of calibration methods for spatially resolved iV extraction.

Calibration method	Required inputs	Key assumptions	Strengths	Critical limitation
Spectral fitting (full-spectrum or high-energy tail fit) (Section 2.3.1)	Absolute luminescence spectrum Sample temperature (T) Absorptivity (A) (full-spectrum)	Generalised Planck law directly applies Tail-fit assumes A is ~constant, well above Eg (often taken ~1)	Most theory-direct Can be very accurate *if* A and T are known	Highly sensitive to the selected fitting window choice (tail-fit) Full-spectrum accuracy hinges on reliable A and T Spatial mapping can be slow/expensive (micro-PL or hyperspectral complexity)
Narrow-BPF high-energy tail imaging (Section 2.3.2)	Narrow BPF placed in the high-energy tail of PVK samples Single calibration constant from imaging a uniform calibrated source (calibration lamp + integrating sphere)	Absorptivity is assumed to be constant (A~1) over the BPF band Detection system response ~ constant over the narrow BPF	Simple single-step calibration and highly accurate Avoids needing spectrally resolved luminescence per pixel Calibration avoids multiplying each optical efficiency	A ~constant assumption becomes less reliable for thin PVK layers, typical of tandems Requires detailed analysis of the validity of the method for subcells in the tandem devices Original validation used only two filters and lacks guidelines for filter selection for different PVKs
Scaling-factor approach (Section 2.3.3)	Subcell-separating BPFs Spectrally resolved A or EQE per subcell Wavelength-dependent system response f built from: (a) calibration lamp + integrating sphere (f_1) and (b) camera QE datasheet + measured optics transmission (f_2)	Often uses $A \approx$ EQE Manufacturer QE_{camera} is accurate	Demonstrated across devices, including monolithic tandems Reported accuracy ~1%	Needs accurate subcell A/EQE (hard to determine for tandem subcells; EQE requires complete tandem) Using the wide BPF for the PVK subcell amplifies errors from inaccuracies in A/EQE Uncertainty in QE_{camera} datasheet can create systematic error

Calibration-cell method (Section 2.3.4)	Calibration cell with known iV	Calibration and measured cells must have identical optical properties	Very fast Cancels explicit f and A when the match is perfect Highly accurate if the calibration and measured cells have identical optical properties	Fails when the properties of the measured and the calibration cell differ

All calibration strategies reviewed above (Sections 2.3.1–2.3.4) infer iV from luminescence within the generalised Planck framework and differ primarily in their handling of the two wavelength-dependent terms: the sample optical term (A or EQE) and the detection-system response $f(\lambda)$. Table 2.1 compares the main calibration strategies reported in the literature, highlighting the required inputs, key assumptions, and practical limitations, particularly for monolithic PVK/Si tandems. In practice, methods that avoid constant-absorptivity approximations typically require spectrally resolved A or EQE and wavelength-dependent calibration, which is particularly challenging for tandem subcells. Conversely, methods that simplify calibration by assuming near-constant optical terms over a restricted detection window require careful selection and validation of that window for tandem device structures. In addition, approaches that depend strongly on device-specific optical properties often require recalibration or re-characterisation when applied to samples with different optical structures (e.g., thickness, texture, or composition). These trade-offs motivate the calibration strategy developed in Chapters 3 and 4.

2.4 Supplementary characterisation techniques

In addition to PC, PL-, and EL-based techniques, several complementary methods are essential for device analysis and calibration in support of iV estimation. These include current–voltage (I–V) measurements to assess electrical performance, as well as A and EQE measurements to evaluate optical properties and carrier collection efficiency. This section describes these supplementary techniques.

2.4.1 Current-voltage measurement

Current–voltage (I–V) measurements are a widely adopted characterisation technique used to evaluate the overall electrical performance of PV devices. The measurement involves recording the current flowing through the device as a function of applied voltage. The measured current is typically normalised to the device's active area, yielding a current density (J), that enables consistent comparison across devices of different sizes. *J*–*V* characterisation can be performed under both illumination (light *J*–*V*) and dark conditions (dark *J*–*V*) [67]. Light *J*–*V* measurements are typically conducted under standard test conditions (STC), using the AM1.5G spectrum at 100 mW/cm^2. Figure 2.12 shows a representative light *J*–*V* curve of a solar cell.

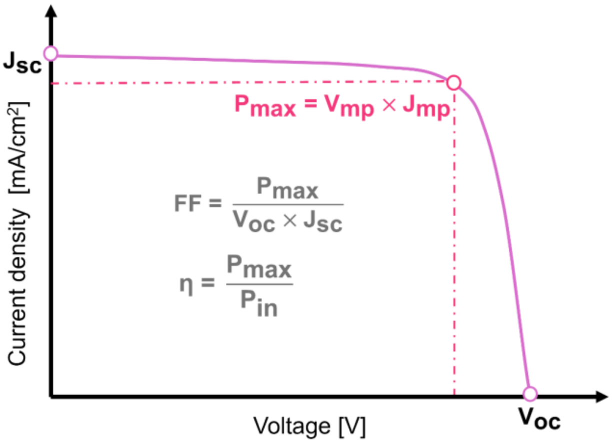

Figure 2. 12 – Typical *J*-*V* curve of a solar cell.

To interpret the measured light *J*–*V* curves in terms of physical mechanisms, an analytical description is provided by the one-diode or two diode model [67]. The single-diode model with five parameters is the commonly used due to its simplicity and sufficient accuracy for many applications and is given by [67]:

$$J(V) = J_{\mathrm{Ph}} - J_0\left[exp\left(\frac{q(V + JR_s)}{n_{\mathrm{d}} \cdot k_{\mathrm{B}}T}\right) - 1\right] - \frac{V + JR_s}{R_{sh}} \tag{2.28}$$

where J_{ph} is the generated photocurrent density in the solar cell, J_0 is the diode saturation current (associated with recombination), n_{d} is the ideality factor (typically $2/3 \leq n_{\mathrm{d}} \leq 2$) and R_{sh} is the shunt resistance. The one-diode model Equation 2.28 forms the foundation for extracting standard solar cell performance metrics:

- **Short circuit current (J_{sc}):** The current density measured at zero terminal voltage (V_{term} = 0 mV), which is approximately equal to J_{ph}. Therefore, J_{sc} primarily reflects the optical generation and carrier collection efficiency.
- **Open circuit voltage (V_{oc}):** The V_{term} across the solar cell when no current flows (J = 0 mA/cm^2). It corresponds to the maximum achievable voltage, governed by recombination and other loss mechanisms.
- **Maximum power point (MPP):** The point on the *J*–*V* curve where the product of voltage and current density is maximised, yielding the maximum electrical output:

$$P_{\max} = V_{\mathrm{MP}} \cdot J_{\mathrm{MP}} \tag{2.29}$$

where $P_{\max}$ is the maximum output power per unit area, V_{MP} and J_{MP} are voltage and current density at MPP, respectively.

- **Fill factor (*FF*):** *FF* is a figure of merit that characterises the shape of the *J*–*V* curve. A value closer to the ideal rectangular form signifies higher power extraction efficiency and reduced losses. It is calculated by dividing the maximum deliverable power to the product of V_{oc} and J_{sc}:

$$FF = \frac{P_{\max}}{V_{\mathrm{oc}} \cdot J_{\mathrm{sc}}} \tag{2.30}$$

- **Power conversion efficiency (*η*):** The fraction of incident solar power converted into electrical power:

$$\eta = \frac{P_{\max}}{P_{\mathrm{in}}} \tag{2.31}$$

where P_{in} is the incident light power per unit area. It represents the overall solar cell performance.

- **Series resistance (R_s):** It represents resistive losses originating from the contacts, bulk semiconductor layers, and interconnections. A high R_s primarily impacts FF and the slope of the *J*–*V* curve near V_{oc}.
- **Shunt resistance (R_{sh}):** It represents current leakage paths through the device, often due to material defects or fabrication imperfections. A low R_{sh} primarily impacts the FF and the slope of the *J*–*V* curve near J_{sc}.

Dark *J*–*V* measurements are performed in the absence of illumination, with carriers driven through the device electrically. By sweeping the voltage and recording the resulting current, the dark *J*–*V* curve is obtained. This curve reflects the electrical behaviour of the cell, unaffected by optical factors such as absorption or carrier-collection efficiency (J_{sc} = 0 mA/cm^2), and thus provides a more controlled assessment of charge transport and recombination mechanisms [67]. Therefore, fitting the dark *J*–*V* curve to a one- or two-diode model enables accurate extraction of key parameters [67], including R_s, R_{sh}, n_d and J_0.

The experimental setup for *J*–*V* measurements includes an SMU to apply a controlled voltage sweep and simultaneously record the current. For light *J*–*V*, a calibrated solar simulator operating under STC (AM1.5G spectrum, 100 mW/cm^2) is used. The irradiance is monitored with a certified reference cell, and a spectral-mismatch correction factor is applied to account for differences between the simulator spectrum and the AM1.5G reference spectrum. For dark J–V, the same setup is placed in a light-tight enclosure to eliminate any photoexcitation.

2.4.2 Absorptivity

The total Absorptivity, A_{tot}, describes how much of the incident light at a given wavelength is absorbed by a solar cell. A_{tot} cannot be directly quantified, as absorbed photons are converted into other forms of energy within the device. Instead, it can be determined indirectly by measuring two complementary optical properties at a given wavelength: total reflectance (R_{tot}), the fraction of incident light reflected from the surface, and transmittance (T_{trans}), the fraction of light transmitted through the device. The absorptivity can then be calculated by quantifying these components and applying the principle of energy conservation:

$$A_{\text{tot}}(\lambda) = 1 - R_{\text{tot}}(\lambda) - T_{\text{trans}}(\lambda) \tag{2.32}$$

In samples with negligible transmittance [$T_{\text{trans}}(\lambda) \approx 0$], such as devices with opaque back contacts, the absorptivity can be approximated by:

$$A_{\text{tot}}(\lambda) = 1 - R_{\text{tot}}(\lambda) \tag{2.33}$$

It is worth mentioning that the measured A_{tot} comprises two physical contributions: band-to-band absorptivity (A_{BB}) and parasitic absorptivity, where the free-carrier absorptivity (A_{FC}) is the dominant component [85, 94]. The physical process responsible for A_{BB} is the band-to-band absorption, where a photon with energy equal to or higher than the bandgap (E_{g}) excites an electron from the valence band (E_{V}) to the conduction band (E_{C}). This process generates electron–hole pairs that can contribute to the photocurrent if collected efficiently [85]. In contrast, A_{FC} stems from intraband transitions, where photons are absorbed by free carriers (typically in highly doped layers or contact materials), raising them to higher energy states within the same band [85]. Hence, A_{FC} does not generate additional carriers; instead, it results in thermal losses via non-radiative mechanisms.

In the context of luminescence, distinguishing between A_{BB} and A_{FC} is particularly important. Luminescence emission originates from radiative recombination (carriers generated by $h\nu \geq E_g$), a process that involves only A_{BB}. It should be noted that while the energy from A_{FC} is also eventually emitted as thermal radiation, this process is fundamentally different, and its emission intensity is negligible compared to the strong luminescence signal generated by A_{BB}. Therefore, for all practical purposes in luminescence analysis, the contribution from A_{FC} is considered to be zero [85]. Accordingly, throughout this thesis, the absorptivity term 'A' used in luminescence-related equations, such as the generalised Planck law [83], refers exclusively to A_{BB}.

In practice, A_{tot} can be determined using a spectrophotometer equipped with an integrating sphere, which accurately captures both R_{tot}, and T_{trans} over the relevant wavelength range. In this thesis, A_{tot} was measured using a PerkinElmer Lambda 1050 spectrophotometer fitted with a 150 mm integrating sphere. Furthermore, it is important to note that determining A_{BB} and A_{FC} requires indirect methods. For instance, these components can be inferred from luminescence measurements by comparing them with the measured A_{tot} obtained with a spectrophotometer [85, 93].

2.4.3 External quantum efficiency

The external quantum efficiency (EQE) quantifies the fraction of incident photons at a specific wavelength that are converted into collected charge carriers in a PV device [95]. It represents a comprehensive performance metric, inherently accounting for both optical and electrical losses, as it includes only absorbed photons that generate charge carriers and are successfully collected at the contacts.

The EQE spectrum is distinct from the measured A_{tot}, which is determined using a spectrophotometer and captures all photons absorbed by the device. As discussed, photons absorbed via A_{FC} dissipate as heat without generating charge carriers and thus do not appear in EQE data. In contrast, photons absorbed through A_{BB} create electron–hole pairs within the active layer, contributing to the EQE spectrum if these carriers are successfully collected at the contacts before recombination. Accordingly, EQE can be expressed as:

$$\mathrm{EQE}\ (\lambda) = \eta_c(\lambda) \cdot A_{BB}(\lambda) \tag{2.34}$$

where η_c is the carrier collection probability. Since recombination is an unavoidable process, η_c is always less than or equal to 1 [66, 67].

In today's solar cells, however, η_c approaches unity across a broad wavelength range. Under this condition, the measured EQE spectrum is a good approximation of the A_{BB}. Hence, the EQE is often substituted for A_{BB} in luminescence-based analyses [37, 84, 85]. As an example, Figure 2.13 compares the measured EQE and A_{tot} for an interdigitated back contact (IBC) solar cell, with A_{tot} calculated from the measured R_{tot} using Equation 2.33 ($T_{\mathrm{trans}} = 0$). In the 400 nm to 1000 nm range, the curves show excellent agreement, as A_{BB} is dominant and the η_c is near unity. Beyond 1000 nm, a discrepancy arises: the EQE drops as A_{BB} weakens near the bandgap, while A_{tot} remains high due to the parasitic A_{FC}.

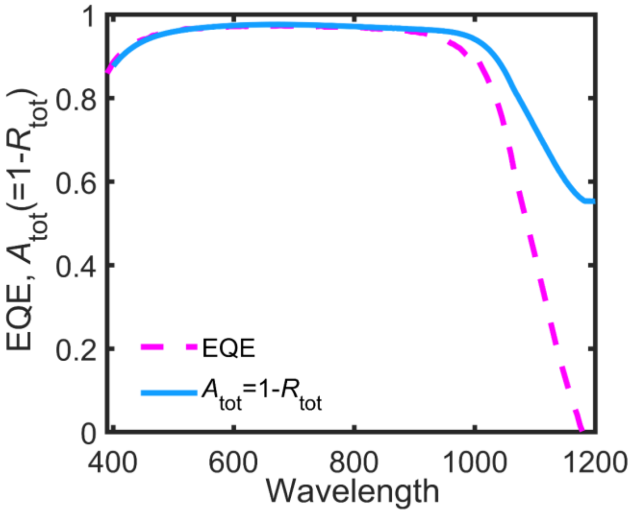

Figure 2. 13 – Comparison of EQE and A_{tot}, calculated from 1-R_{tot} measurements, for an IBC solar cell.

The EQE is experimentally determined by illuminating the device with monochromatic light and measuring the resulting photocurrent relative to the incident photon flux at each wavelength. A typical EQE measurement setup includes a broadband light source (e.g., xenon or halogen lamp), a monochromator to select wavelengths, and a mechanical chopper for lock-in detection. The modulated monochromatic beam is directed onto the device, and the resulting photocurrent, generated in response to the incident photon flux, is measured under short-circuit conditions.

To quantify the photon flux at each wavelength, calibrated reference PDs, typically Si (for 300–1,000 nm) and InGaAs (for 1,000–1,300 nm), with well-known spectral responsivities are used. Positioned in the same optical path, the reference PD converts the incident light into an absolute photon-flux scale, enabling EQE to be directly calculated as the ratio of collected charge carriers to incident photons. For tandem devices, subcell-selective EQE measurements require the use of optical filters and appropriate bias light to isolate the spectral response of each subcell (e.g., blue bias for the bottom cell, red for the top). Finally, integrating the product of the measured EQE and the standard AM1.5G photon-flux spectrum yields the one-sun J_{SC}.

In this thesis, EQE measurements were performed using the PV Measurements QEX7 Spectral Response System..

2.5 Applications of implied voltage determination

Implied voltage iV provides a valuable basis for extracting key device parameters. This section outlines its application in reconstructing pseudo-dark J–iV curves and estimating the intrinsic carrier concentration n_{i}.

2.5.1 Pseudo-dark *J*–i*V*

The performance of a solar cell is governed by the interplay between its inherent recombination and the resistive losses that occur during charge transport. The pseudo-dark *J*–i*V* curve can be used to distinguish between these effects [38, 61-64, 87, 90, 96, 97]. Unlike the conventional dark *J*–*V* curve, which is inherently affected by R_s, the pseudo-dark *J*–i*V* curve is constructed from recording i*V* at varying injection levels, making it independent of R_s [38, 61-63, 87, 90, 96, 97]. Figure 2.14 schematically compares pseudo-dark *J*–i*V* and dark *J*–*V* curves. At low current densities, the curves overlap because resistive losses are negligible, whereas they deviate at higher current densities as the voltage drop across R_s increases with current. This fundamental difference allows for the isolation of recombination-related losses from the resistive losses that occur during charge extraction.

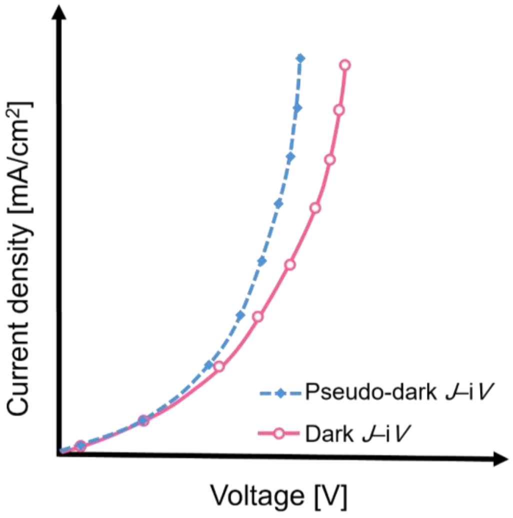

Figure 2. 14 – Schematic comparison of pseudo-dark *J*–i*V* and dark *J*–*V* curves.

It's important to note that this pseudo-dark *J*–i*V* curve can be converted into a pseudo-light *J*–i*V* curve by applying the superposition principle and shifting the curve by the separately measured J_{sc} [67, 96]. A comparison between the pseudo-light *J*–i*V* curve and the standard light *J*–*V* curve then reveals the contribution of R_s under operating conditions [63, 96].

The pseudo-dark *J*–i*V* curve was initially derived by Sinton and Cuevas using a technique referred to as Suns-V_{oc} method [96]. In this approach, a contacted device is illuminated at various light intensities, and the V_{oc} is recorded. Since the measurement is performed at open-circuit, where the net current is zero, R_s does not affect the measurement, allowing the technique to isolate the cell's recombination properties and the measured voltage then corresponds to the i*V* at the given illumination intensities [58]. A similar but contactless approach was later developed by Trupke et al. to determine the pseudo-dark *J*–i*V* curve from PL measurements, in a method known as Suns-PL [61]. In this technique, the sample is again held at open-circuit and excited by a laser at varying intensities. However, instead of recording the terminal voltage, the global PL emission from the sample is captured. With appropriate calibration, the PL signal is converted into i*V*, from which the pseudo-dark *J*–i*V* curve is derived [61]. It is common practice to then convert this curve (obtained from either method) into a pseudo–light *J*-i*V* curve by applying the superposition principle. A key advantage of the Suns-PL method is its applicability to partially processed or uncontacted cell precursors, as it does not require any electrical connections.

This Suns-PL concept was later extended to determine spatially resolved images of the pseudo-dark *J*–i*V* curve. In this advanced method, the PL signal is specifically captured by a camera, thereby obtaining a series of PL images at different illumination intensities. This enables the reconstruction of a local pseudo-dark *J*–i*V* curve for each pixel, revealing spatial variations across the sample [38, 62-64, 90, 97]. It is also worth mentioning that pseudo-dark *J*–i*V* curves can be determined from EL imaging [38, 64, 87]. In EL-based methods, which are applied to fully fabricated devices, the sample is forward-biased in the dark, and the emitted luminescence is recorded by a camera at different injection currents. The EL images are likewise converted into voltage data to construct the corresponding pseudo-dark *J*–i*V* curves.

In monolithic two-terminal tandem solar cells, the subcells are electrically connected in series, and the combined *J*–*V* response of the entire device can only be measured at the terminals. This restricts direct access to the individual performance of each subcell, complicating identification of the subcell limiting overall device efficiency. However, employing PL or EL imaging with proper calibration enables extraction of separate pseudo-dark *J*–i*V* curves for each subcell at various spatial positions [64, 87]. This allows for independent analysis of recombination losses, voltage offsets, and interfacial effects associated with each subcell in the tandem structure.

The practical application of the calibration method developed in this thesis, enabling spatially resolved pseudo-dark *J*–i*V* imaging of individual subcells in PVK/Si tandem devices, is demonstrated in Chapter 4.

2.5.2 Intrinsic carrier concentration

The intrinsic carrier concentration (n_i) is a fundamental parameter in semiconductor physics. It represents the concentration of free electrons and holes in a pure, undoped semiconductor at thermal equilibrium. The value of n_i directly influences key performance metrics, including J_0, V_{oc}, Δn, and recombination rates [67]. Therefore, its precise value is critical for accurate device modelling.

When semiconductor devices are doped or are in a non-equilibrium condition (i.e., under illumination), the presence of excess carriers causes the bandgap to shrink, a phenomenon known as bandgap narrowing (BGN). In this case, the effective intrinsic carrier concentration ($n_{\mathrm{i,eff}}$) is commonly used to account for the BGN effect, allowing the standard semiconductor equations to remain valid. This distinction is crucial, as the fundamental n_{i} is a material constant, whereas $n_{\mathrm{i,eff}}$ is the practical parameter that describes the material's behaviour under specific non-equilibrium conditions. Accordingly, the n_{i} parameter that relates Δn and iV (see Equation 2.5) is equivalent to $n_{\mathrm{i,eff}}$.

Different approaches have been developed to determine the intrinsic carrier concentration in Si samples with high accuracy [98-102]. However, for emerging PV materials, such as PVK, the precise and direct determination of this parameter remains challenging due to the absence of standardised methods.

In Chapter 6, a novel approach is presented to determine this parameter by extracting the iV and Δn values from PL-based measurements and rearranging Equation 2.5. Since this method is performed under illumination (a non-equilibrium condition), the extracted parameter is, by definition, $n_{\mathrm{i,eff}}$. Throughout this thesis, for notational simplicity, the symbol n_{i} will hereafter denote $n_{\mathrm{i,eff}}$, which is the parameter directly accessible from the experimental measurements. This work demonstrates, for the first time, the direct determination of the intrinsic carrier concentration via a fully contactless method that requires minimal information about the material properties.

Chapter 6 provides further details on previous approaches for n_{i} determination in Si samples and a comprehensive discussion of the method developed in this thesis.

2.6 Summary

This chapter introduced the fundamental principles of iV and its link to both photoconductivity and luminescence emission. Various calibration methods for spatially resolved iV imaging in Si and PVK/Si tandem devices were reviewed, highlighting the strengths and inherent limitations of each method. A major limitation of existing techniques is their dependence on detailed optical characterisation, specifically the sample's A (or EQE) and the optical response of the detection system (f). Importantly, the use of a narrow BPF with a limited spectral window to reduce the dependency of the luminescence signal on optical properties, where both A (or EQE) and f can be assumed nearly constant, was previously established on PVK films. While this approach significantly reduces optical dependencies, it still requires an approximate value for A (or EQE) of the measured cells. Furthermore, its applicability has so far only been demonstrated using two specific BPFs. However, a detailed analysis and general procedure for selecting suitable filters with different centre wavelengths or bandwidths has not yet been developed. This limitation restricts its broader application to a wider range of devices and morphologies. Moreover, most other calibration methods require repeating calibration procedures for samples with different optical properties.

To overcome these limitations, the following chapters introduce and analyse a new calibration method based on a single calibration cell combined with a suitable BPF for quantitative iV mapping. Unlike previous approaches, this method eliminates the need for knowledge of the sample's optical properties or a calibration cell with properties identical to the measured device. Its independence from optical properties also removes the need for performing separate calibrations for different samples. The effectiveness of this method is demonstrated on single-junction Si and on individual subcells within PVK/Si tandem structures. Furthermore, its applicability for the contactless quantification of n_i is examined and validated in this thesis (Chapter 6).

Chapter 3 details the proposed calibration methodology, evaluates its performance in extracting iV images across a range of Si configurations, and demonstrates its effectiveness in eliminating dependence on optical property variations.

Chapter 3 – Spatially Resolved Determination of the Implied Voltage in Si Solar Cells

As outlined in Chapter 2, imaging techniques such as PL and EL are powerful tools for extracting spatially resolved iV of Si solar cells and wafers. However, existing quantitative methods for Si solar cells often require separate calibration for each distinct sample type, or in some cases, detailed knowledge of the sample's optical properties, such as A or EQE. These dependencies limit the broader applicability of iV mapping across devices with diverse morphologies and light-management features.

To address these limitations, this chapter introduces a robust and simplified calibration method based on the use of a BPF. This approach enables accurate iV extraction of Si wafers and cells without requiring sample-specific calibration or prior knowledge of the optical properties of either the sample or the detection system.

Section 3.1 presents a systematic approach to select the optimal BPF for minimising iV errors across c-Si samples with different optical properties. Section 3.2 investigates the impact of key optical parameters, including p, front reflectance (R), and d on the iV extraction using different BPFs. Section 3.3 provides experimental validation of the method through EL imaging of Si solar cells with varied optical properties. Section 3.4 complements the BPF selection by quantifying its impact on iV imaging accuracy through signal-to-noise (SNR) analysis. Finally, Section 3.5 evaluates the accuracy of the proposed method in extracting iV of Si wafers.

This chapter is based on:
S. Zandi, Z. Hameiri, A. M. Soufiani, J. W. Weber, and T. Trupke, "Simplified method for the conversion of luminescence signals from Si wafers and solar cells into implied voltages," *Solar Energy Materials and Solar Cells*, vol. 269, p. 112716, 2024.
S. Zandi, A. M. Soufiani, J. W. Weber, Z. Hameiri, and T. Trupke "Novel method for the extraction of implied voltages of Si wafers and solar cells from luminescence-based measurements", 40th European Photovoltaic Solar Energy Conference, 2023.

3.1 Methodology – BPF assessment

As discussed in Chapter 2, a major limitation of using a calibration cell to determine iV is its sensitivity to the optical properties of the sample. Therefore, a set of calibration cells is needed as samples with different optical properties require a set of calibration cella with a similar structure (see relevant discussion in Section 2.3.4 in Chapter 2).

Recent work by Soufiani et al. [50] showed that, for PVK devices, applying a narrow BPF can effectively eliminate the need for detailed knowledge of $A(\lambda)$, as it remains close to unity and nearly constant over the filtered range. Inspired by this approach, the implementation of a BPF combined with a calibration-cell-based approach for determining iV of Si solar cells using a single calibration cell is investigated. In this section, a systematic modelling approach is developed to identify the optimal BPF range that minimises iV errors arising from differences in optical properties between the calibration and measured cells.

To examine the impact of optical properties on luminescence emission, Si cells with Lambertian front surfaces (which scatter light equally in all directions) were modelled. The absorptivity of such cells (with different p), assuming perfect rear reflection, is given in [92]:

$$A(\lambda) = \frac{1 - R(\lambda)}{\dfrac{1 - R(\lambda)}{p \times \alpha(\lambda) \times d} + 1} \tag{3.1}$$

where α is the absorption coefficient and R is the front reflection.

While Equation 3.1 is valid for weakly absorbed light, it is a sufficient approximation for the analysis conducted here. The theoretical upper limit for c-Si cells with perfectly randomised surfaces is $p = 4n_r^2 \sim 50$, where n_r is the refractive index of c-Si [92]. For simplicity, a wavelength-independent reflectance [$R(\lambda) = 10\%$] is considered. To quantify the impact of different surface properties on both the absorptance and the emitted luminescence intensity, p was varied. Figure 3.1(a) presents the spectral absorptance $A(\lambda)$ for p ranging from $p = 3$ (representing a planar cell with poor light trapping from factors like natural internal reflection at the unpassivated rear surface) to $p = 50$ (for a sample with ideal Lambertian texturing and perfect rear reflector). Equation 2.13 can then be used to calculate the associated $\phi^{\text{absolute}}(\lambda)$ as shown in Figure 3.1(b); the parameters used in these simulations are summarised in the figure caption. Due to the high absorption coefficient of c-Si in the short wavelength range ($\lambda < 1{,}000$ nm), the absorptance is close to unity and thus almost independent of p. Consequently, $\phi^{\text{absolute}}(\lambda)$ is also almost independent of p in this spectral range. In contrast, in the long wavelength range, increasing p enhances the absorptivity, as increasing the optical path length increases the light absorption probability. In this range, the peak position of the luminescence spectra is red shifted when p increases [14]. At the limit of weak absorption, i.e., in the long wavelength tail of the emission spectrum, the emitted photon flux increases in proportion to p. As a result, the emitted luminescence intensity varies by up to a factor of 50 between samples with the same iV but different light trapping properties.

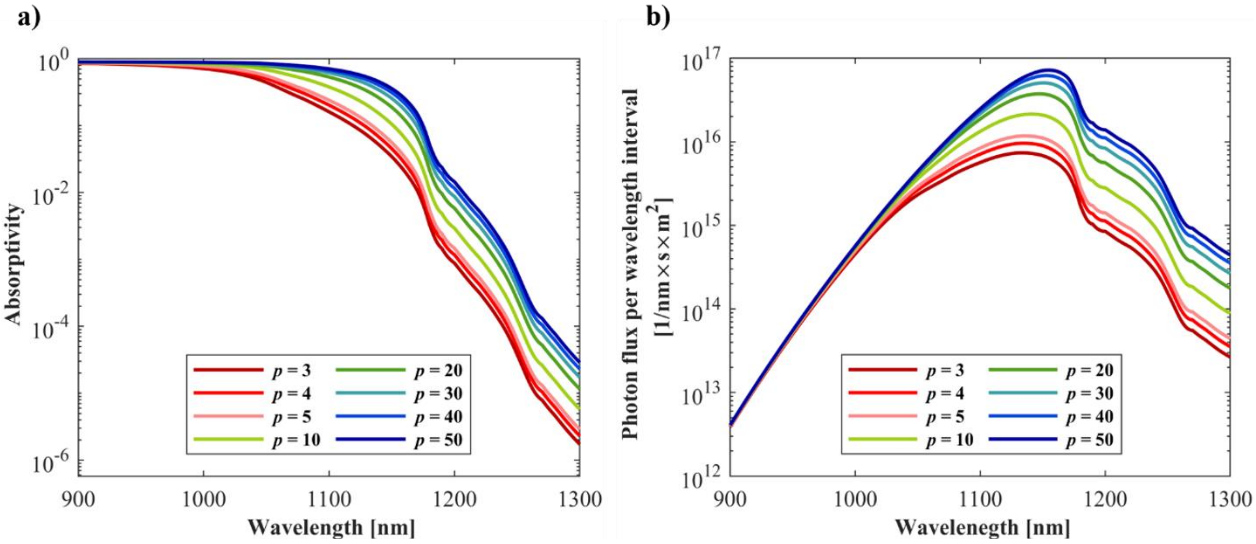

Figure 3. 1 – (a) Absorptivity and (b) absolute photon flux per wavelength interval of c-Si solar cells with different p between 3 and 50, assuming $R(\lambda)$ = 10%, $\alpha(\lambda)$ that is based on Ref. [103], $\phi_{\text{BB}}(\lambda)$ at room temperature (T = 25 °C), d = 180 µm, and iV = 680 mV**.**

To model ϕ^{detect}, the spectral response of the detection system (f in Equation 2.14) is approximated by an assumed camera quantum efficiency, $\text{QE}_{\text{camera}}$. The representative $\text{QE}_{\text{camera}}$ curves for the Si-based and InGaAs-based detectors, reproduced from [104], are shown in Figure 3.2(a). Figure 3.2(b) compares the resulting ϕ^{detect} from c-Si solar cells (with p = 5, 20, and 40) using an InGaAs camera (solid lines) and a Si camera (dotted lines), with the Si camera data scaled by a factor of 50. The ϕ^{detect} from the Si camera is considerably lower than that of the InGaAs camera due to its much lower $\text{QE}_{\text{camera}}$ at wavelengths above 1,000 nm. Notably, Si-detected spectra are also less sensitive to variations in p at longer wavelengths compared to those detected with the InGaAs camera.

The detected luminescence signal thus varies, both in intensity and spectral shape, for samples with the same iV but different light trapping properties (different p). Therefore, calibrating the imaging system using a calibration cell with specific p can yield substantial errors in estimating the iV of measured cells with different p, particularly when InGaAs detectors are used.

To address this problem, a BPF can be mounted in front of the camera to restrict the detected luminescence signal to short wavelengths, where variations in the detected luminescence signal are much less pronounced [as shown in Figure 3.2(b)], and iV errors are, therefore, significantly reduced.

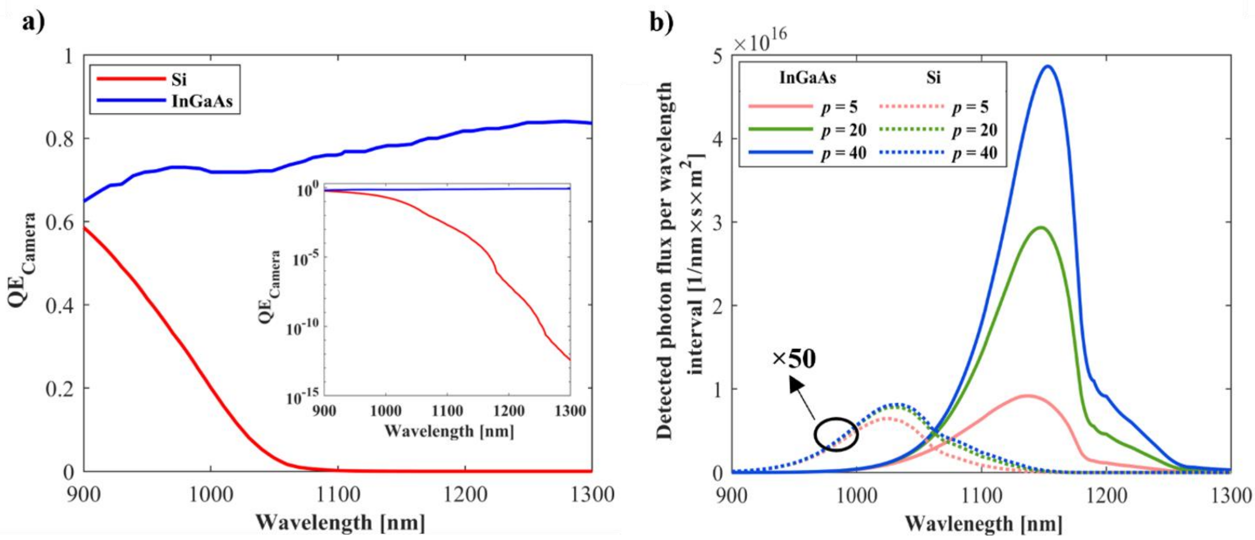

Figure 3. 2 – (a) Typical QE$_{\text{camera}}$ of Si-based (red line) and InGaAs-based (blue line) detectors, reproduced from [104]. (b) Luminescence photon flux per wavelength interval from a c-Si solar cell with p = 5, 20, and 40 as detected by InGaAs (solid lines) and Si cameras (dotted lines). Data for the Si camera is scaled by ×50 for representation on the same scale.

To ensure that the calibration process remains unaffected by the optical properties of the samples, the procedure depicted in Figure 3.3 to determine the suitable spectral properties of the BPF was used. First, $\Delta\phi_{\text{cell}}^{\text{detect}}$ of the measured cells with varying p was calculated for both InGaAs and Si cameras. Then, a cell with p = 20 was assumed as the calibration cell ($\Delta\phi_{\text{calib}}^{\text{detect}}$), and the i$V$ of all solar cells (with different p) was determined using Equation 2.27. For the simulation of the different BPFs, the cut-on wavelength (λ_1) was fixed at 975 nm while the cut-off wavelength (λ_2) was varied between 1,000 nm and 1,300 nm. In the experiments, BPFs with these properties were created through the combination of a longpass filter (LPF) and a shortpass filter (SPF).

3.2 BPF selection – simulation and analysis

Using the method described above, this section presents the effects of key optical parameters, namely p, R, and d, on the accuracy of iV extraction using different BPFs. This modelling enables the identification of suitable BPF configurations that minimise errors across devices with varying optical characteristics.

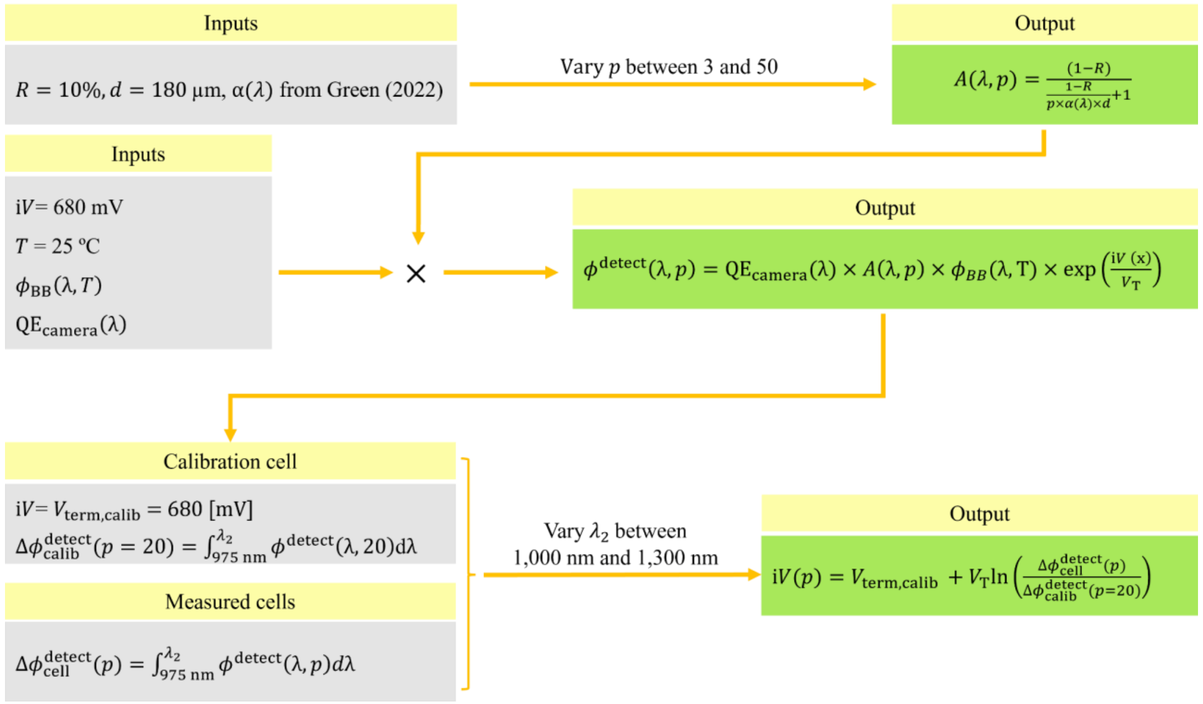

Figure 3. 3 – A schematic of the procedure for the selection of an appropriate BPF by estimating the iV error of cells with different p using a calibration cell with p = 20.

3.2.1 Impact of different texturing

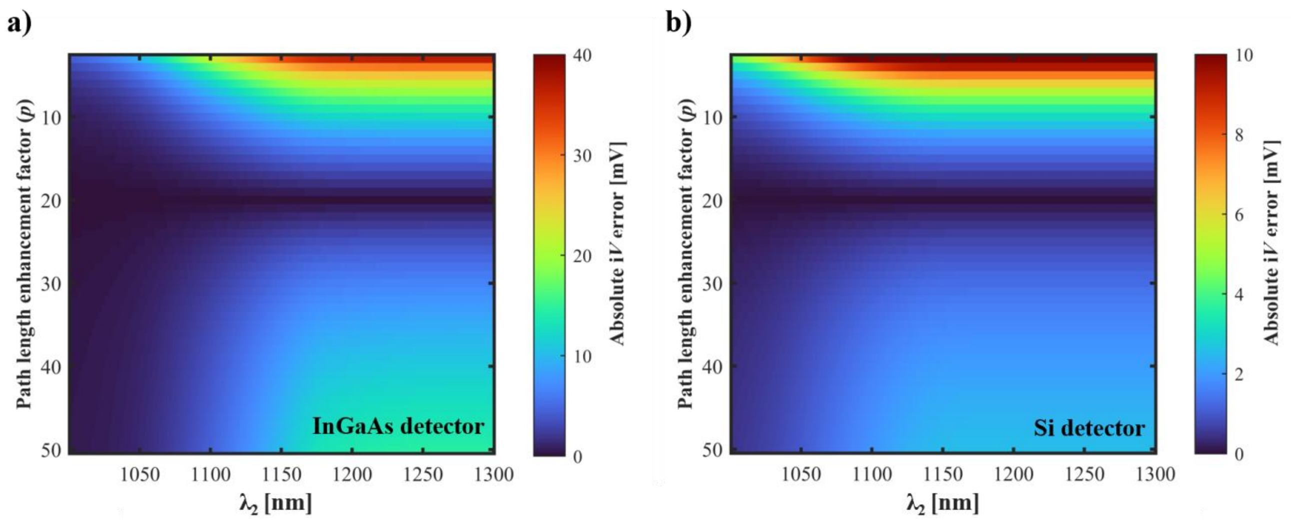

Figure 3. 4 – Absolute iV error maps as a function of λ_2 for solar cells with different values of p using (a) InGaAs and (b) Si cameras. Note that different colour scales are used (InGaAs: 0–40 mV, Si: 0–10 mV), reflecting the different error ranges.

Figure 3.4 presents the iV error maps as a function of λ_2 for a detection system based on an InGaAs camera [Figure 3.4(a)] and a Si camera [Figure 3.4 (b)]. The iV error is defined as the difference between the estimated iV via luminescence (using Equation 2.27) and the simulated true implied voltage, iV_{true} (in this modelling, 680 mV). Note that in this section, the measured and calibration cells have similar thicknesses and front reflection characteristics. Variations in R modulate the emitted luminescence signal via optical coupling, an effect that is particularly pronounced at shorter wavelengths. Discrepancies in d directly scale the emitted luminescence intensity by linearly altering the absorptivity. The impact of variations in these parameters on the accuracy of iV determination is discussed in Sections 3.2.2 and 3.2.3.

As expected, for test samples with p = 20, the simulations yield zero error for all λ_2 values, since the calibration cell and test cell have the same optical properties. The absolute error increases with increasing λ_2 for measured cells with other values of p. This reflects the fact that the emitted luminescence intensity is much more sensitive to the optical properties (i.e., to p) of a sample at longer wavelengths. When using the selected Si-based camera, the absolute iV error is within 10 mV, regardless of p and λ_2, which is much smaller than the error in iV obtained with InGaAs cameras (up to 40 mV). It is worth noting that for both types of cameras, the maximum error is observed for cells with a very low p, representing samples with planar or polished surfaces or extremely poor light trapping, which is uncommon in typical Si PV applications. In the more common range of p, estimated here to be between 10 and 50, the maximum voltage error using Si cameras is limited to 3 mV. Hence, for some applications, and depending on the specific spectral sensitivity of the camera, a filter is not required if Si cameras are used, as the $\mathrm{QE}_{\mathrm{camera}}$ effectively acts as an SPF, limiting the detected signal to the short wavelength tail of the emitted luminescence.

In Figure 3.4 the error in iV was calculated, assuming a calibration cell with p = 20. To investigate the impact of the optical properties on the determined errors when different *calibration cells* with other p values are used, a figure-of-merit, the root-mean-square error (RMSE), was defined. The RMSE aggregates the errors presented in Figure 3.4 over different λ_2 values into a single representative metric. The RMSE of iV was calculated as:

$$\mathrm{RMSE} = \sqrt{\frac{\sum_{i=1}^{m}(\mathrm{i}V(i,\lambda_2) - \mathrm{i}V_{\mathrm{true}})^2}{n}} \tag{3.2}$$

where m stands for the number of cells with different p (m = 48) while iV_{true} is the simulated iV (680 mV).

Figure 3.5 shows the calculated RMSE for calibration cells with different p (p_{calib}) as a function of λ_2 for the two types of cameras. Consistent with Figure 3.4, in the case of the InGaAs camera, the RMSE increases noticeably as λ_2 increases (for the range above 1,100 nm). For both cameras, it seems that a calibration cell with p = 20 provides the minimum RMSE across the entire λ_2 range. Nevertheless, if a filter with a λ_2 below 1,100 nm is used, the impact of the calibration cell optical properties on the i*V* accuracy is minimised. Of course, if the expected range for the optical properties of the measured cells is well known, the calibration cell should be selected accordingly.

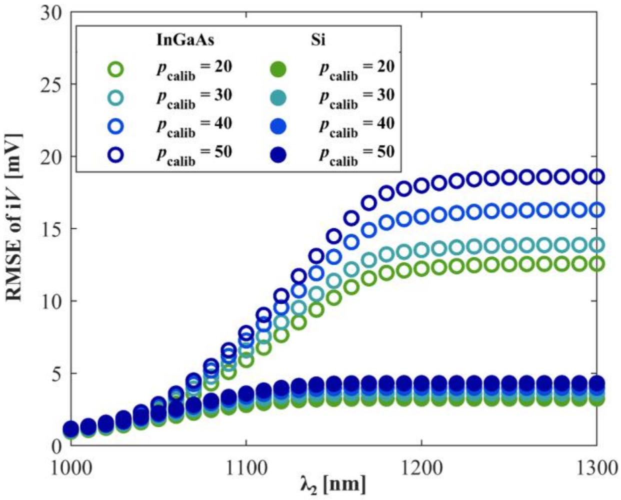

Figure 3. 5 – RMSE as a function of λ_2 for calibration cells with different *p* (20, 30, 40, and 50) measured with InGaAs (open symbols) and Si (filled symbols) cameras. The measured cells are cells with *p* ranging from 3 to 50.

3.2.2 Impact of variations in front reflection

Differences between the front reflection of the calibration cell and the measured cells can also cause errors in i*V*. In the previous simulations (Figure 3.4 and Figure 3.5), a constant front reflection was assumed for both cells [a wavelength-independent $R = 10\%$]. To investigate the effect of front reflection on i*V* error, *R* of the calibration cell was assumed to be 10%, while *R* of the measured cells was varied between 1% and 20% (wavelength independent).

Figure 3.6 shows i*V* error as a function of λ_2 for cells with three different *p* ($p = 5$, 25, and 40) and different *R* (between 1% and 20%). Note that a cell with $p = 20$ was used as the calibration cell.

In the case of the InGaAs camera [Figure 3.6(a)], the impact of variations in *R* on i*V* error reduces at longer wavelengths (the shaded region gets narrower). This trend can be explained by Equation 3.1. At longer wavelengths where absorption is weak, the first term in the denominator dominates, and the impact of *R* effectively cancels out. As a result, the absorptivity, and thus the luminescence signal, becomes largely independent of *R*. In contrast, at shorter wavelengths, where the absorption of Si is high, the first term in the denominator becomes much smaller than one, making the absorptivity and luminescence signal approximately proportional to 1-*R.* Therefore, *R*-related errors are more pronounced in this regime. This effect also accounts for the enhanced sensitivity to *R* observed in the sample with $p = 40$ compared to $p = 5$, as the condition for the first term to become negligible is fulfilled at shorter wavelengths. Figure 3.6(b) shows the i*V* error associated with the Si camera. Since the QE_{camera} of the Si camera restricts luminescence detection predominantly to the shorter wavelengths, the integrated luminescence signal remains relatively constant when λ_2 is varied. Hence, unlike the InGaAs case, the error remains largely independent of λ_2 values.

Therefore, while the effect of *R* variation on the i*V* error changes with sample properties and the detection system, the resulting error deviation is limited to approximately ±2.5 mV under all tested conditions.

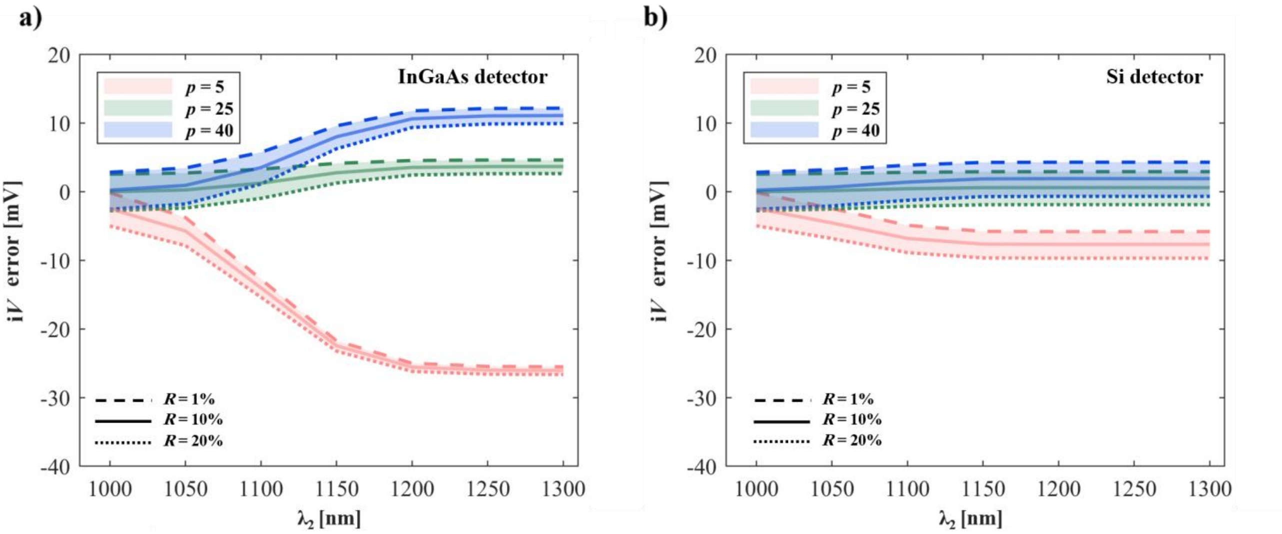

Figure 3. 6 – The i*V* errors for cells with different *p* (5, 25, and 40) measured with (a) InGaAs and (b) Si cameras. The shaded regions represent the associated errors due to the uncertainty in *R*. Note that a cell with *p* = 20 is used as the calibration cell.

3.2.3 Impact of variations in absorber thickness

Differences between the thicknesses of the calibration and measured cells can also impact i*V* error. It is noted that it is challenging to distinguish between impacts of *d* and *p* [see Equation 3.1]. To overcome this challenge, a thickness-related scaling factor was defined.

As the thickness of the measured cell may differ from the thickness of the calibration cell, a scaling factor needs to be determined. Using Equations 2.16 and 3.1 (to *A* calculation), the detected luminescence was calculated for calibration cells (with *p* = 20) with thicknesses between 45 and 720 µm for both InGaAs and Si cameras, while λ_2 was varied in the range 1,000 to 1,300 nm (λ_1 was set to 975 nm). The thickness of the measured cell was fixed at 180 µm. The ratio between the detected signal of the calibration cells with different thicknesses ($\Delta\phi_{\mathrm{diff}}^{\mathrm{calib}}$) and that of the calibration cell with a thickness of 180 µm ($\Delta\phi_{\mathrm{base}}^{\mathrm{calib}}$), identical to the measured cell, is defined as $\Delta\phi_{\mathrm{ratio}}$. Figures 3.7(a) and (b) show the calculated $\Delta\phi_{\mathrm{ratio}}$ for the InGaAs and Si cameras, respectively, as a function of their equivalent thickness ratio (d_{ratio}). To extract the relationship between $\Delta\phi_{\mathrm{ratio}}$ and d_{ratio} for each λ_2, different fitting functions were employed. Linear and single-exponential functions were initially evaluated. However, neither captured the dependence of $\Delta\phi_{\mathrm{ratio}}$ on d_{ratio} across the entire λ_2 range. This behaviour is attributed to spectral variations in absorptivity within the detection band: at shorter wavelengths, the absorptivity is higher and relatively insensitive to thickness, whereas at longer wavelengths, the absorptivity is lower and scales approximately linearly with thickness. As the detector integrates the photon flux up to the λ_2 limit, the measured signal represents a weighted sum of thickness-independent and thickness-dependent contributions. A bi-exponential function (Equation 3.3) was therefore selected, as it provides the flexibility to capture these optical behaviours across all investigated λ_2 values. The grey lines in Figure 3.7 show the corresponding bi-exponential fits. The four extracted coefficients ($a_{\mathrm{Thick.}}$, $b_{\mathrm{Thick.}}$, $c_{\mathrm{Thick.}}$, and $e_{\mathrm{Thick.}}$) are summarised in Tables 3.1 and 3.2.

$$\Delta\phi_{\mathrm{ratio}}(d_{\mathrm{ratio}}) = a_{\mathrm{Thick.}} \times \exp(b_{\mathrm{Thick.}} \times d_{\mathrm{ratio}}) + c_{\mathrm{Thick.}} \times \exp(e_{\mathrm{Thick.}} \times d_{\mathrm{ratio}}) \tag{3.3}$$

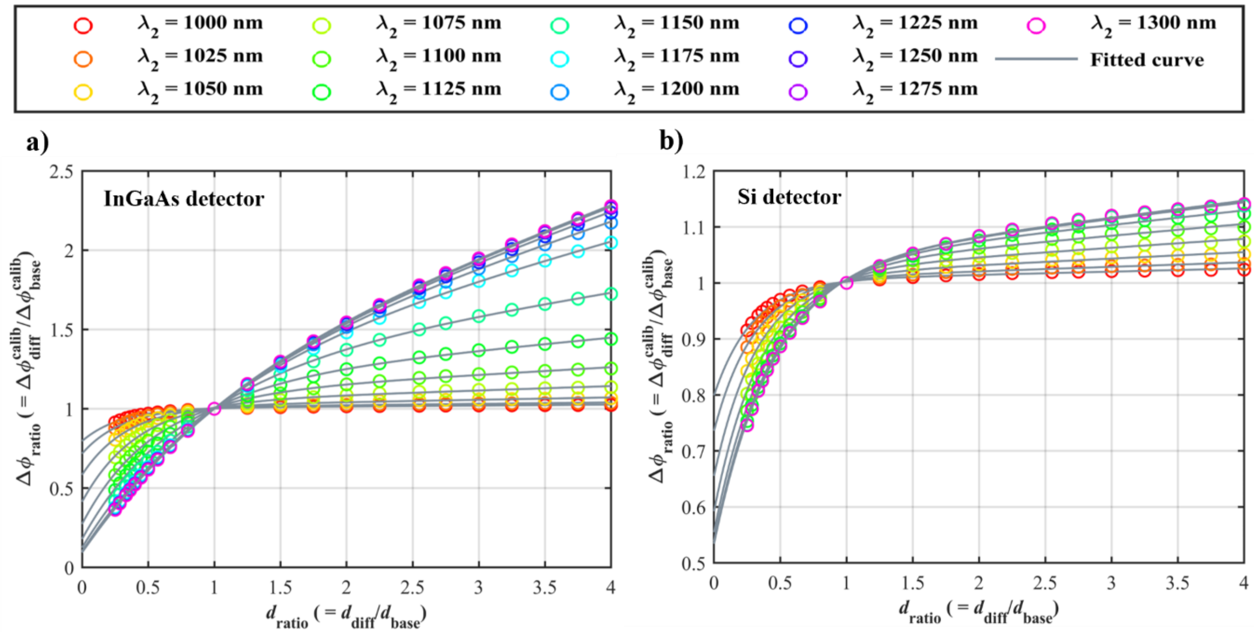

Figure 3. 7 – The $\Delta\phi_{\mathrm{ratio}}$ as a function of d_{ratio} for different λ_2 using (a) an InGaAs camera and (b) a Si camera. Open symbols depict the calculated relationship between $\Delta\phi_{\mathrm{ratio}}$ and d_{ratio} for specific λ_2 (1,000 – 1,300 nm). Grey lines represent the bi-exponential fitting curves associated with the corresponding λ_2.

Figure 3.8 presents the absolute errors in iV as a function of p when the calibration cell has half the thickness of the measured cell, using a BPF with λ_1 = 975 nm and λ_2 = 1,075 nm (p = 20 for the calibration cell) for both InGaAs and Si cameras. Three cases are compared: (1) uncorrected measurement (blue dashed lines), (2) calibration and measured cells with identical thicknesses (red dashed lines), and (3) thickness-corrected measurement (solid lines). As A is related to the product d×p, the errors in the uncorrected case are lower than those in the corrected case when $p < 13$ (with a minimum when $p = 10$, half of the correct p, as the thickness is doubled). The corrected curve is identical to the case where the calibration and measured cells have identical thickness, demonstrating that the thickness-related correction factor indeed removes the effect of thickness variation. As previously shown, measurements using an InGaAs camera are more sensitive to iV errors as well as variations in thickness compared to the Si camera for this λ_2. Note that modern solar cells typically fall within a narrow thickness range; therefore, it is recommended to use calibration samples of similar thickness. However, when a geometrical mismatch exists between the calibration cell and the device under test, the proposed correction successfully removes the impact of thickness variation. Applying the thickness correction factor is straightforward and can be implemented during post-processing, as the cell thickness is easily measured, enabling accurate iV extraction.

Table 3. 1 – Extracted fitting coefficients for thickness correction (InGaAs detector).

InGaAs detector				
λ_2	$a_{\text{Thick.}}$	$b_{\text{Thick.}}$	$c_{\text{Thick.}}$	$e_{\text{Thick.}}$
1,000	1.033	0.0056	-0.2068	-3.4327
1,025	1.0059	0.0083	-0.2885	-3.2710
1,050	1.0136	0.0139	-0.4295	-2.9430
1,075	1.0369	0.0244	-0.6230	-2.4190
1,100	1.0855	0.0378	-0.8117	-1.9093
1,125	1.1733	0.0532	-0.9940	-1.4532
1,150	1.3096	0.0721	-1.1845	-1.0732
1,175	1.4264	0.0967	-1.3243	-0.8430
1,200	1.4415	0.1098	-1.3441	-0.7931
1,225	1.4479	0.1162	-1.3526	-0.7706
1,250	1.4515	0.1192	-1.3572	-0.7600
1,275	1.4524	0.1199	-1.3584	-0.7573
1,300	1.4528	0.1202	-1.3589	-0.7561

Table 3. 2 – Extracted fitting coefficients for thickness correction (Si camera).

Si detector				
λ_2	$a_{\text{Thick.}}$	$b_{\text{Thick.}}$	$c_{\text{Thick.}}$	$e_{\text{Thick.}}$
1,000	1.0033	0.0056	-0.2040	-3.4372
1,025	1.0053	0.0077	-0.2692	-3.3018
1,050	1.0095	0.0110	-0.3538	-3.0698
1,075	1.0161	0.0150	-0.4236	-2.7819
1,100	1.0238	0.0192	-0.4688	-2.5160
1,125	1.0298	0.0231	-0.4910	-2.3289
1,150	1.0316	0.0258	-0.4968	-2.2489
1,175	1.0314	0.0266	-0.4970	-2.2385
1,200	1.0314	0.0266	-0.4970	-2.2384
1,225	1.0314	0.0266	-0.4970	-2.2384
1,250	1.0314	0.0266	-0.4970	-2.2384
1,275	1.0314	0.0266	-0.4970	-2.2384
1,300	1.0314	0.0266	-0.4970	-2.2384

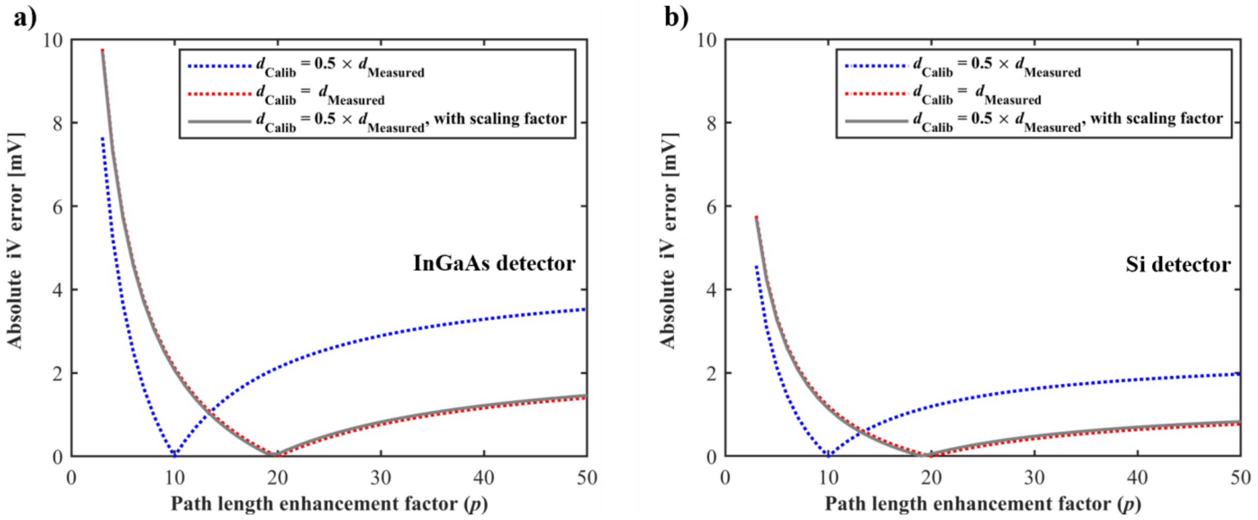

Figure 3. 8 – Absolute i*V* errors as a function of *p* of the measured cell (with BPF in the range 975–1,075 nm) using (a) InGaAs and (b) Si detectors.

3.3 Experimental validation

The effectiveness of the proposed method in obtaining accurate i*V* images is demonstrated through EL measurements on three different types of Si solar cells. To investigate a wide range of light trapping performance, measurements were conducted on both planar and textured passivated emitter and rear contact (PERC) solar cells [105] with an area of 4 cm^2 and a thickness of 468 ± 4 μm. A uniform (as indicated by PL imaging) textured IBC cell [106] was used for calibration purposes (area of 155 cm^2 and thickness of 147 ± 4 μm).

3.3.1 Experimental procedure

To assess the optical behaviour of these samples, EQE measurements were performed on all devices using a spectral response measurement system (PV Measurements; QEX7). Spectral EL measurements of the Si solar cells were carried out using an InGaAs spectrometer (Avantes; AvaSpec-NIR256-1.7-HSC-EVO). The spectral response, f, of the spectrometer was determined by calibrating the spectrometer with a blackbody source (Omega; BB705) with a stable and well-known spectral irradiance at various temperatures. For calibration, the blackbody temperature was set to 800 °C. Once the temperature stabilised, the blackbody was connected to the spectrometer using an optical fibre with a 1,500 μm core diameter and a numerical aperture (NA) of 0.5. The spectrometer then captured the emitted radiance spectrum, which was subsequently compared to the known blackbody spectrum to calibrate the spectrometer's response.

For the spatially resolved EL imaging of the Si solar cells, a custom-built EL/PL imaging system was employed [37, 107]. The system utilises a Si CMOS camera (FLI; KL400 BI), cooled to −10 °C, equipped with a 957 nm fixed LPF and various optional SPFs. The injected current and the terminal voltage, V_{term}, were recorded simultaneously using a SMU (Keithley; 2461). All images were acquired under identical conditions: a fixed V_{term}, an exposure time of 5 s, and five averages per image at a measured temperature of 23.5 ± 0.2 °C.

Both spectral and spatially resolved EL measurements of the three Si cells were acquired by injecting a specific current density into each device. The injected current was chosen such that the resulting V_{term} was approximately 590 ± 0.5 mV for all cells, a value selected to minimise voltage drops across R_s. For both the textured and planar PERC cells, R_s was estimated to be approximately 0.5 $\Omega\cdot\mathrm{cm}^2$, resulting in voltage drops of 1.1 mV for the textured PERC (injected current density of 2.05 $\mathrm{mA/cm^2}$) and 0.6 mV for the planar PERC (injected current density of 1.20 $\mathrm{mA/cm^2}$). Conversely, the IBC cell exhibited significantly lower R_s, leading to a negligible voltage drop of less than 0.01 mV (injected current density of 0.45 $\mathrm{mA/cm^2}$).

3.3.2 Implied voltage determination from spectral emissions

Figure 3.9(a) shows the EQE as a function of wavelength for the three cells, along with the EL photon flux (per wavelength interval), measured at the same V_{term} (see Section 3.3.1 for full experimental details). The textured PERC cell emits a significantly higher photon flux compared to the other cells, particularly at long wavelengths. This enhancement in photon flux is attributed to the superior light-trapping properties of the textured cell, which results in an increased optical path length and enhanced absorption of the low-energy photons. As anticipated, the planar cell exhibits the lowest emitted photon flux at longer wavelengths, attributed to its limited path length enhancement. The IBC cell falls between these extremes, indicating inferior light trapping performance compared to the textured PERC cell as a result of a combination of less effective surface texture, lower rear surface reflection and potential parasitic absorption in the rear metal contacts. The EQE measurements of the three cells, shown as dotted lines in Figure 3.9(a), demonstrate a consistent trend, with the textured PERC showing higher EQE at longer wavelengths, reflecting its superior light-trapping performance. It is noted that an unexpected slight upward trend is observed in the EL spectrum of the textured cell (below 1,000 nm); this observation is not yet understood and will be the subject of future work. Nevertheless, overall, the spectral data presented in Figure 3.9(a) confirm the anticipated behaviour, namely, the emitted photon fluxes are comparable among the three cells at short wavelengths, but there are significant deviations at longer wavelengths.

Figure 3.9(b) illustrates the spectral EL photon flux as it would be detected by a Si detector, calculated from the experimental data of Figure 3.9(a) using the typical spectral sensitivity of a Si detector. The sensitivity of Si-based spectrometers drops sharply above 900 nm, often resulting in poor SNRs and unreliable data, which makes accurate spectral measurements over this range challenging. To avoid such complications, the photon flux as would be detected by a Si camera was calculated. This was achieved by taking the flux measured by the InGaAs spectrometer, dividing it by the spectrometer's quantum efficiency, which was reasonably assumed to be unity in this range, and then multiplying the result by the assumed QE_{camera} for the Si detector [Figure 3.2(a)]. As shown in Figure 3.9(b), using a Si detector suppresses the impact of long-wavelength deviations observed in the EL spectra (caused by variations in the optical properties of the samples) as this region lies outside its effective detection range, where the spectral response of the detector approaches zero.

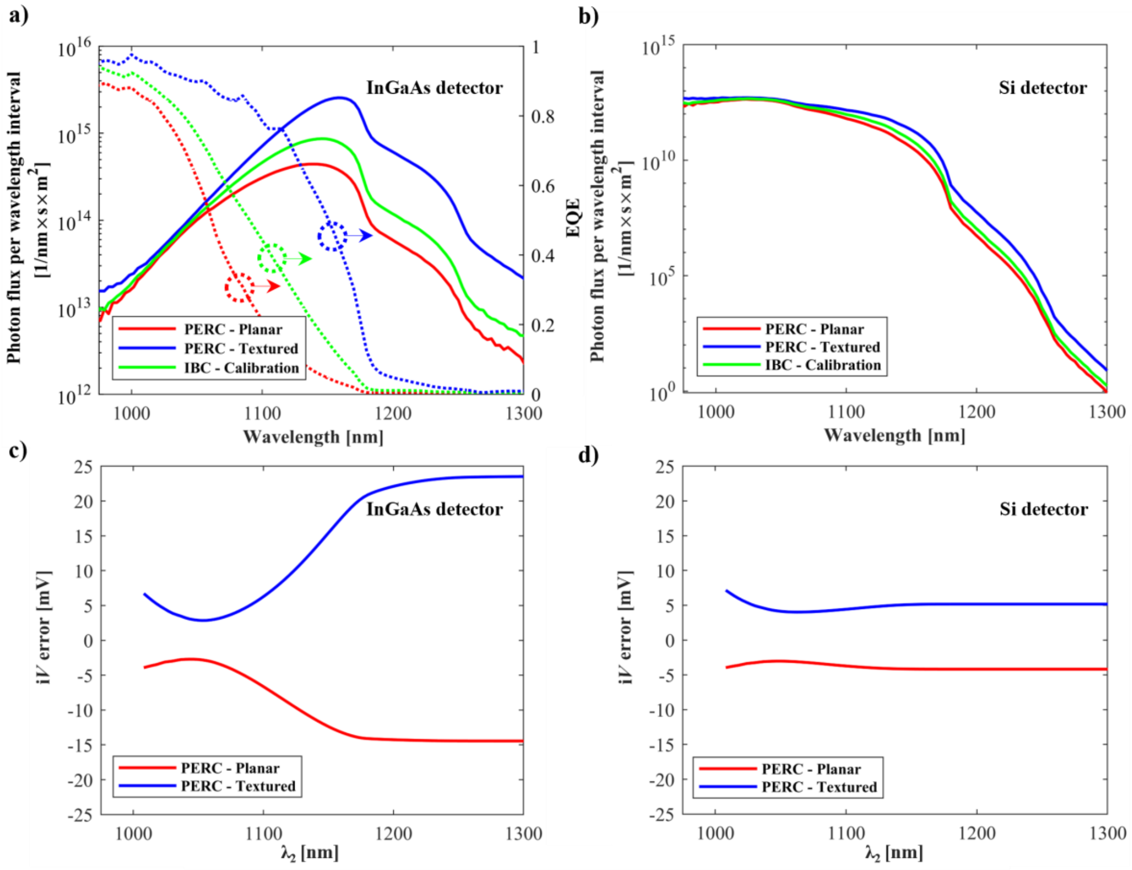

Figure 3. 9 – (a) Measured photon flux per wavelength interval and EQE of the three investigated cells (see text for details) as a function of wavelength using an InGaAs spectrometer and (b) the calculated photon flux assuming a Si detector. The determined i*V* errors for the planar and textured PERC cells using (c) InGaAs, and (d) Si detectors.

Figure 3.9(c) and (d) illustrate the calculated iV errors for the measured textured and planar PERC cells using the IBC cell as the calibration cell with InGaAs and Si detectors, respectively. The iV errors associated with the measurements carried out with the InGaAs detector show a significant increase as λ_2 increases. Specifically, at 1,300 nm, the iV error reaches −14.5 mV and 23.5 mV for the planar and textured cells, respectively. On the other hand, when the Si detector is used, the associated error exhibits a weaker dependence on λ_2 and is significantly smaller (below 5.2 mV for λ_2 = 1,300 nm). In line with the modelling depicted in Figure 3.4 and Figure 3.6, a remarkably low absolute iV error of less than 5 mV can be achieved when λ_2 falls within the range of 1,025 to 1,085 nm. The observed deviation in the iV error for λ_2 below 1,020 nm, towards higher values for the textured cell and lower values for the planar cell, can be attributed to measurement artefacts in the short wavelength tail of the luminescence spectra, where the emitted signal becomes very small.

3.3.3 Implied voltage determination from luminescence images

Figure 3.10 displays EL images of the three cells, measured at an identical V_{term} (see Section 3.3.1 for full experimental details), employing only the 975 nm LPF, i.e., without an additional SPF. The median EL count for each cell is also provided. The EL intensity of the textured PERC cell is 1.4 times higher than that of the IBC cell. The planar PERC cell has the lowest count rate.

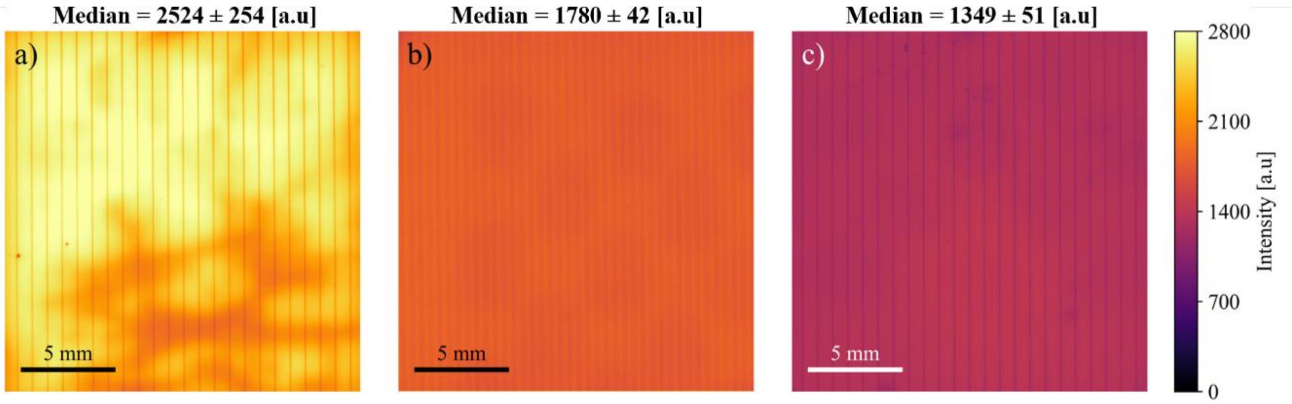

Figure 3. 10 – EL intensity images acquired by a Si camera with a 975 nm LPF and no additional SPF: (a) textured PERC, (b) textured IBC, and (c) planar PERC cells. Measurements were performed at a V_{term} of 590 ± 0.5 mV. All images are presented using the same colour scale. For each image, the median EL intensity is reported. The associated standard deviation quantifies the spatial non-uniformity of the EL intensity across the cell.

As the V_{term} was identical during the measurement, these variations in the EL intensity between cells are mostly attributed to the differences in their optical properties. Using the IBC cell for calibration and applying Equation 2.27, the errors associated with converting the median count rates from these images into iV maps were 6.3 mV (PERC, textured cell) and −9.9 mV (PERC, planar cell), after correcting for the different thicknesses. Note that the iV errors estimated from the EL images are slightly larger than those derived from the spectral luminescence analysis using the Si-based detector in the previous section [Figure 3.9(d)]. This discrepancy likely arises from a difference between the actual (EL images) and assumed (spectral analysis) QE_{camera} of the Si detector.

The impact of an additional SPF on the detected luminescence images is demonstrated in Figure 3.11. The figure presents the EL images of the cells captured under identical measurement conditions as above, but with an additional 1,025 nm SPF in front of the camera lens. The V_{term} was maintained at 590 ± 0.5 mV, ensuring consistency across the measurements. As expected from the modelling results [Figure 3.1(b) and Figure 3.2(b)], the median EL count for the three cells is nearly identical (307 ± 5) in the presence of the SPF. This clearly highlights the effectiveness of the SPF in restricting the detected EL signal to a spectral range in which the luminescence emission is significantly less dependent on the optical properties of the cells, primarily reflecting the variations in iV between the cells. Note that while all three images are plotted on the same colour scale, the scales used in Figure 3.10 and Figure 3.11 are different. The reduction in the count values is attributed to the blocking effect of the SPF on the low-energy portion of the emitted luminescence.

Figure 3.12 shows the calibrated iV images of the textured (a) and planar (b) PERC cells. The calibration process involved applying Equation 2.27 while using the median EL count of the IBC cell for the calibration. Remarkably, for both cells, the median iVs determined from the EL images are within 1 mV of the measured terminal voltage. While the planar cell exhibits a relatively uniform iV distribution, the textured cell reveals some degree of non-uniformity.

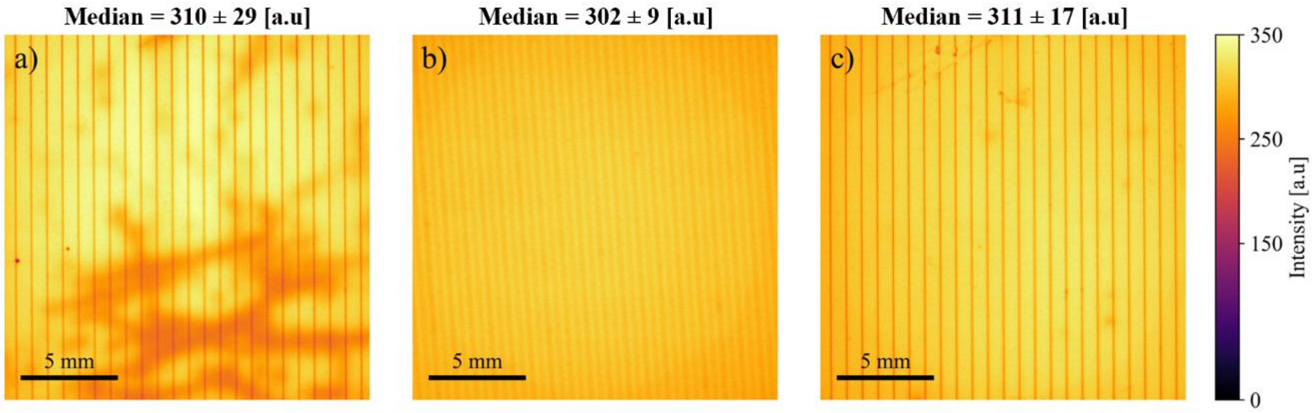

Figure 3. 11 – EL images obtained using the Si camera equipped with a BPF (975 – 1,025 nm) at a V_{term} of 590 ± 0.5 mV: (a) textured PERC, (b) textured IBC, and (c) planar PERC cells. For each image, the median EL intensity is reported. The associated standard deviation quantifies the spatial non-uniformity of the EL intensity across the cell.

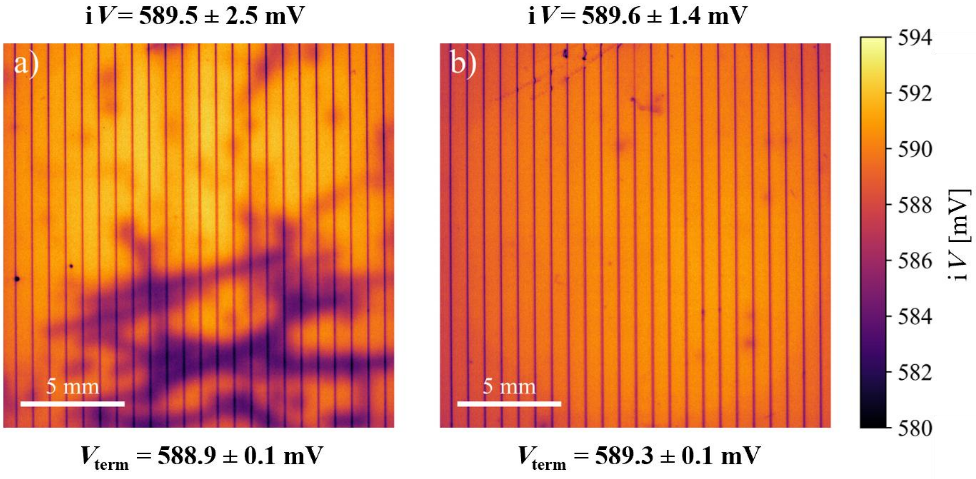

Figure 3. 12 – Calibrated iV images of the PERC cells with (a) textured and (b) planar surfaces. The EL images were captured using a Si camera equipped with a BPF (975 – 1,025 nm). For each image, the estimated median iV is reported and the associated standard deviation reflects spatial inhomogeneity in the iV distribution.

Figure 3.13 presents a comparison between the measured and simulated iV errors as a function of λ_2 after thickness correction. To conduct the measurements, the Si camera was used with a fixed LPF of 975 nm, complemented by various additional SPFs (1,000 nm, 1,025 nm, 1,050 nm, and 1,075 nm). In each case, the median iV from the EL image was used to estimate the iV error. The figure also includes the estimated iV errors that were calculated based on the modelling shown in Figure 3.6, assuming a calibration cell with $p = 20$ and measured cells with $p = 5$ (representing a planar surface) and $p = 40$ (indicating a high-quality textured surface). Given the absence of reflectance data in the study, the associated uncertainty ranges were included as well (shaded regions).

To assess the reproducibility of the results, EL imaging of the same cells was repeated one week apart. The ratio between the average EL counts obtained from the two corresponding EL images was calculated. These ratios were then converted into corresponding median iV values. Since the calculated iV depends on both the calibration and measured cells, the total uncertainty was determined by adding their respective contributions in quadrature (i.e., as the square root of the sum of their squares) [108]. As these uncertainties are independent of the SPF used, their average is presented as the error bars in Figure 3.13. Both uncertainties were found to be relatively small: less than 1 mV for the planar PERC cell and less than 2 mV for the textured PERC cell.

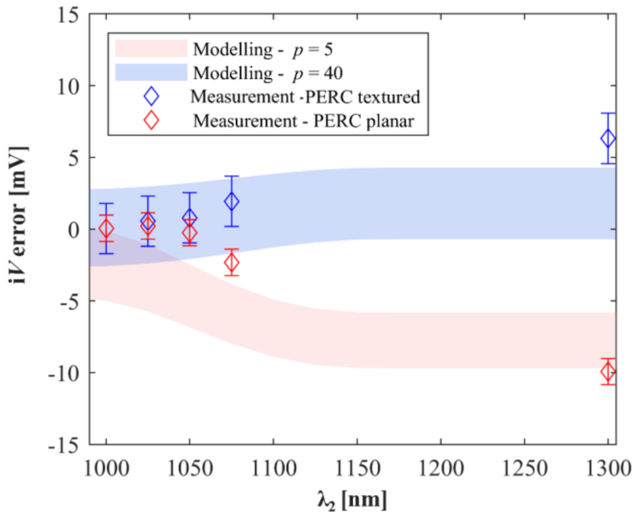

Figure 3. 13 – Measured and modelled iV errors as a function of λ_2. The iV errors were calculated considering the thickness scaling factor. The blue and red shaded regions indicate the modelled iV error ranges assuming solar cells with a p = 40 (textured cell) and 5 (planar cell) using a calibration cell with p = 20 (identical to Figure 3.6).

The estimated iV errors from the measurements closely align with the modelling results, indicated by the shaded regions. However, a slight discrepancy of approximately 2 mV is observed between the iV errors derived from the experimental measurements and those derived from the simulation results. This can potentially be attributed to the difference between the assumed and actual QE_{camera} of the Si detector within the wavelength range above 1,000 nm (unfortunately, the camera manufacturer does not provide the actual QE_{camera} information beyond this wavelength). Additionally, there may be variation in the actual p of the measured cells compared to the assumptions made in the modelling. Importantly, the measured errors consistently remain below 3 mV when a SPF with λ_2 of 1,050 nm or shorter is used for both types of cells. This highlights the effectiveness of the proposed method in determining iV with high accuracy. Importantly, this is achieved without any knowledge of the optical properties of the measured samples.

Therefore, the experimental validation confirms that the method is robust to both systematic and random sources of error. Systematic errors, mainly arising from differences in optical properties, were quantified through modelling and validated experimentally by comparing the image-derived iV with the measured V_{term}. Random errors were assessed through repeated measurements, confirming the high reproducibility of the technique. A comprehensive uncertainty analysis of additional experimental factors is provided in Chapter 5.

3.4 Signal-to-noise ratio

As introduced in Section 2.2.2.1, SNR is a key determinant of luminescence image quality. Here, SNR analysis is used to evaluate the choice of wavelength-selective filters. While the use of an additional SPF significantly improves the accuracy of the determined implied voltages, it comes at the cost of reduced luminescence signal and thus, a lower SNR. To assess the image quality, identify noise sources, and optimise the measurement setup, SNR analysis has been commonly employed [109, 110].

SNR is calculated as the ratio of the measured signal to the total noise at each pixel:

$$\mathrm{SNR} = \frac{S_\mathrm{c}}{N_\mathrm{c}} \tag{3.4}$$

where, S_c and N_c represent the signal recorded by the camera after dark signal subtraction and the total noise of the camera, respectively. Electronic charges generated in each pixel are quantised by the analog-to-digital converter inside the camera, and the final images are reported in unit of digital counts [110]. In Equation 3.4, both S_c and N_c are in units of digital counts. This conversion from electronic charge to counts depends on the camera's gain (g), given by:

$$S_c = \frac{S_\mathrm{e}}{g} \tag{3.5}$$

where S_e is the measured signal by the camera in units of electrons, and the gain, g, of the camera has units of electrons/count. The camera's gain can be obtained either from the datasheet or through experimental measurement [111].

Similarly, the total noise in units of electrons, N_e, can be determined by the camera's gain:

$$N_\mathrm{c} = \frac{N_\mathrm{e}}{g} \tag{3.6}$$

To assess the total noise present in an image, it is essential to consider the contributions from various noise sources. The main sources of image noise are dark noise, read noise, and shot noise. Thus, the camera noise can be expressed as [110, 111]:

$$N_\mathrm{e} = \sqrt{N_\mathrm{dark}^2 + N_\mathrm{read}^2 + N_\mathrm{shot}^2} \tag{3.7}$$

where N_dark is dark noise, N_read is read noise and N_shot is the shot noise. These three individual noise sources are expressed in units of electrons.

In the above Equation N_dark, which is highly dependent on the camera's temperature, can be calculated from the dark signal using:

$$N_\mathrm{dark}^2 = \frac{I_\mathrm{dark}}{q} \times t_\mathrm{exp} \tag{3.8}$$

where I_{dark} is the dark current (in A), and t_{exp} is the exposure time (in units of s). N_{dark} can be obtained by acquiring dark images using different exposure times. The slope of the average signal in counts with respect to t_{exp} yields $I_{\text{dark}}/(q\times g)$, which can then be multiplied by the camera's gain to obtain I_{dark}/q.

N_{read} of a camera can be determined by subtracting two sequential dark images acquired with the minimum exposure time, resulting in negligible contribution of dark noise. The standard deviation of the subtracted image yields $2\times N_{\text{read}}^2$.

N_{shot} is the noise associated with the detected luminescence signal and is often the main contributor to the overall noise in the measurements. It can be determined by:

$$N_{\text{shot}}^2 = S_c \times g \tag{3.9}$$

All luminescence imaging of the cells in this chapter was performed using the cooled Si CMOS camera with a gain of approximately 17 electrons/count. For these measurements, the camera temperature was maintained at −10 °C and the exposure time was set to 5 s. As 5 s was the longest integration time used, the reported dark noise represents an upper limit. Under these conditions of low camera temperature and short exposure time, the contribution of N_{dark} to the overall noise was found to be negligible, with approximately 9–10 electrons. The estimated N_{read} was approximately 30 electrons. However, N_{shot} exhibited significant variation across different cells and filters due to variations in emitted luminescence intensity, with values ranging from 42 to 210 electrons. The dominant contribution to the measurement noise was shot noise.

Figure 3.14 illustrates the calculated SNR as a function of λ_2 for the IBC, planar, and textured PERC cells for two V_{term} values of 590 mV and 680 mV with exposure times of 5 s and 0.5 s, respectively. The SNR decreases with decreasing λ_2, as the detected signal is reduced. Following Ref. [112], an SNR of 45 was set as the minimum value to obtain high-quality measurements in a laboratory environment. To achieve an SNR above this minimum requirement for measurements taken at V_{term} = 590 mV and an exposure time of 5 s, an SPF with λ_2 > 1,010 nm is required in the imaging setup. No limitations are observed when the V_{term} is set to 680 mV. For measurements on typical industrial solar cells under 1 Sun equivalent excitation conditions and for an acquisition time of 0.5 s, the addition of an SPF thus does not result in a drop of the SNR below 45.

To conclude, although the modelling suggests that using an SPF with the shortest possible λ_2 is desirable for minimising iV errors, it is important to meet the required SNR to maintain high-quality iV maps. In light of this, it is recommended to use a filter with a λ_2 in the range 1,010 nm < λ_2 ≤ 1,050 nm to strike a good balance between minimising errors in the quantified iV (within 3 mV) and achieving sufficient SNR using exposure times that are practical for laboratory or production line applications.

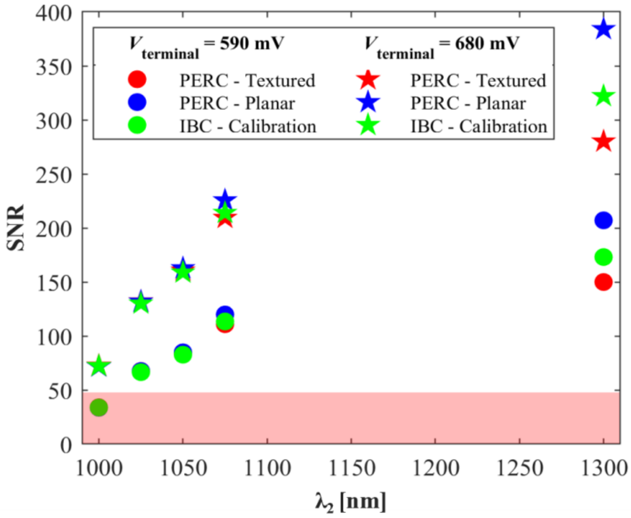

Figure 3. 14 – The SNR as a function of λ_2 for the textured and planar PERC, and IBC cells at V_{term} = 590 mV (circles) and V_{term} = 680 mV (stars) with exposure times of 5 s and 0.5 s, respectively. The red region indicates the range where the SNR is below 45, which was defined as the lower limit of an acceptable SNR.

3.5 Implied voltage measurements of wafers

The proposed method is not limited to fully fabricated solar cells; it can also be applied at various stages of the fabrication process. This versatility is demonstrated here by extracting iV values of Si wafers using a calibrated cell; however, calibration wafers can also be used.

PL imaging was conducted using a commercial system (BT Imaging; LIS-R1) equipped with an 808 nm laser source and a SPF (λ_2 = 1,025 nm). The calibration process was carried out by acquiring PL images of the textured PERC cell (used in the previous sections) under 1 sun illumination while simultaneously recording its V_{term}. The test samples comprised three planar Si wafers, with their key properties summarised in Table 3.3. To validate the extracted iV values, QSSPC measurements were performed using a commercial system (Sinton Instruments; WCT-120TS) at a temperature of 25 °C. More details about the experimental procedure were described in Chapter 2, Section 2.2.1.

Figure 3.15 presents the spatially resolved iV of the three wafers, captured under 0.5 sun illumination [(a) and (b)] and 1 sun illumination (c). The wafers in panels (a) and (b) exhibit relatively uniform iV distributions, while the wafer in panel (c) shows noticeable non-uniformity, indicating localised variations in material properties or surface passivation. Table 3.3 compares the global harmonic mean iV values extracted from PL with those measured via QSSPC. Note that the reported values include the standard deviation, which quantifies the spatial variation of iV across the device. The extracted iV images from PL imaging were within ±5 mV of those measured by QSSPC. Considering the optical differences between the calibration cell and the test wafers, this level of agreement is consistent with the modelling results. Moreover, when measurement uncertainties inherent to the QSSPC technique, such as generation rate and wafer thickness [76-78], as detailed in Section 2.2.1, are accounted for, the accuracy and reliability of the proposed method are further validated.

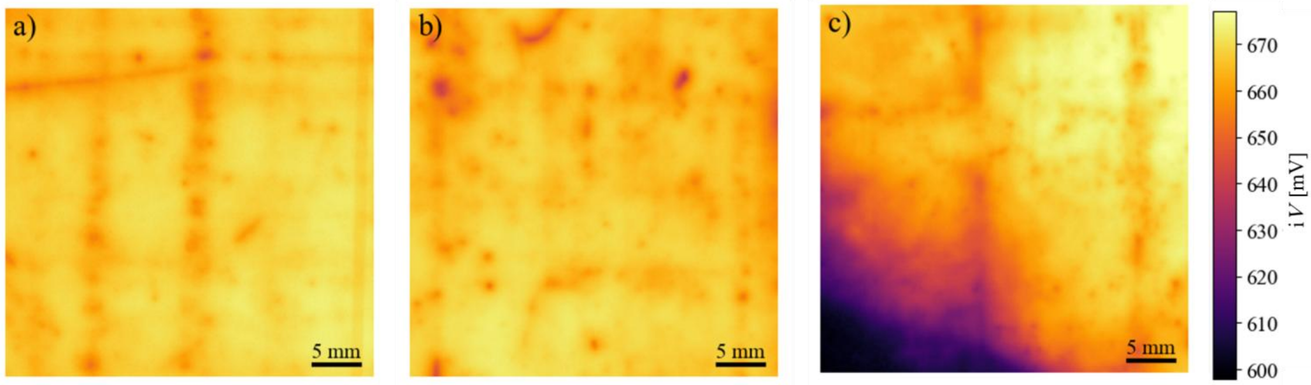

Figure 3. 15 – Extracted iV maps of the three planar Si wafers, calibrated with a textured PERC cell. The PL images were captured using a Si camera equipped with a SPF with λ_2 = 1,025 nm.

Table 3. 3 – Key specifications and extracted iV values of the three planar Si wafers, obtained from PL imaging (using the harmonic mean across each wafer) and QSSPC measurements. The wafers listed as (a), (b), and (c) correspond to the panels in Figure 3.15. Reported standard deviations (for PL-based) reflect spatial inhomogeneity in the iV distribution.

Si wafers (Figure 3.15)	Thickness (d) [µm]	Bulk resistivity [Ω·cm]	Estimated iV from PL imaging [mV]	Extracted iV from QSSPC [mV]
(a)	204 ± 5	7.73 ± 0.32	**667.2 ± 3.16**	**661.8**
(b)	200 ± 5	7.54 ± 0.04	**665.6 ± 3.78**	**661.3**
(c)	202 ± 5	7.72 ± 0.1	**656.0 ± 18.45**	**660.6**

3.6 Summary

This chapter introduced a novel approach to overcoming the challenges associated with accurately quantifying iV from luminescence images of Si wafers and solar cells. Conventional methods typically require multiple sample-specific calibrations to account for optical property variations between test samples, resulting in added complexity and potential inaccuracies. To address this, a simplified approach based on using a BPF was proposed, which eliminates the need for multiple calibrations or detailed knowledge of the optical response of the experimental system, while ensuring robust and accurate results.

Using a proper BPF restricts detection to the short-wavelength region, where sample-specific optical effects on the luminescence signals are minimal. Therefore, the iV calibration can be performed using a single calibration cell, independent of the optical characteristics of the measured device.

Key aspects of the method were identified and validated through comprehensive modelling and experimental measurements. A theoretical model was developed to quantify the error in iV associated with different BPFs, accounting for variations in optical properties, including p, R, and d, as well as differences in the detection system. Through experimental measurements, the accuracy of the proposed method in extracting iV images from EL images of Si solar cells was demonstrated using a single calibration cell that had very different optical properties compared to the measured cells. SNR analysis was also conducted to assess suitable experimental conditions for high-quality iV mapping while minimising errors.

The results showed that Si cameras, unlike InGaAs detectors, inherently suppress long-wavelength signals due to their spectral sensitivity, reducing iV errors and, in some cases, eliminating the need for external BPFs. Nevertheless, regardless of the detection system used, limiting detection to shorter wavelengths ($\lambda_2 \leq 1{,}050$ nm) significantly reduces iV errors. To achieve a balance between minimising iV errors and maintaining sufficient SNR, BPFs with λ_2 in the range 1,010 nm < $\lambda_2 \leq 1{,}050$ nm are recommended. Within this window, iV errors can be effectively limited to 3 mV for the typical Si solar cell and 5 mV for the Si wafers, regardless of the sample's optical properties or the detection system.

The presented method will enable new capabilities for luminescence imaging, allowing for the quantification of key electrical parameters in both research and industrial applications for single-junction and tandem devices. Chapter 4 will evaluate the applicability of this method for subcell iV estimation in PVK/Si tandem devices.

Chapter 4 – Spatially Resolved Determination of the Implied Voltage in PVK/Si Tandem Cells

In Chapter 3, a robust calibration method for iV mapping of Si cells and wafers using a suitable BPF was introduced. By restricting detection to short wavelengths, the method eliminates the need for sample-specific calibration, significantly simplifying and generalising the calibration process across devices with various optical properties.

Conventional methods for subcell iV imaging within two-terminal PVK/Si tandem devices (discussed in Chapter 2, Section 2.3) require precise knowledge of the spectral response of the imaging system and the optical properties of the device. However, these spectral characteristics vary between systems and samples, and their determination poses significant challenges. This dependency limits the broader applicability of such methods and often demands repeated, sample-specific calibration procedures. To overcome these limitations, this chapter extends the technique presented in Chapter 3 to obtain iV images of individual subcells. By carefully selecting BPFs, the method eliminates the need for spectral characterisation of the measurement system and the device under test.

This chapter begins by outlining the methodology for identifying suitable BPFs for each subcell (Section 4.1). Section 4.2 presents simulation results evaluating various BPFs and their impact on subcell iV extraction using a single calibration cell. Section 4.3 experimentally validates the proposed method. Section 4.4 demonstrates its application for extracting pseudo-dark J–iV characteristics of each subcell, while Section 4.5 provides supplementary validation on additional tandem devices. Finally, Section 4.6 introduces an alternative calibration approach, using a calibration light source.

This chapter is based on:

S. Zandi, S. Nie, Y. Zhu, T. G. Allen, E. Aydin, E. Ugur, J. Zheng, G. Wang, X. Liu, X. Hao, A. Ho-Baillie, S. De Wolf, T. Trupke, Z. Hameiri, "Luminescence-based implied voltage imaging of tandem solar cells using bandpass filters," *Small Methods*, vol. 9, p. 2401003, 2025. (S. Zandi and S. Nie contributed equally to this work)

S. Zandi, S. Nie, Y. Zhu, T. G. Allen, E. Aydin, E. Ugur, J. Zheng, G. Wang, X. Liu, A. Ho-Baillie, X. Hao, S. De Wolf, T. Trupke, Z. Hameiri, "Implied voltage of subcells in tandem devices from luminescence images – The beauty of using a narrow bandpass filter," 41st European Photovoltaic Solar Energy Conference, 2024.

S. Zandi, S. Nie, R. L. Chin, Y. Zhu, J. W. Weber, J. Zheng, A. Ho-Baillie, T. Trupke, Z. Hameiri, "Implied voltage images of each subcell in perovskite/Si tandem solar cells using luminescence measurements," Asia Pacific Solar Research Conference, 2023.

S. Nie, **S. Zandi**, R. L. Chin, Y. Zhu, J. W. Weber, G. Wang, J. Zheng, A. Ho-Baillie, Z. Hameiri, "Luminescence-based implied voltage imaging of tandem solar cells via bandpass filter method," 34th International Photovoltaic Science and Engineering Conference, 2023.

4.1 Methodology – BPF assessment

For monolithic PVK/Si tandems, a recently developed approach for subcell iV mapping is the scaling-factor method presented by Fischer et al. [59] (Section 2.3.3). It requires wavelength-dependent calibration of the imaging system and spectrally resolved subcell A or EQE. In practice, obtaining accurate subcell A or EQE is particularly challenging for tandem subcells, and EQE measurements typically require a completed tandem device, limiting use at early fabrication stages. The narrow-BPF approach introduced by Soufiani et al. [50] (Section 2.3.2) and demonstrated on PVK devices reduces this burden by restricting detection to a window where the optical term can be treated as approximately constant. However, tandem application still requires careful window selection and validation (discussed in Section 4.6).

The primary approach adopted in this thesis integrates a narrow BPF with a calibration-cell-based method. Building on the framework established in Chapter 3, a suitable BPF was shown to minimise the impact of optical properties on the luminescence signal, enabling iV extraction across diverse Si samples using a single calibration cell. This section presents a detailed methodology for extending this approach to iV determination of subcells in PVK/Si tandem devices. To evaluate the method's accuracy, the use of different BPFs across PVK/Si tandem devices with varying optical and electrical properties is investigated. It should be noted that due to the distinct emission spectra of the top and bottom subcells, extending this approach to tandem devices requires one dedicated calibration cell and a BPF for each subcell.

Four representative PVK/Si tandem solar cells from published studies (Cell I [113], Cell II [114], Cell III [115], and Cell IV [116]) were used in this section. These cells feature different structures and optical properties, aiming to represent the variety of modern tandem devices. Their different EQE data were extracted [113-116] and provided in Figure 4.1(a). By assuming the same iV for each type of subcell [1,150 mV (top cell) and 700 mV (bottom cells), close to the V_{oc} values], the corresponding ϕ^{absolute} was calculated using Equation 2.13 [see Figure 4.1(b)]. Figure 4.1(c) shows a representative $\mathrm{QE}_{\mathrm{camera}}$ characteristic of a Si detector, reproduced from the camera datasheet (Excelitas; pco.edge 4.2 Bi) [117], which was then used as the system's spectral response to calculate ϕ^{detect} (via Equation 2.14). Figure 4.1(d) shows the calculated ϕ^{detect} on a logarithmic scale, with the inset displaying the same data on a linear scale for better visualisation. This is referred to as the *practical scenario* in the simulations.

In Figure 4.1(b) and (d), the simulated luminescence spectra of the four cells are aligned closely at short wavelengths, but diverge at long wavelengths, as expected due to their very different optical properties. Nevertheless, the luminescence spectra of these very different PVK/Si cells converge in the wavelength range below 730 nm for the PVK cells and below 1,050 nm for the Si cells. Consequently, the detected luminescence signal in the short wavelength range is comparatively insensitive to variations in the optical properties of the device. Instead, it predominantly reflects the variations in iV. The observed behaviour aligns with the findings of Chapter 3 for the Si samples and with measurements by Soufiani et al. [50] for PVK films, which is attributed to EQE or A remaining constant over the short wavelength regime, irrespective of structural differences. This spectral insensitivity supports the use of a single calibration cell for subcell iV extraction in PVK/Si tandem devices and confirms the broader applicability of the proposed method in Chapter 3.

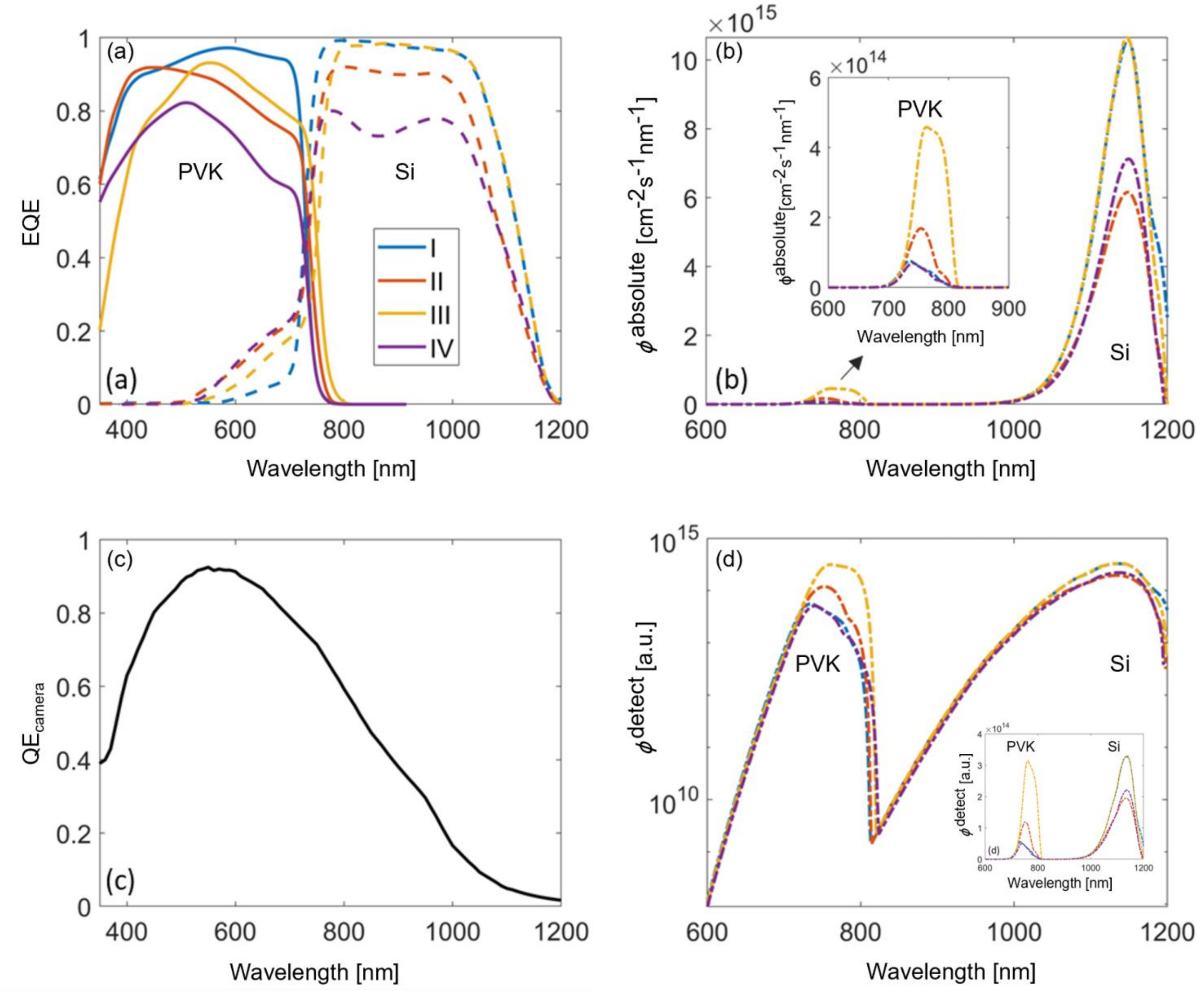

Figure 4. 1 – (a) EQE spectra of four different PVK/Si tandem solar cells (Cell I [113], Cell II [114], Cell III [115], and Cell IV [116]), (b) their ϕ^{absolute} assuming T = 298 K, and iV of 1,150 mV (top cell) and 700 mV (bottom cell), (c) a typical $\text{QE}_{\text{camera}}$ of a Si-based detector (reproduced from a datasheet [117]), and (d) ϕ^{detect} by this camera on a logarithmic scale. The inset in (d) shows the detected signals on a linear scale for better comparison.

Moreover, to evaluate the accuracy of the proposed method under extreme conditions, the extracted EQEs of the four cells (Cells I-IV) were utilised to generate a "*worst-case scenario*". In this scenario, the EQEs of the PVK subcells were reduced by 40%, while the EQEs of the Si subcell were set to be 20% lower than those depicted in Figure 4.1(a), as shown in Figure 4.2(a). The 40% reduction for the PVK was determined based on EQE measurements of tandem cells after severe degradation [118]. While most Si subcells maintained stable performance (<10% change), a 20% reduction was considered as the upper limit [118]. Hence, in this context, the worst-case scenario is defined as a situation in which a tandem solar cell operates at an exceptionally low level while still remaining functional. Thus, the selected scenario reflects a plausible condition within the realm of practical performance, rather than an unrealistic worst-case situation. Subsequently, ϕ^{detect} in this worst-case scenario [Figure 4.1(b)] was calculated by assuming an iV of 800 mV (500 mV) for the PVK (Si) subcells, appropriate values for underperforming tandem solar cells. Again, the luminescence spectra of different cells converge for wavelengths below 730 nm for the PVK cells and below 1,050 nm for the Si cells.

The impact of specific calibration cell parameters on the extraction of iV of tandem subcells was evaluated using six calibration cells, comprising three PVK calibration cells and three Si calibration cells, with various optical properties and different PVK bandgaps. Their EQEs are provided in Figure 4.3, while their $V_{\mathrm{term,calib}}$ was set to 1,000 mV for the PVK and 600 mV for the Si calibration cells.

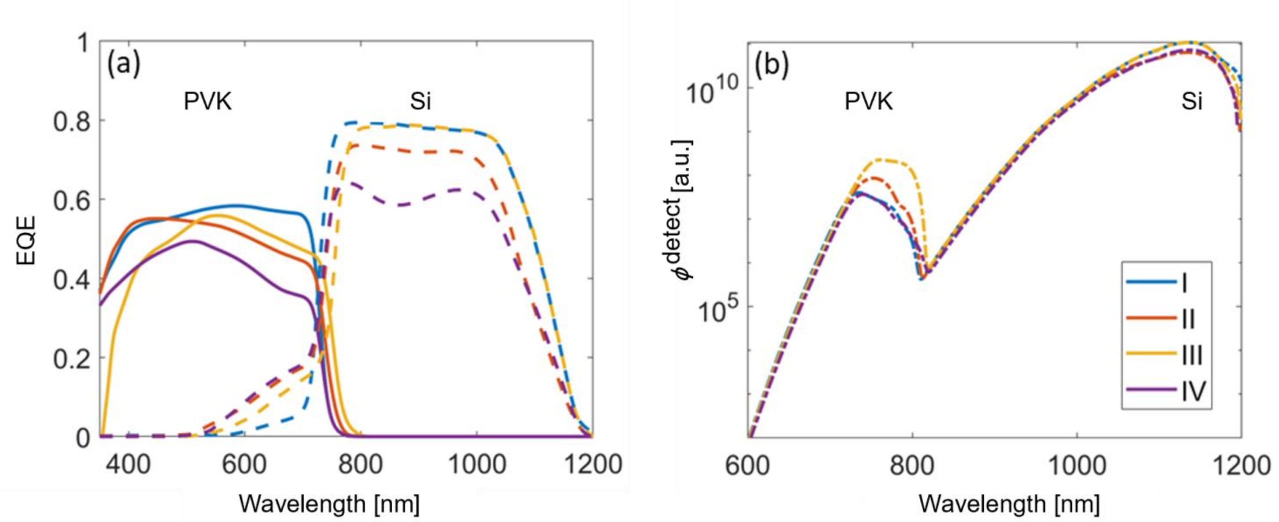

Figure 4. 2 – (a) EQEs of the four PVK/Si tandem solar cells that were used for the worst-case scenario, and (b) the corresponding ϕ^{detect} by the Si camera, assuming T = 298 K, and iV of 800 mV (top cell) and 500 mV (bottom cells).

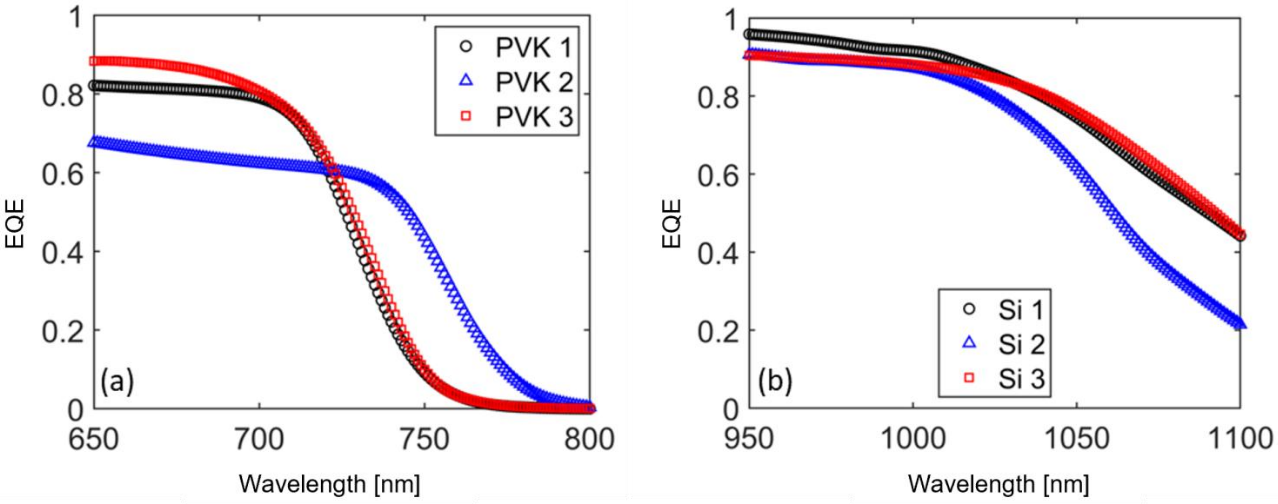

Figure 4. 3 – EQE as a function of the wavelength for (a) PVK and (b) Si single-junction calibration cells.

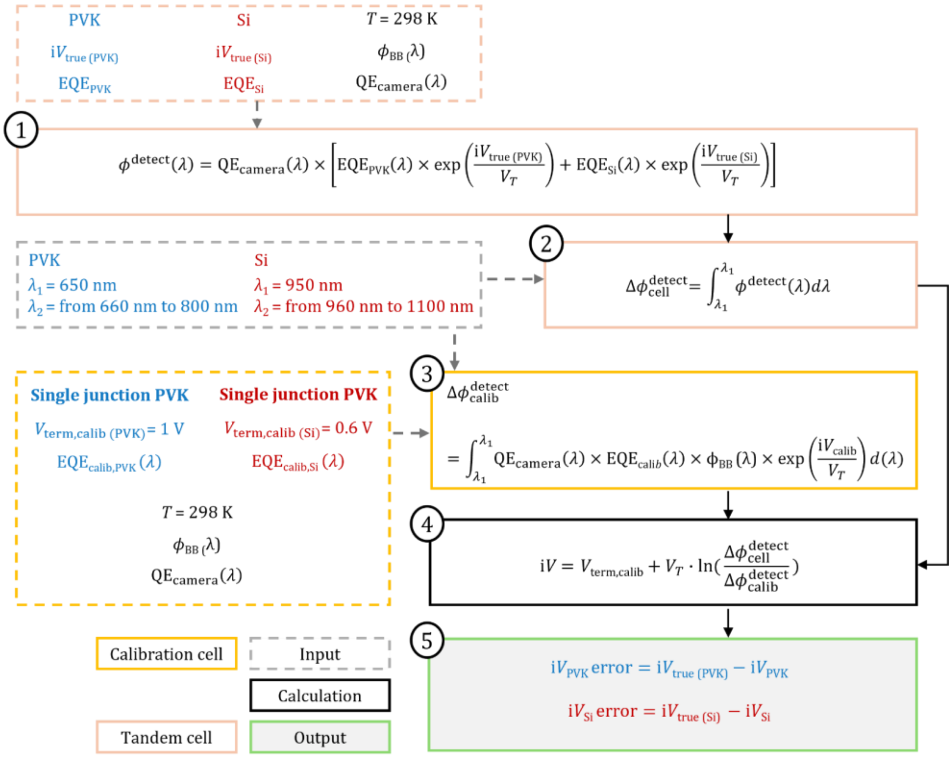

Figure 4. 4 – Simulation procedure to determine the iV error for each of the subcells.

Figure 4.4 outlines the simulation procedure used to identify suitable BPFs for each subcell. Two scenarios were considered for the tandem test cells: the *worst-case scenario* (Figure 4.2) and the *practical scenario* (Figure 4.4), each involving four tandem cells. The detected luminescence signal by the Si camera was then determined for the calibration cells ($\Delta\phi^{\text{detect}}_{\text{calib}}$) and the tandem subcells treated as the measured devices ($\Delta\phi^{\text{detect}}_{\text{cell}}$, as defined earlier). This calculation was carried out within the wavelength range of λ_1 = 650 nm and 660 nm ≤ λ_2 ≤ 800 nm for the PVK subcell, as well as λ_1 = 950 nm and 960 nm ≤ λ_2 ≤ 1,200 nm for the Si subcells. The procedure also incorporated the reported EQE for each respective cell and the $\mathrm{QE_{camera}}$ as the system's spectral response. Subsequently, iV for each subcell was extracted by calculating the ratio of $\Delta\phi_{\mathrm{cell}}^{\mathrm{detect}}$ from the subcell to $\Delta\phi_{\mathrm{calib}}^{\mathrm{detect}}$ from the corresponding calibration cell, using Equation 2.27. The iV error was then quantified as the difference between iV_{true} and the estimated iV.

4.2 BPF selection – simulation and analysis

Building on the described methodology, this section presents the impact of using BPFs with different λ_2 on the accuracy of iV extraction for each subcell. Suitable BPFs are identified for both practical and worst-case scenarios, minimising iV errors caused by optical mismatches between the calibration cells and the measured subcells.

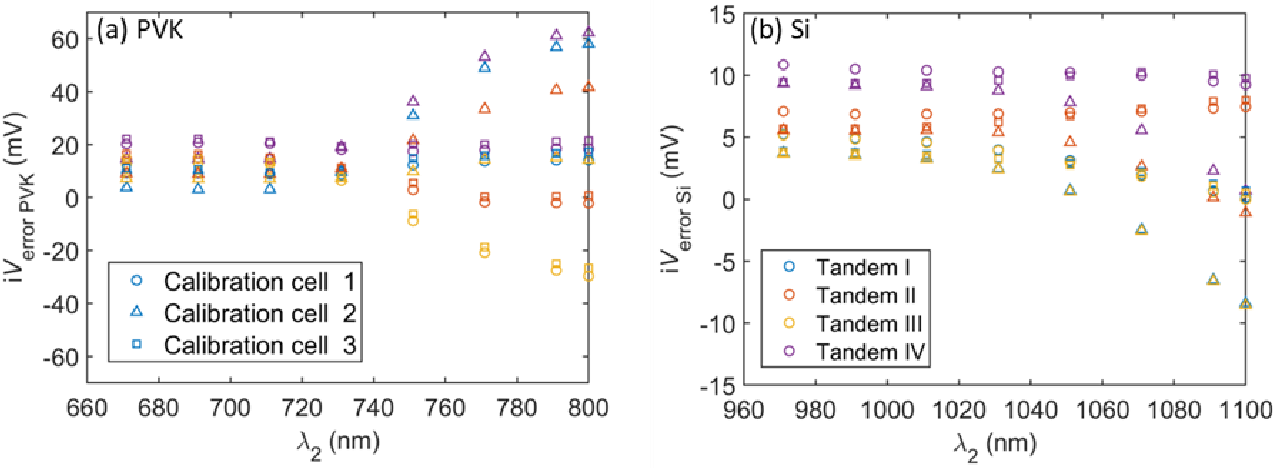

Figure 4. 5 – iV error distribution for the **worst-case scenario** as a function of λ_2, for (a) PVK and (b) Si subcells. The symbol represents the calibration cell that was used, while the colour of the symbol indicates the corresponding tandem subcells.

Figure 4.5 illustrates the distributions of the iV errors across the 12 cases (four subcells × three calibration cells) as a function of λ_2, for the **worst-case scenario**. A positive error (iV_{true} – estimated iV) here indicates that the EQE of the tandem subcell is lower than the EQE of the calibration cell within the detection range. However, in real measurements, this direct interpretation may not always be valid due to inherent uncertainties in experimentally determining the EQE of subcells in tandem devices [89]. For PVK cells, a shorter λ_2 noticeably reduces the iV error, indicating the insensitivity of the luminescence spectra to the cells' optical properties. By restricting the detection range of the luminescence signal to a shorter wavelength (λ_2 ≤ 730 nm), the absolute iV error can be maintained below 19 mV (2.3%) for these subcells. For Si subcells, the iV errors are smaller compared to the PVK subcells, exhibiting less variation across the 12 cases in relation to λ_2. The lower iV errors observed for the Si subcells can be attributed to a combination of factors. As discussed in Chapter 3 and shown in Figure 4.1(c), the QE_{camera} of the Si-based camera drops sharply at long wavelengths (above 1,000 nm), making it highly insensitive to luminescence in this spectral region. This, in turn, suppresses the impact of long-wavelength deviations in the EL spectra, contributing to the lower iV errors observed for the Si subcells. Additionally, the EQE mismatch between some Si calibration cells and their corresponding tandem subcells further minimises variations in the detected luminescence and iV error. Nevertheless, the absolute iV errors of Si subcells remain below 12 mV (2.4%) for $\lambda_2 < 1{,}100$ nm.

Additionally, simulations for the **practical-case scenario** were conducted. As depicted in Figure 4.6, the iV error is significantly reduced compared to Figure 4.5, especially at shorter λ_2. The maximum absolute iV error is 7 mV (0.6%) for the PVK subcells and 5 mV (0.7%) for the Si subcells when λ_2 is limited to 730 nm (PVK) and 1,050 nm (Si).

Notably, the 5 mV error obtained for the Si subcells aligns with the value reported in Chapter 3 for a single-junction Si cell incorporating both p and R mismatch [Figure 3.6(b)]. This comparison is more appropriate than the 3 mV error estimated for a typical Si solar cell influenced primarily by a variation in p, as the presence of the PVK top cell in the tandem structure inherently alters both R and the light-trapping behaviour of the Si subcell. A more detailed investigation of the uncertainties associated with single-junction calibration in tandem architectures will be presented in Chapter 5, confirming the method's robustness and establishing confidence intervals for high-resolution iV imaging.

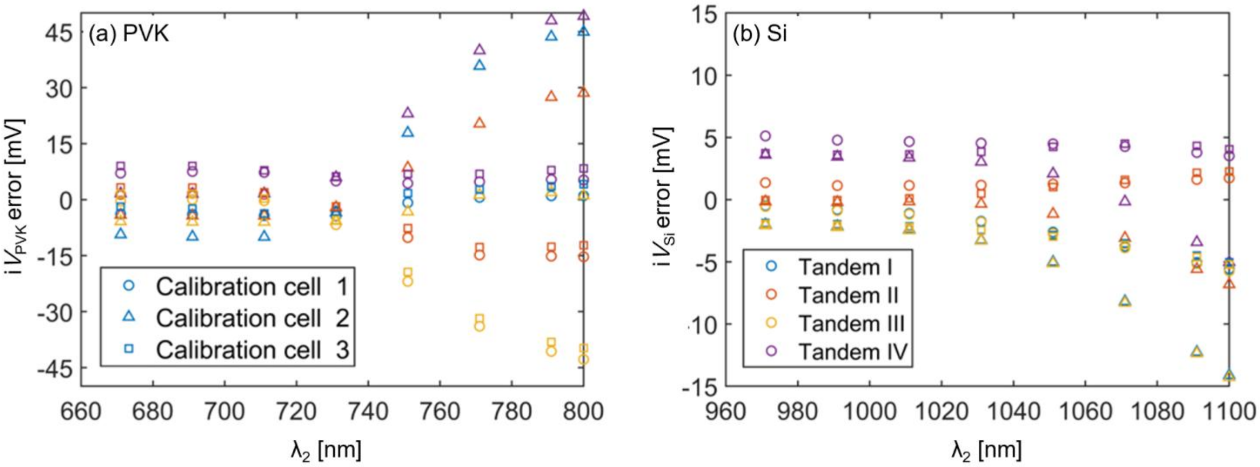

Figure 4. 6 – iV error distributions for the **practical scenario** as a function of λ_2 for (a) top and (b) bottom cells. The symbol represents the calibration cell that was used, with the colour of the symbol indicating the corresponding tandem subcells.

4.3 Experimental validation

To validate the performance of the proposed calibration method under realistic conditions, a series of experiments was conducted. In this section, the method for i*V* imaging of subcells is experimentally assessed using two well-characterised monolithic PVK/Si tandem devices (Sections 4.3.1–4.3.3). Section 4.4 presents the application of this method to extract spatially resolved pseudo-dark *J*–i*V* curves in each subcell of these devices. Section 4.5 then extends the validation to two additional tandem devices measured with a different setup and calibration cells.

4.3.1 Sample characteristics

The two monolithic PVK/Si tandem devices used to demonstrate the accuracy of the method were sourced from different suppliers. Their main properties are described below:

- **Tandem 1:** This tandem device, previously reported by Aydin et al. [119], has an active area of 1.04 cm^2. The architecture integrates a p-i-n PVK top cell onto a double-sided-textured Si heterojunction (Si HJT) bottom cell. The top cell incorporates a 1.68 eV bandgap PVK absorber layer with the composition $Cs_{0.05}FA_{0.8}MA_{0.15}Pb(I_{0.755}Br_{0.255})_3$. The hole transport layer (HTL) is a self-assembled monolayer of [2-(9H-carbazol-9-yl)ethyl] phosphonic acid (2PACz). The electron transport layer (ETL) stack includes lithium fluoride (LiF), fullerene (C_{60}), and tin oxide (SnO_2). An ultrathin (5 nm) indium zinc oxide (IZO) layer acts as the recombination junction, electrically coupling the subcells [119]. Full details about the fabrication process are provided in Ref. [119].
- **Tandem 2:** The second device, described by Wang et al. [120], has an active area of 1.21 cm^2. It features a p-i-n PVK top cell built upon a rear-textured Si HJT bottom cell. The top cell includes a 1.67 eV bandgap PVK absorber layer with the composition $Cs_{0.15}FA_{0.65}MA_{0.2}Pb(I_{0.8}Br_{0.2})_3$. The HTL is a synthesised self-assembled monolayer of (2-(3,6-diphenyl-9H-carbazol-9-yl)ethyl) phosphonic acid (Ph-2PACz), while the ETL stack consists of LiF, C_{60}, and SnO_2 layers. The subcells are electrically interconnected via a 20 nm indium tin oxide (ITO) recombination layer. Further fabrication details can be found in Ref. [120].

Figure 4.7 shows the measured EQE spectra of both tandem cells and their light *J*–*V* characteristics measured under forward scan under AM1.5G illumination (100 mW/cm^2).

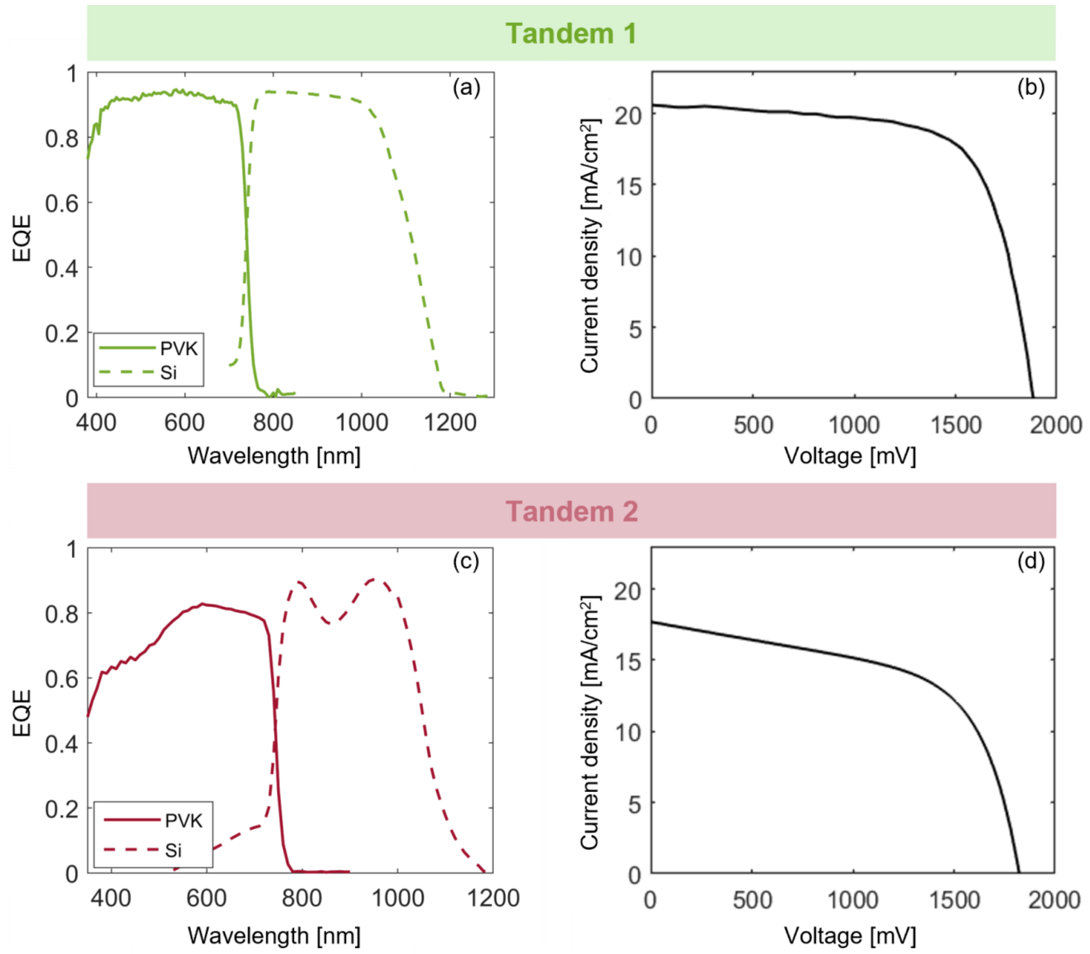

Figure 4. 7 – (a, c) EQE spectra as a function of wavelength for Tandem 1 and Tandem 2, respectively. (b, d) Light *J*–*V* curves of Tandem 1 and Tandem 2 measured under AM1.5G illumination (100 mW/cm^2), respectively.

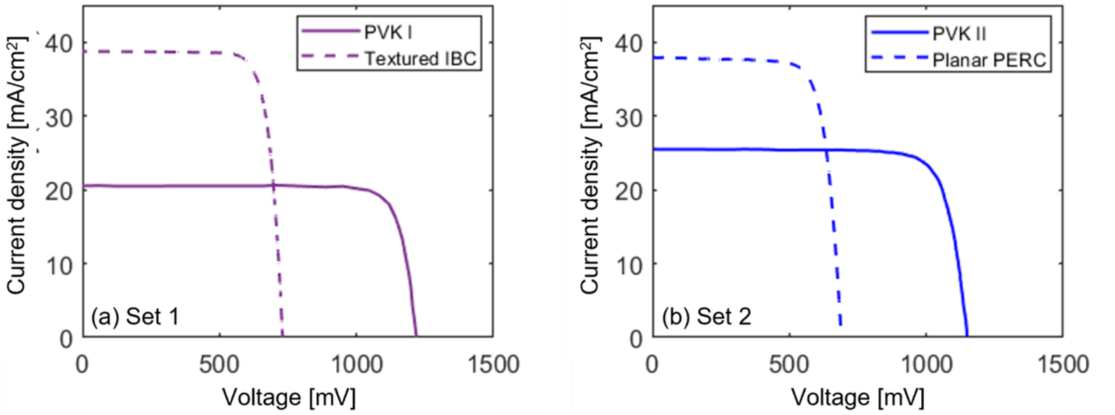

Figure 4. 8 – Forward scan *J*–*V* curves of the single-junction calibration cells measured under AM1.5G illumination (100 mW/cm^2): (a) Set 1 and (b) Set 2.

To demonstrate the insensitivity of the proposed method to the optical properties, two sets of calibration cells with significantly different optical properties were employed. Figure 4.8 shows the associated *J*-*V* curves of Set 1 and Set 2 and their main characteristics are described below:

- **Set 1:** The set includes a textured IBC Si cell [106], utilised to calibrate the Si bottom cell. It also includes a single-junction PVK solar cell (PVK I) featuring an absorber with a bandgap of ~1.67 eV, a composition of $Cs_{0.15}FA_{0.65}MA_{0.2}Pb(I_{0.8}Br_{0.2})_3$, and an active area of 0.07 cm^2 [120], used to calibrate the PVK top cell. This PVK device has a p-i-n configuration, where the HTL is the self-assembled monolayer Ph-2PACz. The ETL stack consists of LiF, C_{60}, and bathocuproine (BCP). Full fabrication details of the PVK cell are provided in Ref. [120].
- **Set 2**: This set includes a planar PERC Si cell, used to calibrate the Si subcell. It also comprises **a** single-junction PVK device (PVK II) with a composition of $Cs_{0.05}FA_xMA_{1-x}PbI_3$, a bandgap of ~1.55 eV, and an active area of 0.14 cm^2 [121], employed for the calibration of the PVK subcell. This cell has an n-i-p structure, where the HTL is 2,2′,7,7′-tetrakis(N,N-di-p-methoxyphenylamine)-9,9′-spirobifluorene (Spiro-OMeTAD), doped with 1-dodecanethiol (DDT). The ETL is a SnO_2 layer with potassium chloride (KCl) passivation. Detailed fabrication procedures for the PVK cell are described in Ref. [121].

Note that discrepancies between the iV and V_{term} in single-junction PVK solar cells have often been reported, primarily due to band energy misalignment [87, 122, 123]. However, for high-performance PVK devices, this discrepancy is minimal [123, 124]. Therefore, when such devices are employed as calibration samples, such as the cells used here, the impact on iV accuracy is negligible. Nevertheless, to address potential concerns in broader applications, a new approach is introduced in Chapter 5.

4.3.2 Experimental procedure

EL images of each subcell under different current injections were acquired using a CMOS camera (FLI; KL400 BI) [37, 107] equipped with two BPFs that were selected based on the simulations presented above (Figures 4.5 and 4.6). A BPF centred at 720 nm with an 18 nm bandwidth was used for the top cell, while a BPF with a transmission range between 975 nm and 1,025 nm was used for the bottom cell, as shown in Figure 4.9.

An SMU (Keithley; 2461) was used to inject different currents while simultaneously measuring V_{term} using a four-probe measurement. For both single-junction and tandem cells, V_{term} typically stabilised within 30–50 s after current injection. Once V_{term} stabilised, a few EL images were captured while the corresponding V_{term} values were recorded. The reported EL image and V_{term} are the averaged values. All EL images were taken at a sample temperature of 23 ± 0.5 °C.

Set 1 and Set 2 were utilised for calibration using a similar procedure as described in Section 3.2.1. EL images of these calibration cells were captured at a low current injection level, where the voltage drops across R_s are negligible, ensuring that iV closely approximates V_{term}. For Set 1, the EL images were obtained at V_{term} of 590 mV (injected current density of 0.45 mA/cm^2) for the IBC cell and 1,019 mV (8.5 mA/cm^2) for the PVK I cell, while for Set 2 they were captured at 580 mV (0.75 mA/cm^2) for the PERC cell and 980 mV (0.5 mA/cm^2) for the PVK II cell.

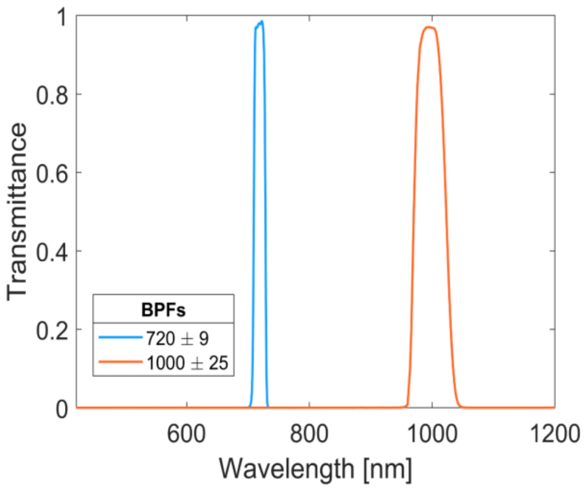

Figure 4. 9 – Transmittance spectra of the BPFs used for the iV measurement.

4.3.3 Implied voltage determination

Implied voltage images of each subcell within **Tandem 1** and **Tandem 2** were extracted from EL images under current injection densities of 1.5 mA/cm^2 and 0.66 mA/cm^2, respectively. Different currents were used since the properties and performance of the two tandem devices differ significantly (see Section 4.3.1). Under these conditions, the impact of voltage drop due to R_s is negligible; thus, the iV obtained from the images should closely approximate V_{term}. Consequently, the proposed calibration methods can be validated by comparing the sum of the calculated iV of the subcells to the measured V_{term} of the stack.

Figure 4.10 shows the spatial iV maps of the subcells in Tandem 1 [(a)–(d)] and Tandem 2 [(e)–(h)], with iV maps extracted using Calibration Set 1 [(a), (b), (e), and (f)], and Set 2 [(c), (d), (g), and (h)]. Estimated iV images of the PVK subcells are shown in panels (a), (c), (e), and (g), while the Si subcells are displayed in panels (b), (d), (f), and (h). The PVK subcells exhibit higher absolute iV values than the Si subcells, consistent with their larger bandgap. However, their iV images also show pronounced spatial variation, likely arising from localised differences in recombination activity, potentially caused by morphological imperfections or interface-related defects.

Table 4.1 summarises the global harmonic mean iV across each subcell and compares their sum with the corresponding measured V_{term}. Note that the reported standard deviations reflect spatial inhomogeneity in iV distribution. Across all subcells, iV values extracted using Set 2 are approximately 3 mV higher than those from Set 1. This is because Set 1 comprises planar Si and 1.55 eV PVK cells, while Set 2 uses a textured Si IBC and 1.67 eV PVK cells, which more closely match the optical structure of the tandem devices. Hence, this difference can be potentially attributed to an optical mismatch between the calibration and measured cells. The observed difference also falls within the predicted range of iV error discussed in Chapter 3 (for Si subcell) and the modelling results presented in Section 4.2**.** Despite this, both calibration sets yield iV values that agree with the measured V_{term} within 1% (i.e., < 11 mV), confirming the accuracy and robustness of the method.

Table 4. 1 – Estimated harmonic mean iV of subcells and the entire tandem devices and their corresponding V_{term}. Note that the reported standard deviations represent spatial inhomogeneity in the iV distribution.

Tandem, current injection level	Calibration cells	PVK top cell: Estimated iV [mV]	Si bottom cell: Estimated iV [mV]	Entire device: Estimated iV [mV]	Measured V_{term} [mV]
Tandem 1, 1.50 [mA/cm²]	**Set 1**	1,104.3 ± 4.6	523.7 ± 2.4	**1,628.1 ± 5.4**	**1,629 ± 1**
	Set 2	1,105.8 ± 4.6	526.5 ± 2.4	**1,632.3 ± 5.4**	
Tandem 2, 0.66 [mA/cm²]	**Set 1**	1,089.5 ± 8.7	611.3 ± 6.8	**1,700.8 ± 11.8**	**1,694 ± 2.5**
	Set 2	1,091.0 ± 8.7	614.1 ± 6.8	**1,705.1 ± 11.8**	

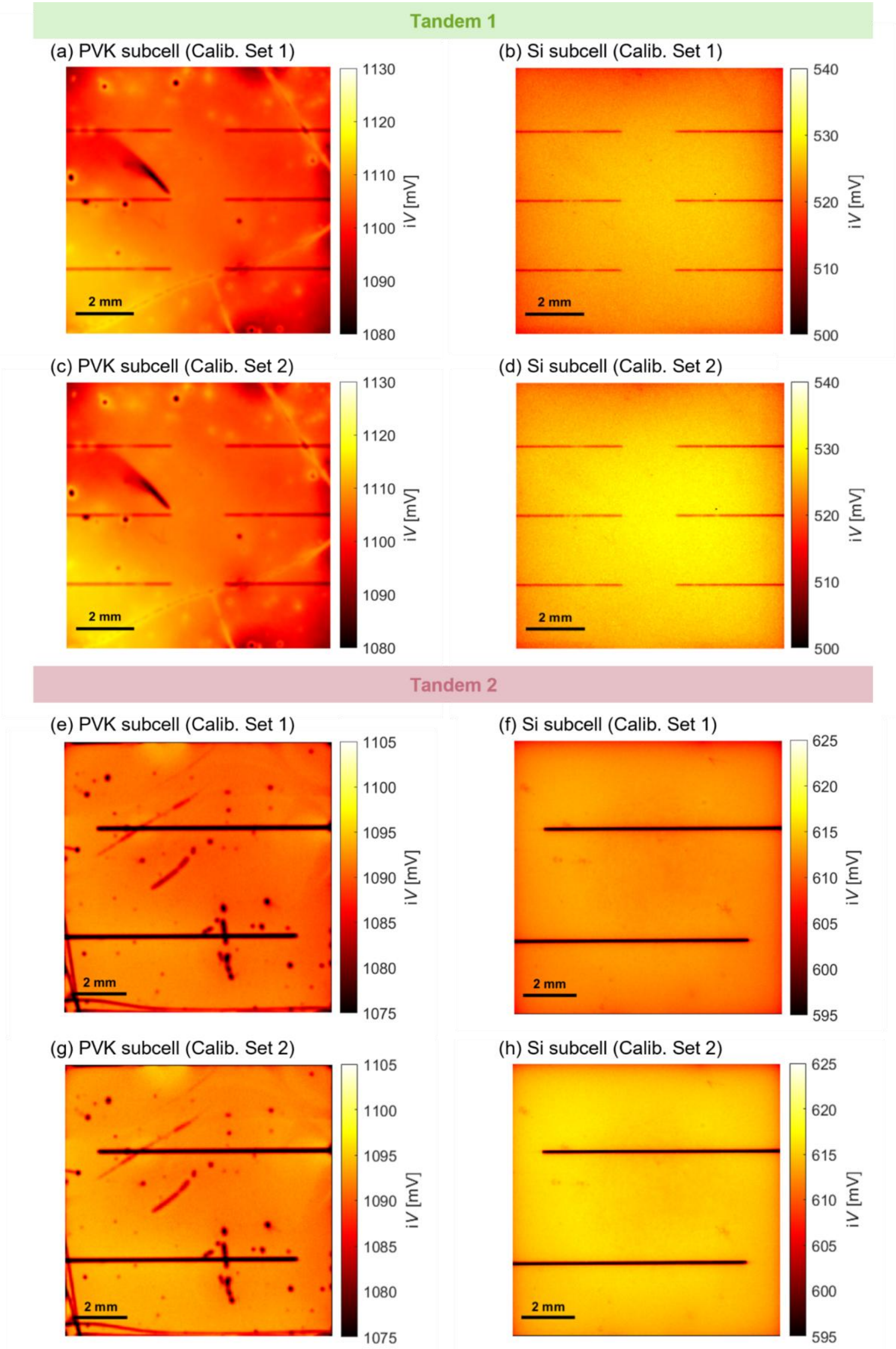

Figure 4. 10 – Spatial i*V* maps of PVK (a, c, e, g) and Si (b, d, f, h) subcells in Tandem 1 (a–d) and Tandem 2 (e–h). Maps in the first row (a–d) were extracted using Calibration Set 1 (a, b, e, f), while those in the second row were extracted using Calibration Set 2 (c, d, g, h).

4.4 Spatially resolved pseudo-dark *J*–i*V* measurement

The spatial resolution of the proposed i*V* extraction approach enables detailed analysis of local variations across different regions of each subcell. Specifically, since the injected current density in EL measurements corresponds to the total recombination current, plotting it as a function of the derived i*V* allows reconstruction of the pseudo-dark *J*–i*V* curve in a spatially resolved manner for each of the subcells.

For proof-of-concept demonstration, the i*V* image of each subcell within **Tandem 1** was determined using Calibration **Set 1** at different injected current densities, ranging from 1.5 mA/cm^2 to 28 mA/cm^2. By computing the mean i*V* across these i*V* images, the global pseudo-dark *J*–i*V* curves of the top and bottom subcells were generated. Figure 4.11(a) presents the calculated pseudo-dark *J*–i*V* and the measured dark *J*–*V* of Tandem 1. The difference between the estimated pseudo-dark *J*–i*V* and the measured dark *J*-*V* of the tandem cell is within 1% at a low current injection level (where the effects of the R_s are negligible). At high current densities, significant discrepancies are observed due to the impact of R_s [125]. This also provides opportunities for quantifying the injection-dependent R_s. Here, R_s of 3.1 ± 0.2 Ω·cm^2 was extracted at an injected current density of 24 mA/cm^2.

The developed method can be employed to derive **local** pseudo-dark *J*–i*V* curves of individual subcells within tandem solar cells. The inset of Figure 4.11(b) illustrates i*V* images of the PVK and Si subcells at a current density injection of 24 mA/cm^2. Three regions of interest (ROIs) were selected in the inset of Figure 4.11(b), where the mean variation in the i*V* of PVK is about 65 mV. The local pseudo-dark *J*–i*V* of these ROIs in the PVK and Si subcells is compared in Figure 4.11(b). As expected, the three local pseudo-dark *J*–i*V* curves of the Si cell are mostly identical. However, there is a significant difference in the local pseudo-dark *J*–i*V* measurements across the PVK cell. Notably, ROI-3 exhibits noticeably lower performance than the other ROIs, which is attributed to high recombination losses and/or high R_s in this particular region. This type of information can be crucial for assessing the origin of various losses in each subcell, thereby aiding in the development of large-area high-efficiency PVK/Si tandem cells. It is important to note that the results presented here assume a uniform current distribution across the device. However, this assumption is invalid at high current injection, as the R_s could induce variations in the i*V* and current at different regions of the cell. Alternatively, the proposed method could leverage PL measurements by extracting i*V* images at several illumination intensities and converting the absorbed photon flux to an equivalent photogenerated-current density, thus removing the impact of R_s. By comparing PL- and EL-based i*V* images, R_s and recombination features can be distinguished. It is worth mentioning that for samples with high diffusion lengths, any spatially confined defect of high recombination activity tends to deplete neighbouring regions of excess charge carriers, resulting in excess charge carrier gradients and smearing of the PL image [43]. This affects the accuracy of the extracted local pseudo-dark *J*–i*V*, especially at low injection levels. However, as PVKs have a relatively low diffusion length [126], the impact of lateral carrier flow on the extracted local pseudo-dark *J*–i*V* is expected to be minor.

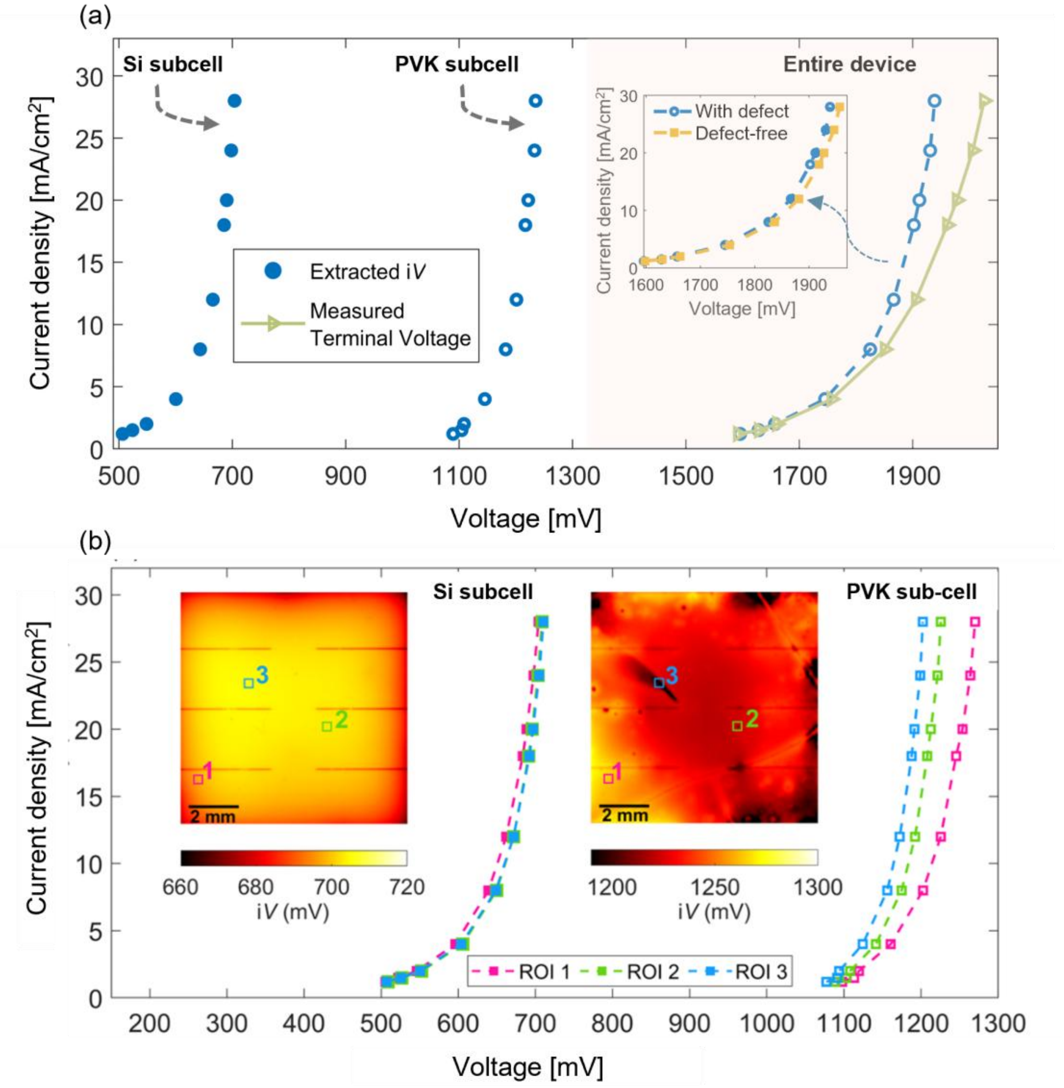

Figure 4. 11 – (a) Comparison of the global pseudo-dark *J*-i*V* extracted from the mean of the i*V* images of the PVK (open symbols) and Si (filled symbols) subcells using calibration Set 1, alongside the estimated pseudo-dark *J*–i*V* of the tandem cell (dashed line) and the measured dark *J*-*V* (green line). The inset shows the global pseudo-dark *J*-i*V* of the tandem cell extracted before and after removing the defective regions. (b) Local pseudo-dark *J*-i*V* curves of PVK (open symbols) and Si (filled symbols) subcells at three ROIs marked in the inset i*V* images. The inset shows the i*V* images of the Si and PVK subcells, were extracted at an injected current density of 24 mA/cm^2.

The capability to spatially resolve pseudo-dark *J*–i*V* offers the ability to quantify the losses associated with different defects. By eliminating the defective regions in the i*V* images, the pseudo-dark *J*–i*V* curve of defect-free tandem subcells can be extracted. The inset of Figure 4.11(a) presents the pseudo-dark J–iV curve of the defect-free tandem cell. This curve was obtained by first identifying defective and low-performing regions in the PVK subcell, where the iV was more than 30% below the maximum iV across the image at each current injection level. The corresponding iV values were then replaced with the median iV of the remaining portions of the image. An improvement of approximately 15 mV improvement is noticeable at a current density of 24 mA/cm^2, representing the expected performance of a uniformly good tandem cell. This can assist in identifying performance-limiting local defects and evaluating their impacts on the overall device performance.

4.5 Supplementary validation on additional tandem devices

Additional validation was performed using two other tandem devices (Tandem 3 and Tandem 4) with compositions and structures similar to Tandem 1 and Tandem 2, respectively.

To further assess the suitability of the method, different calibration cells and setups were utilised.

Calibration Set 3 included a high-performance PVK cell with a bandgap of 1.67 eV and an active area of 0.07 cm^2. The device has a p–i–n configuration, where the absorber layer is a PVK with the composition $Cs_{0.15}MA_{0.2}FA_{0.65}PbI_{2.4}Br_{0.6}$, the HTL is Ph-2PACz, and the ETL stack consists of LiF, C_{60}, and BCP. **Calibration Set 4** comprised a high-quality PVK cell with a bandgap of 1.55 eV and an active area of 0.053 cm^2. The device has a p–i–n configuration, where the absorber layer is a perovskite with the composition $FA_{0.85}MA_{0.10}Cs_{0.05}PbI_3$, the HTL is MeO-4PACz ([4-(3,6-dimethoxy-9H-carbazol-9-yl)butyl]phosphonic acid) and the ETL stack consists of C_{60} and SnO_2, with a PDADI2 (1,3-diaminopropane dihydroiodide) interlayer at the PVK/C_{60} interface. **In both calibration sets**, a Si HJT single-junction cell with an active area of 1.21 cm^2 was also included for the calibration of the Si subcell.

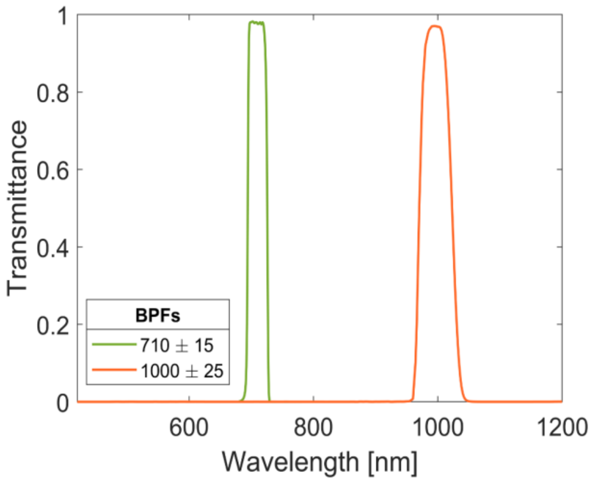

Figure 4. 12 – Transmittance spectra of the BPFs used for the iV measurement of the additional tandem device.

EL images were acquired using a CMOS camera (Excelitas; pco.edge) equipped with narrow BPFs centred at 710 ± 15 nm ($\lambda_2 < 730$ nm) and 1,000 ± 25 nm ($\lambda_2 < 1050$ nm) [shown in Figure 4.12] to capture the luminescence images of the PVK and Si subcells, respectively. The SMU (Keithley; 2461) was used to inject current while simultaneously measuring V_{term} using a four-probe measurement.

Figure 4.13 depicts iV images of Tandem 3 [(a), (b)] and Tandem 4 [(c), (d)], captured at injected current densities of 3 mA/cm^2 and 2.2 mA/cm^2, respectively. The left panels [(a), (c)] correspond to the PVK subcells, while the right panels [(b), (d)] correspond to the Si subcells. Tandem 3 displays a largely uniform iV distribution. However, some features can still be identified in both subcell images. The reduced EL signal in the bottom-right corner of the Si cell represents a local voltage drop of around 12 mV relative to the harmonic mean of the image. By contrast, the top cell in Tandem 4 displays significant non-uniformity, which is dominated by a low-quality region in the centre of the cell (marked by the green box). A comparison of harmonic mean iV values reveals that this central region exhibits a drop of more than 30 mV relative to the harmonic mean of the entire subcell. Notably, the corresponding area in the Si subcell (marked by the green box) shows a significant voltage rise of a similar magnitude. This is attributed to reduced interlayer resistivity under low injection conditions, where lateral current can flow between the subcells [127]. In monolithic tandem devices, the total voltage remains uniform, leading to compensation for local voltage losses in the PVK top cells by a corresponding voltage increase in the Si subcells [127].

Table 4. 2 – Calculated harmonic mean iV of subcells and the entire Tandem 3 and Tandem 4 at injected current densities of 3 mA/cm^2 and 2.2 mA/cm^2, and the corresponding V_{term}. Note that the reported standard deviations reflect spatial inhomogeneity in the iV distribution.

Tandem, current injection level	Calibration cells	PVK top cell: Estimated iV [mV]	Si bottom cell: Estimated iV [mV]	Entire device: Estimated iV [mV]	Measured V_{term} [mV]
Tandem 3, 3 [mA/cm^2]	**Set 3**	1,140.1 ± 8.1	620.3 ± 4.3	**1,760.4 ± 12.4**	**1,762 ± 1.0**
Tandem 4, 2.2 [mA/cm^2]	**Set 4**	993.7 ± 13.9	605.6 ± 10.7	**1,599.3 ± 24.6**	**1,608 ± 1.0**

Table 4.2 summarises the global harmonic mean iV of each subcell and compares their sum with the corresponding measured V_{term}. The reported standard deviations represent the spatial inhomogeneity in the iV distribution. Consistent with the experimental results presented in Section 4.3.3, the estimated iV of the tandem devices differs from the V_{term} by less than 9 mV.

Importantly, this deviation lies within the expected error range established in Section 4.2, further confirming the accuracy of the proposed method across different devices and calibration sets.

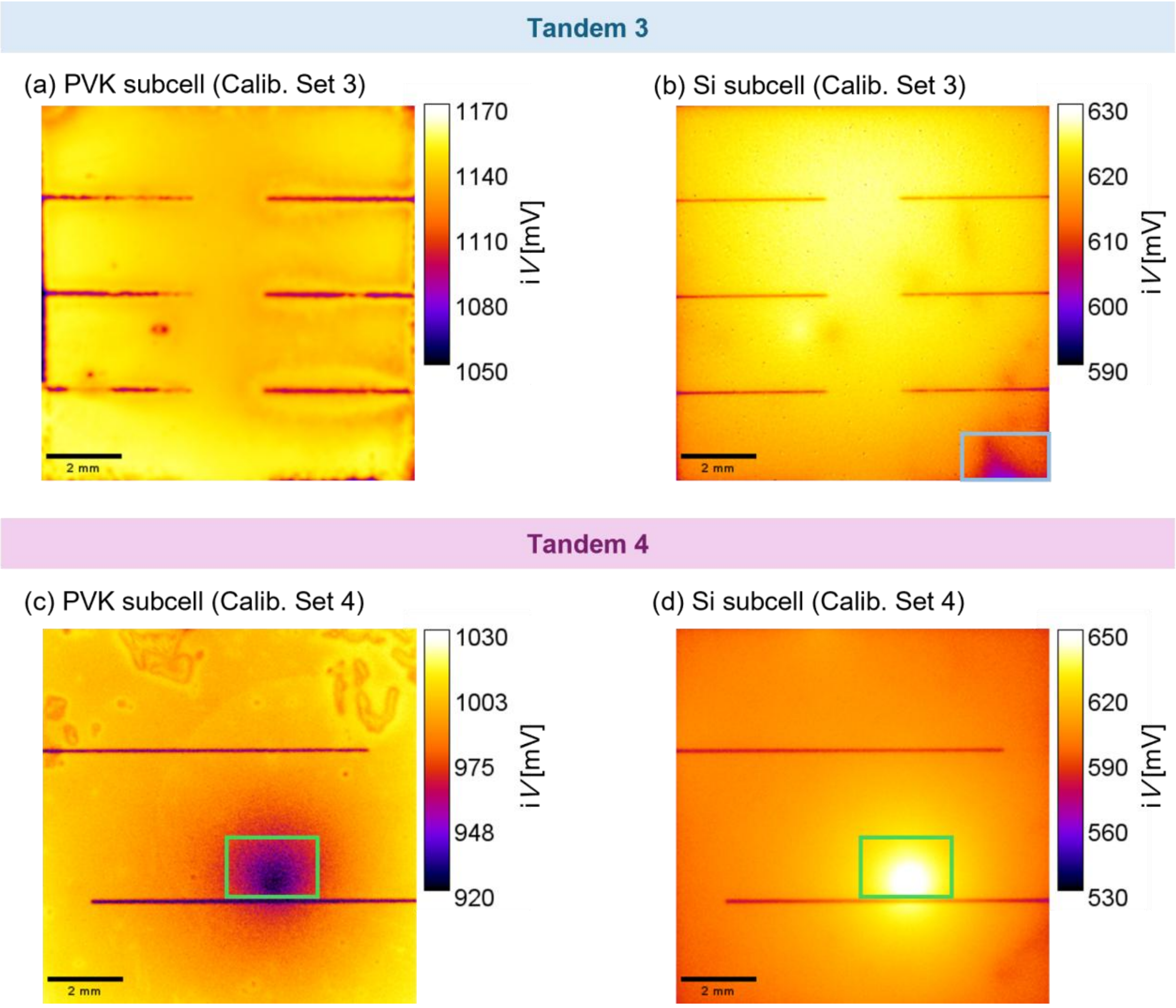

Figure 4. 13 – iV images of PVK (a, c) and Si (b, d) subcells in Tandem 3 (a, b) and Tandem 4 (c, d). The iV maps of the subcells in Tandem 3 and Tandem 4 were extracted using Calibration Set 3 (a, b) and Calibration Set 4 (c, d), respectively.

4.6 Light source-based calibration

Although the presented method for subcell iV determination offers high accuracy, it relies on access to high-performance calibration cells. When such calibration cells are unavailable, a different calibration strategy is needed. This section introduces a light source-based method that uses a calibrated lamp with a well-characterised photon flux for iV extraction.

This approach is similar to the method presented by Soufiani et al. [50], in which iV is derived from a simplified form of the generalised Planck's law [83] (see Equation 2.23):

$$\mathrm{i}V = V_{\mathrm{T}} \times \ln\left(\frac{\Delta\phi_{\mathrm{cell}}^{\mathrm{detect}}}{f \cdot C \cdot \Delta\phi_{\mathrm{BB}}}\right) \tag{4.1}$$

Here, the absorptivity term A is replaced with a wavelength-independent calibration constant C. As demonstrated in both this thesis and in Ref. [50], restricting the detection range to the short-wavelength region via an appropriate BPF yields an A (or EQE) spectrum that is effectively constant within the selected region. This simplification allows the use of C in place of A, thereby eliminating the need for detailed optical data or sample-specific calibration in the calibration cell-based method.

Based on this concept, Ref. [50] demonstrated that using a constant value for C ($C \approx 1$) and applying Equation 4.1 enables accurate iV determination across PVK films using BPFs centred at 720 ± 13 nm and 740 ± 13 nm. However, the correlation between the appropriate constant value of C and the corresponding BPF range that supports this approximation, particularly in the context of tandem solar cells, has not been fully investigated. This section addresses these gaps by (a) quantifying the BPF ranges that maintain the validity of the constant-C assumption, and (b) identifying suitable C intervals that minimise iV error across individual subcells in PVK/Si tandem devices, accurate for different tandem devices regardless of their material properties.

To determine f, a light source with a known spectrum was utilised. In the case of tandem solar cells, f must be determined individually for the spectral range of each subcell, owing to the use of different BPFs for the top and bottom cells. The determination of f is required only once for each subcell unless there is a change in the detection system.

Simulations were performed to quantify the errors resulting from the suggested simplification (constant f and C). They also illustrate the effectiveness of the narrow BPFs in determining accurate iV regardless of the optical properties of the measured cells. The simulation procedure is outlined in Figure 4.14. First, $\phi^{\text{detect}}(\lambda)$ was calculated based on EQE and the assumed iV for each type of subcell. Both the worst-case (Figure 4.2) and the practical (Figure 4.1) scenarios were considered. Subsequently, $\phi^{\text{detect}}(\lambda)$ was integrated across various wavelength ranges, with fixed cut-on wavelengths λ_1 = 650 nm for PVK cells and λ_1 = 950 nm for Si cells, while systematically varying the cut-off wavelengths λ_2, from 660 nm to 800 nm for the PVK cells and from 960 nm to 1,100 nm for the Si cells. For each distinct λ_2, f was determined using a known spectral output [$\phi_{\text{light}}(\lambda)$] from the calibration light source to quantify the error introduced by the simplification of the constant f. Then, the iV of each subcell was extracted, assuming a wavelength-independent C ranging from 0.38 to 0.98 [a range that reflects the EQE range of the cells].

The error in the extracted iV was calculated as the absolute difference between iV_{true} (input value) and the estimated iV. Considering the four cells (Cells I-IV), both the mean errors and the maximum errors were determined.

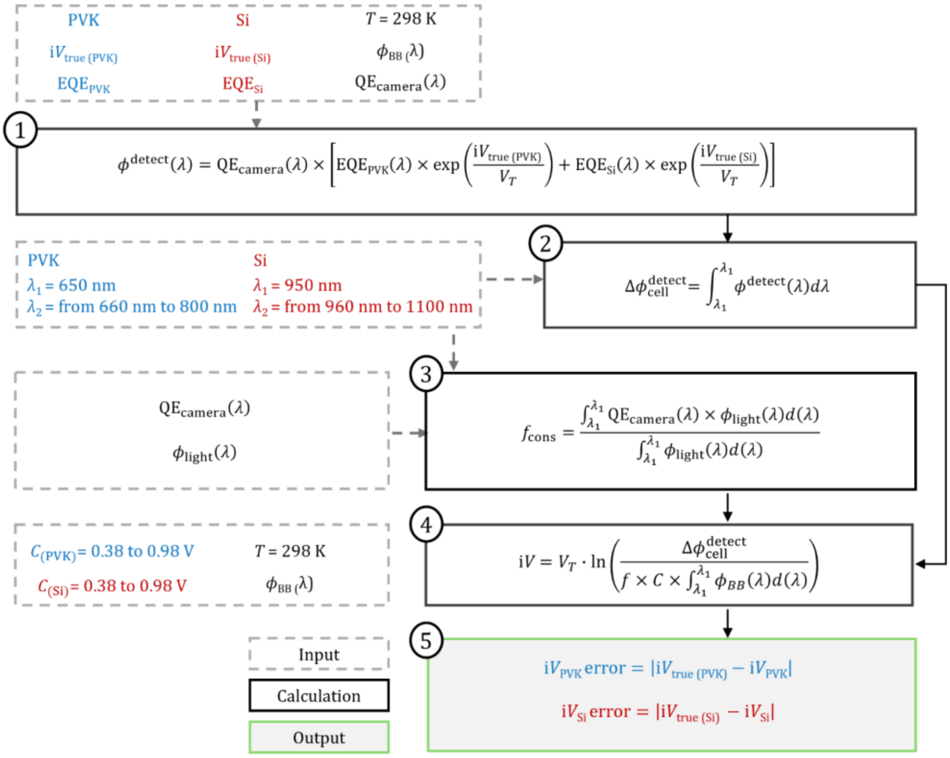

Figure 4. 14 – Simulation procedure to determine the iV error for each subcell using the light source-based calibration method.

4.6.1 BPF selection – simulation and analysis

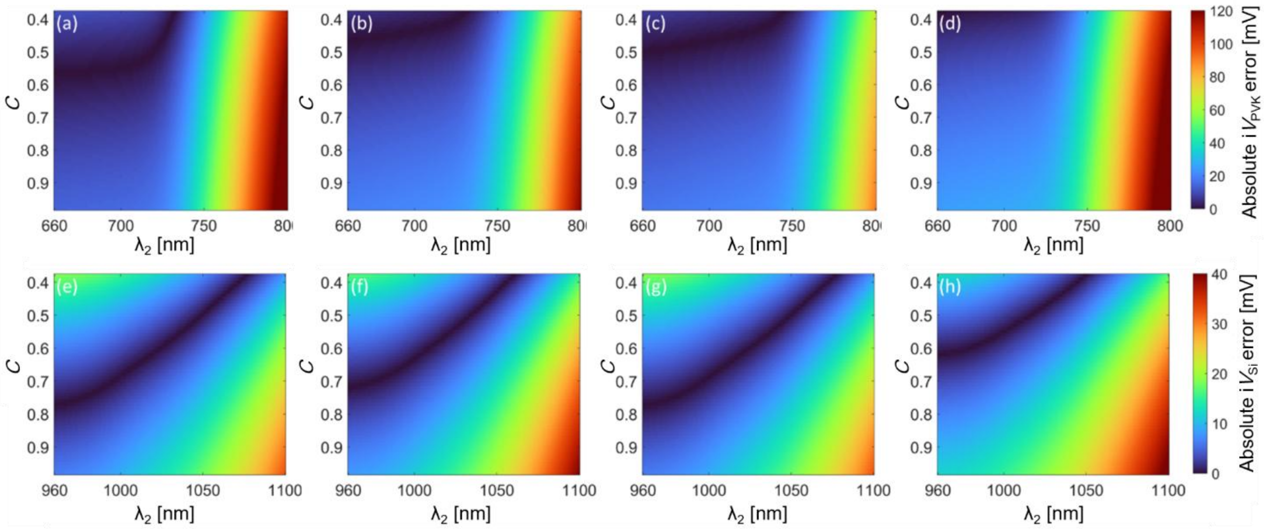

Figure 4. 15 – iV error as a function of λ_2, simulated using the light source-based calibration method, C and λ_2 for (a)-(d) top and (e)-(h) bottom cells of the **worst-case scenario**: (a) and (e) Cell I, (b) and (f) Cell II, (c) and (g) Cell III, (d) and (h) Cell IV.

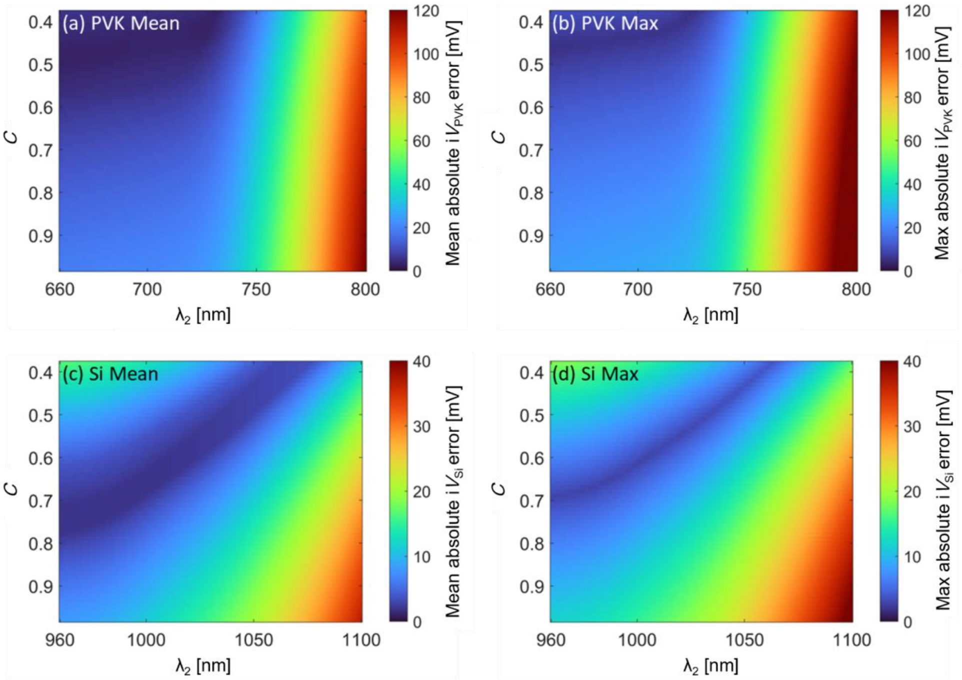

Figure 4. 16 – (a), (c) Mean and (b), (d) maximum absolute iV error maps, calculated using the light source-based calibration method, for the **worst-case scenario** as a function of C and λ_2 for (a), (b) PVK and (c), (d) Si subcells.

The **worst-case scenario** is discussed first, with the absolute iV error maps for all four individual cells shown in Figure 4.15. These maps illustrate the variation in error across different values of λ_2 and C for each cell. The iV error increases with higher λ_2 values, particularly for larger C, indicating greater sensitivity to optical properties at longer wavelengths. The distribution of errors varies across the four cells, reflecting differences in their optical characteristics. To provide a more comprehensive perspective, Figure 4.16 summarises these results by presenting the mean (a, c) and maximum iV errors (b, d) across all four cells. At shorter λ_2 values, the iV error is smaller for any fixed C value, highlighting the effectiveness of the proposed method in reducing iV variations caused by the optical properties of the cell. As λ_2 increases, the iV error rises, reflecting the greater sensitivity of the luminescence signal to the device's optical properties at longer wavelengths. Moreover, the assumption of constant f becomes unacceptable at longer λ_2 as the spectrum of the calibration lamp starts to have an impact. Similar to the cell-based approach, the iV errors for the Si subcells are lower than those of the PVK subcells. As previously discussed, the QE_{camera} of the Si camera limits the detected luminescence signal to shorter wavelengths, yielding reduced iV errors for the Si subcells compared to the PVK subcells. The lowest iV error is expected when C aligns with the actual EQE range within that specific wavelength range. However, accurately quantifying the EQE of each tandem subcell is not always an easy task. Nevertheless, by limiting the detection range of the luminescence signal to a shorter wavelength range (for instance, λ_2 = 730 and 1,025 nm for the PVK and Si cells, respectively), the resulting iV error can be maintained below 32 mV for the PVK and 19 mV for Si, even in this worst-case scenario, irrespective of the selected C.

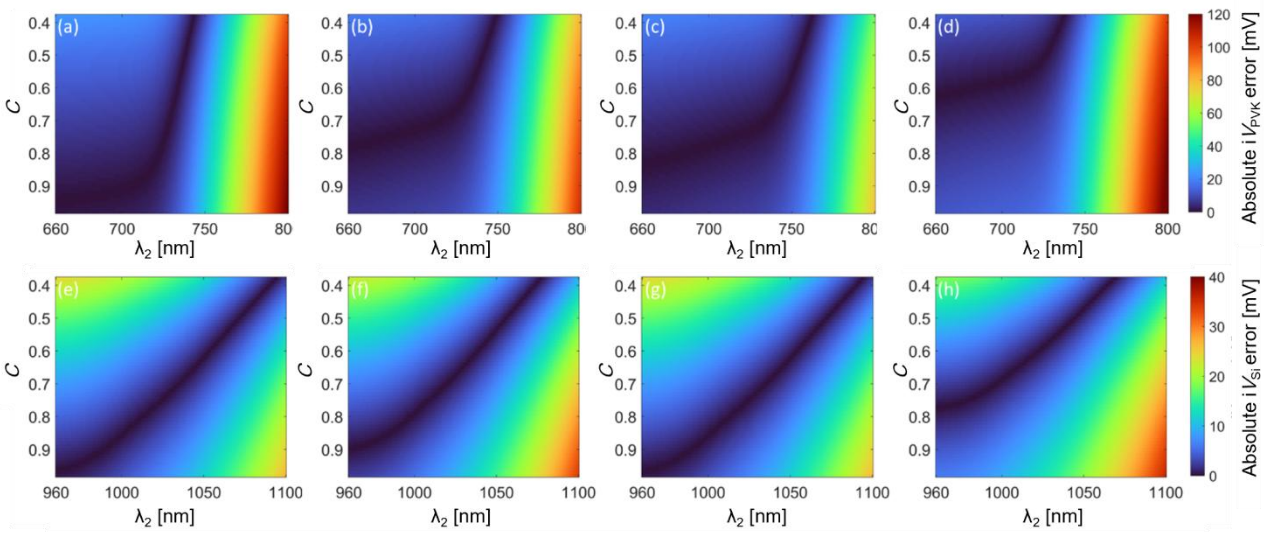

Figure 4. 17 – iV error as a function of C and λ_2, calculated using the light source-based calibration method, for (a)-(d) top and (e)-(h) bottom cells of the **practical scenario**: (a) and (e) Cell I, (b) and (f) Cell II, (c) and (g) Cell III, (d) and (h) Cell IV.

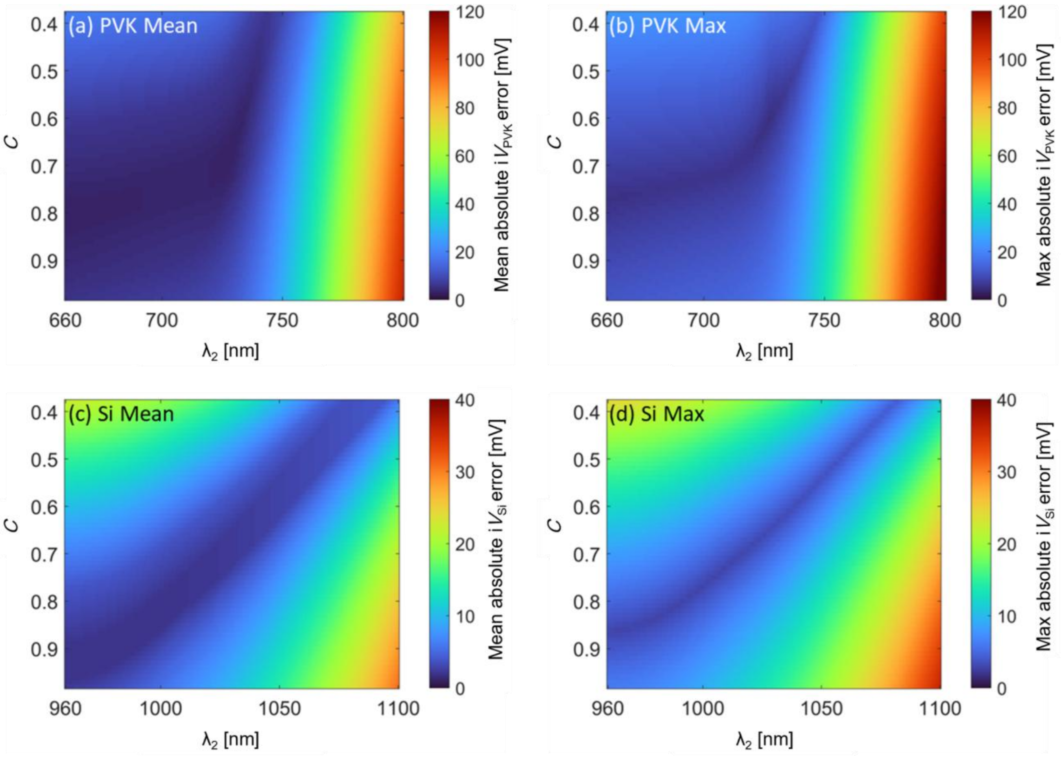

Figure 4. 18 – (a), (c) Mean and (b), (d) maximum absolute iV error maps, calculated using the light source-based calibration method, for the **practical scenario** as a function of C and λ_2 for (a), (b) PVK and (c), (d) Si cells.

The absolute iV error maps for all individual cells considering the **practical scenario** are presented in Figure 4.17. Compared to the worst-case scenario (Figure 4.15), the maximum iV error shifts slightly toward longer wavelengths. Figure 4.18 displays the mean (a, c) and maximum (b, d) absolute iV errors for the practical scenario. By confining the detection range of the luminescence signal to 730 nm (for PVK) and 1,025 nm (for Si), the iV errors remain below 19 mV (1.65%, for PVK) and 17 mV (2.4%, for Si), regardless of C. The relatively modest improvement observed in the case of Si, compared to the worst-case scenario, is likely attributable to the $\mathrm{QE}_{\mathrm{camera}}$, which already attenuates long wavelengths. Furthermore, in the practical scenario, selecting C within the range of 0.55-0.65 for PVK limits the maximum iV error to less than 9 mV (0.8%). For Si, restricting C to the range of 0.65-0.75 limits the maximum iV error to less than 6 mV (0.9%). Hence, these C ranges are recommended for common tandem devices. When utilising PL imaging, the developed method is fully contactless and versatile, allowing its application to both precursors and complete devices without the need for prior knowledge of their EQE, enabling the quantification of iV with high accuracy.

The modelling results demonstrate that this approach enables reliable iV quantification when high-quality reference cells are unavailable. However, this flexibility introduces a trade-off compared to the previously discussed approach: the light source calibration approach requires a narrower detection range (smaller λ_2) to achieve comparable accuracy and minimise iV errors. Using a calibration cell allows a broader detection range, resulting in a stronger luminescence signal, shorter measurement times, and improved SNR.

4.6.2 Experimental Validation

4.6.2.1 Experimental procedure

In the light-source-based method, f is determined by a blackbody radiation source (Omega; BB705) with a stable and well-known spectrum, following the procedure described in Section 2.3.2. The blackbody radiation source was coupled with an optical fibre (1,500 μm/0.5 NA) into an integrating sphere, where the absolute spectral photon flux at the integrating sphere's output port was measured. The integrating sphere was positioned at the same height as the measured cells. Once the blackbody radiation source was stabilised at a temperature of 1,027 °C, the emitted signal was captured by the imaging setup with the BPF. Accordingly, f can be derived via Equation 2.22 by comparing the acquired luminescence image from the integrating sphere's output, $\Delta\phi_{\mathrm{light}}^{\mathrm{detect}}$, with the known spectral photon flux of the blackbody over the spectral transmission range of the BPF, $\Delta\phi_{\mathrm{light}}$. It should be mentioned that the emitted luminescence from the blackbody was directly measured using a spectrometer before and after connecting the fibre and integrating sphere to assess losses within the optical fibre and integrating sphere.

4.6.2.2 Implied voltage determination

Based on the modelling results in the previous section, C values of 0.65 for the PVK subcell and 0.75 for the Si subcell were chosen to determine iV via Equation 4.1. The corresponding iV images of the top and bottom subcells in Tandem 1 [(a), (b)] and Tandem 2 [(c), (d)] are shown in Figure 4.19. Table 4.3 summarises the global harmonic mean iV calculated from the subcell images and the V_{term} of the tandem devices. Compared to the V_{term}, the estimated iV differs by 7 mV (0.06%) and 15 mV (0.40%) for Tandem 1 and Tandem 2, respectively. The obtained iV errors are slightly higher than those obtained using the calibration cells (see Table 4.1), primarily due to deviations in the estimated iV for the PVK subcell. Nevertheless, both methods estimate iV values within 1% of V_{term}, highlighting the accuracy of the proposed methods for determining the iV of tandem cells.

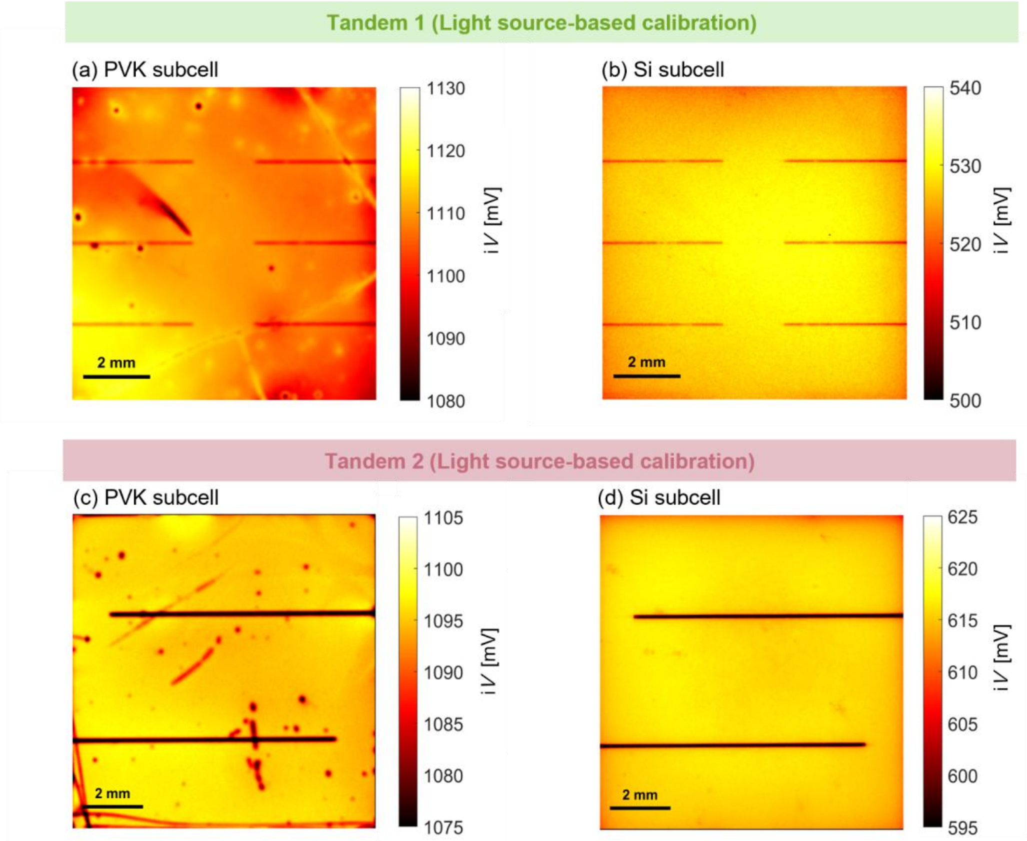

Figure 4. 19 – iV images of (a), (c) PVK and (b), (d) Si subcells obtained using the light-source based calibration method. Note that C of 0.65 (0.75) for PVK (Si) subcell was used.

Table 4. 3 – Harmonic mean iV of subcells and the entire tandem devices. Note that the reported standard deviations for the estimated iV values represent spatial inhomogeneity in the iV distribution.

Tandem, current injection level	PVK sub cell: Estimated iV [mV]	Si bottom cell: Estimated iV [mV]	Entire device: Estimated iV [mV]	Measured V_{term} [mV]
Tandem 1, 1.50 [mA/cm²]	1,108.8 ± 4.6	527.3 ± 2.4	**1,636.1 ± 5.4**	**1,629 ± 2**
Tandem 2, 0.66 [mA/cm²]	1,094.0 ± 8.7	614.8 ± 6.8	**1,708.9 ± 11.8**	**1,694 ± 2.5**

As discussed previously, this method (light-source based calibration) does not require accurate information regarding the EQE of each of the subcells and only utilises a constant C. To investigate (again) the impact of assuming constant C, the iV errors were calculated for Tandem 1, assuming a constant C ranging between 0.38 and 0.98 (for each subcell), as depicted in Figure 4.20. The lower limits of C, as suggested by the above simulation (Figure 4.18), are indicated by dash-dotted lines. Consistent with the simulation results, the recommended C range results in a maximum error of 15 mV. The error decreases to 7 mV (indicated by the black star) if C of 0.65 (0.75) for the PVK (Si) subcell is used, and further to 5 mV (square) when the mean EQEs for each subcell within the detected wavelength range are utilised. Given that the proposed method aims to estimate the iV of *any* tandem cells within an acceptable range of error, the recommended C values can be generally applied. Additional knowledge regarding the EQE of the measured cell can further reduce the associated error.

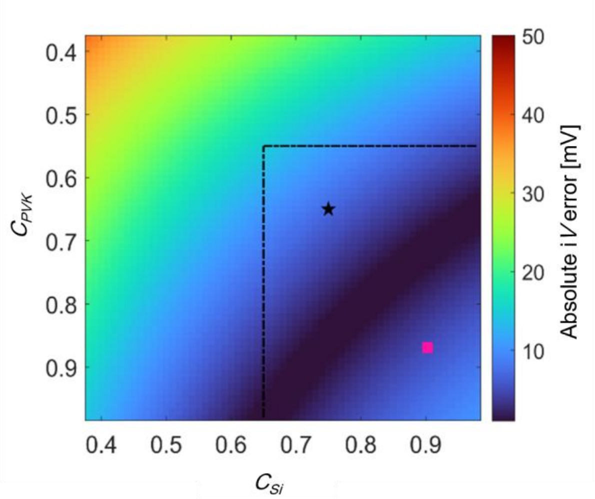

Figure 4. 20 – Absolute iV error map as a function of C. The dash-dotted lines mark the lower limits of C as suggested by the simulation results (Figure 4.18). The star indicates the C values used in Figure 4.19(a) and (b) for iV calculation of Tandem 1. The square marks the mean of the measured EQEs of the PVK and Si subcells.

4.6.3 Spatially resolved pseudo-dark J–iV measurement

Similar to the cell-based calibration method, this approach can also be used to construct the pseudo-dark J–iV curve for each subcell and, subsequently, the entire tandem device. As a demonstration, Figure 4.21 compares the pseudo-dark J–iV curves of Tandem 1 obtained using both the light source-based calibration method (assuming C values of 0.65 and 0.75 for the PVK and Si subcells, respectively) and the cell-based calibration method (using Set 1). The pseudo-dark J–iV curves obtained from each approach are nearly identical, with a variation of less than 5 mV.

Ultimately, depending on whether a high-performance calibration cell or a calibrated light source is available, the appropriate calibration method can be adopted. By selecting a suitable narrow BPF, accurate iV image quantification with less than 1% error can be achieved for tandem subcells with diverse optical properties and compositions. Notably, this accuracy does not require detailed knowledge of the optical properties of the measured device or the spectral response of the imaging system.

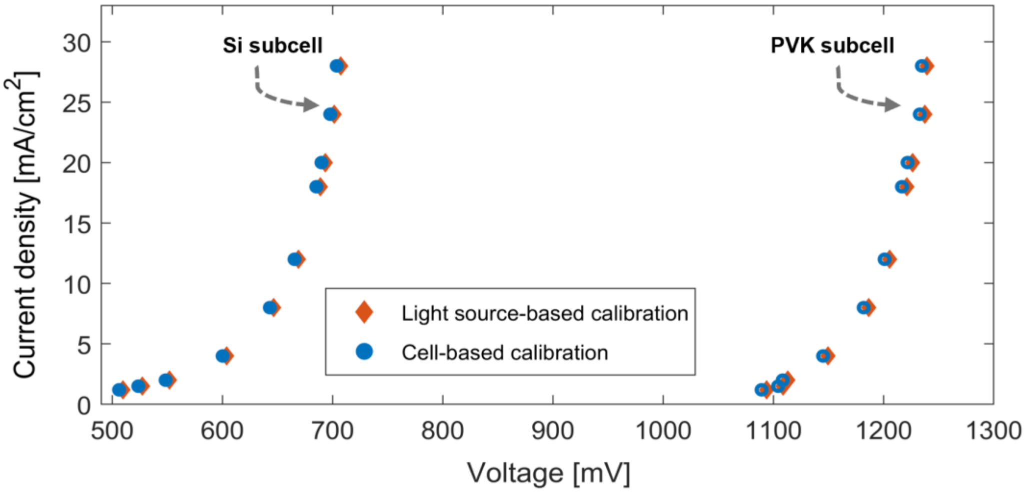

Figure 4. 21 – Comparison of the global pseudo-dark J–iV extracted from the mean of the iV images of the PVK (open symbols) and Si (filled symbols) subcells using cell-based calibration (blue) and light source-based calibration (orange) method.

4.7 Summary

In this chapter, a luminescence-based technique was developed to extract iV images of individual subcells in PVK/Si tandem devices, with a reduced sensitivity to optical properties. Building on the method introduced in Chapter 3, this approach employs a carefully selected narrow BPF to suppress variations caused by sample-specific characteristics, making the detected signal largely independent of the optical properties of the subcells and the measurement system.

Simulations across various tandem structures identified an optimal range for the BPF of $\lambda_2 \leq 730$ nm for PVK and $\lambda_2 \leq 1{,}050$ nm for Si, enabling accurate iV extraction for each subcell with an error of less than 1%. Therefore, iV can be determined for each subcell using a single-junction calibration cell, regardless of differences in their structural or optical properties. This method was experimentally validated and further applied to extract spatially resolved pseudo-dark J–iV curves of each subcell, allowing for detailed investigation of local defects and their performance impact.

As this method requires high-performance single-junction calibration cells, particularly for PVK, an alternative approach (light source-based calibration) using a calibrated light source and the simplified Planck's law was also developed. In this method, the absorptivity A is replaced by a constant calibration C. Simulations were conducted to identify suitable BPFs and the corresponding C ranges that minimise iV errors for each subcell. The simulations showed that by using appropriate BPF ranges ($\lambda_2 \leq 730$ nm for PVK, while $\lambda_2 \leq 1{,}025$ nm for Si) and selecting the optimised C values for each subcell, iV can be determined with an error within 1%. Experimental measurements then confirmed the simulation results by extracting iV maps of subcells within the PVK/Si tandem devices. Similar to the previous method, this approach is also applicable for establishing pseudo-dark J–iV characteristics.

Both methods presented in this chapter enable accurate determination of subcell iV in tandem devices, with the calibration process required only once for a given measurement system. Beyond this, these techniques offer several advantages: they are fast, non-destructive, and applicable at various fabrication stages, from early precursors to fully processed devices. They also support inline quality monitoring and facilitate spatially resolved performance analysis across tandem structures.

To further assess the robustness of the proposed iV extraction technique for tandem subcells using a narrow BPF, the following chapter presents a systematic analysis of its associated uncertainty sources. While both calibration approaches are practical, using calibration cells provides added simplicity and flexibility. As such, the uncertainty analysis focuses specifically on the calibration-cell-based method.

Chapter 5 – Uncertainty Analysis of the Implied Voltage in PVK/Si Tandem Cells

Chapter 4 introduced a new method for obtaining spatially resolved iV maps of subcells within PVK/Si tandem devices using a suitable narrow BPF. The key innovation of this technique is its ability to suppress the influence of sample-specific optical properties, thereby eliminating the need for complex spectral characterisation of the device and measurement system. Although the accuracy of this method has been experimentally validated and supported by device simulations across various tandem configurations in the previous chapter, structural and experimental factors may still introduce uncertainties into the measurements. A systematic uncertainty analysis is therefore necessary to ensure reliable results under real-world conditions.

Accordingly, this chapter presents a systematic investigation into the uncertainty sources associated with the BPF-based iV mapping technique. The primary objective is to develop a detailed framework for identifying, quantifying, and propagating the various uncertainties to determine the total error in the final iV measurement for each subcell. This analysis will focus specifically on the calibration cell-based approach, which is more practical method due to its operational simplicity and flexibility. The results of this investigation will provide clear confidence limits for the measured data and offer practical guidelines for minimising measurement error.

This chapter begins with an initial classification of the primary sources of uncertainty (Section 5.1). The following sections discuss each source in detail. Section 5.2 investigates uncertainties arising from property mismatches between the calibration and measured cells. Section 5.3 evaluates the impact of optical interactions in tandem structures. Section 5.4 then analyses the influence of experimental setup conditions. Finally, Section 5.5 integrates these individual error sources to determine the total measurement uncertainty.

5.1 Classification of uncertainty source

Despite the robustness of the BPF-based method, presented in the previous chapter, its accuracy can still be affected by several factors. Identifying and quantifying these sources is essential to minimise the impact. As illustrated in Figure 5.1, these uncertainties can be categorised into three primary groups: (a) differences between the properties of the calibration and measured subcells, such as variations in front/back reflectance, bandgap mismatches, and discrepancies between iV and terminal voltage in PVK cells; (b) optical interactions within the tandem device, including luminescence coupling (LC) effects and spectral overlap near the BPF cut-off region; and (c) setup-related factors, including illumination angle and temperature fluctuations.

In the following sections, each source of uncertainty is systematically investigated and its individual contribution quantified.

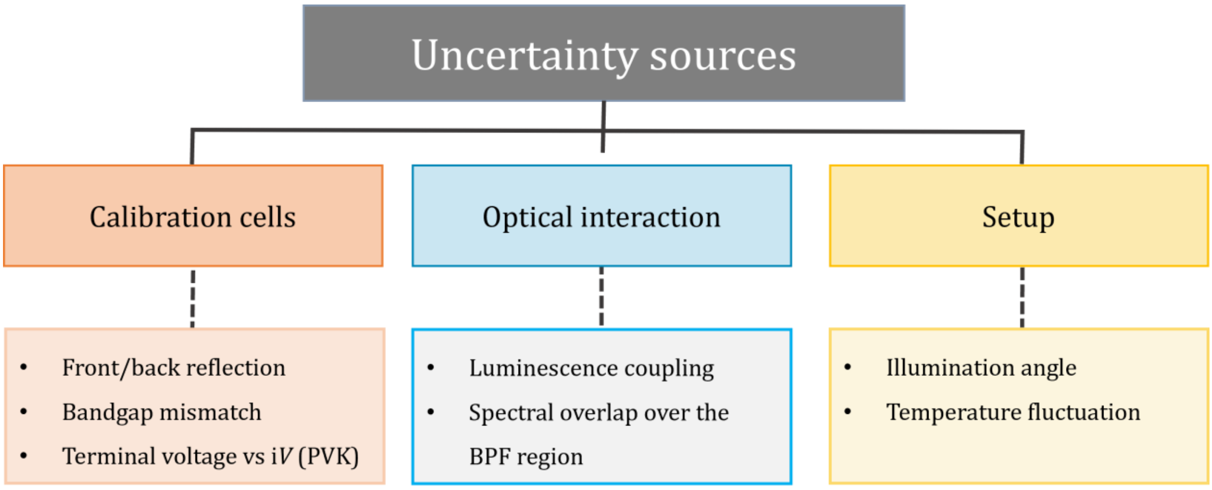

Figure 5. 1 – Summary of the key uncertainty sources using the BPF method.

5.2 Calibration and measured cells

5.2.1 Impact of front and rear reflection

The front and rear reflectance affect absorptivity [66, 67]. This, in turn, influences the emitted luminescence intensity and spectrum (see Equation 2.13), and ultimately the extracted iV. Since single-junction cells are used for calibration, their front and rear reflectance is expected to differ from those of the subcells within the tandem device, due to possible optical interactions between the subcells [128, 129]. The PVK stack affects the front reflectance of the Si subcell, while the Si subcell, in turn, modifies the rear reflectance of the PVK layer [119, 130].

Although the Si subcell is optically coupled to the overlying PVK subcell, this interaction has minimal impact on the accuracy of iV extraction when the proposed BPF-based method is used. This is because PVK materials commonly employed as top cells (with $E_g \geq 1.6$ eV) are effectively transparent over the spectral range that Si subcell emits luminescence (950–1,200 nm), which lies well beyond their absorption edge [131, 132]. However, the presence of the PVK stack and other layers, such as transparent conducting oxides and recombination/contact layers, can still affect light propagation within the Si subcell by altering R and p compared to single-junction cells [130, 132, 133]. In Chapter 3, the impact of variations in these two parameters (R and p) on the iV extraction of Si-based devices using a single calibration cell was systematically evaluated. As shown in Figure 3.6 (for $\lambda_2 \leq 1{,}025$ nm), across a wide range of Si cells the resulting iV error remains below 7 mV (~1%), confirming that the potential impact of using a single-junction Si cell for calibration on the accuracy of the BPF method is minimal.

For the PVK subcell, the impact of rear reflectance mismatch between the calibration and measurement configurations, arising from the underlying Si subcell and interconnection layers, was not studied in earlier chapters. To evaluate its maximum possible effect, three single-junction PVK devices representing extreme optical scenarios were simulated [Figure 5.2(a)]. Importantly, across all structures the PVK stack included a 1.62 eV $Cs_xFA_{1-x}PbI_{2-x}Br_x$ absorber and a silver (Ag) rear reflector. The rear-side architecture was then varied to represent different scenarios:

- a planar device with a black rear sheet, representing minimal rear reflection
- a planar device with a transparent rear sheet, providing high rear reflection from a planar surface
- a textured device with a transparent rear sheet, where all layers are modelled as conformally coating the rear texture to achieve maximum light trapping.

The Setfos optimiser (Fluxim AG; Setfos) [134] was used to determine the properties (e.g., d, n_r, and extinction coefficient k) of the rear sheet for each case and simulate the corresponding absorptance spectrum of the PVK layer. The final parameters for all layers are summarised in Table 5.1.

Figure 5.2(b) presents the modelled absorptivity spectra for the PVK layer in each of the three cases. As expected, the PVK structure with the black sheet on the rear shows the lowest absorptivity, particularly above 500 nm. The transparent planar configuration exhibits higher absorptivity due to increased rear reflection, while the textured design further enhances absorption across the entire spectrum by increasing the optical path length and improving light-trapping efficiency.

Table 5. 1 – Layer structure, thicknesses, and complex refractive indices used in the Setfos simulations of the PVK devices with different back sheets.

Layer	*d* [nm]	n_r and k
MgF_2	111	[135]
ITO	110	[136]
SnO_2	9	[134]
C_{60}	15	[137]
$Cs_xFA_{1-x}PbI_{2-x}Br_x$ [1.62 eV]	440	[138]
NiO	20	[139]
Transparent sheet (planar)	114	n_r = 1.24 and k = 0
	[Calculated using the Setfos optical optimiser]	
Transparent sheet (textured)	200	n_r = 1.67 and k = 0
	[Calculated using the Setfos optical optimiser]	
Black sheet (planar)	100	n_r = 2.97 and k = 1.06
	[Calculated using the Setfos optical optimiser]	
Ag	300	[140]

The corresponding ϕ^{detect} of each structure was calculated using Equation 2.14, assuming a fixed i*V* of 1,100 mV, a temperature of 23 °C, and using the representative QE_{camera} of the Si camera [Figure 4.1(c)]. The resulting ϕ^{detect} are shown in Figure 5.2(c). Noticeable differences are observed at long wavelengths, particularly between the textured and planar configurations. In contrast, at shorter wavelengths, especially below 730 nm, the three spectra converge, suggesting that in this wavelength range, the luminescence signal becomes relatively insensitive to the impact of rear reflection. This supports the robustness of the BPF method when confined to the short-wavelength regime.

To evaluate the impact of the differences between the various ϕ^{detect} spectra, the analysis approach described in Chapters 3 and 4 (summarised in Figures 3.3 and 4.4) was utilised. Using the calculated ϕ^{detect} [Figure 5.2(c)], the corresponding i*V* was extracted using Equation 2.27, assuming a fixed λ_1 of the BPF (λ_1 = 650 nm) and variable λ_2 ranging from 660 to 800 nm. Each configuration was used as the calibration cell, and the i*V* error was then calculated by comparing the extracted i*V* of the other two configurations with the input value defined in this study (1,100 mV).

Figure 5.2(d) presents the estimated i*V* error as a function of λ_2. The colour of the circle represents the calibration cell used, while the colour of the 'x' marker indicates the corresponding measured PVK cell. For example, consider the data point marked by a blue circle containing a green 'x'. This point corresponds to the case in which the PVK cell with the black rear sheet (blue circle) was used as a calibration cell to determine the i*V* of the planar PVK cell with a transparent rear sheet (green 'x'). The plotted value, therefore, indicates the resulting iV error for this particular calibration/measured pair at the given λ_2. As expected from the observations in the previous chapters, the iV errors increase as λ_2 increases, regardless of the calibration/measured cell combination. This reflects the greater sensitivity of the extracted iV to the spectral shape of the luminescence signal at longer wavelengths. Nevertheless, the analysis shows that even for these extreme scenarios, the iV error remains within ±12 mV for $\lambda_2 \leq 730$ nm. Hence, by using this threshold, the maximum uncertainty due to rear reflectance mismatch between the single-junction PVK calibration cell and the measured PVK subcell in the tandem device can be significantly reduced.

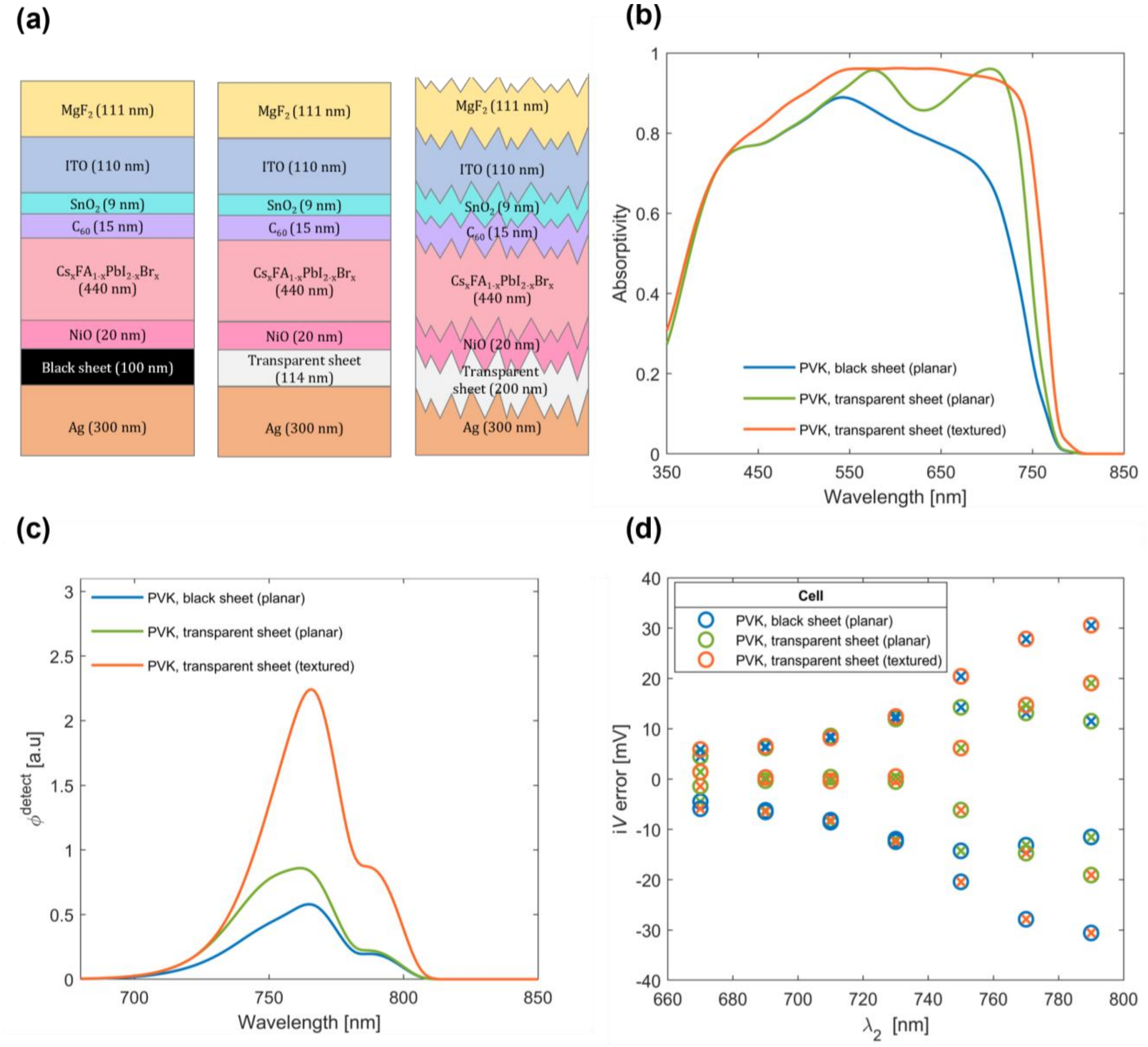

Figure 5. 2 – Simulated (a) PVK device structures with different back sheets, (b) their absorptivity spectra, (c) corresponding ϕ^{detect} at fixed iV = 1,100 mV and T = 23 °C, and (d) iV error as a function of λ_2 for the different configurations (the colour of the circle represents the calibration cell used, while the colour of the 'x' marker indicates the corresponding measured PVK cell).

5.2.2 Bandgap mismatch

The bandgap of PVK cells can be tuned [17, 18]. Since the material bandgap has a significant impact on the emitted luminescence spectrum [141-143], a bandgap mismatch between the PVK calibration and measured cells can affect the accuracy of iV extraction. While the previous chapter demonstrated that narrow BPFs enable accurate iV extraction regardless of differences in composition between the calibration and measured cells, the analysis was limited to a small number of cases. In this section, the investigation is extended to a broader range of PVK compositions. Simulations were performed on PVK solar cells where the bandgap of the PVK absorber layer was varied from 1.55 eV to 1.68 eV, in 0.02 eV intervals, using Setfos [134]. This range was selected to represent the commonly used wide-bandgap PVK compositions in tandem applications [16, 18, 19]. The simulation parameters and layer properties are listed in Table 5.2.

Table 5. 2 – Layer properties used in the simulated PVK devices with varying bandgap.

Layer	d [nm]	n_r and k
Glass	Incoherent	[144]
ITO (Front)	159.5	[145]
NiO_x	19.9	[145]
PVK (Vary bandgap)	461.6	[145]
C60	22.1	[145]
SnO_2	8	[145]
ITO (bottom)	175	[145]
Ag	300	[140]

Figure 5.3(a) presents the spectral absorptance, A, of the modelled PVK cells. As expected, as the bandgap increases, the absorption edge shifts to shorter wavelengths. The corresponding ϕ^{detect} [Figure 5.3(b)], calculated at a constant iV of 1,100 mV using the Si camera spectral response [Figure 4.1(c)], shows reduced intensity and a shift of the spectral peak toward shorter wavelengths with increasing bandgap. This trend is explained by the energy offset between the material's bandgap and the $\Delta\mu$ (q·iV). Since the iV is held constant in this analysis, and thus $\Delta\mu$ is also constant, the energy offset increases as the bandgap widens. This greater offset reduces the radiative recombination rate, leading to a decrease in luminescence intensity and a shift of the emission peak toward higher photon energies [83, 146].

To assess the impact of bandgap mismatch, the iV error was calculated for each pair of calibration and measured cells (a total of 8 × 8 combinations from the simulated bandgaps). Figure 5.4 presents the iV errors as a function of λ_2, and the inset shows a zoom-in at λ_2 = 730 nm. The colour of the circle represents the calibration cell used, while the colour of the 'x' marker indicates the corresponding measured PVK cell. As expected, the iV error increases significantly at longer wavelengths. However, for $\lambda_2 \leq$ 730 nm, the error remains below ±3 mV, highlighting the robustness of the BPF method in achieving accurate iV extraction when an appropriate wavelength range is selected, despite the bandgap mismatch.

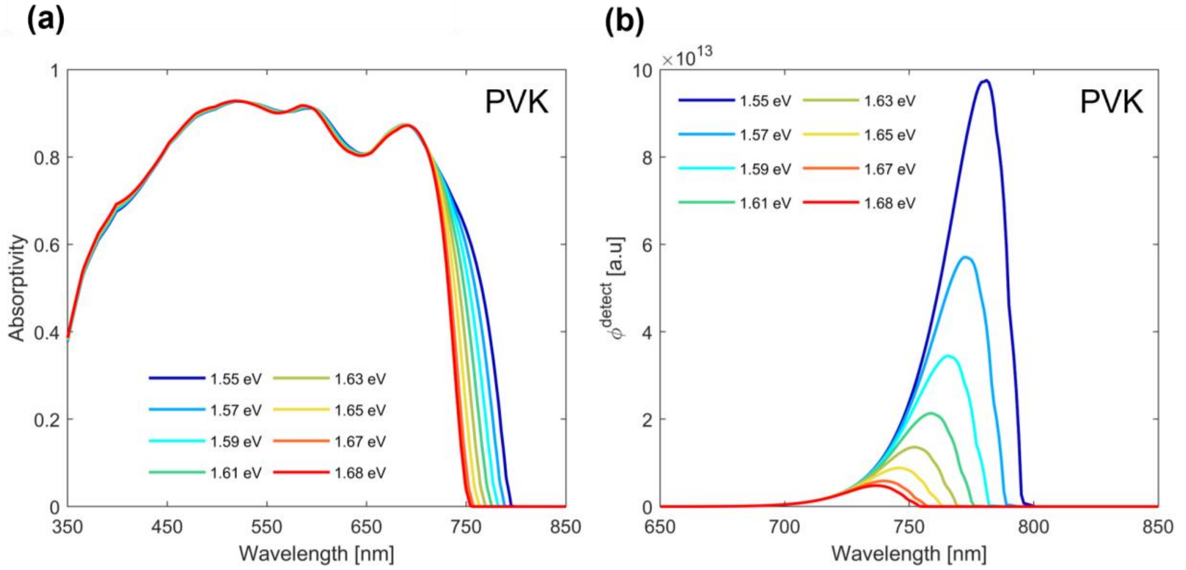

Figure 5. 3 – (a) Simulated absorptivity spectra of PVK cells with varying bandgaps and (b) the corresponding ϕ^{detect} assuming iV = 1,100 mV and T = 23 °C.

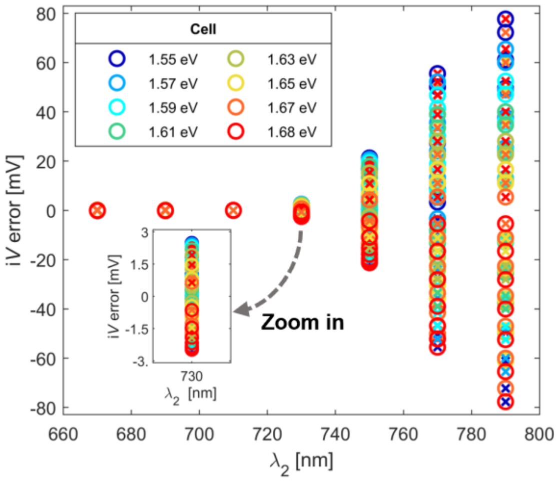

Figure 5. 4 – Calculated iV error as a function of λ_2, Circles represent the calibration cells and 'x' markers denote the corresponding measured cells. The inset shows a zoom-in of the associated iV error at λ_2 = 730 nm.

5.2.3 Terminal voltage vs. implied voltage discrepancies

In conventional solar cells, such as Si solar cells, V_{term} is a good approximation of iV, specifically under low current injection conditions where the effect of R_s is negligible. However, a mismatch between

V_{term} and iV is often reported in PVK solar cells, even at low current injection [87, 122-124]. This discrepancy, which can range from 10 mV to 250 mV [123, 124], arises from factors such as: (a) energy band misalignment between the PVK layer and charge transport layers [122, 123], (b) surface recombination [122, 123], (c) poor charge transport properties [124], and (d) ion migration [124]. Nevertheless, for well-optimised PVK cells where these non-ideal loss pathways are suppressed, the difference is minimal, and V_{term} provides an accurate approximation of iV [123, 124].

The method's applicability might become challenging if such a well-optimised device for a calibration cell is not available, as quantitatively assessing this mismatch requires applying other complex and time-consuming processes. To address this potential limitation, this section investigates the use of an LED as a simple, cost-effective, and widely applicable alternative to broaden the use of the proposed method.

Since LEDs emit light via the same radiative recombination process as solar cells their emission is related to their iV [86]. The V_{term} of an LED closely matches its iV under low current injection level [147], making it highly suitable for voltage calibration. For compatibility with the BPF method, the LED emission must fall within the filter’s detection range. Additionally, since solar cells emit with an approximately Lambertian angular distribution [148], it is preferable to use an LED with a similar emission profile. For demonstration purposes, among the many available options, a planar AlGaInP (aluminium gallium indium phosphide) LED (Marubeni; SMBB760D-1100) was selected. This LED features Lambertian emission, a nominal peak wavelength of 760 nm, and an active area of 1 mm^2. It offers high radiative efficiency, stable emission, and superior reliability, making it well suited for this study.

In the following section, the suitability of using the commercial 760 nm LED as a calibration reference for determining the iV of PVK subcell is experimentally assessed.

5.2.3.1 Spectral emission analysis of LED

This section provides a spectrally resolved assessment of the LED's performance as a calibration source. It begins by comparing its EL spectrum to that of a single-junction PVK solar cell. The PVK cell used for this comparison has a bandgap of 1.67 eV and an active area of 0.07 cm^2. The composition of the absorber layer is $Cs_{0.15}MA_{0.2}FA_{0.65}PbI_{2.4}Br_{0.6}$. Full fabrication details are provided in Ref. [120]. EL spectra were measured with a Si spectrometer (Aventus; AvaSpec-VRS2048CL-EVO) coupled to a 1,500 µm, NA 0.5 fibre. An SMU (Keithley; 2461) was employed to inject different currents while simultaneously measuring the terminal voltage in a 4-wire configuration.

EL spectra were measured by biasing the LED with 0.5 mA/cm^2 and the PVK cell with 2.14 mA/cm^2 to achieve a comparable terminal voltage of 1,125.5 ± 3 mV. Figure 5.5 compares the measured EL spectra of the 760 nm LED (solid) and the PVK solar cell (dashed). The spectra closely overlap in the short-wavelength region, indicating that the luminescence in this range is largely insensitive to the sample's optical properties. This spectral match lies within the detection window of the BPF established in Chapter 4 for iV determination of PVK devices ($\lambda_2 \leq 730$ nm). Hence, the LED can serve as a calibration source for PVK-based devices.

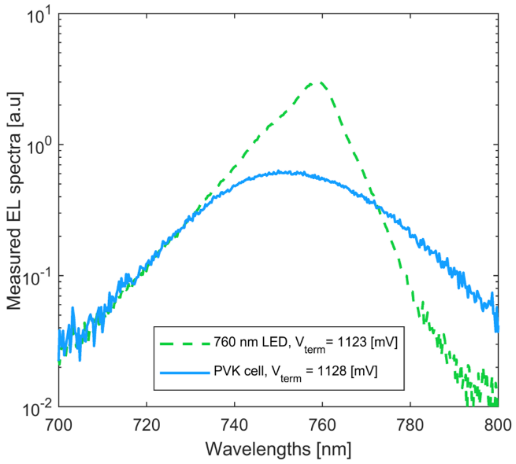

Figure 5. 5 – Measured EL spectra of the 760 nm LED (green) and the PVK cell (blue) at similar V_{term}, acquired using a Si spectrometer.

To further assess the link between EL spectra and terminal voltage, EL spectra were recorded across a wide range of injection currents. Figure 5.6(a) shows the EL spectra under different current injection levels. Across all injection levels, the peak emission wavelength remains stable at 758 ± 0.35 nm, which aligns well with the manufacturer's specifications. Figure 5.6(b) plots the integrated luminescence intensity versus the terminal voltage at different injection levels (symbols) on the left axis, together with the J–V characteristic on the right axis. At low injection levels ($J < 0.01$ mA/cm^2), the data exhibit a clear exponential trend, consistent with the relationship given in Equation 2.14. To quantify this behaviour, a linear fit was applied to the natural logarithm of the luminescence signal versus terminal voltage (V_{term}), where the slope corresponds to $1/V_{\mathrm{T}}$. The extracted V_{T} is 25.57 mV, in good agreement with the theoretical value at room temperature (~25.5 mV at 23 °C). However, at higher injection currents, the measured EL intensity systematically deviates from this ideal exponential behaviour. This deviation arises due to complex and interconnected factors inherent to the III-V based LEDs [149]. Full quantitative analysis of these effects would require sophisticated device modelling [150], which is beyond the scope of this thesis. Nevertheless, the observed non-ideal behaviour can be qualitatively attributed to several mechanisms: (a) dynamic effective R_s, where resistive losses increase at high injection levels due to factors such as device self-heating [149]; (b) a reduction in radiative efficiency at high carrier densities, commonly referred to as efficiency drop, which in AlGaInP-based LEDs is often attributed to thermally activated carrier leakage from the active region [151]; and (c) modifications to the electronic band structure, where the competing effects of band-filling (a blueshift) and bandgap renormalisation (a redshift) impact the final emission spectrum [149, 152]. It should be noted that, as these effects are dynamic and interdependent, a static R_s derived from a single J–V fit is insufficient to correct for these discrepancies. To avoid these non-idealities, LED-based calibration in this study is limited to the low-current regime (J < 0.01 mA/cm^2), where such effects are negligible and V_{term} provides a reliable proxy for the iV.

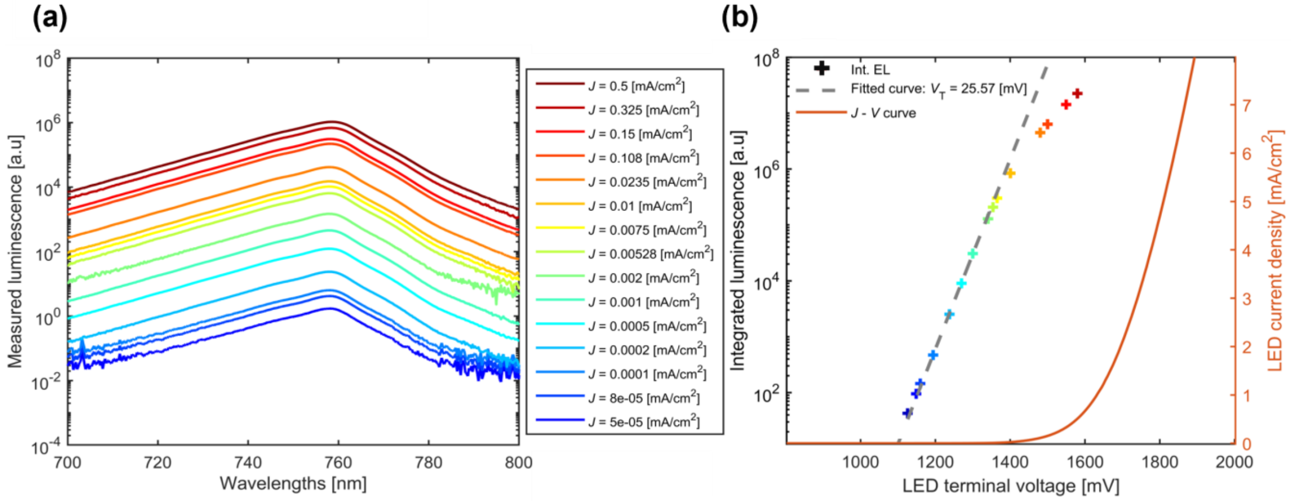

Figure 5. 6 – (a) Measured luminescence of the 760 nm LED under different current injection and (b) Spectrally integrated luminescence intensity (left-axis) and LED current density (right-axis) versus terminal voltage. The dashed line is a linear fit to the semi-log luminescence data, with V_T determined from the inverse of the slope.

5.2.3.2 Implied voltage determination from luminescence images

Having established the ideal operating characteristics of the LED, this section validates its use as a calibration cell for iV imaging. The use of the LED as a calibration was first validated on a single-junction PVK cell, leveraging its simpler structure, before being applied to the tandem devices that are the focus of this section.

The validation was performed by extracting the iV map of a PVK cell using two separate calibration cells: a high-performance PVK cell and the 760 nm LED. The test PVK cell was a p-i-n configured cell with a bandgap of ~1.55 eV and an active area of 0.05 cm^2. Its layer stack was identical to that of the PVK cell in calibration Set 4, described in Chapter 4, Section 4.5. The calibration PVK cell was a p-i-n structure with a bandgap of ~1.67 eV and an active area of 0.07 cm^2. Its layer stack was identical to that of the PVK cell in calibration Set 3, described in Chapter 4, Section 4.5, although it is a different sample.

The EL images of the PVK cells and the LED were acquired with the same camera and optical setup previously used for iV extraction of the subcells in Tandem 3 and Tandem 4 (see Chapter 4, Section 4.5). It is worth highlighting that, in line with the findings of Chapter 4, which identified an optimal BPF with $\lambda_2 \leq 730$ nm to minimise sample-specific effects on iV extraction, a 710±15 nm BPF was employed. The iV of the measured cells was then extracted by applying Equation 2.27, using the calibration device's harmonic mean EL intensity.

To acquire the EL images, the test device was biased at 4 mA/cm^2 (V_{term} = 1,033.5 mV), the calibration PVK cell at 0.71 mA/cm^2 (V_{term} = 1,071.0 mV), and the LED at 2×10^{-4} mA/cm^2 (V_{term} = 1,191.5 mV). These low injection currents ensure that the V_{term} of all the devices provides a reliable proxy for their iV.

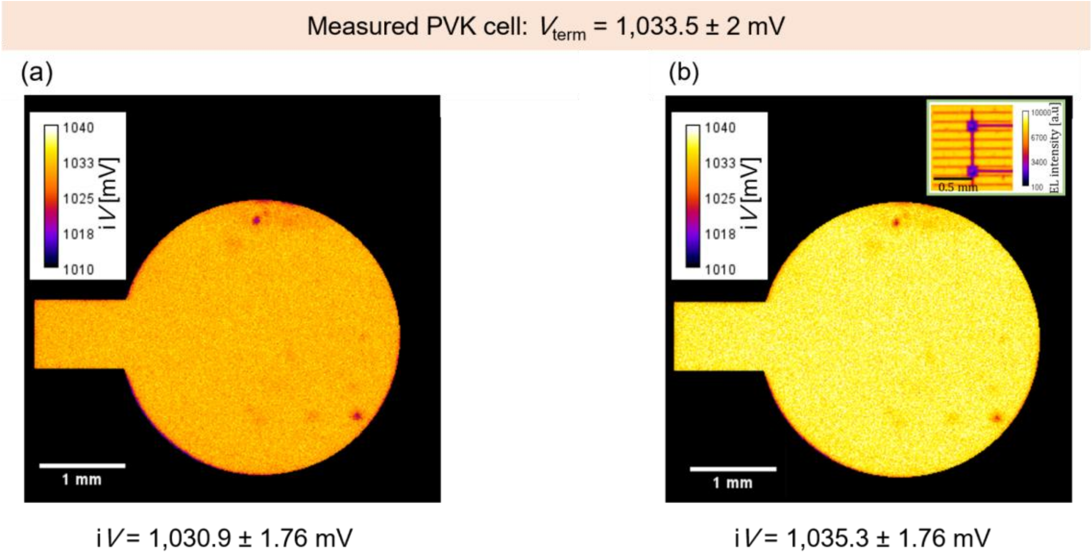

Figure 5. 7 – Extracted iV images of the 1.55 eV PVK cell, obtained using (a) the 1.67 eV PVK cell and (b) the 760 nm LED as calibration devices. The reported iV values, provided below each graph, are harmonic means calculated from each iV map, with standard deviations reflecting spatial inhomogeneity. The inset (b) shows the raw EL image of the LED used for calibration.

Figure 5.7 depicts the estimated iV images of the test PVK solar cell, obtained using (a) the PVK cell and (b) the LED as the calibration device; the inset in (b) shows the raw EL image of the LED. The iV map of the PVK cell reveals high spatial uniformity, reflected in the low standard deviation (±1.76 mV). A comparison of the two calibration methods shows that the harmonic mean iV obtained using the LED is slightly higher, by less than 5 mV, than that obtained from the PVK calibration cell. Importantly, both estimated iV values are within 3 mV of the measured terminal voltage. Therefore, despite the significant structural differences between the LED and the PVK device, this close quantitative agreement confirms that an LED, in conjunction with a suitable BPF, provides a reliable calibration approach for iV characterisation in PVK solar cells.

Building upon its validation on a single-junction PVK cell, the LED calibration device was extended to iV determination of the PVK subcell in tandem solar cells, assessing its applicability to more complex architectures. The analysis was performed on Tandem 3 and Tandem 4, the same devices for which the subcell iV values were previously determined using cell-based calibration (Chapter 4, Section 4.5).

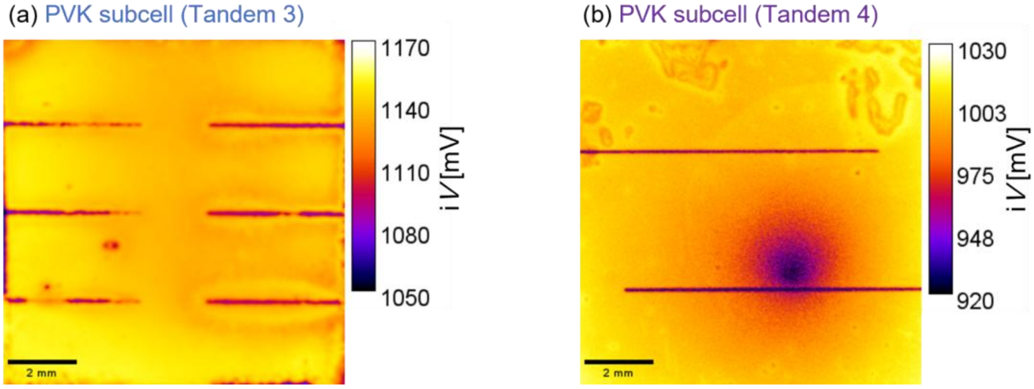

Figure 5. 8 – iV images of the PVK subcells in (a) Tandem 3 and (b) Tandem 4, using 760 nm LED for the calibration.

Figure 5.8 presents the iV maps of the PVK subcells in Tandem 3 (a) and Tandem 4 (b), obtained using the LED as a calibration device. The resulting iV maps show excellent qualitative agreement with those previously obtained via cell-based calibration (see Figure 4.13). A quantitative comparison of the harmonic-mean iV values from both calibration methods is summarised in Table 5.3. For both devices, the PVK subcell iV values determined by the LED method differ by less than 4 mV from the cell-based results. Moreover, the summed iV of the entire tandem devices, calibrated using the LED, deviates from the measured terminal voltage by less than 7 mV. This difference falls within the uncertainty range established in Chapter 4 through modelling and experimental measurements.

Therefore, this high level of accuracy confirms that the combination of an appropriate bandpass filter and a commercial LED, possessing the specific properties detailed in this section, can serve as a reliable calibration device for iV determination in PVK subcells, particularly when a high-performance PVK reference cell is not available. This robust approach addresses the potential limitations of cell-based calibration and could also be extended to other emerging PV technologies for simplified iV characterisation.

Table 5. 3 – The two tandem devices, using cells or the LED for calibration. The uncertainties represent the spatial variation of iV across each subcell.

Tandem, current injection level	Calibration cell	PVK top cell: Estimated iV [mV]	Si bottom cell: Estimated iV [mV]	Entire device: Estimated iV [mV]	Measured terminal voltage [mV]
Tandem 3, 3 [mA/cm^2]	**PVK cell and Si HJT**	**1,140.1 ± 8.1**	620.3 ± 4.3	**1,760.4 ± 12.4**	1,762 ± 1
	LED and Si HJT	**1,136.9 ± 8.1**	620.3 ± 4.3	**1,757.3 ± 12.4**	1,762 ± 1
Tandem 4, 2.2 [mA/cm^2]	**PVK cell and Si HJT**	**993.7 ± 13.9**	605.6 ± 10.7	**1,599.3 ± 24.6**	1,608 ± 1
	LED and Si HJT	**996.1 ± 13.9**	605.6 ± 10.7	**1,601.7 ± 24.6**	1,608 ± 1

5.3 Optical interaction in tandem structures

5.3.1 Luminescence coupling

Luminescence coupling (LC) is an intrinsic phenomenon in monolithic tandem solar cells, where photons emitted through radiative recombination in the high-bandgap top subcell are re-absorbed by the lower-bandgap bottom subcell [153]. Specifically in PVK/Si tandems, the high radiative efficiency of PVK materials results in a substantial portion, often above 50%, of emitted photons being reabsorbed by the Si subcell [154, 155]. This reabsorption alters the excess carrier distribution in both subcells, which is directly reflected in their respective iV. Therefore, while LC reduces the externally detected luminescence from the top cell and enhances that of the bottom cell, it accurately represents the contribution of each subcell to the overall iV. Consequently, LC does not introduce any uncertainty in iV estimation from the detectable luminescence emission, regardless of the calibration method.

5.3.2 Spectral overlap over the BPF region

In tandem solar cells, the EQE spectra of the individual subcells may exhibit partial overlap, raising concerns that luminescence from the non-targeted subcell could affect the detected signal and introduce uncertainty in the iV estimation of the targeted subcell. For instance, the long-wavelength tail of a PVK top cell's emission could extend into the spectral band used for analysing the Si bottom cell, causing experimental artefacts.

However, the PVK top cells and Si bottom cells in PVK/Si tandems have significantly different bandgap energies [29], resulting in well-separated luminescence spectra. PVK subcells ($E_g \sim 1.6$–1.7 eV) emit primarily in the visible to near-infrared region, typically peaking around 750–800 nm, whereas crystalline Si emits between 950 and 1,350 nm, with a peak near 1,150 nm [64, 87]. As the emission from each subcell tapers off well before entering the other's luminescence range, intrinsic spectral overlap is minimal. This distinct spectral gap is quantitatively confirmed by the luminescence spectra calculated for the four tandem cells in the previous chapter [Figure 4.1(d)] and is consistent with experimental results reported in the literature [64, 87]. The use of optical filters designed to isolate each subcell's emission reinforces this separation. The suggested BPFs, with their narrow transmission windows, further minimises crosstalk.

5.4 Experimental setup-related effect

5.4.1 Illumination angle

In the analyses presented thus far in this thesis, a normal incidence ($\theta = 0°$) has been assumed for calculating A (or EQE) and the luminescence spectrum. However, in practical experimental setups, deviations from normal incidence can occur due to factors such as sample tilt, optical misalignment between the illumination source and the sample stage, or imperfections in the beam's collimation, causing light to strike the sample at a range of angles.

To evaluate the influence of illumination angle on iV extraction, optical simulations were conducted using SunSolve [163], considering both planar and textured Si solar cells under illumination angles of 0° and 45°. The schematics of the modelled PERC devices are presented in Figure 5.9(a), where the layer properties and thicknesses are identical and the main distinction is in the front surface morphology. A summary of the key parameters and layer configurations for these simulated devices is provided in Table 5.4.

As depicted in Figure 5.9(b), increasing the illumination angle results in a slight reduction in absorptivity, primarily in the visible and near-infrared regions. In textured cells, this reduction diminishes at longer wavelengths due to enhanced light trapping. These angular effects are reflected in the calculated ϕ^{detect} at a fixed iV, presented in Figure 5.9(c). For the planar cell, ϕ^{detect} under 45° illumination is consistently lower than that at normal incidence across the spectrum. In textured cells, a small angular dependence is observed at shorter wavelengths, while the signals converge at longer wavelengths, aligning with the absorptance behaviour.

Table 5. 4 – Input parameters used in the simulation of the planar and textured PERC solar cells.

Component/Layer	properties	*d*	n_r and *k*
Absorber	c-Si (at 295 K)	180 [μm]	[103]
Front anti reflection coating	SiN_x	75 [nm]	[156]
Rear passivation	Al_2O_3	10 [nm]	[157]
	SiNx	100 [nm]	[156]
Front metallisation	5 busbars	---	---
	120 fingers	---	---
Rear contact	5 busbars	---	---

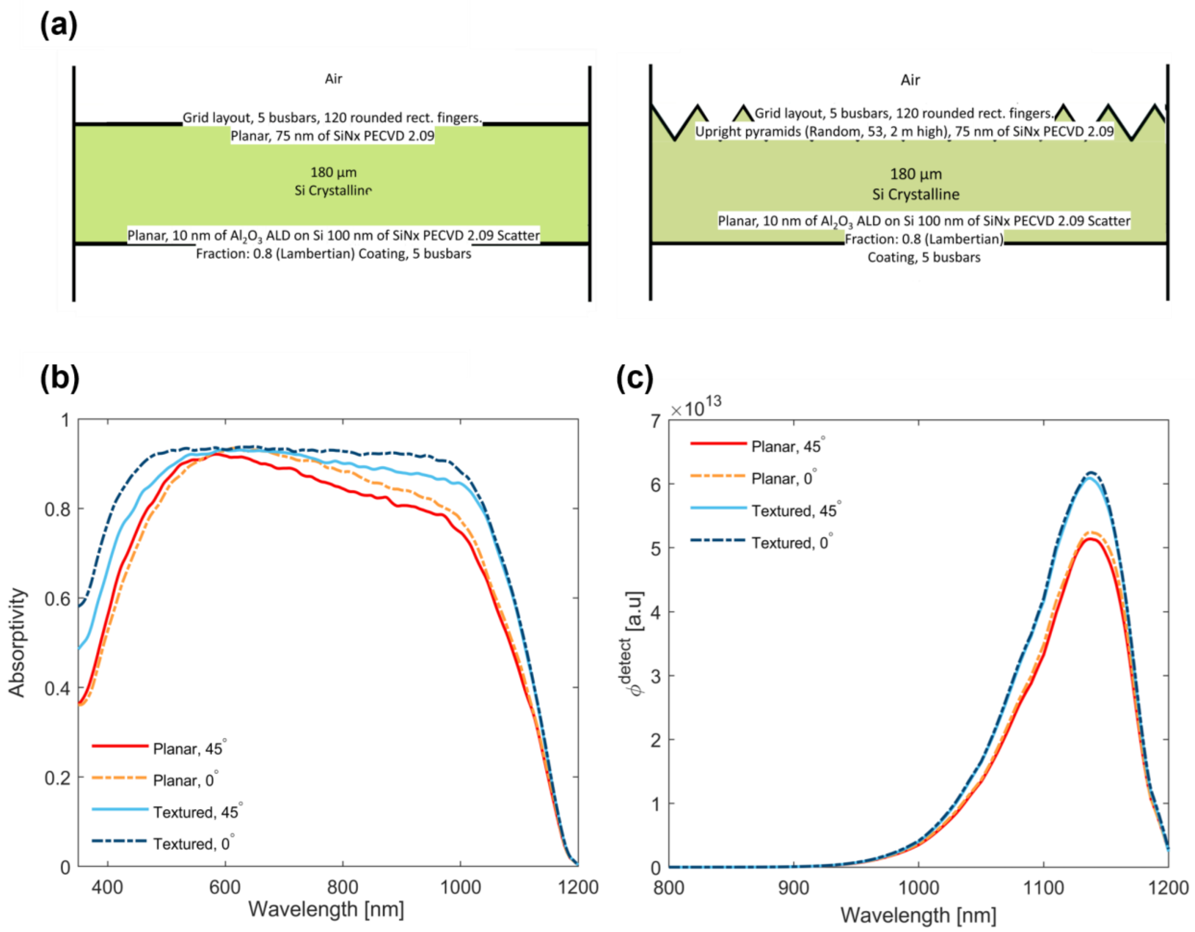

Figure 5. 9 – (a) Schematic of the simulated PERC cells with planar and textured interfaces using SunSolve [158], (b) absorptivity spectra and (c) ϕ^{detect} for representative Si solar cells with planar (red) and textured (blue) interfaces under illumination at 0° (dashed lines) and 45° (solid lines).

The optical simulations reveal that angular variation in the incident light mainly impacted the amount of light reflected from the front surface. Hence, the resulting spectral changes suggest a comparable impact on i*V* extraction via the BPF method, as investigated in Section 3.2.2. Figure 5.10 presents the i*V* error as a function of λ_2, for different pairs of calibration and measured cells. Similar to previous figures, the colour of the circle represents the calibration cell used, whereas the colour of the 'x' marker indicates the corresponding measured device. The rise in iV error, reaching up to ~6 mV at longer λ_2, is primarily attributed to structural differences between planar and textured cells, rather than the illumination angle itself. When comparing 0° and 45° illumination within the same cell structure, the angular impact on iV remains below 1 mV across the entire BPF range. These findings indicate that angular sensitivity is effectively encompassed within the existing reflectance-related uncertainty (Section 3.2.2). As such, no additional angular correction is required when applying the BPF method for iV imaging.

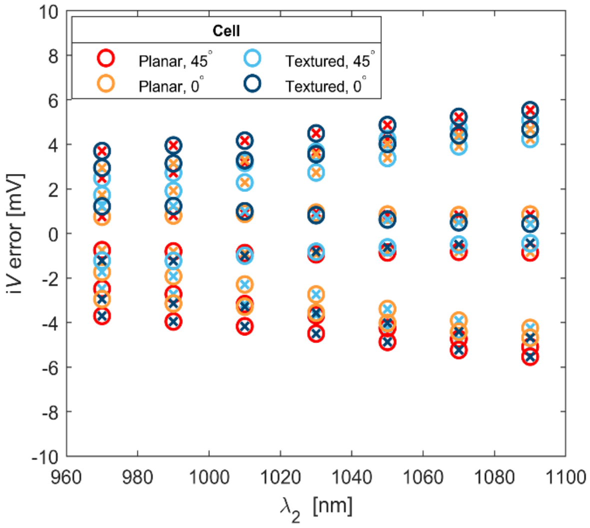

Figure 5. 10 – iV error as a function of λ_2 for the planar and textured cells under illumination at 0° and 45°. Circles represent the calibration cells while the 'x' markers denote the corresponding measured cells.

5.4.2 Temperature variation

The extraction of iV from luminescence signals is sensitive to temperature variations, primarily due to the exponential temperature dependence of key parameters in the luminescence emission model. Even minor temperature fluctuations can significantly affect the accuracy of iV estimation. Although temperature-controlled systems are often used for such measurements, deviations of ± 1°C from the set temperature (T_{set}) are expected. Therefore, a detailed analysis of temperature-induced uncertainty is necessary.

The methodology developed in this thesis builds upon the framework established by Equation 2.27, which is widely used for determining iV. However, this equation relies on the assumption that both the measured and calibration devices are at identical temperatures, without accounting for deviations in either device. To accurately assess the uncertainty introduced by temperature fluctuations, a more generalised model is needed. This requires revisiting the derivation from Equations 2.25 to 2.27

without simplification and including full descriptions of the measured and calibration cells, along with the detection response function f (Equation 2.15). Therefore, a more comprehensive relationship can be derived:

$$\begin{aligned} \mathrm{i}V(T_{\mathrm{cell}}) = {} & V_{\mathrm{T,cell}} \times \frac{V_{\mathrm{term,calib}}(T_{\mathrm{calib}})}{V_{\mathrm{T,calib}}} + V_{\mathrm{T,cell}} \times \ln\left(\frac{\Delta\phi_{\mathrm{cell}}^{\mathrm{detect}}(T_{\mathrm{cell}})}{\Delta\phi_{\mathrm{calib}}^{\mathrm{detect}}(T_{\mathrm{calib}})}\right) \\ & + V_{\mathrm{T,cell}} \times \ln\left(\frac{\int_{\lambda_1}^{\lambda_2} f_2(\lambda) \cdot A_{\mathrm{calib}}(\lambda, T_{\mathrm{calib}}) \cdot \phi_{\mathrm{BB}}(\lambda, T_{\mathrm{calib}}) d\lambda}{\int_{\lambda_1}^{\lambda_2} f_2(\lambda) \cdot A_{\mathrm{cell}}(\lambda, T_{\mathrm{cell}}) \cdot \phi_{\mathrm{BB}}(\lambda, T_{\mathrm{cell}})\, d\lambda}\right) \end{aligned} \tag{5.1}$$

where $\Delta\phi_{\mathrm{cell}}^{\mathrm{detect}}$, A_{cell}, $V_{\mathrm{T,cell}}$, and T_{cell} correspond to the measured device. $\Delta\phi_{\mathrm{calib}}^{\mathrm{detect}}$, A_{calib}, $V_{\mathrm{term,calib}}$, $V_{\mathrm{T,calib}}$, and T_{calib} correspond to the calibration cell.

Assuming equal measurement temperatures ($T_{\mathrm{cell}} = T_{\mathrm{calib}}$) and identical optical properties ($A_{\mathrm{cell}} = A_{\mathrm{calib}}$), the above expression simplifies to Equation 2.27.

Temperature-related uncertainty in iV can be assessed using Equation 5.1. The temperature dependence of both V_{T} and ϕ_{BB} is well-defined. Meanwhile, $\Delta\phi^{\mathrm{detect}}$, A, and $V_{\mathrm{term,calib}}$ are material-dependent and require temperature-dependent evaluation. Assuming different deviations between T_{set} and the actual temperatures of the calibration and measured cells, Equation 5.1 can be rewritten as:

$$\begin{aligned} \mathrm{i}V(T_{\mathrm{set}}) = {} & V_{\mathrm{Tset}} \times \frac{V_{\mathrm{term,calib}}(T_{\mathrm{set}} + \delta T_1)}{V_{\mathrm{Tset}}} + V_{\mathrm{Tset}} \times \ln\left(\frac{\Delta\phi_{\mathrm{cell}}^{\mathrm{detect}}(T_{\mathrm{set}} + \delta T_2)}{\Delta\phi_{\mathrm{calib}}^{\mathrm{detect}}(T_{\mathrm{set}} + \delta T_1)}\right) \\ & + V_{\mathrm{Tset}} \times \ln\left(\frac{\int A_{\mathrm{calib}}(\lambda, T_{\mathrm{set}} + \delta T_1) \cdot \phi_{\mathrm{BB}}(\lambda, T_{\mathrm{set}})}{\int A_{\mathrm{cell}}(\lambda, T_{\mathrm{set}} + \delta T_2) \cdot \phi_{\mathrm{BB}}(\lambda, T_{\mathrm{set}})}\right) \end{aligned} \tag{5.2}$$

where δT_1 and δT_2 are the temperature deviations from T_{set} of the calibration and measured samples, respectively. Hence, to quantify iV uncertainty under temperature fluctuations, the temperature coefficients of $\Delta\phi^{\mathrm{detect}}$, A (or EQE) of both measured and calibration devices, and $V_{\mathrm{term,calib}}$ must be quantified. The following sections perform this analysis for both Si and PVK solar cells.

5.4.2.1 Temperature uncertainty in Si solar cells

A planar PERC Si solar cell [16] with an area of 4 cm^2 and a thickness of 468 ± 4 µm was used for this assessment. The sample was mounted on a temperature-controlled stage (Linkam; LTS420), and thermocouples were placed in contact with the sample to accurately monitor its temperature.

The EQE and spectral EL measurements were carried out over a temperature range of 24°C to 40 °C. EL spectra were acquired using an InGaAs spectrometer (Avantes; AvaSpec-NIR256-1.7-HSC-EVO), while EQE measurements were conducted using the PV Measurements system (PV Measurements; QEX7). For the EL measurement, throughout the temperature-dependent measurements, the current injection level was kept constant at 0.45 mA/cm², while the V_{term} was monitored using the SMU (Keithley; 2461).

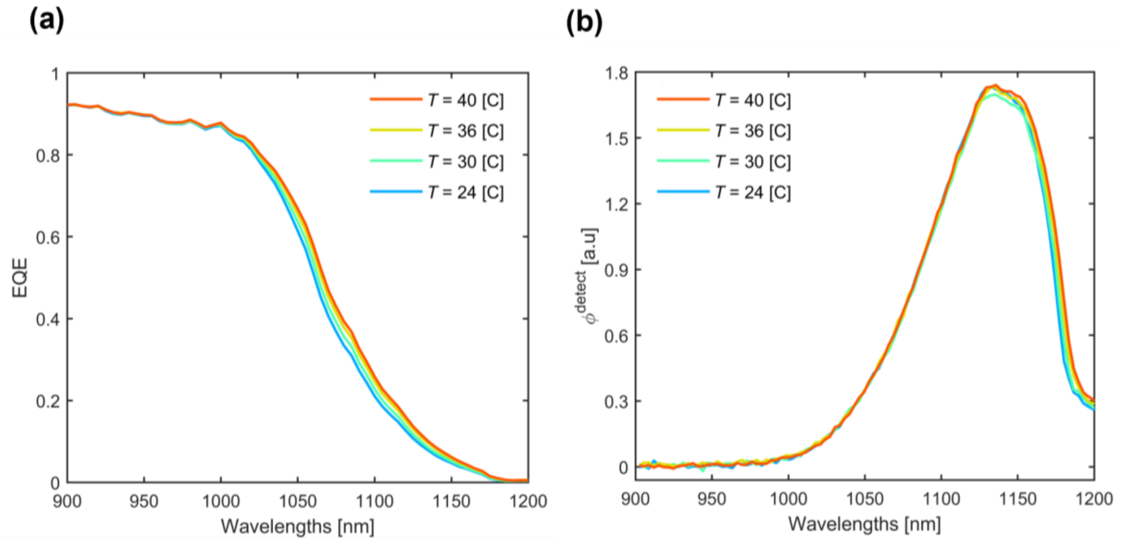

Figure 5. 11 – (a) EQE and (b) ϕ^{detect} measurements of the PERC cell at different temperatures, ranging from 24 °C to 40 °C (with a current injection of 0.45 mA/cm²).

Measurements of the EQE and ϕ^{detect} for a representative Si solar cell as a function of temperature are presented in Figure 5.11(a) and (b), respectively. Consistent with previous studies [91, 159, 160], both $\Delta\phi^{\mathrm{detect}}$ and the EQE of Si devices are nearly temperature-independent around room temperature. In contrast, the measured V_{term}, recorded during EL measurements, decreases with increasing temperature, as illustrated in Figure 5.12. A linear fit (dashed line) yields a temperature coefficient of -2.2 mV/°C for V_{term}. This value is consistent with the typical range reported for Si solar cells (between −1.5 and −2.5 mV/°C), depending on the device structure and material quality [91], and is used in the following analysis.

Hence, the logarithmic terms in Equation 5.2, which include $\Delta\phi^{\mathrm{detect}}$ and A (equivalent to the measured EQE), cancel out, resulting in a simplified form of the equation:

$$\mathrm{i}V(T_{\mathrm{set}}) = V_{\mathrm{term,calib}}(T_{\mathrm{set}} + \delta T_1) \tag{5.3}$$

The associated uncertainty in iV is given by:

$$\delta \mathrm{i}V = \delta V_{\mathrm{term,calib}} \tag{5.4}$$

where $\delta V_{\mathrm{term,calib}}$ is temperature-induced uncertainty in $V_{\mathrm{term,calib}}$, evaluated from the temperature coefficient.

Thus, temperature-related uncertainty in iV for Si solar cells stems primarily from variations in $V_{\mathrm{term,calib}}$. To minimise this, particular attention must be given to accurately monitoring the calibration cell's temperature, **a requirement that applies only once during the initial calibration step**. When the calibration is performed at a known and stable temperature, the effect of temperature variations on subsequent iV estimations for the measured samples becomes negligible. Therefore, by effectively suppressing temperature-related uncertainty, this method eliminates the need for extensive correction procedures in later measurements.

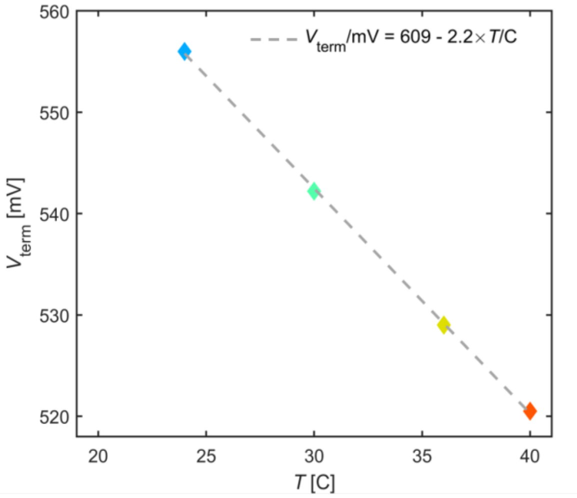

Figure 5. 12 – Measured V_{term} of the PERC cell at different temperatures, ranging from 24 °C to 40 °C (at a current injection of 0.45 mA/cm^2).

5.4.2.2 Temperature uncertainty in PVK solar cells

The analysis was performed on two distinct single-junction PVK solar cells, including:

- **PVK 1:** A device featuring an absorber with a bandgap of approximately ~1.55 eV, a composition of $FA_{0.75}MA_{0.25}PbI_{2.75}Cl_{0.20}Br_{0.05}$. The cell has an active area of 0.165 cm^2. Additional details regarding this device are currently unavailable, as they have not yet been published.
- **PVK 2:** A device featuring an absorber layer with a bandgap of ~1.65 eV, a composition of $(Cs_{0.22}FA_{0.78})_{0.95}MA_{0.05}Pb(Br_{0.15}I_{0.85})_{0.96}Cl_{0.04}$. The active area is 0.165 cm^2. This PVK device has a p-i-n configuration, where the HTL is the Poly-TPD (poly[N,N'-bis(4-butylphenyl)-N,N'-bis(phenyl)benzidine]). The ETL stack consists of C_{60} and BCP. Full details of the other layers and the fabrication process are available in Ref. [161].

The PVK cells were mounted on a temperature-controlled stage (Linkam; T95-PE), enclosed in a nitrogen environment to prevent degradation. The temperature dependency of the PL and A measurements was carried out over the temperature range of 20 to 40 °C. To ensure thermal and electronic stability, before each measurement, the sample was kept in the dark for 10 minutes to stabilise the temperature, followed by 90 s of illumination to reach steady-state conditions.

PL measurements were performed using a hyperspectral imaging system (Photon etc.; IMA™) with a laser excitation wavelength of 532 nm and an illumination intensity of approximately 0.1 sun. A 543 nm LPF was placed in the detection path to block scattered laser light reaching the camera. PL spectra were acquired using an optical microscope equipped with a 5× objective lens (NA = 0.15) and a CCD Si camera (Hamamatsu; C13440-20CU). The calibration procedure for the PL spectra is described in a recent publication [161]. Measurements were taken with an exposure time of 0.8 s. The V_{term} of the PVK cells was recorded simultaneously during each PL acquisition using an SMU (Keithley; 2401). The absorptance spectrum was determined from measurement of spectral $R_{\text{tot}}(\lambda)$ and $T_{\text{trans}}(\lambda)$, by applying Equation 2.32. These measurements were performed using a white light source (Olympus; TH4-200) and the same CCD camera.

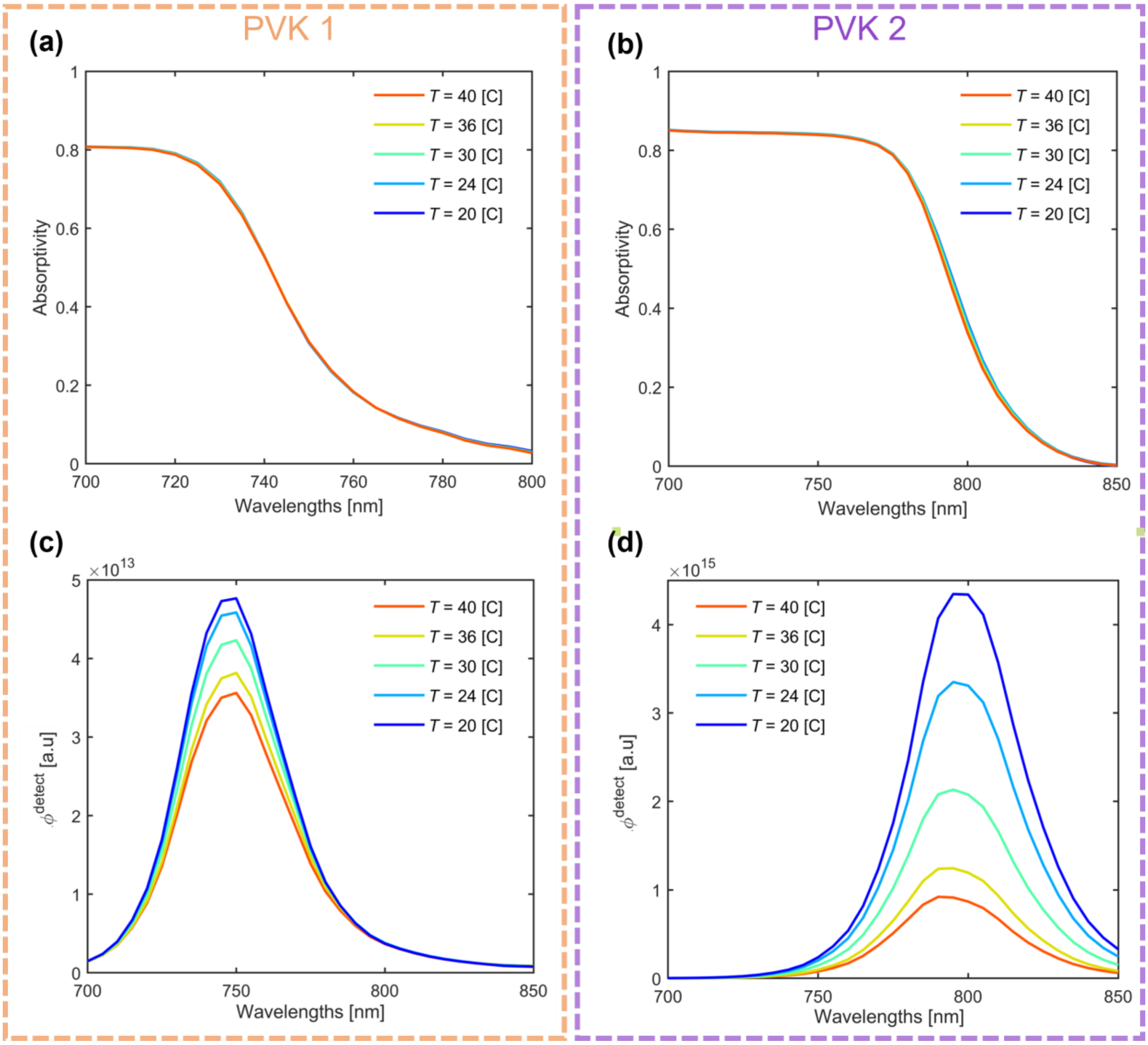

Figure 5. 13 – The measured A (a, b) and ϕ^{detect} (c, d) spectra of the PVK 1 (left) and PVK 2(right) at different temperatures, ranging from 20 °C to 40 °C.

Figure 5.13 illustrates the measured A (a, b) and the ϕ^{detect} (c, d) for PVK 1 (left column) and PVK 2 (right column) at various temperatures. The A spectra of PVK 1 and PVK 2 exhibit no significant variation across the investigated temperature range. The absorption edge remains well-defined and constant, indicating minimal temperature dependence. In contrast, ϕ^{detect} spectra exhibit a pronounced temperature dependence. The ϕ^{detect} decreases with increasing temperature, while the peak emission wavelength remains constant, approximately 750 nm for PVK 1 and 790 nm for PVK 2, consistent with a fixed absorption edge.

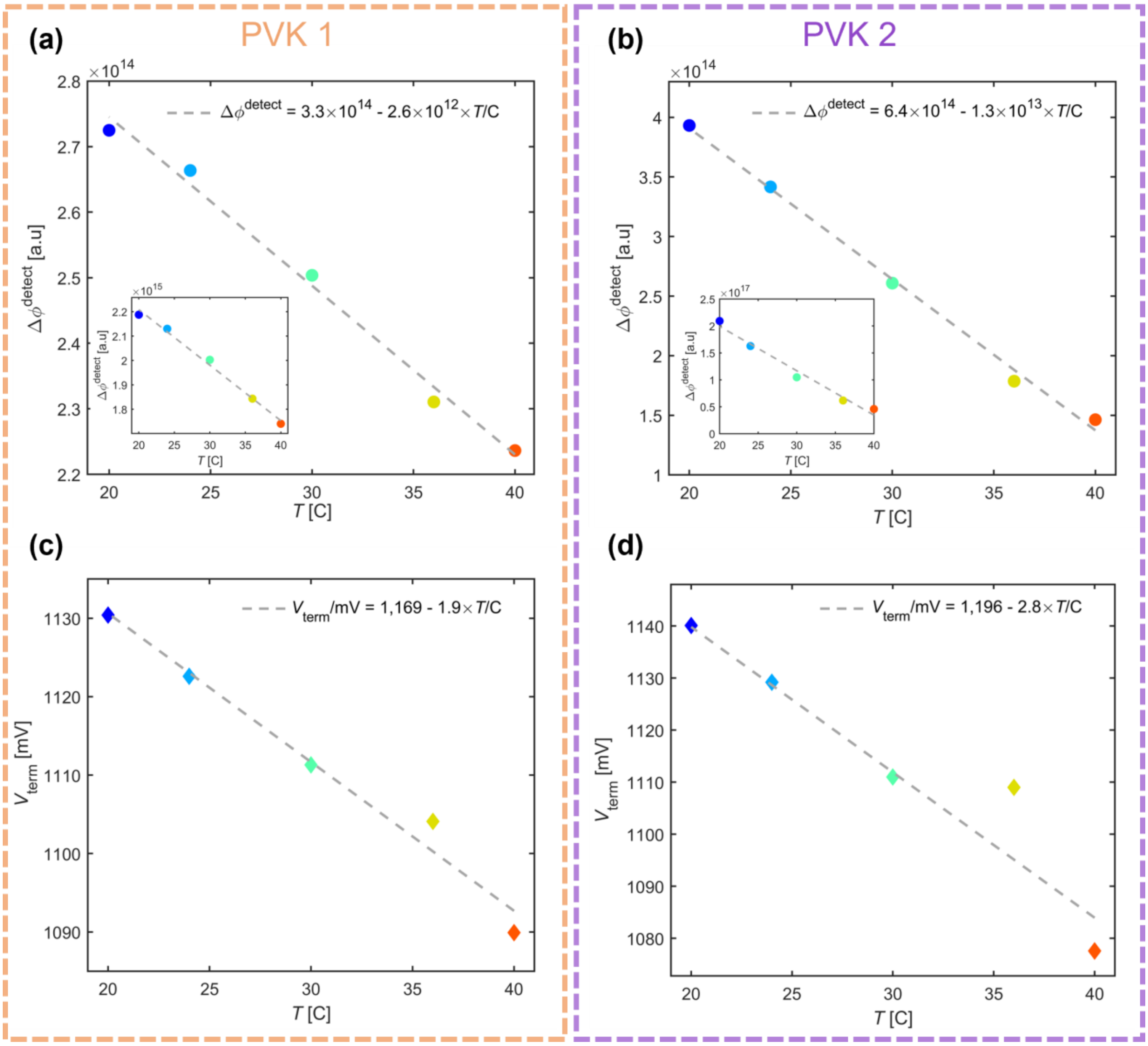

Figure 5. 14 – The temperature dependence of $\Delta\phi^{\text{detect}}$ (a, b) and V_{term} (c, d) for PVK 1 (left) and PVK 2 (right). ϕ^{detect} was integrated up to λ_2 = 730 nm; the insets (inner plots) in (a) and (b) correspond to the extended integration of ϕ^{detect} ($\Delta\phi^{\text{detect}}$) over the entire wavelength range (up to 850 nm). Dashed lines show linear fits weighted toward the room temperature.

Figures 5.14 (a) and (b) quantify these trends over the proposed BPF range for PVK-based devices, providing $\Delta\phi^{\mathrm{detect}}$ for PVK 1 and PVK 2, respectively. $\Delta\phi^{\mathrm{detect}}$ was calculated by integrating the ϕ^{detect} spectra up to λ_2 = 730 nm, while the insets show the corresponding integrals over the full spectral range for comparison. Figures 5.14 (c) and (d) present the simultaneously measured V_{term} as a function of temperature for both devices. Linear regressions (dashed lines) were fitted to quantify the relationship between temperature and each parameter, with a greater weight given to the measurement near room temperature. The resulting equations are displayed in each panel. Both $\Delta\phi^{\mathrm{detect}}$ and V_{term} decrease linearly with temperature, with PVK 2 showing higher sensitivity. Although $\Delta\phi^{\mathrm{detect}}$ is clearly temperature-dependent, its impact on iV is largely suppressed by the logarithmic term in Equation 2.17. For instance, applying the fitted relationships and Equation 2.17, a 1 °C change in temperature modifies iV by ~0.25 mV for PVK 1 and ~1.0 mV for PVK 2. Meanwhile, the temperature dependence of V_{term}, derived from the linear fits, is −1.9 mV/°C for PVK 1 and −2.8 mV/°C for PVK 2.

While these individual temperature dependencies are valuable, the total measurement uncertainty, described in Equation 5.2, arises from the coupled interaction between both $\Delta\phi^{\mathrm{detect}}$ and V_{term}. To rigorously assess this interaction and propagate the error, a Monte Carlo simulation was implemented. The simulation modelled a realistic case where the iV of the measured cell (PVK 1) is estimated using the calibration cell (PVK 2) with different optical properties. It consisted of 300,000 trials, with the temperatures of the two cells varying independently within ±1 °C of T_{set} = 24 °C. The iV error was defined as the difference between the "true" iV of PVK 1 at T_{set} and the estimated iV using Equation 5.2, accounting for the temperature dependence of $\Delta\phi_{\mathrm{calib}}^{\mathrm{detect}}$, $\Delta\phi_{\mathrm{cell}}^{\mathrm{detect}}$, and $V_{\mathrm{term,calib}}$.

Figure 5.15 shows the resulting iV error distribution. The 90% confidence interval, indicated by the red dashed lines, spans from −0.52 mV to 2.2 mV, while the maximum iV error of 2.9 mV is out of this range. Furthermore, the peak of the distribution, at 0.9 mV, represents the most probable error and aligns with the black vertical line, corresponding to the iV when both devices are at T_{set} (δT_1 and δT_2 = 0). This offset is temperature-independent and stems from differences in the optical properties of the two PVK devices within the BPF range, consistent with the findings presented in Chapter 4. Hence, to quantify the iV error arising solely from temperature fluctuations, the systematic offset (0.9 mV) must be subtracted from the total error shown in the graph. For the PVK cells in this study, a ±1 °C temperature variation yields an iV error within ±2 mV.

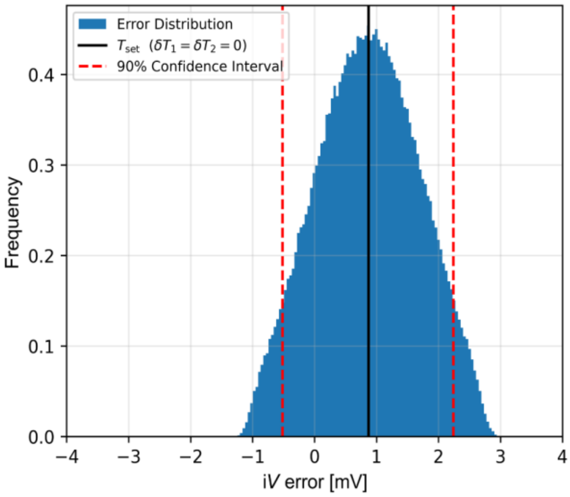

Figure 5. 15 – Distribution of i*V* error from Monte Carlo simulations, with the 90% confidence interval indicated by dashed lines. The black line shows the associated i*V* error when both devices are at T_{set} (δT_1 and δT_2=0).

5.5 Total uncertainty

The total uncertainty (δi*V*) associated with i*V* estimation via the BPF method is calculated through quadratic summation of individual major uncertainty sources:

$$\delta iV = \sqrt{\delta R_{\mathrm{F/B}}{}^2 + \delta E_{\mathrm{g}}{}^2 + \delta T_{\mathrm{temp}}{}^2} \tag{5.5}$$

where $\delta R_{\mathrm{F/B}}$, δE_{g}, and δT_{temp} correspond to uncertainties arising from front/back reflection, bandgap mismatch, and temperature variation, respectively.

In this study, total uncertainty values are reported specifically for BPFs with λ_2 of 730 nm and 1,050 nm for PVK and Si subcells, respectively, consistent with prior recommendations for BPF selection to ensure accurate i*V* estimation.

For the Si subcell, the dominant sources of uncertainty are $\delta R_{\mathrm{F/B}}$ and δT_{temp}, contributing absolute uncertainties of 7 mV and 2.2 mV, respectively, with a ±1°C deviation from the T_{set}. Applying Equation 5.5, these values correspond to the δi*V* of 7.3 mV, demonstrating the robustness of the BPF method under realistic conditions.

For the PVK subcell, modelling resulted in a maximum absolute uncertainty of 12 mV for $\delta R_{\mathrm{F/B}}$ and 3 mV for δE_{g}. The temperature-related uncertainty, δT_{temp}, was determined to be 2 mV for the examined device and assuming a ±1°C deviation from the T_{set}. It should be noted that this value is specific to the PVK sample studied; given the broad variation in composition and structure across PVK devices, users are encouraged to apply the methodology presented here to assess δT_{temp} of their own devices. Therefore, applying Equation 5.5 yields δi*V* of 12.5 mV for the PVK subcell.

5.6 Summary

This chapter evaluated the uncertainties associated with the BPF-based iV calibration method for PVK/Si tandem solar cells. Focusing on the calibration cell-based approach presented in Chapter 4, this chapter established a rigorous framework to identify, quantify, and propagate the key uncertainty sources. These sources were grouped into three categories: (a) differences between the properties of the calibration and measured subcells, (b) optical interactions within the tandem device, and (c) setup-related factors.

Each source was examined through experiments and numerical modelling. The analysis identified that the major contributors to the total error were front/back reflectance differences, bandgap mismatch (for the PVK subcell), and temperature variation, assuming a ±1 °C deviation from T_{set}. Other potential factors, such as luminescence coupling, spectral overlap, and illumination angle, were confirmed to have a negligible impact within the optimal BPF range. Accounting for all significant contributions, the maximum absolute iV uncertainty was determined to be 7.3 mV for the Si subcell and 12.5 mV for the PVK subcell, over the selected BPF ($\lambda_2 \leq 1050$ nm for Si; $\lambda_2 \leq 730$ nm for PVK).

As part of this analysis, two key methodological advancements were made. First, the potential limitation of using PVK cells for calibration, arising from the mismatch between terminal voltage and iV, was addressed by employing a spectrally matched LED as a calibration device. Second, a dedicated analytical model was developed to accurately capture the coupled impact of temperature on the estimated iV.

These findings validate the robustness and accuracy of the presented calibration method for iV estimation using suitable BPFs. They establish this method as a precise, scalable, and practical tool for high-resolution iV imaging, supporting advanced diagnostics and quality control in both single-junction and PVK/Si tandem solar cells. In addition, the method has strong potential for determining other key physical parameters. The next chapter demonstrates the application of this framework to extract n_{i} from PL measurements.

Chapter 6 – Extraction of the Intrinsic Carrier Concentration via Photoluminescence

The intrinsic carrier concentration, n_i, is a fundamental parameter that determines the electrical properties and performance of semiconductor devices [57]. In PV cells, n_i strongly influences key performance factors, including minority carrier densities, recombination rates, and overall efficiency [57]. Accurate determination of n_i is therefore essential for precise device modelling and the development of advanced materials.

While n_i has been accurately established for c-Si [57, 67], existing extraction methods often require complex experimental measurements, specific device structures, or detailed material-specific knowledge. These limitations make them less suitable for emerging semiconductors, such as PVK materials, where fundamental material properties remain uncertain.

This chapter introduces a fully contactless PL-based method for determining n_i without requiring dedicated device structures or material-specific parameters. The approach involves two key components: (a) the calibrated iV extraction method developed in this thesis, and (b) a dynamic calibration technique for quantifying the excess carrier concentration Δn from PL measurements [162]. Owing to its simplicity and independence from a device architecture, the technique is well-suited for estimating n_i in a wide range of materials, including emerging semiconductor technologies.

Section 6.1 begins with a review of conventional n_i extraction methods for c-Si materials. Section 6.2 describes the theoretical basis of the developed PL-based approach; Section 6.3 details the associated uncertainty analysis; and Section 6.4 presents the experimental validation.

This chapter is based on:
S. Zandi, Y. Zhu, A. H. T. LE, J. W. Weber, R. L. Chin, T. Trupke, Z. Hameiri, "Contactless approach for estimating intrinsic carrier concentration using luminescence," Asia Pacific Solar Research Conference, 2024.

6.1 Review of methods to determine intrinsic carrier concentration in c-Si

Decades of research have enabled scientists to accurately determine most of Si's electro-optical parameters [57, 67], including n_i [98-100, 102]. This section reviews the main experimental methods and analytical models developed to improve the accuracy of n_i estimation.

In the early 1990s**,** Sproul and Green proposed a method that fits measured I–V (J–V) data of specially fabricated Si p-n devices to an analytical model [98, 99]. To simplify the analysis, they used a PERC solar cell structure, in which the conventional rear contact was replaced with a planar aluminium layer that acted as a rectifying Schottky diode [98, 99]. In their initial study [98], n_i was determined by fitting the measured I_{sc}–V_{oc} curves at 300 K, obtained by recording I_{sc} and V_{oc} of a solar cell under varying illumination intensities. In a subsequent study [99], the same framework was extended to the temperature range 77–300 K by fitting the dark J–V curves. Using these approaches, the reported uncertainty in n_i was estimated to be less than 3% at 300 K [98, 99], increasing to approximately 17% at 77 K [99]. A critical aspect of the approach is that several material-specific parameters, including carrier mobility, dopant density, and various recombination mechanisms, must be accurately determined through independent measurements [98, 99]. Therefore, the reliability of these methods is highly sensitive to the accuracy of the material parameters and, as later shown [101], the reported n_i values did not account for BGN, leading to systematic errors.

Another technique for n_i extraction, introduced by Misiakos et al. [100], is based on low-frequency capacitance measurements performed on p-i-n or similar devices under high-injection conditions [100]. Under high injection, the diode's intrinsic region dominates the capacitance behaviour, and with appropriate semiconductor modelling, the measured data can accurately translate into an estimate of n_i. Compared to the approach of Sproul and Green [98, 99], this method is less sensitive to uncertainties in material properties and has demonstrated uncertainties below 1% [100]. However, it requires specially designed devices with very low doping and carefully controlled layer structures to meet the necessary measurement conditions. Therefore, its applicability to conventional solar cell device architectures and broader material systems is limited [100].

While these experimental methods established baseline values for n_i, analytical models have enabled more precise estimation under a broader range of measurement conditions, including varying temperatures, doping profiles, and injection regimes. Altermatt et al. demonstrated that the reported n_i values by Sproul and Green were affected by BGN, a factor initially neglected [101]. By incorporating an analytical BGN model, the corrected values from Sproul's method aligned closely with those reported by Misiakos et al. [100], resolving a long-standing discrepancy at room temperature [101]. Building on this, Couderc et al. developed an improved analytical model capable of accurately calculating n_i across a wide temperature range [102].

Although the above approaches provide accurate n_i values, particularly for c-Si, they encounter significant challenges when applied to new or emerging materials. These methods typically require specially designed device structures, controlled measurement conditions, and detailed knowledge of sample properties. For materials like PVK, this is particularly challenging as there is considerable uncertainty in determining their fundamental material parameters.

The following section introduces a novel method developed in this thesis for extracting n_i from PL measurements.

6.2 Methodology

As mentioned in Chapter 2, n_i is related to iV and Δn by [58]:

$$n_\mathrm{i} = \sqrt{\Delta n(\Delta n + N_\mathrm{dop})} \times \exp\left[-\frac{\mathrm{i}V}{2V_\mathrm{T}}\right] \tag{6.1}$$

Various calibration methods have been developed to extract Δn and N_dop from PL measurements [162-164]. Among them, a recently proposed dynamic calibration method [162] has been shown to be more robust to measurement noise and does not require prior knowledge of the doping concentration. When needed, it can also estimate N_dop directly [162]. Together with the method developed in this thesis, contactless extraction of n_i is enabled without requiring special structures or knowledge about the material properties. This is particularly relevant for non-Si materials like PVK.

Since PVKs (and many other emerging materials) are used in their intrinsic or undoped form for PV applications [165], Equation 6.1 can be simplified by assuming $N_\mathrm{dop} << \Delta n$:

$$n_\mathrm{i} = \Delta n \times \exp\left[-\frac{\mathrm{i}V}{2V_\mathrm{T}}\right] \tag{6.2}$$

Hence, reliable estimation of n_i requires accurate determination of both Δn and iV. The adopted method for extracting these parameters is described in the following sections.

6.2.1 Implied voltage determination

The iV extraction can be performed by applying the method proposed in this thesis using PL measurements. Based on the findings in the previous chapters and the identification of a suitable BPF, the iV of any measured sample, regardless of its optical properties, can be accurately quantified by applying Equation 2.27.

6.2.2 Excess carrier concentration determination

The determination of Δn can be carried out by comparing QSS and non-QSS (Non-quasi-steady-state) measurements [162]. The PL signal depends on Δn through a quadratic function [163]:

$$\Delta\phi^{\mathrm{detect}} = A_{\mathrm{i}} \times B_{\mathrm{rad}} \times (\Delta n + N_{\mathrm{dop}}) \times \Delta n \qquad (6.3)$$

where A_{i} is a calibration constant, and B_{rad} is the radiative recombination coefficient [166, 167]. Although related, A_{i} is different from f_1 and f_2 (see Equation 2.15 in Chapter 2).

Assuming a homogeneous carrier concentration across the depth of the sample, Δn can be obtained as a function of time, t, from the continuity equation [168]:

$$\frac{d\Delta n}{dt} = G(t) - \frac{\Delta n}{\tau(\Delta n)} \qquad (6.4)$$

Rearranging the above yields a direct expression for $\tau(\Delta n)$:

$$\tau(\Delta n) = \frac{\Delta n}{G(t) - \frac{d\Delta n}{dt}} \qquad (6.5)$$

For monochromatic illumination the generation rate, G, can be calculated from the absorptivity A, and the sample's thickness d [65, 163, 169]:

$$G(t) = \phi_{\mathrm{inc}}(t) \times A/d \qquad (6.6)$$

where ϕ_{inc} is the photon flux incident in the sample plane.

Under QSS condition, the excitation light changes slowly; hence $G >> \mathrm{d}\Delta n/\mathrm{d}t$ and $\tau \approx \frac{\Delta n}{G}$. Assuming an identical τ under QSS and non-QSS conditions (using Equation 6.5 for the non-QSS lifetime) at a specific injection level, Δn^*,the following can be obtained for the measured device:

$$\frac{d\Delta n_{\mathrm{Non-QSS}}}{dt} = G_{\mathrm{non-QSS}}(\Delta n^*) - G_{\mathrm{QSS}}(\Delta n^*) \qquad (6.7)$$

Where $G_{\mathrm{non-QSS}}$ and G_{QSS} are the generation rate at the non-QSS and QSS measurement conditions, respectively.

Since $\Delta\phi^{\mathrm{detect}}$ is directly related to Δn through a quadratic relationship (Equation 6.3), Δn^* in Equation 6.7 can be replaced with the PL signal of the measured device at that specific injection level, $\Delta\phi_{\mathrm{cell}}^{\mathrm{detect},*}$. This substitution allows for the direct experimental determination of Δn without requiring prior knowledge of material-specific parameters such as the radiative recombination coefficient [162].

$$\frac{d\Delta n_{\text{non-QSS}}}{dt} = G_{\text{non-QSS}}\left(\Delta\phi_{\text{cell}}^{\text{detect},*}\right) - G_{\text{QSS}}\left(\Delta\phi_{\text{cell}}^{\text{detect},*}\right) \tag{6.8}$$

By integrating this relationship, $\Delta n_{\text{non-QSS}}$ can be determined at any particular time:

$$\Delta n_{\text{non-QSS}}(t_0) = \Delta n_{\text{non-QSS}}(t_{\text{end}}) - \int_{t_0}^{t_{\text{end}}} \frac{d\Delta n_{\text{non-QSS}}}{dt}\,dt \tag{6.9}$$

Once both Δn and iV are determined, n_{i} can be extracted using Equation 6.2. However, the accuracy of this extraction depends on the accuracy of each measured parameter, as uncertainties in Δn and iV can propagate and affect the calculated n_{i} value. Therefore, a comprehensive uncertainty analysis is presented in the following section to quantify potential errors and assess the reliability of the proposed method.

6.3 Uncertainty – simulation and analysis

A comprehensive simulation analysis was conducted to evaluate the propagation of uncertainties from the input parameters to the calculated n_{i}, using the framework outlined in Ref [162].

1. First, the 'ground truth' values were chosen, and then uncertainties in the input parameters were introduced to quantify the resulting uncertainties in n_{i}. Table 6.1 summarises the input parameters. These inputs are primarily divided into two groups:
    a. Sample properties include E_{g}, d, A, T, N_{dop}, and τ. It also includes the 'ground true' n_{i}, calculated according to Ref. [102] at a temperature of 23 °C.
    b. System parameters consist of the photon flux of the excitation light source under QSS ($\phi_{\text{inc,QSS}}$) and non-QSS ($\phi_{\text{inc,non-QSS}}$) conditions, as well as $\Delta\phi_{\text{calib}}^{\text{detect}}$ and $V_{\text{term,calib}}$ from the calibration cell. It should be noted that to model the excitation photon flux under non-QSS conditions, an exponential decay function with a peak flux ($\phi_{\text{inc,peak}}$) was assumed.
2. Knowing $\phi_{\text{inc,QSS}}$, $\phi_{\text{inc,non-QSS}}$, A, and d, the associated generation rates, $G_{\text{QSS}}(t)$ and $G_{\text{non-QSS}}(t)$, were calculated using Equation 6.6.
3. Then, the corresponding $\Delta\phi_{\text{cell}}^{\text{detect}}$ and Δn of the measured cell were derived using Equations 6.3 and 6.4, assuming $A_{\text{i}} = 10^{20}$ [162], B_{rad} from Ref. [167], and an injection-dependent τ (see Table 6.1).
4. The associated iV of the sample was determined by applying Equation 6.1.
5. Finally, using $V_{\text{term,calib}}$ and Equations 2.27, $\Delta\phi_{\text{calib}}^{\text{detect}}$ was obtained, assuming a calibration cell with identical optical properties as the measured cell.

Table 6.1 – Input parameters used in the modelling.

Parameter	Description	Value, Si
n_i [cm^{-3}]	Intrinsic carrier concentration	7.0012×10^9 [102]
E_g [eV]	Bandgap	1.125 [170]
d [µm]	Thickness	180 ± 7.20
A	Absorptivity at laser excitation wavelength	0.8 ± 0.03
T [C]	Temperature	23 ± 1
τ [ms]	Lifetime	$\tau(\Delta n) = \frac{\Delta n}{\Delta n(\Delta n + N_{\text{dop}})} \cdot \tau_{\text{a}} + \tau_{\text{b}}$* [162]
B_{rad} [cm^{3}s^{-1}]	Radiative recombination coefficient	5.234×10^{-15} [167]
N_{dop} [cm^{-3}]	Bulk doping concentration	1×10^{13}
$\phi_{\text{inc,peak}}$[cm^{-2}s^{-1}]	Maximum photon flux of the incident light	$(2 \pm 0.08) \times 10^{19}$
t_G [ms]	Illumination duration	0.1
$V_{\text{term,calib}}$ [mV]	Terminal voltage of the calibration cell	700 ± 2

*$\tau_{\text{a}} = 0.1$ [ms] $\tau_{\text{b}} = 0.2$ [ms]

Once the ground truth values for iV and Δn were established, the methodology shown in Figure 6.1 was followed to evaluate the associated uncertainty. Various sources of uncertainty were considered. The primary uncertainty in Δn arises from uncertainties in the generation rate, which is influenced by uncertainties in d, A, and the calibration of ϕ_{inc} [162]. Here, a 4% uncertainty in each of these parameters was assumed, based on previous experimental observations (mainly due to typical calibration tolerances, and repeatability issues).

The uncertainty in iV primarily stems from the uncertainty in the device temperature, differences in optical properties between the measured and calibration cells, and the temperature dependence of these properties. As demonstrated in Chapter 3, using a BPF for iV determination of Si samples (wafers and cells) reduces the iV error to below ±5 mV. Propagating this maximum deviation yields a corresponding relative uncertainty of ±20% in $\Delta\phi_{\text{calib}}^{\text{detect}}$. Furthermore, ±1 °C relative to T_{set} was considered as an uncertainty in the sample temperature, consistent with practical observations. It is noted that, although temperature variation can affect A at longer wavelengths, Δn calculations use A at the laser excitation wavelength (808 nm), which can be assumed to be temperature-independent [159, 171, 172].

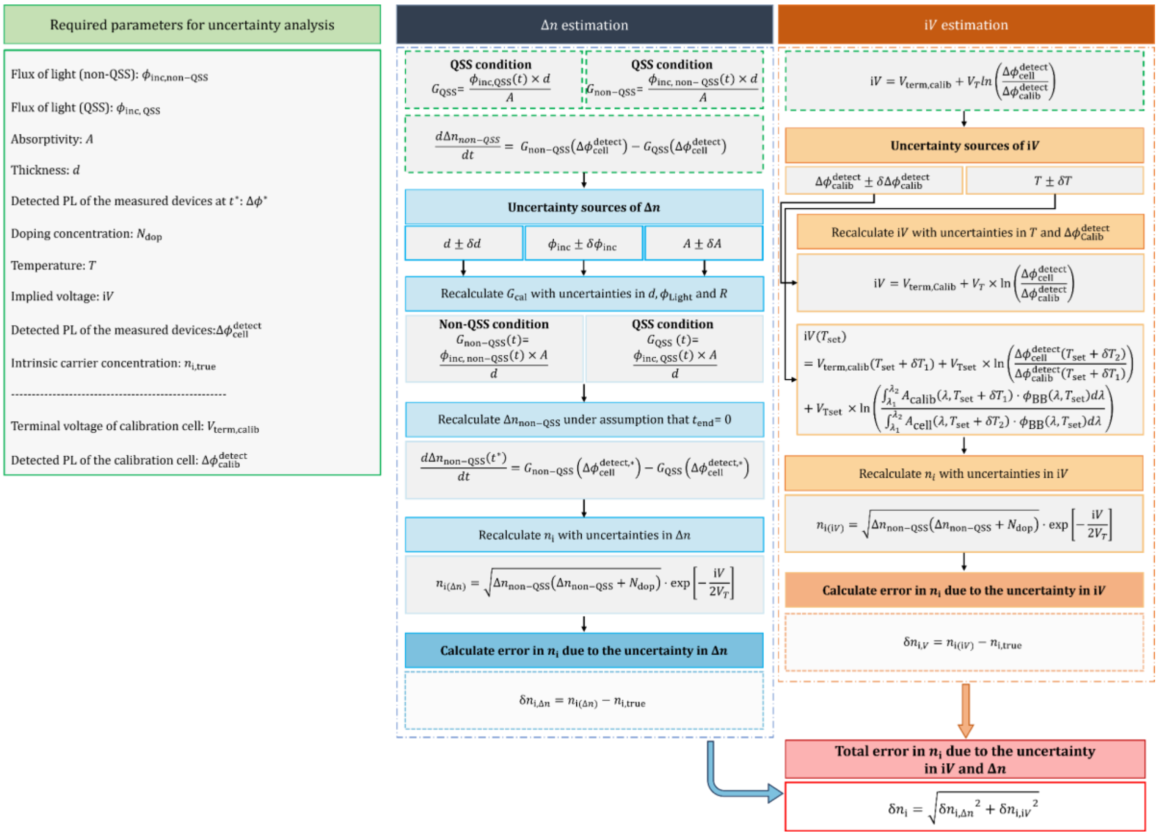

Figure 6. 1 – Flowchart of the uncertainty analysis.

6.3.1 Uncertainty in n_{i} from excess carrier determination

According to Equation 6.2, Δn and n_{i} have a linear relationship. Thus, any uncertainty in the determination of Δn is directly transferred to the uncertainty in n_{i}. The uncertainty in Δn primarily arises from the estimation of the generation rate. Figure 6.2 presents a 3D map illustrating the absolute uncertainty in n_{i} resulting from ±4% variations in d, A, and ϕ_{inc}, viewed from the front (a) and rear (b) perspectives. As discussed, variations of up to 4% represent the upper limit based on previous experimental observations across multiple measurements.

The maximum uncertainty, around 12.3%, appears at two diagonally opposite corners of the surface, labelled as ROIs 1 and 2. Since G is directly proportional to both A and ϕ_{inc} and inversely proportional to d, these ROIs represent the extreme cases of their impact. For instance, in ROI 1, d is overestimated while A and ϕ_{inc} are underestimated, leading to a significant overestimation of Δn and, consequently, a substantial uncertainty in n_{i}. Due to the symmetric nature of this relationship, a similar magnitude of uncertainty appears in ROI 2. In the intermediate regions, opposing variations in d, A, and ϕ_{inc} often partially compensate each other, maintaining G near its ground truth value and thereby minimising the resulting uncertainty in n_{i}.

Figure 6.2 provides a representative sensitivity analysis, mapping the impact of variations in Δn-related parameters onto the resulting n_i estimation (assuming input variations of up to ±4%). However, in this study, those variations were significantly reduced through repeated measurements and using well-calibrated instruments. For the measured Si HJT sample, the uncertainty in d was limited to approximately 2.8% (±5 μm), in A to about 1.3% (±0.01), and in ϕ_inc to about ±4%. Thus, the uncertainty in n_i arising from Δn is expected to be limited to 8.0% for this sample.

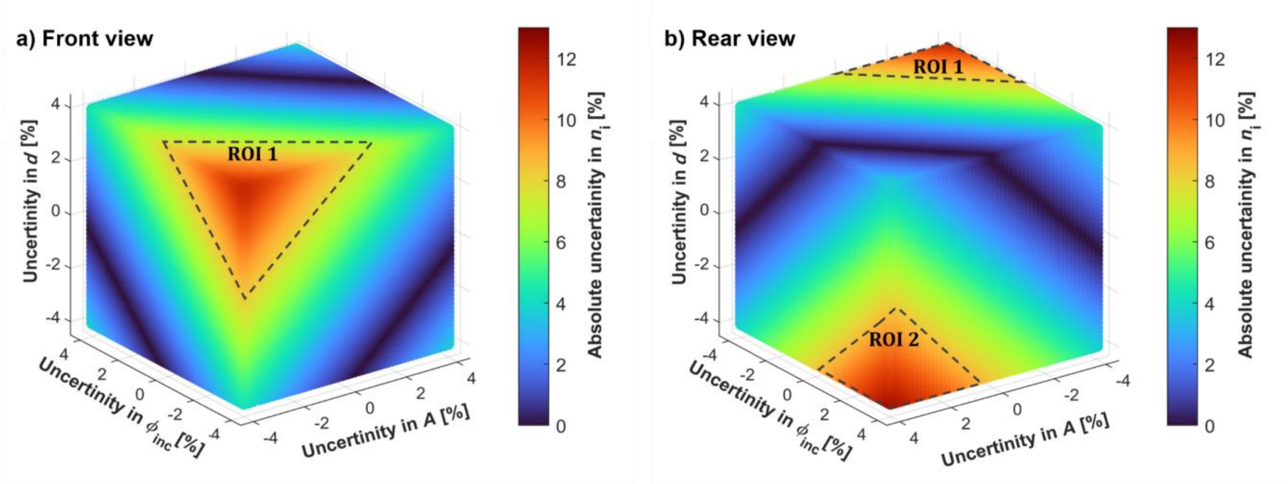

Figure 6. 2 – Absolute uncertainty in n_i due to ±4% variations in d, A, and ϕ_inc: (a) front view, and (b) rear view. ROI 1 and ROI 2 indicate areas with the maximum uncertainties.

6.3.2 Uncertainty in n_i from implied voltage determination

Since n_i is exponentially related to iV (Equation 6.2), uncertainties in iV are expected to have a significant impact on the determination of n_i. For instance, as shown in Figure 6.3(a), at room temperature, a ±0.3% (~±2 mV) uncertainty in iV results in an approximate ±4% uncertainty in n_i.

As described in previous chapters, the uncertainty in iV itself arises from two primary sources: optical mismatches between the calibration and measured cells, and deviations between the set and actual sample temperatures. While the contribution of optical mismatch, reflected in the ±20% uncertainty in $\Delta\phi_\mathrm{calib}^\mathrm{detect}$ [173], is relatively straightforward to quantify, the impact of temperature variation, assumed to be within ±1 °C based on experimental observations, requires further detailed analysis.

To evaluate the temperature-related uncertainty in iV, the same approach described in Chapter 5, Section 5.4.2, was adopted. As demonstrated there, the temperature-induced uncertainty in iV for Si solar cells is dominated by the uncertainty in $V_\mathrm{term,calib}$, which depends on the temperature coefficient of the calibration cell. Consistent with that analysis, a representative value of −2 mV/K is assumed below.

Figure 6.3(b) presents a 2D colourmap illustrating the absolute uncertainty in n_i resulting from a ±20% variation in $\Delta\phi_\mathrm{calib}^\mathrm{detect}$ and ±1 °C deviation between the actual temperature and T_set. A maximum deviation of 14.2% occurs when both parameters are simultaneously overestimated or underestimated.

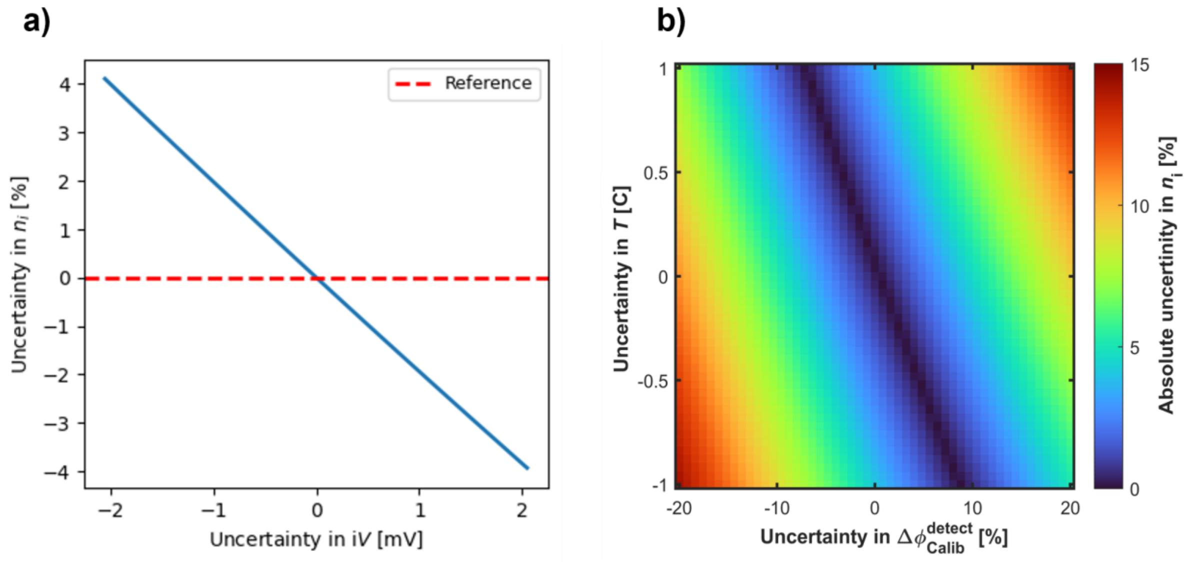

Figure 6. 3 – a) Absolute uncertainty in n_i as a function of uncertainty in iV at room temperature (solid line). The dashed line represents the reference n_i assuming zero uncertainty. (b) Absolute uncertainty in n_i resulting from ±20% variation in $\Delta\phi_\mathrm{calib}^\mathrm{detect}$ and ±1°C variation in T.

6.3.3 Total uncertainty

The total uncertainty in n_i (δn_i) is determined by propagating the uncertainties from the calculated Δn and iV:

$$\delta n_\mathrm{i} = \sqrt{\delta {n_{\mathrm{i},\Delta n}}^2 + \delta {n_{\mathrm{i},V}}^2} \tag{6.10}$$

where $\delta n_{\mathrm{i},\Delta n}$ and $\delta n_{\mathrm{i,i}V}$ represent the uncertainties in n_i contributed by the uncertainties in Δn and iV, respectively.

As detailed in previous sections for the typical Si sample in the modelling, the maximum uncertainty contributions from Δn and iV were found to be approximately 12.3% and 14.2%, respectively. Adding these values in quadrature using Equation 6.10 yields a maximum total uncertainty in n_i (δn_i) of approximately 18.8%.

6.4 Experimental validation

To support the proposed method, this section presents experimental validation of n_i extraction in crystalline Si-based materials.

6.4.1 Samples and setup

Initial validation experiments were conducted on a textured Si HJT solar cell, fabricated from high-resistivity wafers (≥ 1,000 Ω·cm) [174]. The device had a thickness of 180 ± 5 µm and an $A = 0.92 \pm 0.01$ at the laser excitation wavelength of 808 nm. The iV calibration was achieved using simultaneous V_{term} and PL measurements of a textured PERC cell with a thickness of 460 ± 4 µm [16].

Figure 6.4 shows the schematic of the experimental setup for these measurements. The setup included a uniform laser source with an illumination area of 5×5 cm^2. For QSS measurements, the laser was modulated using a sinusoidal wave (shifted to positive values) at a low frequency of 1 Hz. This low frequency provides a gradual change in light intensity, ensuring valid QSS conditions. In contrast, non-QSS measurements were conducted using square pulse illumination, where the step-down region of the pulse was used for the analysis. For both modulation types, the peak intensity was set to 3.70 suns.

The laser intensity, ϕ_{inc}, was measured using a reference Si photodiode (PD-1), while an InGaAs photodiode (PD-2) collected the resulting luminescence signal of the measured ($\Delta\phi_{\text{cell}}^{\text{detect}}$) and calibration ($\Delta\phi_{\text{calib}}^{\text{detect}}$) devices. Both collected signals, from PD-1 and PD-2, were then amplified by separate transimpedance preamplifiers (AMPs) before being recorded simultaneously by a DAC, along with V_{term} when relevant.

The photon flux of the laser (ϕ_{inc}) was calibrated using a reference Si HJT solar cell. This reference cell, which is distinct from the high-resistivity Si HJT cell used for the n_i measurement, has an active area of 1.21 cm^2 and a known EQE. The cell was placed in the sample position, and its I_{sc} was measured with a multimeter (Keysight; 34461A) at various illumination intensities. To ensure an accurate I_{sc} measurement, a reverse bias of -2 V was applied to the cell. This approach counteracts the internal voltage drop caused by the inherent R_s of the cell, which is most significant at high current injection. The ϕ_{inc} was then calculated via:

$$\phi_{\text{inc}} = \frac{I_{sc}}{q \times A} \times \text{EQE} \tag{6.11}$$

The PL emission was focused onto the PD-2 through a lens, with LPF and a suitable BPF (λ_2 = 1,050 nm), as listed in Table 6.2, to block the excitation light and minimise the effect of optical properties on the voltage calibration process, respectively. While this narrow BPF improves measurement accuracy, it also significantly reduces the collected PL signal. To maintain a high SNR, the PL signal amplifier, AMP-2 (Femto; DHPCA-100), was set to a high gain of 10^8 V/A (1.66 μs rise time). However, operating at such a high gain requires validation, as the amplifier's response time could potentially distort the rapid signal decay in non-QSS measurements. Therefore, a control measurement was performed at a lower, faster gain of 10^7 V/A (0.2 μs rise time). This test yielded an identical PL decay curve, confirming that the recorded PL signal at 10^8 V/A is attributable to the sample and not limited by the amplifier's performance.

The sample temperature was maintained at a setpoint of 23 °C using a custom-built Peltier stage. The stage was made from copper, and the temperature was regulated using a Pt-1000 Class B resistive sensor, compliant with the IEC 751 standard. This sensor has a calibrated uncertainty of ±0.42 °C at 23 °C, while the controller provides a temperature stability of ±0.03 °C. Over the measurement, the solar cell was held in place by vacuum to ensure good thermal and electrical contact. Additionally, a K-type thermocouple was attached to the sample's front surface to further monitor temperature fluctuation during laser illumination. Therefore, accounting for all sources of variation, including measurement uncertainty and laser-induced heating, the sample temperature was maintained within ±1 °C of the setpoint (T_{set} = 23 °C) during experiments.

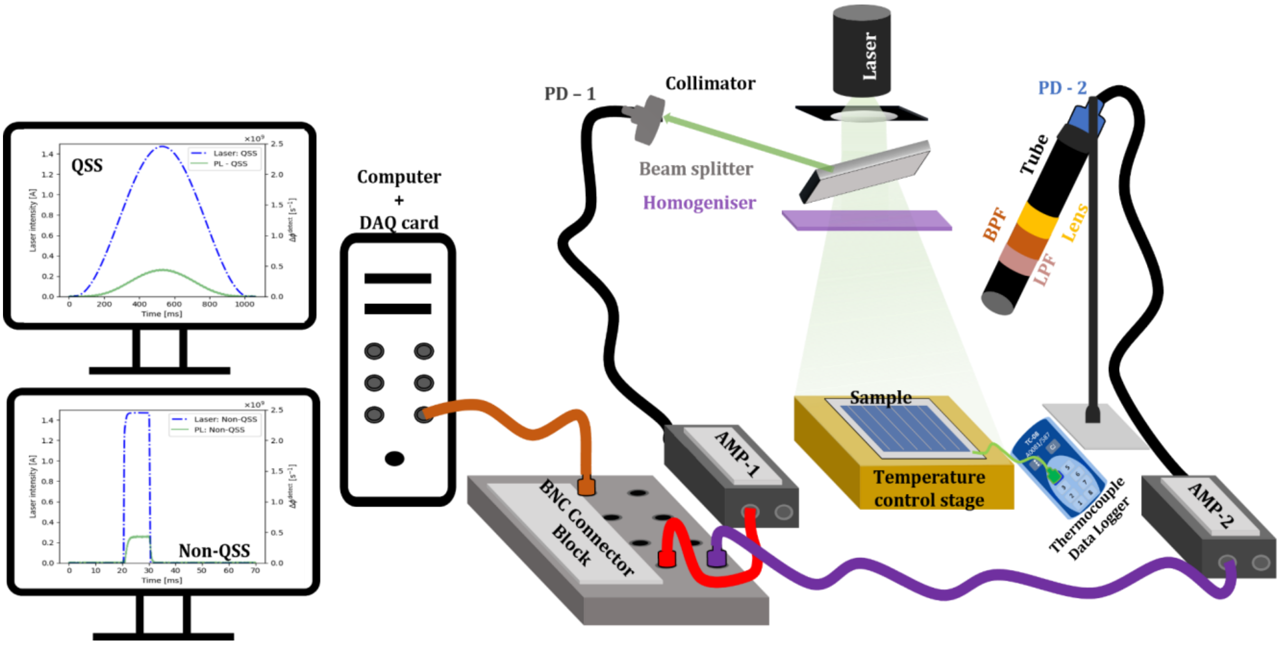

Figure 6. 4 – Experimental setup, see text for details.

Table 6.2 – Measurement parameters.

Parameter	Si Measurements
Laser excitation [nm]	808
QSS	Sinusoidal modulation (1 s)
Non-QSS	Square modulation (0.01 s)
T_{set} [°C]	23
PD1 and PD2	InGaAs and Si
LPF [nm]	850
BPF [nm]	950 – 1,050

6.4.2 Results and discussion

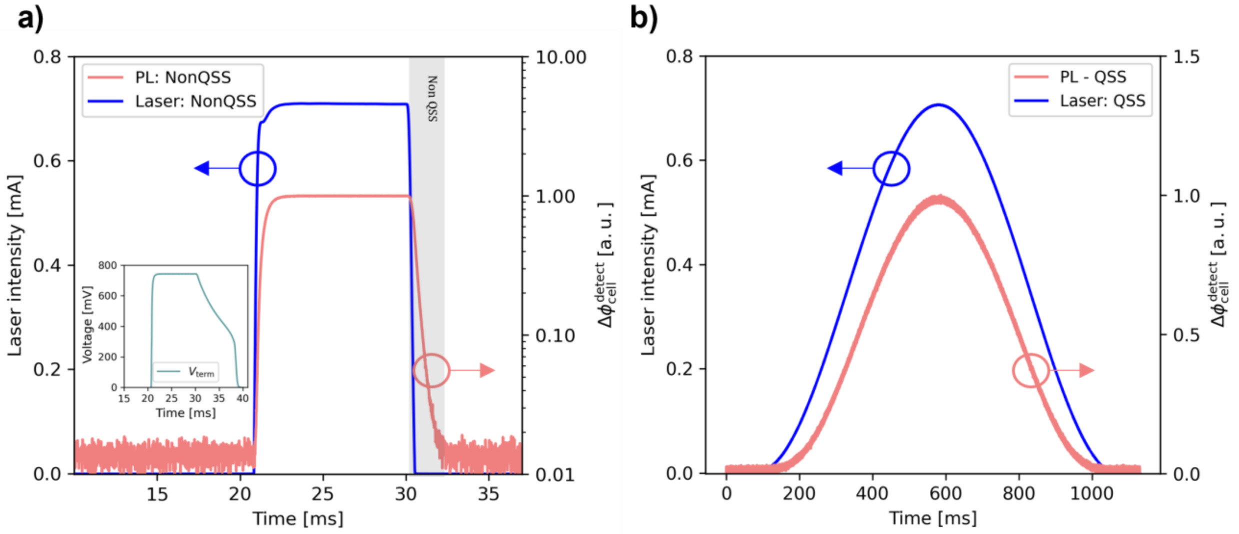

Figure 6. 5 – Measurement of the Si HJT cell under (a) non-QSS and (b) QSS conditions. In the non-QSS case, the analysis is based exclusively on the sharp step-down region (highlighted in grey). In contrast, QSS conditions are established through slow modulation of the excitation. The blue and red curves represent the laser intensity and $\Delta\phi_{\text{cell}}^{\text{detect}}$, respectively, while the inset in (a) shows the measured V_{term}. All the signals, $\Delta\phi_{\text{cell}}^{\text{detect}}$, laser intensity, and V_{term} were recorded simultaneously.

Figure 6.5 shows the raw measurement data for the high resistivity Si HJT cell under (a) non-QSS and (b) QSS conditions. In both cases, the laser intensity, $\Delta\phi_{\text{cell}}^{\text{detect}}$, and V_{term} [shown in the inset of panel (a)], were measured simultaneously. For the non-QSS condition, the sharp step-down region (shaded in grey), corresponding to a purely transient regime**,** was used for analysis. In contrast, QSS conditions were obtained by gradually modulating the laser intensity, as shown in Figure 6.5(b).

Figure 6.6(a) presents the implied voltage iV extracted from the luminescence signal $\Delta\phi_{\text{cell}}^{\text{detect}}$ by applying Equation 2.27, along with the measured V_{term} of the Si HJT cell over time under non-QSS conditions. As detailed earlier for the iV estimation, the planar PERC cell was used as a calibration cell.

Overall, very good agreement is observed. At higher voltages, the discrepancy between iV and V_{term} increases slightly, reaching up to 4 mV, compared to approximately 2 mV at lower voltages. Nevertheless, across the entire voltage range, the median deviation is approximately 2.45 mV. This difference falls within the expected uncertainty range of the method for the BPF with λ_2 = 1,050 nm (see Chapter 3).

As previously discussed, $\Delta n_{\text{non-QSS}}$ can then be obtained over time using Equation 6.10. Figure 6.6(b) shows the extracted $\Delta n_{\text{non-QSS}}$ as a function of time under non-QSS conditions.

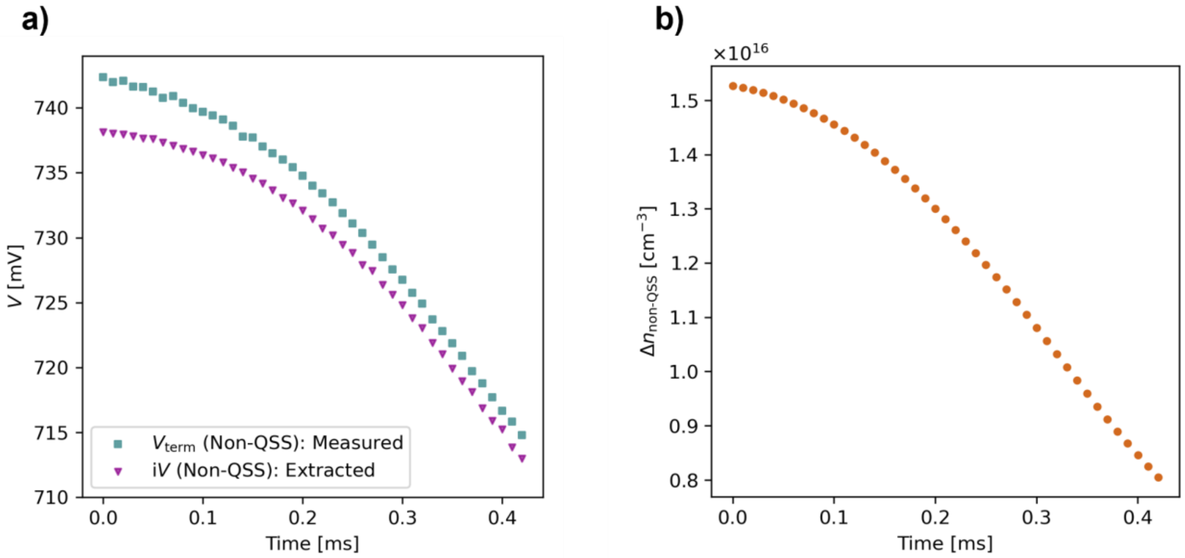

Figure 6. 6 – (a) Comparison between the measured V_{term} and the extracted iV from the $\Delta\phi_{\text{cell}}^{\text{detect}}$ as a function of time under non-QSS conditions. (b) The extracted $\Delta n_{\text{non-QSS}}$ as a function of time under non-QSS conditions.

Since both iV and $\Delta n_{\text{non-QSS}}$ were extracted simultaneously from the PL signal, they can be plotted as a function of each other, as shown in Figure 6.7(a). From this curve and applying Equation 6.1, n_{i} can be determined from any (iV, $\Delta n_{\text{non-QSS}}$) point. Figure 6.7(b) presents the extracted n_{i} at various $\Delta n_{\text{non-QSS}}$, ranging from 0.8 × 10^{16} to 1.5 × 10^{16} cm^{-3}. The horizontal lines denote the corresponding $\Delta n_{\text{non-QSS}}$ bin widths used in the analysis, while the error bars indicate the uncertainty in the n_{i} values. The associated uncertainty was calculated by propagating contributions from both $\Delta n_{\text{non-QSS}}$ and iV determinations, following the analysis presented in the section above. For the Si HJT cell**,** uncertainties of ±2.78% in d, ±1.25% in A, and ±4% in ϕ_{inc} were considered for $\Delta n_{\text{non-QSS}}$, while ±10% in $\Delta\phi_{\text{calib}}^{\text{detect}}$ and ±1 °C in T were included for iV. Accounting for these uncertainties leads to an overall uncertainty of ±12.1% in the estimated n_{i}, which is lower than the uncertainty previously estimated for typical Si samples assumed in the modelling.

The discrepancy between n_i values derived from V_{term} and iV is a direct consequence of the observed offset between these two voltages, as shown in Figure 6.6(a). However, the cause of the slight upward trend in both curves is not yet fully understood. Although this behaviour could be attributed to an underestimation of $\Delta n_{non\text{-}QSS}$ at low injection levels, the underlying cause for this observation remains unclear and requires further investigation. A detailed analysis of this effect is considered a topic for future work, as it lies beyond the timeline of this thesis.

Figure 6.7(b) also compares the extracted values with reference n_i values obtained from the literature [175, 176]. The reference n_i (orange dashed line) accounts for BGN and Fermi-level degeneracy, and was calculated for the extracted $\Delta n_{non\text{-}QSS}$ values at a fixed $N_{dop} = 4 \times 10^{12}$ cm^{-3} and T_{set} = 23 °C. The calculation was performed using the PV Lighthouse online tool [177], which implements the carrier statistics models presented in the literature [175, 176]. The shaded region indicates the uncertainty in the reference n_i, calculated by propagating the uncertainty in the extracted $\Delta n_{non\text{-}QSS}$ for this Si HJT cell and a ±1 °C deviation from T_{set}.

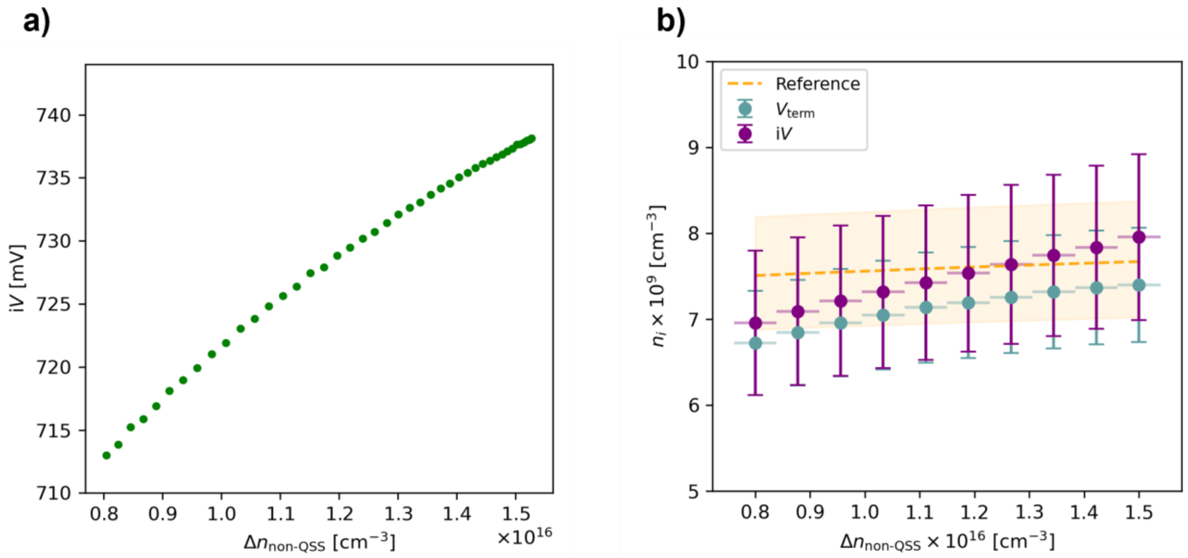

Figure 6. 7 – (a) Extracted iV as a function of the extracted $\Delta n_{non\text{-}QSS}$ under non-QSS conditions. (b) Comparison of n_i values from the literature (dashed line) with those determined using the developed method as a function of $\Delta n_{non\text{-}QSS}$. Error bars and shaded region reflect the associated uncertainty in n_i and horizontal line segments represent the Δn bin width.

The extracted n_i, derived from the estimated iV, remains within 7.3% of the reference value across the entire injection range. This deviation is lower than the modelled uncertainty of ±12.1% for the Si HJT cell. The modelled uncertainty reflects the case in which the maximum expected uncertainties in both iV and Δn occur simultaneously (as described in Equation 6.10). However, the smaller deviation observed in the measurement (7.3%) suggests that the individual measurement uncertainties in iV and Δn have partially compensated for one another, reducing the overall impact on the extracted ni.

While this level of deviation may be considered relatively high for c-Si, it remains well within acceptable limits for emerging materials such as PVKs, where fundamental parameter uncertainties are typically much larger.

6.5 Summary

This chapter demonstrated a novel, fully contactless method for determining n_i using PL measurements. The technique builds on the established framework for iV extraction developed earlier in this thesis and incorporates a dynamic calibration approach for determining Δn, enabling accurate estimation of n_i. Importantly, the method eliminates the need for complex device structures or prior knowledge of material-specific parameters, making it suitable for emerging semiconductor materials where conventional methods are hindered by limited physical parameter information.

A comprehensive uncertainty analysis was conducted to account for various contributing factors affecting the accuracy of n_i, arising from uncertainties in the extracted iV and Δn. Modelling results estimated the maximum uncertainty in extracted n_i for typical Si samples (wafers or solar cells) to be below 19%. Experimental validation on a Si solar cell, which showed a deviation of 7.3% from the theoretical reference value, is significantly lower than the predicted maximum from modelling. This improved result is attributed to well-controlled measurement conditions and the potential partial compensation between the individual uncertainties associated with iV and Δn. These results confirm the overall accuracy of the extraction method.

By leveraging PL imaging and streamlined calibration techniques, the developed method offers a powerful, non-destructive, and structure-independent pathway for quantifying n_i. Although demonstrated here on c-Si, the method's adaptability supports its extension to other material systems, including PVK. By providing a simple and broadly applicable platform for extracting n_i, the approach can facilitate improved precision in device modelling, particularly in carrier lifetime analysis, recombination dynamics, and charge transport simulations. This advancement supports the development of high-quality PV materials and enables more reliable predictions of solar cell performance.

Chapter 7 – Summary

The objective of this thesis was to develop novel luminescence-based characterisation methods, with an emphasis on the accurate determination of spatially resolved iV in Si and PVK/Si tandem solar cells. Existing calibration approaches typically rely on sample-specific calibration or detailed knowledge of the optical properties of both the device and the detection system, limiting their practicality for rapid diagnostics and broad industrial implementation.

In **Chapter 3**, the foundation for this thesis was established by introducing a calibration method for iV imaging in Si solar cells and wafers. A comprehensive modelling framework was developed to quantify the impact of variations in optical parameters on the luminescence signal. The analysis showed that restricting detection to short-wavelength emission by using an appropriately selected BPF minimises luminescence sensitivity to optical variations. The properties of the optimal BPF were determined through simulation and validated with experiments on various Si solar cells and wafer types. Accurate iV imaging of Si wafers and cells with diverse optical properties was achieved using a single calibration cell.

Building on this foundation, **Chapter 4** extended the BPF-based calibration to monolithic two-terminal PVK/Si tandem cells. The modelling in this chapter demonstrated that the luminescence signal is insensitive to variations in optical properties when selecting appropriate BPFs for each subcell. This enabled accurate spatially resolved iV mapping and pseudo-dark J–iV curves of each subcell through a single calibration process. The findings were subsequently validated experimentally on multiple PVK/Si tandem configurations. Due to its robustness and optical independence, the method provides fast and non-destructive iV imaging for subcell analysis throughout the entire device fabrication process, from early-stage precursors to fully completed tandem devices. Although the accuracy of this method was demonstrated across various tandem configurations, structural and experimental factors may introduce uncertainties in the measurements. Therefore, **Chapter 5** conducted a systematic uncertainty analysis to evaluate the method's reliability under practical measurement conditions. The sources of uncertainty were categorised into three groups: (a) optical mismatch between single-junction calibration cells and tandem subcells, (b) internal optical interactions within the tandem stack, and (c) setup-related effects.

Each source was quantitatively assessed, and where applicable, strategies were proposed to minimise or eliminate its contribution to the overall uncertainty.

Finally, **Chapter 6** expanded the application of luminescence-based imaging by developing a novel and fully contactless method for determining n_i. The approach integrates the iV-extraction technique developed in earlier chapters with a previously established method for quantifying Δn. Analytical modelling and experimental validation confirmed the method's accuracy for n_i in Si materials. Unlike conventional techniques, this method does not rely on specially designed device structures or detailed knowledge of material parameters, making it particularly well-suited for emerging PV materials, such as PVKs, where key material properties often remain uncertain.

7.1 Contributions

The contributions of each chapter are summarised in this section:

Chapter 3: Spatially Resolved Determination of the Implied Voltage in Silicon Solar Cells

- A novel calibration method was introduced for determining spatially resolved iV in Si solar cells and wafers using a suitably selected BPF.
- A comprehensive modelling framework was developed to identify the optimal BPF range by quantifying the impact of key optical parameters, including the p, R, and d, on the accuracy of iV extraction. The analysis also incorporated both Si- and InGaAs-based detectors in evaluating the optimal BPF range.
- Si-based detectors, due to their limited sensitivity at longer wavelengths, were shown to inherently suppress luminescence variations arising from optical mismatch and, in some cases, can effectively function as a built-in BPF. However, for both detection systems, limiting the detection range to wavelengths up to 1,050 nm ($\lambda_2 \leq$ 1,050 nm) significantly reduced iV errors across a wide range of devices.
- Experimental validation was performed using both PL and EL imaging of Si wafers and cells with diverse optical properties. A single calibration cell with distinct optical properties from the measured cells was used to extract iV maps of other samples. The results demonstrated strong agreement with model predictions, confirming the robustness of the method. Additionally, a detailed SNR analysis identified a practical range for BPF cut-off wavelengths (1,010 nm < $\lambda_2 \leq$ 1,050 nm), which balances the suppression of optical sensitivity with adequate

signal quality. Within this range, iV errors were consistently below 3 mV for Si solar cells and 5 mV for Si wafers.

Chapter 4: Spatially Resolved Determination of the Implied Voltage in PVK/Si Tandem Cells

- A simulation framework was developed to identify optimal BPF detection windows for each subcell across a wide range of PVK/Si tandem device configurations. Two calibration strategies were investigated:
    - Building on the method developed in Chapter 3, single-junction PVK and Si calibration cells were implemented for iV determination of each subcell within tandem devices. The effectiveness of various BPFs in mitigating optical mismatch between calibration cells and tandem subcells was evaluated across devices with distinct optical properties.
    - In scenarios where dedicated calibration cells are unavailable, an alternative light source–based calibration approach was introduced. This method is based on a simplified form of Planck's law, in which both f and A (or EQE) are treated as constants, with the latter approximated by the modelling-derived calibration constant C. The correlation between the optimal value for C and a suitable BPF were determined.
- The analysis identified BPF cut-offs of $\lambda_2 \leq 730$ nm for the PVK subcell and $\lambda_2 \leq 1{,}050$ nm for the Si subcell, regardless of the optical properties of either the tandem subcells or the calibration cells. For the light source–based method, optimal accuracy was obtained when C was within 0.55–0.65 for the PVK subcell and 0.65–0.75 for the Si subcell, with a slightly narrower BPF required for the Si subcell ($\lambda_2 \leq$,1025 nm). Both approaches achieved iV extraction errors below 1%, with the cell-based calibration consistently yielding slightly lower errors.
- Experimental validation on multiple monolithic PVK/Si tandem devices using EL imaging confirmed the effectiveness of the proposed BPF ranges, with iV values closely matching simulations and remaining within a 1% error margin. In this validation, a blackbody lamp with a well-known photon flux was used as a calibration source for the light source–based approach.
- By acquiring iV images at multiple injection levels, the method enabled spatially resolved pseudo-dark J–iV extraction for each subcell. This revealed localised electrical non-uniformities such as shunting, recombination hotspots, and resistive losses, which are critical for performance analysis and quality control.

- Beyond indoor characterisation, the cell-based calibration approach developed in this thesis has also been extended to outdoor PL imaging of solar cells and modules. A recent study [178] demonstrated that using a single calibration cell with an appropriately selected BPF enables accurate iV mapping of PVK cells and mini modules under direct sunlight. This extension provides a practical pathway for field-stability diagnostics and large-area quality control without the need for sample-specific calibration.

Chapter 5: Uncertainty Analysis of the Implied Voltage in PVK/Si Tandem Cells

a) Differences between the properties of the calibration and measured subcells

- Compared to single-junction cells, the optical properties of each subcell in a tandem configuration are altered. The presence of adjacent layers modifies the front reflectance of the Si subcell and the rear reflectance of the PVK subcell. These variations introduced iV errors of ±7 mV for Si and under ±12 mV for PVK over the selected BPF ranges.
- The impact of bandgap mismatch between calibration and measured PVK cells was also investigated by simulating devices with bandgaps ranging from 1.55 to 1.68 eV. Across this range, iV errors remained within ±3 mV over the BPF range, confirming the method is robust to material variations.
- Discrepancies between iV and V_{term} in low-performance PVK cells used as calibration references can lead to inaccurate iV determination. Although this issue has not been observed in high-performance PVK cells, their limited availability may restrict broader implementation of the method. To overcome this constraint, this chapter demonstrated, for the first time, the novel use of a commercial LED as a calibration device. In this thesis, a planar LED with a peak emission at 760 nm was successfully employed as a calibration device to determine the iV images in both single-junction and tandem PVK configurations, with uncertainties remaining below 1% (less than ±7 mV). This advancement significantly simplifies the calibration procedure and enhances its practicality for widespread use in both research and industrial settings.

b) Optical interactions within tandem devices

- Luminescence coupling was shown not to introduce additional uncertainty. The re-emitted signal continues to accurately represent the subcell-specific iV. Spectral crosstalk was also minimal, as PVK emission (700–800 nm) and Si emission (950–1,350 nm) remained well-separated. The use of narrow BPFs further suppressed any residual spectral overlap.

c) Setup-related effects

- The effect of different illumination angles in PL measurements on iV extraction was evaluated. It was shown that deviations from normal incidence, up to 45°, introduced uncertainties below ±1 mV.
- A generalised temperature-uncertainty model was developed to quantify iV errors arising from thermal fluctuations. For Si cells, $V_{\text{term,calib}}$ was identified as the dominant temperature-sensitive parameter. The specific Si PERC cell used in this study exhibited a coefficient of -2.2 mV/°C, falling within the typical range of −1.5 and −2.5 mV/°C. Therefore, accurate monitoring of the calibration cell's temperature during the initial calibration step ensures that subsequent measurements have minimal sensitivity to temperature, eliminating the need for post-processing corrections. In contrast, over the narrow BPF range, PVK cells exhibited significant temperature dependence in both detected luminescence ($\Delta\phi_{\text{cell}}^{\text{detect}}$, $\Delta\phi_{\text{calib}}^{\text{detect}}$) and $V_{\text{term,calib}}$. Due to the compositional variability of PVKs, dedicated temperature-dependent characterisation is required for each sample. For the specific PVK device studied, the temperature-induced iV uncertainty was determined to be ±2 mV/°C.
- **Total uncertainty**: Accounting for all identified uncertainty sources, the maximum absolute deviation in iV determination remained within 7.3 mV for the Si subcell and 12.5 mV for the PVK subcell, based on the optimised BPFs of Chapter 4 ($\lambda_2 \leq$ 1,050 nm for Si; $\lambda_2 \leq$ 730 nm for PVK). These findings confirm the method's suitability for robust and scalable iV characterisation in both research and industrial tandem PV applications.

Chapter 6: Extraction of the Intrinsic Carrier via Photoluminescence

- A new and novel methodology for determining n_i using PL measurements was described in detail, based on combining the extracted iV with a dynamic calibration approach for Δn determination.
- An uncertainty analysis was presented to assess the influence of key parameters on n_{i} accuracy. For typical Si cells, the total absolute uncertainty remained below 19%. The experimental measurements conducted on Si solar cells confirmed the accuracy of the method, showing an absolute deviation of 7.3% from reference values, well within the range predicted by modelling. Its independence from device structure and material-specific inputs enables accurate n_{i} extraction in emerging PV materials, such as PVK, where conventional techniques are limited by parameter uncertainty and design constraints.

7.2 Limitations of the research

This thesis establishes and validates a luminescence-based framework for iV extraction and extends it to the contactless extraction of n_i. The main limitations that require further investigation to support wider applicability and implementation include:

- The temperature dependence of PVKs is device-specific. Although a temperature uncertainty analysis framework was established, compositional variability in PVKs necessitates temperature characterisation for each device to achieve high accuracy measurements and reliable uncertainty estimates.
- Accurate iV mapping relies on a well-characterised calibration cell. In some scenarios, limited availability of suitable high-performance calibration cells may limit broad deployment. As demonstrated here, this can be mitigated using an LED-based calibration approach.
- The novel contactless method for extracting n_i is well suited to emerging materials where fundamental parameters are often unknown. However, the modelled total uncertainty indicates that current precision is lower than that of established (but more complex) techniques for c-Si. In Si HJT cells, extracted n_i values agreed well with reference values (within a 7.3% absolute deviation), although a slight upward trend with injection level was observed. The origin of this trend, potentially linked to localised defects or injection-dependent recombination dynamics, requires further investigation.

7.3 Future work and practical applications

Future work and practical implementation derived from the outcomes of this thesis are described below:

- While the methodology for iV extraction was demonstrated for PVK, Si, and PVK/Si tandem devices, it can be extended to a wider range of PV technologies, including III–V compounds, CIGS, CdTe, multijunction devices, and other emerging or hybrid absorber materials**.** By tailoring the BPF to match the high-energy tail of each material's emission spectrum, the same contactless calibration framework can be applied for accurate iV extraction in novel tandem architectures where material properties are not yet well-defined.
- In Chapter 5, an analytical framework was developed to quantify the temperature sensitivity of iV by identifying the key temperature-dependent parameters affecting iV extraction. While this approach was applied to Si and PVK cells over moderate temperature ranges, the method itself is

general and can be extended to a wider range of PV materials and operating conditions. Applying this framework to other materials with distinct thermal and optical properties would offer valuable insights into device behaviour under realistic conditions. This is particularly relevant for tandem devices, where the distinct thermal responses of PVK and Si, combined with optoelectronic coupling, can lead to complex, interdependent behaviour. Extending this approach to PVK/Si tandems with further refinement could enable subcell-specific analysis of thermal losses and contribute to improving device stability and thermal robustness. These insights would support progress in resolving key industrialisation barriers, particularly those related to thermal and operational stability.

- In Chapter 6, a new approach for extracting n_i via PL-based measurements was presented and validated on the Si solar cell. A key advantage is its minimal dependence on material properties and device structure, making it well-suited for application to other materials, particularly those whose material properties are less well-known. Future work could focus on utilising this approach for n_i estimation in emerging materials, such as PVK, to enable more accurate quantitative assessment of carrier properties such as lifetime and recombination dynamics. This would be highly beneficial for improving material understanding and accelerating the development of more efficient PV technologies.
- Furthermore, the n_i extraction methodology presented in Chapter 6 has potential for further extension through temperature-dependent measurements. Incorporating such measurements would enable quantification of the temperature dependence of n_i, which plays a critical role in determining recombination dynamics, carrier lifetimes, and overall device behaviour. These measurements would support the development of more accurate physical models and assist in identifying performance-limiting mechanisms under realistic operating conditions.
- The presented method for iV estimation can be well adopted for module characterisation and industrial-scale in-line inspection to quantify the spatial non-uniformities associated with defect-induced and local performance losses across the device. It can be performed in a fully contactless manner and without requiring prior knowledge of the device structure or optical properties, making it suitable for field-testing setups and automated outdoor inspection platforms.
- To support practical deployment of the proposed methods in research and industry, a standardised implementation workflow is recommended. The process begins with accurate iV mapping, by selecting a BPF with a cut-off wavelength matching to the emission spectrum and

performing calibration using either a reference cell or a suitable LED. For n_i determination, this calibrated iV data must be integrated with Δn extraction (e.g., via dynamic calibration) with continuous temperature monitoring. Temperature monitoring (and, where possible, control) is essential for limiting iV uncertainty and extracting accurate n_i values, as n_i is inherently temperature dependent.

References

[1] NASA, "Global temperature - Earth indicator." https://climate.nasa.gov/vital-signs/global-temperature/?intent=121 (accessed 2025).

[2] Intergovernmental Panel on Climate Change (IPCC), "Climate change in data." https://www.ipcc.ch/report/ar6/wg1/resources/climate-change-in-data/ (accessed 2025).

[3] G. W. Crabtree and N. S. Lewis, "Solar energy conversion," *Physics Today,* vol. 60, no. 3, pp. 37-42, 2007.

[4] A. O. Ali *et al.*, "Advancements in photovoltaic technology: A comprehensive review of recent advances and future prospects," *Energy Conversion and Management: X,* p. 100952, 2025.

[5] International Energy Agency (IEA), "Solar PV." https://www.iea.org/energy-system/renewables/solar-pv (accessed 2025).

[6] Lazard, "Levelized cost of energy +." https://www.lazard.com/media/eijnqja3/lazards-lcoeplus-june-2025.pdf (accessed 2025).

[7] DNV, "Energy transition outlook 2024: A global and regional forecast to 2050." https://www.dnv.com/energy-transition-outlook/carbon-capture-storage/ (accessed 2024).

[8] AltEnergyMag, "Solar photovoltaic (PV) market." https://www.altenergymag.com/content.php?post=44561 (accessed 2025).

[9] Solar Power Europe, "Global market outlook for solar power 2025–2029." https://www.solarpowereurope.org/insights/outlooks/global-market-outlook-for-solar-power-2025-2029/detail (accessed 2025).

[10] A. A. Yaroshevsky, "Abundances of chemical elements in the Earth's crust," *Geochemistry International,* vol. 44, pp. 48-55, 2006.

[11] C. Battaglia, A. Cuevas, and S. De Wolf, "High-efficiency crystalline silicon solar cells: Status and perspectives," *Energy & Environmental Science,* vol. 9, no. 5, pp. 1552-1576, 2016.

[12] M. A. Green, "Silicon solar cells: Evolution, high-efficiency design and efficiency enhancements," *Semiconductor Science and Technology,* vol. 8, no. 1, p. 1, 1993.

[13] A. Smets, K. Jäger, O. Isabella, R. Van Swaaij, and M. Zeman, *Solar Energy: The Physics and Engineering of Photovoltaic Conversion, Technologies and Systems*. Bloomsbury Publishing, 2016.

[14] A. Ndiaye, A. Charki, A. Kobi, C. M. Kébé, P. A. Ndiaye, and V. Sambou, "Degradations of silicon photovoltaic modules: A literature review," *Solar Energy,* vol. 96, pp. 140-151, 2013.

[15] A. M. Oni, A. S. Mohsin, M. M. Rahman, and M. B. H. Bhuian, "A comprehensive evaluation of solar cell technologies, associated loss mechanisms, and efficiency enhancement strategies for photovoltaic cells," *Energy Reports,* vol. 11, pp. 3345-3366, 2024.

[16] M. A. Green, "Radiative efficiency of state-of-the-art photovoltaic cells," *Progress in Photovoltaics: Research and Applications,* vol. 20, no. 4, pp. 472-476, 2012.

[17] M. Victoria *et al.*, "Solar photovoltaics is ready to power a sustainable future," *Joule,* vol. 5, no. 5, pp. 1041-1056, 2021.

[18] C. Ballif, F. J. Haug, M. Boccard, P. J. Verlinden, and G. Hahn, "Status and perspectives of crystalline silicon photovoltaics in research and industry," *Nature Reviews Materials,* vol. 7, no. 8, pp. 597-616, 2022.

[19] National Renewable Energy Laboratory (NREL), "Best research-cell efficiency chart." https://www2.nrel.gov/pv/cell-efficiency (accessed 2025).

[20] A. Richter, M. Hermle, and S. W. Glunz, "Reassessment of the limiting efficiency for crystalline silicon solar cells," *IEEE Journal of Photovoltaics,* vol. 3, no. 4, pp. 1184-1191, 2013.

[21] W. Shockley and H. Queisser, "Detailed balance limit of efficiency of p-n junction solar cells," *Journal of Applied Physics,* vol. 32, no. 3, pp. 510–519, 1961.

[22] K. Alberi *et al.*, "A roadmap for tandem photovoltaics," *Joule,* vol. 8, no. 3, pp. 658-692, 2024.

[23] F. Martinho, "Challenges for the future of tandem photovoltaics on the path to terawatt levels: A technology review," *Energy & Environmental Science,* vol. 14, no. 7, pp. 3840-3871, 2021.

[24] T. Leijtens, K. A. Bush, R. Prasanna, and M. D. McGehee, "Opportunities and challenges for tandem solar cells using metal halide perovskite semiconductors," *Nature Energy,* vol. 3, no. 10, pp. 828-838, 2018.

[25] F. Fu *et al.*, "Monolithic perovskite-silicon tandem solar cells: From the lab to fab?," *Advanced Materials,* vol. 34, no. 24, p. 2106540, 2022.

[26] J. S. Manser, J. A. Christians, and P. V. Kamat, "Intriguing optoelectronic properties of metal halide perovskites," *Chemical Reviews,* vol. 116, no. 21, pp. 12956-13008, 2016.

[27] M. A. Green, "Intrinsic concentration, effective densities of states, and effective mass in silicon," *Journal of Applied Physics,* vol. 67, no. 6, pp. 2944-2954, 1990.

[28] M. A. Green, A. Ho-Baillie, and H. J. Snaith, "The emergence of perovskite solar cells," *Nature Photonics,* vol. 8, no. 7, pp. 506-514, 2014.

[29] C. Zhang and N.-G. Park, "Materials and methods for cost-effective fabrication of perovskite photovoltaic devices," *Communications Materials,* vol. 5, no. 1, p. 194, 2024.

[30] L. Yan, C. Han, B. Shi, Y. Zhao, and X. Zhang, "A review on the crystalline silicon bottom cell for monolithic perovskite/silicon tandem solar cells," *Materials Today Nano,* vol. 7, p. 100045, 2019.

[31] M. A. Green *et al.*, "Solar cell efficiency tables (Version 63)," *Progress in Photovoltaics: Research and Applications,* vol. 32, no. 1, pp. 3-13, 2024.

[32] L. Duan *et al.*, "Stability challenges for the commercialisation of perovskite–silicon tandem solar cells," *Nature Reviews Materials,* vol. 8, no. 4, pp. 261-281, 2023.

[33] M. De Bastiani, M. Babics, E. Aydin, A. S. Subbiah, L. Xu, and S. De Wolf, "All set for efficient and reliable perovskite/silicon tandem photovoltaic modules?," *Solar RRL,* vol. 6, no. 3, p. 2100493, 2022.

[34] E. Aydin *et al.*, "Pathways toward commercial perovskite/silicon tandem photovoltaics," *Science,* vol. 383, no. 6679, p. eadh3849, 2024.

[35] T. Trupke, R. Bardos, M. Schubert, and W. Warta, "Photoluminescence imaging of silicon wafers," *Applied Physics Letters,* vol. 89, no. 4, 2006.

[36] T. Fuyuki, H. Kondo, T. Yamazaki, Y. Takahashi, and Y. Uraoka, "Photographic surveying of minority carrier diffusion length in polycrystalline silicon solar cells by electroluminescence," *Applied Physics Letters,* vol. 86, no. 26, 2005.

[37] Z. Hameiri *et al.*, "Photoluminescence and electroluminescence imaging of perovskite solar cells," *Progress in Photovoltaics: Research and Applications,* vol. 23, no. 12, pp. 1697-1705, 2015.

[38] A. D. Bui *et al.*, "Contactless and spatially resolved determination of current–voltage curves in perovskite solar cells via photoluminescence," *Solar RRL,* vol. 5, no. 8, p. 2100348, 2021.

[39] A. Mahboubi Soufiani, Y. Zhu, N. Mussakhanuly, J. S. Yun, T. Trupke, and Z. Hameiri, "Contactless series resistance imaging of perovskite solar cells via inhomogeneous illumination," *Solar RRL,* vol. 5, no. 12, p. 2100655, 2021.

[40] S. Nie, S. T. Kristensen, A. Gu, R. L. Chin, T. Trupke, and Z. Hameiri, "Photoluminescence-based spatially resolved temperature coefficient maps of silicon wafers and solar cells," *IEEE Journal of Photovoltaics,* vol. 10, no. 2, pp. 585-594, 2019.

[41] Z. Hameiri, P. Chaturvedi, and K. R. McIntosh, "Imaging the local ideality factor by contactless photoluminescence measurement," *Applied Physics Letters,* vol. 103, no. 2, p. 023501, 2013.

[42] M. Glatthaar, J. Haunschild, M. Kasemann, J. Giesecke, W. Warta, and S. Rein, "Spatially resolved determination of dark saturation current and series resistance of silicon solar cells," *Physica Status Solidi–Rapid Research Letters,* vol. 4, no. 1-2, pp. 13-15, 2010.

[43] S. Nie, Y. Zhu, O. Kunz, T. Trupke, and Z. Hameiri, "Advanced photoluminescence imaging using non-uniform excitation," *Progress in Photovoltaics: Research and Applications,* vol. 30, no. 4, pp. 349-359, 2022.

[44] H. Sio, S. P. Phang, T. Trupke, and D. MacDonald, "An accurate method for calibrating photoluminescence-based lifetime images on multi-crystalline silicon wafers," *Solar Energy Materials and Solar Cells,* vol. 131, pp. 77-84, 2014.

[45] B. Hallam, B. Tjahjono, T. Trupke, and S. Wenham, "Photoluminescence imaging for determining the spatially resolved implied open circuit voltage of silicon solar cells," *Journal of Applied Physics,* vol. 115, no. 4, p. 044901, 2014.

[46] P. Würfel, "The chemical potential of radiation," *Journal of Physics C: Solid State Physics,* vol. 15, no. 18, p. 3967, 1982.

[47] M. Tebyetekerwa *et al.*, "Quantifying quasi-Fermi level splitting and mapping its heterogeneity in atomically thin transition metal dichalcogenides," *Advanced Materials,* vol. 31, no. 25, p. 1900522, 2019.

[48] J. K. Katahara and H. W. Hillhouse, "Quasi-Fermi level splitting and sub-bandgap absorptivity from semiconductor photoluminescence," *Journal of Applied Physics,* vol. 116, no. 17, p. 173504, 2014.

[49] I. L. Braly *et al.*, "Hybrid perovskite films approaching the radiative limit with over 90% photoluminescence quantum efficiency," *Nature Photonics,* vol. 12, no. 6, pp. 355-361, 2018.

[50] A. M. Soufiani *et al.*, "Implied open-circuit voltage imaging via a single bandpass filter method—its first application in perovskite solar cells," *Advanced Functional Materials,* vol. 33, no. 3, p. 2210592, 2023.

[51] O. Breitenstein, H. Höffler, and J. Haunschild, "Photoluminescence image evaluation of solar cells based on implied voltage distribution," *Solar Energy Materials and Solar Cells,* vol. 128, pp. 296-299, 2014.

[52] C. Shen, H. Kampwerth, and M. A. Green, "Photoluminescence based open circuit voltage and effective lifetime images re-interpretation for solar cells: The influence of horizontal balancing currents," *Solar Energy Materials and Solar Cells,* vol. 130, pp. 393-396, 2014.

[53] M. Stolterfoht *et al.*, "How to quantify the efficiency potential of neat perovskite films: Perovskite semiconductors with an implied efficiency exceeding 28%," *Advanced Materials,* vol. 32, no. 17, p. 2000080, 2020.

[54] M. Kasemann, L. M. Reindl, B. Michl, W. Warta, A. Schütt, and J. Carstensen, "Contactless qualitative series resistance imaging on solar cells," *IEEE Journal of Photovoltaics,* vol. 2, no. 2, pp. 181-183, 2012.

[55] S. Jafari, M. Abbott, D. Zhang, J. Wu, F. Jiang, and Z. Hameiri, "Bulk defect characterization in metalized solar cells using temperature-dependent Suns-V_{oc} measurements," *Solar Energy Materials and Solar Cells,* vol. 236, p. 111530, 2022.

[56] T. Trupke, E. Pink, R. Bardos, and M. Abbott, "Spatially resolved series resistance of silicon solar cells obtained from luminescence imaging," *Applied Physics Letters,* vol. 90, no. 9, 2007.

[57] S. M. Sze, Y. Li, and K. K. Ng, *Physics of Semiconductor Devices*. John Wiley & Sons, 2021.

[58] R. A. Sinton and A. Cuevas, "Contactless determination of current–voltage characteristics and minority-carrier lifetimes in semiconductors from quasi-steady-state photoconductance data," *Applied Physics Letters,* vol. 69, no. 17, pp. 2510-2512, 1996.

[59] O. Fischer *et al.*, "Versatile implied open-circuit voltage imaging method and its application in monolithic tandem solar cells," *Progress in Photovoltaics: Research and Applications,* vol. 33, no. 1, pp. 40-53, 2025.

[60] S. Zandi *et al.*, "Luminescence-based implied voltage imaging of tandem solar cells using bandpass filters," *Small Methods,* vol. 9, no. 4, p. 2401003, 2025.

[61] T. Trupke, R. Bardos, M. Abbott, and J. Cotter, "Suns-photoluminescence: Contactless determination of current-voltage characteristics of silicon wafers," *Applied Physics Letters,* vol. 87, no. 9, p. 093503, 2005.

[62] A. Dasgupta *et al.*, "Visualizing macroscopic inhomogeneities in perovskite solar cells," *ACS Energy Letters,* vol. 7, no. 7, pp. 2311-2322, 2022.

[63] A. D. Bui *et al.*, "Spatially resolved power conversion efficiency for perovskite solar cells via bias-dependent photoluminescence imaging," *Cell Reports Physical Science,* vol. 4, no. 11, p. 101641, 2023.

[64] A. Al-Ashouri *et al.*, "Monolithic perovskite/silicon tandem solar cell with >29% efficiency by enhanced hole extraction," *Science,* vol. 370, no. 6522, pp. 1300-1309, 2020.

[65] R. A. Sinton, A. Cuevas, and M. Stuckings, "Quasi-steady-state photoconductance, a new method for solar cell material and device characterization," 25th IEEE Photovoltaic Specialists Conference. 1996.

[66] P. Würfel, *Physics of solar cells: From principles to new concepts*. Wiley-VCH, 2008.

[67] M. A. Green, *Solar cells: Operating principles, technology, and system applications*. Prentice-Hall, 1982.

[68] S. Siebentritt, T. P. Weiss, M. Sood, M. H. Wolter, A. Lomuscio, and O. Ramirez, "How photoluminescence can predict the efficiency of solar cells," *Journal of Physics: Materials,* vol. 4, no. 4, p. 042010, 2021.

[69] G. Masetti, M. Severi, and S. Solmi, "Modeling of carrier mobility against carrier concentration in arsenic-, phosphorus-, and boron-doped silicon," *IEEE Transactions on Electron Devices,* vol. 30, no. 7, pp. 764-769, 2005.

[70] Z. Hameiri, F. Rougieux, R. Sinton, and T. Trupke, "Contactless determination of the carrier mobility sum in silicon wafers using combined photoluminescence and photoconductance measurements," *Applied Physics Letters,* vol. 104, no. 7, p. 073506, 2014.

[71] D. Klaassen, "A unified mobility model for device simulation—I. Model equations and concentration dependence," *Solid-State Electronics,* vol. 35, no. 7, pp. 953-959, 1992.

[72] S. Kasap, "Hall effect in semiconductors," *Electron. Booklet,* vol. 1, no. 1, pp. 1-3, 2001.

[73] N. D. Reynolds, C. D. Panda, and J. M. Essick, "Capacitance-voltage profiling: Research-grade approach versus low-cost alternatives," *American Journal of Physics,* vol. 82, no. 3, pp. 196-205, 2014.

[74] D. K. Schroder, *Semiconductor material and device characterization*. John Wiley & Sons, 2015.

[75] Sinton Instruments, "Photoconductance lifetime testers." https://www.sintoninstruments.com/ (accessed 2025).

[76] K. McIntosh and R. A. Sinton, "Uncertainty in photoconductance lifetime measurements that use an inductive-coil detector," 23rd European Photovoltaic Solar Energy Conference and Exhibition. 2008.

[77] A. F. Thomson, Z. Hameiri, N. E. Grant, C. J. Price, Y. Di, and J. Spurgin, "Uncertainty in photoconductance measurements of the emitter saturation current," *IEEE Journal of Photovoltaics,* vol. 3, no. 4, pp. 1200-1207, 2013.

[78] T. Roth, J. Hohl-Ebinger, E. Schmich, W. Warta, S. W. Glunz, and R. A. Sinton, "Improving the accuracy of Suns-V_{oc} measurements using spectral mismatch correction," 33rd IEEE Photovoltaic Specialists Conference. 2008.

[79] R. Bardos, T. Trupke, M. C. Schubert, and T. Roth, "Trapping artifacts in quasi-steady-state photoluminescence and photoconductance lifetime measurements on silicon wafers," *Applied Physics Letters,* vol. 88, no. 5, p. 053504, 2006.

[80] D. Macdonald and A. Cuevas, "Trapping of minority carriers in multicrystalline silicon," *Applied Physics Letters,* vol. 74, no. 12, pp. 1710-1712, 1999.

[81] D. Neuhaus, P. Cousins, and A. Aberle, "Trapping and junction-related perturbations of the effective excess carrier lifetime," 3rd IEEE World Conference on Photovoltaic Energy Conversion. 2003

[82] M. Planck, *The theory of heat radiation*. Blakiston, 1914.

[83] P. Würfel, S. Finkbeiner, and E. Daub, "Generalized Planck's radiation law for luminescence via indirect transitions," *Applied Physics A,* vol. 60, pp. 67-70, 1995.

[84] G. El-Hajje *et al.*, "Quantification of spatial inhomogeneity in perovskite solar cells by hyperspectral luminescence imaging," *Energy & Environmental Science,* vol. 9, no. 7, pp. 2286-2294, 2016.

[85] T. Trupke, E. Daub, and P. Würfel, "Absorptivity of silicon solar cells obtained from luminescence," *Solar Energy Materials and Solar Cells,* vol. 53, no. 1-2, pp. 103-114, 1998.

[86] U. Rau, "Reciprocity relation between photovoltaic quantum efficiency and electroluminescent emission of solar cells," *Physical Review B—Condensed Matter and Materials Physics,* vol. 76, no. 8, p. 085303, 2007.

[87] F. Lang *et al.*, "Revealing fundamental efficiency limits of monolithic perovskite/silicon tandem photovoltaics through subcell characterization," *ACS Energy Letters,* vol. 6, no. 11, pp. 3982-3991, 2021.

[88] P. Fassl *et al.*, "Revealing the internal luminescence quantum efficiency of perovskite films via accurate quantification of photon recycling," *Matter,* vol. 4, no. 4, pp. 1391-1412, 2021.

[89] M. Meusel, C. Baur, G. Létay, A. Bett, W. Warta, and E. Fernandez, "Spectral response measurements of monolithic GaInP/Ga(In)As/Ge triple-junction solar cells: Measurement artifacts and their explanation," *Progress in Photovoltaics: Research and Applications,* vol. 11, no. 8, pp. 499-514, 2003.

[90] Z. Hameiri and P. Chaturvedi, "Spatially resolved electrical parameters of silicon wafers and solar cells by contactless photoluminescence imaging," *Applied Physics Letters,* vol. 102, no. 7, 2013.

[91] I. Zafirovska, M. K. Juhl, A. Ciesla, R. Evans, and T. Trupke, "Low temperature sensitivity of implied voltages from luminescence measured on crystalline silicon solar cells," *Solar Energy Materials and Solar Cells,* vol. 199, pp. 50-58, 2019.

[92] E. Yablonovitch and G. D. Cody, "Intensity enhancement in textured optical sheets for solar cells," *IEEE Transactions on Electron Devices,* vol. 29, no. 2, pp. 300-305, 1982.

[93] C. Barugkin, T. Allen, T. K. Chong, T. P. White, K. J. Weber, and K. R. Catchpole, "Light trapping efficiency comparison of Si solar cell textures using spectral photoluminescence," *Optics Express,* vol. 23, no. 7, pp. A391-A400, 2015.

[94] A. Fell *et al.*, "Modeling parasitic absorption in silicon solar cells with a near-surface absorption parameter," *Solar Energy Materials and Solar Cells,* vol. 236, p. 111534, 2022.

[95] J. Hartman and M. Lind, "Spectral response measurements for solar cells," *Solar Cells,* vol. 7, no. 1-2, pp. 147-157, 1982.

[96] R. A. Sinton and A. Cuevas, "A quasi-steady-state open-circuit voltage method for solar cell characterization," 16th European Photovoltaic Solar Energy Conference. 2000.

[97] A. Delamarre, L. Lombez, and J.-F. Guillemoles, "Contactless mapping of saturation currents of solar cells by photoluminescence," *Applied Physics Letters,* vol. 100, no. 13, p. 131108, 2012.

[98] A. Sproul, M. Green, and J. Zhao, "Improved value for the silicon intrinsic carrier concentration at 300 K," *Applied Physics Letters,* vol. 57, no. 3, pp. 255-257, 1990.

[99] A. Sproul and M. Green, "Intrinsic carrier concentration and minority-carrier mobility of silicon from 77 to 300 K," *Journal of Applied Physics,* vol. 73, no. 3, pp. 1214-1225, 1993.

[100] K. Misiakos and D. Tsamakis, "Accurate measurements of the silicon intrinsic carrier density from 78 to 340 K," *Journal of Applied Physics,* vol. 74, no. 5, pp. 3293-3297, 1993.

[101] P. P. Altermatt, A. Schenk, F. Geelhaar, and G. Heiser, "Reassessment of the intrinsic carrier density in crystalline silicon in view of band-gap narrowing," *Journal of Applied Physics,* vol. 93, no. 3, pp. 1598-1604, 2003.

[102] R. Couderc, M. Amara, and M. Lemiti, "Reassessment of the intrinsic carrier density temperature dependence in crystalline silicon," *Journal of Applied Physics,* vol. 115, no. 9, p. 093705, 2014.

[103] M. A. Green, "Improved silicon optical parameters at 25°C, 295 K and 300 K including temperature coefficients," *Progress in Photovoltaics: Research and Applications,* vol. 30, no. 2, pp. 164-179, 2022.

[104] Photon etc., "Alizé 1.7 - Scientific SWIR Camera." https://www.photonetc.com/products/alize-1-7 (accessed 2025).

[105] M. A. Green, "The passivated emitter and rear cell (PERC): From conception to mass production," *Solar Energy Materials and Solar Cells,* vol. 143, pp. 190-197, 2015.

[106] P. Verlinden, "Interdigitated back contact solar cells," *Photovoltaic Solar Energy: From Fundamentals to Applications,* pp. 92-103, 2016.

[107] A. M. Soufiani *et al.*, "Lessons learnt from spatially resolved electro-and photoluminescence imaging: Interfacial delamination in $CH_3NH_3PbI_3$ planar perovskite solar cells upon illumination," *Advanced Energy Materials,* vol. 7, no. 9, p. 1602111, 2017.

[108] J. R. Taylor, *An introduction to error analysis: The study of uncertainties in physical measurements*. MIT Press, 2022.

[109] I. T. Young, J. J. Gerbrands, and L. J. Van Vliet, *Fundamentals of image processing*. Delft University of Technology, 1998.

[110] D. Hinken, C. Schinke, S. Herlufsen, A. Schmidt, K. Bothe, and R. Brendel, "Experimental setup for camera-based measurements of electrically and optically stimulated luminescence of silicon solar cells and wafers," *Review of Scientific Instruments,* vol. 82, no. 3, 2011.

[111] D. Chung, B. Mitchell, M. Goodarzi, R. A. Sinton, D. Macdonald, and T. Trupke, "Uncertainty in photoluminescence metrology on multicrystalline silicon bricks and cross validation with wafers," *IEEE Journal of Photovoltaics,* vol. 7, no. 6, pp. 1701-1709, 2017.

[112] International Electrotechnical Commission, "IEC TS 60904-13 photovoltaic devices; part 13: Electroluminescence of photovoltaic modules." https://www.iec.ch/ (accessed 2018).

[113] X. Y. Chin *et al.*, "Interface passivation for 31.25%-efficient perovskite/silicon tandem solar cells," *Science,* vol. 381, no. 6653, pp. 59-63, 2023.

[114] Y. Wu *et al.*, "27.6% perovskite/c-Si tandem solar cells using industrial fabricated TOPCon device," *Advanced Energy Materials,* vol. 12, no. 27, p. 2200821, 2022.

[115] F. Sahli *et al.*, "Fully textured monolithic perovskite/silicon tandem solar cells with 25.2% power conversion efficiency," *Nature Materials,* vol. 17, no. 9, pp. 820-826, 2018.

[116] P. S. C. Schulze *et al.*, "25.1% high-efficiency monolithic perovskite silicon tandem solar cell with a high bandgap perovskite absorber," *Solar RRL,* vol. 4, no. 7, p. 2000152, 2020.

[117] Excelitas Technologies, "pco.edge 4.2 BI USB sCMOS Camera." https://www.excelitas.com/product/pcoedge-42-bi-usb-scmos-camera (accessed 2025).

[118] S. Albrecht *et al.*, "Monolithic perovskite/silicon-heterojunction tandem solar cells processed at low temperature," *Energy & Environmental Science,* vol. 9, no. 1, pp. 81-88, 2016.

[119] E. Aydin *et al.*, "Enhanced optoelectronic coupling for perovskite/silicon tandem solar cells," *Nature,* vol. 623, no. 7988, pp. 732-738, 2023.

[120] G. Wang *et al.*, "Molecular engineering of hole-selective layer for high band gap perovskites for highly efficient and stable perovskite-silicon tandem solar cells," *Joule,* vol. 7, no. 11, pp. 2583-2594, 2023.

[121] X. Liu *et al.*, "Perovskite solar cells based on spiro-OMeTAD stabilized with an alkylthiol additive," *Nature Photonics,* vol. 17, no. 1, pp. 96-105, 2023.

[122] M. Stolterfoht *et al.*, "The impact of energy alignment and interfacial recombination on the internal and external open-circuit voltage of perovskite solar cells," *Energy & Environmental Science,* vol. 12, no. 9, pp. 2778-2788, 2019.

[123] P. Caprioglio *et al.*, "On the relation between the open-circuit voltage and quasi-Fermi level splitting in efficient perovskite solar cells," *Advanced Energy Materials,* vol. 9, no. 33, p. 1901631, 2019.

[124] J. Warby *et al.*, "Mismatch of quasi–Fermi level splitting and V_{oc} in perovskite solar cells," *Advanced Energy Materials,* vol. 13, no. 48, p. 2303135, 2023.

[125] D. Alonso-Álvarez and N. Ekins-Daukes, "SPICE modelling of photoluminescence and electroluminescence based current-voltage curves of solar cells for concentration applications," *Journal of Green Engineering,* vol. 5, no. 4, pp. 33-48, 2016.

[126] B. Chen *et al.*, "Enhanced optical path and electron diffusion length enable high-efficiency perovskite tandems," *Nature Communications,* vol. 11, no. 1, p. 1257, 2020.

[127] I. J. Djeukeu, J. Horn, M. Meixner, E. Wagner, S. W. Glunz, and K. Ramspeck, "Subcell-resolved electroluminescence imaging of monolithic perovskite/silicon tandem solar cell for high-throughput characterization," *Solar RRL,* vol. 8, no. 19, p. 2400469, 2024.

[128] Y. Jiang *et al.*, "Optical analysis of perovskite/silicon tandem solar cells," *Journal of Materials Chemistry C,* vol. 4, no. 24, pp. 5679-5689, 2016.

[129] K. Jäger, J. Sutter, M. Hammerschmidt, P.-I. Schneider, and C. Becker, "Prospects of light management in perovskite/silicon tandem solar cells," *Nanophotonics,* vol. 10, no. 8, pp. 1991-2000, 2021.

[130] P. Tockhorn *et al.*, "Nano-optical designs for high-efficiency monolithic perovskite–silicon tandem solar cells," *Nature Nanotechnology,* vol. 17, no. 11, pp. 1214-1221, 2022.

[131] V. M. Caselli, Z. Wei, M. M. Ackermans, E. M. Hutter, B. Ehrler, and T. J. Savenije, "Charge carrier dynamics upon sub-bandgap excitation in methylammonium lead iodide thin films: Effects of Urbach tail, deep defects, and two-photon absorption," *ACS Energy Letters,* vol. 5, no. 12, pp. 3821-3827, 2020.

[132] R. Santbergen *et al.*, "Minimizing optical losses in monolithic perovskite/c-Si tandem solar cells with a flat top cell," *Optics Express,* vol. 24, no. 18, pp. A1288-A1299, 2016.

[133] M. Wright *et al.*, "Design considerations for the bottom cell in perovskite/silicon tandems: A terawatt scalability perspective," *Energy & Environmental Science,* vol. 16, no. 10, pp. 4164-4190, 2023.

[134] Fluxim AG, "Setfos." https://www.fluxim.com/ (accessed 2025).

[135] J. M. Siqueiros, R. Machorro, and L. E. Regalado, "Determination of the optical constants of MgF_2 and ZnS from spectrophotometric measurements and the classical oscillator method," *Applied Optics,* vol. 27, no. 12, pp. 2549-2553, 1988.

[136] Z. C. Holman *et al.*, "Infrared light management in high-efficiency silicon heterojunction and rear-passivated solar cells," *Journal of Applied Physics,* vol. 113, no. 1, 2013.

[137] T. Stübinger, "Optische Modellierung und Charakterisierung von organischen Donor-Akzeptor Solarzellen," Perspektivenverl., Bayreuth, Germany, 2005.

[138] J. Werner *et al.*, "Complex refractive indices of cesium–formamidinium-based mixed-halide perovskites with optical band gaps from 1.5 to 1.8 eV," *ACS Energy Letters,* vol. 3, no. 3, pp. 742-747, 2018.

[139] S. Altazin, L. Stepanova, J. Werner, B. Niesen, C. Ballif, and B. Ruhstaller, "Design of perovskite/crystalline-silicon monolithic tandem solar cells," *Optics Express,* vol. 26, no. 10, pp. A579-A590, 2018.

[140] E. D. Palik, *Handbook of optical constants of solids*. Academic Press, 1998.

[141] S. Adjokatse, H.-H. Fang, and M. A. Loi, "Broadly tunable metal halide perovskites for solid-state light-emission applications," *Materials Today,* vol. 20, no. 8, pp. 413-424, 2017.

[142] G. E. Eperon, S. D. Stranks, C. Menelaou, M. B. Johnston, L. M. Herz, and H. J. Snaith, "Formamidinium lead trihalide: A broadly tunable perovskite for efficient planar heterojunction solar cells," *Energy & Environmental Science,* vol. 7, no. 3, pp. 982-988, 2014.

[143] F. Hao, C. C. Stoumpos, R. P. Chang, and M. G. Kanatzidis, "Anomalous band gap behavior in mixed Sn and Pb perovskites enables broadening of absorption spectrum in solar cells," *Journal of the American Chemical Society,* vol. 136, no. 22, pp. 8094-8099, 2014.

[144] M. R. Vogt *et al.*, "Measurement of the optical constants of soda-lime glasses in dependence of iron content and modeling of iron-related power losses in crystalline Si solar cell modules," *IEEE Journal of Photovoltaics,* vol. 6, no. 1, pp. 111-118, 2015.

[145] S. Manzoor *et al.*, "Optical modeling of wide-bandgap perovskite and perovskite/silicon tandem solar cells using complex refractive indices for arbitrary-bandgap perovskite absorbers," *Optics Express,* vol. 26, no. 21, pp. 27441-27460, 2018.

[146] K. Tvingstedt *et al.*, "Radiative efficiency of lead iodide based perovskite solar cells," *Scientific Reports,* vol. 4, no. 1, p. 6071, 2014.

[147] Y. Lian *et al.*, "Ultralow-voltage operation of light-emitting diodes," *Nature Communications,* vol. 13, no. 1, p. 3845, 2022.

[148] T. Mochizuki *et al.*, "Solar-cell radiance standard for absolute electroluminescence measurements and open-circuit voltage mapping of silicon solar modules," *Journal of Applied Physics,* vol. 119, no. 3, 2016.

[149] E. F. Schubert, *Light-emitting diodes*. Cambridge University Press, 2018.

[150] O. A. Fedorova, K. A. Bulashevich, and S. Y. Karpov, "Critical aspects of AlGaInP-based LED design and operation revealed by full electrical-thermal-optical simulations," *Optics Express,* vol. 29, no. 22, pp. 35792-35805, 2021.

[151] P. Altieri *et al.*, "Internal quantum efficiency of high-brightness AlGaInP light-emitting devices," *Journal of Applied Physics,* vol. 98, no. 8, 2005.

[152] V. Kulakovskii, E. Lach, A. Forchel, and D. Grützmacher, "Band-gap renormalization and band-filling effects in a homogeneous electron-hole plasma in $In_{0.53}Ga_{0.47}As$/InP single quantum wells," *Physical Review B,* vol. 40, no. 11, p. 8087, 1989.

[153] C. Baur, M. Hermle, F. Dimroth, and A. W. Bett, "Effects of optical coupling in III-V multilayer systems," *Applied Physics Letters,* vol. 90, no. 19, 2007.

[154] K. Jäger, P. Tillmann, E. A. Katz, and C. Becker, "Perovskite/silicon tandem solar cells: Effect of luminescent coupling and bifaciality," *Solar RRL,* vol. 5, no. 3, p. 2000628, 2021.

[155] K. Nguyen *et al.*, "The role of luminescent coupling in monolithic perovskite/silicon tandem solar cells," *Small,* vol. 20, no. 46, p. 2403461, 2024.

[156] M. R. Vogt, "Development of physical models for the simulation of optical properties of solar cell modules," Technische Universität Hannover, Hannover, Germany, 2016.

[157] P. Kumar, M. K. Wiedmann, C. H. Winter, and I. Avrutsky, "Optical properties of Al_2O_3 thin films grown by atomic layer deposition," *Applied Optics,* vol. 48, no. 28, pp. 5407-5412, 2009.

[158] PV Lighthouse, "SunSolve Power." https://sunsolve.com/power/ (accessed 2025).

[159] S. M. Zhang *et al.*, "Illumination-dependent temperature coefficients of the electrical parameters of modern silicon solar cell architectures," *Nano Energy,* vol. 98, p. 107221, 2022.

[160] C. R. Osterwald, M. Campanelli, T. Moriarty, K. A. Emery, and R. Williams, "Temperature-dependent spectral mismatch corrections," *IEEE Journal of Photovoltaics,* vol. 5, no. 6, pp. 1692-1697, 2015.

[161] L. C. Chang *et al.*, "Enhanced efficiency and stability for the inverted high-bandgap perovskite solar cell via bottom passivation strategy," *Solar RRL,* vol. 8, no. 19, p. 2400391, 2024.

[162] Y. Zhu, T. Trupke, and Z. Hameiri, "A dynamic calibration method for injection-dependent charge carrier lifetime measurements," *Small Methods,* vol. 5, no. 9, p. 2100440, 2021.

[163] T. Trupke, R. Bardos, and M. Abbott, "Self-consistent calibration of photoluminescence and photoconductance lifetime measurements," *Applied Physics Letters,* vol. 87, no. 18, 2005.

[164] Z. Hameiri, F. Rougieux, R. Sinton, and T. Trupke, "Contactless determination of the carrier mobility sum in silicon wafers using combined photoluminescence and photoconductance measurements," *Applied Physics Letters,* vol. 104, no. 7, 2014.

[165] F. Peña-Camargo *et al.*, "Revealing the doping density in perovskite solar cells and its impact on device performance," *Applied Physics Reviews,* vol. 9, no. 2, 2022.

[166] S. Hubbard, "Recombination," *Photovoltaic Solar Energy: From Fundamentals to Applications,* pp. 39-46, 2016.

[167] H. T. Nguyen, S. C. Baker-Finch, and D. Macdonald, "Temperature dependence of the radiative recombination coefficient in crystalline silicon from spectral photoluminescence," *Applied Physics Letters,* vol. 104, no. 11, 2014.

[168] H. Nagel, C. Berge, and A. G. Aberle, "Generalized analysis of quasi-steady-state and quasi-transient measurements of carrier lifetimes in semiconductors," *Journal of Applied Physics,* vol. 86, no. 11, pp. 6218-6221, 1999.

[169] J. A. Giesecke, M. C. Schubert, and W. Warta, "Self-sufficient minority carrier lifetime in silicon from quasi-steady-state photoluminescence," *Physica Status Solidi (a),* vol. 209, no. 11, pp. 2286-2290, 2012.

[170] W. Bludau, A. Onton, and W. Heinke, "Temperature dependence of the band gap of silicon," *Journal of Applied Physics,* vol. 45, no. 4, pp. 1846-1848, 1974.

[171] K. Shanks *et al.*, "An experimental analysis of the optical, thermal and power to weight performance of plastic and glass optics with AR coatings for embedded CPV windows," *Solar Energy Materials and Solar Cells,* vol. 200, p. 110027, 2019.

[172] M. Ledinsky *et al.*, "Temperature dependence of the urbach energy in lead iodide perovskites," *Journal of Physical Chemistry Letters,* vol. 10, no. 6, pp. 1368-1373, 2019.

[173] S. Zandi, Z. Hameiri, A. M. Soufiani, J. W. Weber, and T. Trupke, "Simplified method for the conversion of luminescence signals from silicon wafers and solar cells into implied voltages," *Solar Energy Materials and Solar Cells,* vol. 269, p. 112716, 2024.

[174] A. H. T. Le, A. Srinivasa, S. G. Bowden, Z. Hameiri, and A. Augusto, "Temperature and illumination dependence of silicon heterojunction solar cells with a wide range of wafer resistivities," *Progress in Photovoltaics: Research and Applications,* vol. 31, no. 5, pp. 536-545, 2023.

[175] P. P. Altermatt *et al.*, "Numerical modeling of highly doped Si:P emitters based on Fermi–Dirac statistics and self-consistent material parameters," *Journal of Applied Physics,* vol. 92, no. 6, pp. 3187-3197, 2002.

[176] K. R. McIntosh and P. P. Altermatt, "A freeware 1D emitter model for silicon solar cells," 35th IEEE Photovoltaic Specialists Conference. 2010.

[177] PV Lighthouse, https://www.pvlighthouse.com.au (accessed 2025).

[178] F. Gayot *et al.*, "Outdoor implied open-circuit voltage imaging of perovskite solar cells using sunlight excitation," *Joule,* vol. 9, p. 101946, 2025.